a-Si: H/c-Si heterojunction solar cells: back side assessment and improvement

Silvia Martin de Nicolas

To cite this version:

Silvia Martin de Nicolas. a-Si: H/c-Si heterojunction solar cells: back side assessment and improvement. Other [cond-mat.other]. Université Paris Sud - Paris XI, 2012. English. NNT : 2012PA112253 . tel-00763300

HAL Id: tel-00763300
https://theses.hal.science/tel-00763300

Submitted on 10 Dec 2012

UNIVERSITE PARIS-SUD

ÉCOLE DOCTORALE : STITS
Laboratoire de Génie Électrique de Paris

DISCIPLINE PHYSIQUE

THÈSE DE DOCTORAT

soutenue le 22/10/2012

par

Sílvia MARTÍN DE NICOLÁS

a-Si:H/c-Si heterojunction solar cells: back side assessment and improvement

Composition du jury :

Pere ROCA i CABARROCAS	Rapporteur
Isidro MARTÍN	Rapporteur
Lars KORTE	Examinateur
Cédric DUCROS	Examinateur
Jean-Paul Kleider	Directeur de thèse
Delfina Muñoz	Encadrant

Abstract

Amongst available silicon-based photovoltaic technologies, a-Si:H/c-Si heterojunctions (HJ) have raised growing attention because of their potential for further efficiency improvement and cost reduction. Compared to conventional homojunction technologies, HJ solar cells benefit from lower fabrication temperatures (around 200°C), cost-effective processes (thin layers are deposited on large-scale), better temperature coefficient and lower silicon consumption (thinner wafers can be used due to excellent passivation quality). Nowadays, the Japanese company Sanyo has already proven 23.7% of conversion efficiencies on large-area HJ devices within an industrial-compatible process flow. However, in spite of these excellent results, the full potential of this kind of structures has not been completely explored yet, and an extensive work on the HJ architecture is being conducted by several groups.

In this thesis, research on n-type a-Si:H/c-Si heterojunction solar cells developed at the *Institut National de l'Énergie Solaire* is presented. Technological and physical aspects of HJ devices are reviewed, with the focus on the comprehension of the back side role. Then, an extensive work to optimise amorphous layers used at the rear side of our devices as well as back contact films is addressed.

The influence of plasma-enhanced chemical vapour deposition (PECVD) process parameters on the properties of amorphous layers is investigated with the aim of enhancing their electrical characteristics. It is evidenced that properties of a-Si:H layers as well as resulting passivation quality are extremely sensitive to deposition conditions. It is shown that the higher the deposition pressure and the larger the distance between the parallel electrodes in the PECVD chamber, the better the passivation quality of the (n)a-Si:H layers at lower PH3 flow rates.

Through the development and implementation of high-quality intrinsic and n-doped a-Si:H films on HJ solar cells, the needed requirements at the back side of devices are established. A comparison between different back surface fields (BSF) with and without the inclusion of a buffer layer is presented and resulting solar cell output characteristics are discussed. When no rear buffer layer is used, a highly doped BSF is necessary to create the appropriate band bending to be able to collect charge carriers. However, conversion efficiencies are limited since the density of defects is not optimised at the heterointerface. Then, it is shown that the minimization of recombination losses at the rear a-Si:H/c-Si interface is also of key importance.

A discussion on the back contact of HJ solar cells is also presented. A new back TCO approach based on boron-doped zinc oxide (ZnO:B) layers is studied. Then, this part of the work focuses on the deposition of ZnO thin films by low pressure chemical vapour deposition (LPCVD). With the aim of developing high-quality ZnO:B layers well-adapted to their use in HJ devices, different deposition parameters are studied, and their influence on solar cells is assessed. It is found that higher values of electron mobility can be obtained on layers with larger grain sizes, since electron scattering phenomena at the grain boundaries are reduced. Besides, in this work a degradation of the ZnO film's lateral conduction under air exposure is evidenced. As a way to further enhance the ZnO characteristics and stability, post-deposition treatments such as post-hydrogen plasma or excimer laser annealing are investigated.

Throughout this work it is evidenced that the back side of HJ solar cells plays an important role on the achievement of high efficiencies. However, the enhancement of the overall device performance due to the back side optimisation is always dependent on phenomena taking place at the front side of devices. The use of the optimised back side layers developed in this thesis, together with improved front side layers and a novel metallisation approach have permitted a record conversion efficiency over 22%, thus demonstrating the great potential of this technology.

Résumé

La diminution du coût des cellules photovoltaïques en silicium cristallin (c-Si) passe par une augmentation de leur rendement de conversion alliée à la réduction en épaisseur des tranches de silicium (≤200 μm). On peut espérer atteindre des rendements de 19-20% avec du très bon matériau multicristallin mais seuls des matériaux monocristallins de très bonne qualité permettront d'approcher petit à petit les limites théoriques des cellules silicium (29%). Le rendement maximum sous un soleil jamais atteint par une cellule en silicium est de 24,7% (surface 4cm2) avec une technologie homojonction améliorée grâce à des méthodes issues de la microélectronique (émetteur sélectif, BSF localisé, passivation par SiO2 thermique…). Ces méthodes sont cependant loin d'être industrialisables à des coûts raisonnables, et les recherches essaient d'en simplifier certains aspects afin de permettre des coûts de fabrication viables.

Parmi les technologies photovoltaïques à base de silicium, les cellules solaires à hétérojonction a-Si:H/c-Si (HJ) ont montré une attention croissante en ce qui concerne leur fort potentiel d'amélioration du rendement et de la réduction de coûts. Par rapport aux homojonctions, les HJs profitent de plus basses températures de fabrication (autour de 200°C), des procédés rentables (des couches minces sont déposées en grand échelle), un meilleur coefficient de température et une consommation plus faible du silicium (des wafers plus minces peuvent être utilisés en raison de l'excellente qualité de passivation de surface). Actuellement, la société japonaise Sanyo a déjà prouvé 23.7% de rendement de conversion avec des dispositifs à HJ de grande surface et un procédé pouvant être industriel. Cependant, malgré ces résultats excellents, le plein potentiel de cette structure n'a pas été encore complètement exploré et un vaste travail sur l'architecture HJ est conduit par plusieurs groupes.

Dans cette thèse, des investigations sur les cellules solaires à hétérojonction a-Si:H/c-Si de type (n) développées à l'Institut National de l'Énergie Solaire (INES) sont présentées. Les aspects technologiques et physiques du dispositif à HJ ont été revus, en mettant l'accent sur la compréhension du rôle joué par la face arrière.

L'influence de paramètres de processus de la technique de dépôt chimique en phase gazeuse assisté par plasma (PECVD) sur les propriétés des couches de silicium amorphe est examinée dans le but d'améliorer leurs caractéristiques électriques. Il a été mis en évidence que les propriétés de couches d'a-Si:H, aussi bien que leur qualité de passivation résultant, sont extrêmement sensibles aux conditions de dépôt. On montre que plus la pression de dépôt et la distance inter électrodes sont grandes, meilleure est la qualité passivation des couches (n)a-Si:H déposées à bas débits de PH3.

À travers le développement et la mise en œuvre des films de a-Si:H intrinsèques et dopés

(n) de haute qualité des cellules solaires à HJ, les conditions requises en face arrière des dispositifs ont été établies. Une comparaison entre plusieurs types de champ surface arrière (BSF), avec et sans l'introduction d'une couche buffer, est présentée et les caractéristiques des cellules solaires résultants sont discutées. Si aucune couche buffer n'est utilisée en face arrière, un BSF fortement dopé est nécessaire pour créer une courbure de bandes adéquate permettant de collecter efficacement les porteurs de charge. Cependant, le rendement de conversion est limité puisque la densité de défauts n'est pas optimisée à l'interface. Alors, on montre que la minimisation des pertes de recombinaison à l'arrière de l'interface a-Si:H/c-Si a aussi une importance capitale.

Une discussion autour du contact arrière de cellules solaires à HJ est aussi présentée. Une nouvelle approche d'oxyde transparent conducteur (TCO) en face arrière basé sur les couches d'oxyde de zinc dopé au bore (ZnO:B) est étudié. Cette partie du travail se concentre sur le dépôt des films minces de ZnO par la technique de dépôt chimique en phase gazeuse aux organométalliques à basse pression (LPCVD). Dans le but de développer des couches de ZnO:B de haute qualité bien adaptées à leur utilisation dans des dispositifs à HJ, différents paramètres de dépôt sont étudiés et leur influence sur des cellules solaires est évaluée. Il est montré que des valeurs plus hautes de mobilité électrique peuvent être obtenues sur des couches possédant de plus grandes tailles de grain, car les phénomènes de dispersion des électrons aux joints de grains sont réduits. En plus, dans ce travail une dégradation de la conduction latérale des films de ZnO en contact à l'air est mise en évidence. Comme voie alternative pour améliorer les caractéristiques du ZnO ainsi que sa stabilité, des traitements après dépôt comme le post plasma d'hydrogène ou le recuit laser sont examinés.

Au cours de ce travail il est montré que la face arrière des cellules solaires à HJ joue un rôle important sur l'accomplissement de hauts rendements. Cependant, l'augmentation de la performance globale du dispositif dû à l'optimisation de la face arrière de la cellule est toujours dépendante des phénomènes ayant lieu en face avant des dispositifs. L'utilisation des films optimisés pour la face arrière des HJs développées dans cette thèse, associée à des couches améliorées pour la face avant et une nouvelle approche de métallisation nous a permis d'atteindre un rendement de conversion record de plus de 22%, démontrant ainsi le grand potentiel de cette technologie à HJ de a-Si:H/c-Si.

Table of contents

1. Introduction

Solar cells convert the energy of photons coming from the sun into electricity using the photovoltaic effect. Generally speaking, the photovoltaic effect is the generation of electron-hole pairs in a material under light exposure, and their separation by an internal electric field. Solar cells were first commercially introduced in the late 1950's in space applications for powering satellites. However, terrestrial applications did not take long to be developed, and nowadays there is a broad choice of promising solar cell technologies for satisfying the energy demand in a sustainable and environmentally friendly way.

In this chapter, the world's photovoltaics context will be introduced, and a review of current solar cells' technologies will be given, the focus being on the silicon wafer-based devices. Surface passivation techniques will be described, and the amorphous/crystalline silicon heterojunction concept, in which this thesis is based on, as well as their state of the art will be presented. Finally, the process followed in this work to fabricate silicon heterojunction solar cells will be described, and the main research objectives will be established.

1.1. Status of world's photovoltaics

Why photovoltaics? There was a time when this was a difficult question to answer. Fossil fuel was plentiful and apparently without end, and the Earth's environment appeared resilient. The photovoltaic (PV) industry was based on the applications of powering satellites and energy supply in remote locations [1]. However, increasing awareness of the environmental impact of non-renewable energy sources, and the obvious economic volatility that comes from reliance on oil and gas, have made the use of renewable energies a focus of interest.

As it is well known, the demand for energy is growing rapidly because of the rapid increase in the worlds' population and the rise in the standard of living, also in emerging countries such as India and China. The majority of this demand has been supplied by fossil fuels (oil, coal, and natural gas). In 2009, they accounted for more than 80% of the total world primary energy supply [2]. In this context, the use of renewable energy sources combined with a rational use of energy represents a fundamental vector of a responsible energy policy for the future. Because of their sustainable character, renewable energy technologies are capable of preserving resources, of ensuring security and diversity of energy supply and providing energy services, with minimised environmental impact.

In this sense, photovoltaics has significant values since it is an inexhaustible resource, available anywhere, clean and noiseless. The sun provides approximately a total irradiation of 10^{24} J to the Earth's surface which is about 1800 times the present rate of the world's primary energy consumption [3]. Hence, photovoltaic solar cells are being increasingly used to tap into this huge resource and will play a key role in future sustainable energy system.

World PV market has just surpassed the impressive solar cell production of 23.9 GW by the end of 2010 [4], which represents an increase of 111% from 2009 to 2010. At that time, the world's PV cumulative installed capacity was approaching 40 GW and in 2011, more than 69 GW have been installed globally (see Figure 1.1) being able to produce 85 TWh of electricity every year [5]. Europe still leads the way with more than 51 GW installed as of 2011, representing about 75% of the world's total PV cumulative capacity. Japan (5 GW) and the U.S. (4.4 GW) are next in the ranking, followed by China (3.1 GW).

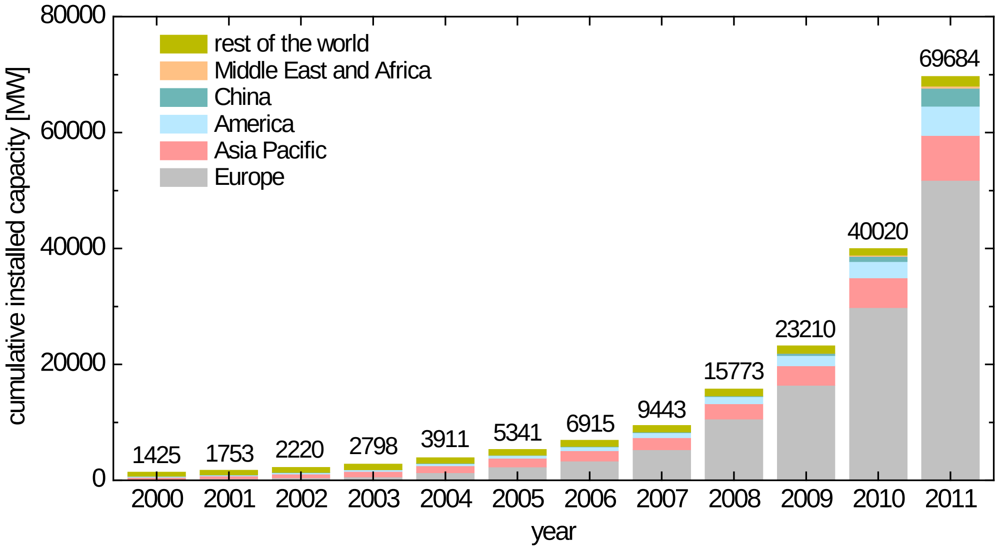

Figure 1.1. Evolution of worldwide cumulative PV installed capacity by region [5].

PV is a real business now and should continue to exhibit such substantial annual increases for some time to come. Much of this growth has been the result of government incentives, but the successes of these policies sometimes overshadow another important component: technology advancement. The reached encouraging deployment has also required a progression of substantial and creative R&D improvement, leading to better device performance and reliability [6]. Nonetheless, the cost of photovoltaic electricity production is still too high to be competitive with fossil fuels [4]. As long as the cost per kilowatt hour for the installed PV system does not reach grid parity with respect to other energy sources, the use of solar energy will not be generalised. Therefore, the development of low-cost cell fabrication technologies without appreciably compromising the cell efficiency should help in achieving the goal of cost-effective PV system.

1.2. Solar cell technologies

The current PV market consists of a wide range of technologies including wafer-based silicon and a variety of thin-film technologies that can be grouped into different families according to their development stage. Crystalline silicon (c-Si) solar cells are subdivided into two main categories: (i) monocrystalline and (ii) multicrystalline silicon, and to date these are the mainstream PV technologies. A typical thickness of several hundreds of microns is used and high conversion efficiencies are obtained. Monocrystalline cells, made of single silicon crystals, are more efficient than multicrystalline cells but are more expensive to manufacture due to material related expenses.

Besides crystalline based technologies, thin-film solar cells account for 10 to 15% of the global PV market share [4]. They are subdivided into three main families [7]: (i) amorphous (a-Si:H) and micromorph silicon (a-Si:H/μc-Si:H), (ii) cadmium-telluride (CdTe), and (iii) copper-indium-(gallium)-diselenide (CIS/CIGS). Application of extremely thin layers of semiconductor materials as active layers in photovoltaic devices offers the promise of low utilisation of raw materials and the use of manufacturing technologies already demonstrated in other industries. Thin films can also be deposited on cheap substrates, including flexible plastics and stainless steel. However, some disadvantages have been found; electrical properties of a-Si:H degrade when material is exposed to illumination due to the generation of light-induced defects, the so-called Staebler-Wronski effect. Even if double and triple junction solar cells have been developed, stabilised efficiencies still remain below 13%.

Chalcopyrites family of compounds, have achieved the highest efficiencies of any polycrystalline thin-film material. For both CIS/CIGS and CdTe technologies, in-line processing for high throughput has been developed. Efforts are made to make use of as much standard equipment as possible. However, many process steps are very specific for these products, making the development of special equipment inevitable [8].

Multi-junction cells using multiple layers of InGaAsP family compounds are developed to absorb and convert more of the incident light into electricity by increasing the number of junctions with a range of different band gap values tailored to the range of photon energies available in the solar spectrum. Combined with light-concentrating optics and sophisticated sun-tracking systems, these cells have demonstrated the highest sunlight-to-electricity conversion efficiencies of any PV technologies, over 40%.

As an approach to move the prices of photovoltaic electricity to those required to be competitive with other power sources, basic research to explore new materials for PV and new cell concepts is being developed. New emerging technologies include dye-sensitised, organic solar cells and quantum dots, which are not yet competitive with other well established technologies due to their relatively low efficiencies to date.

The research progress on PV technologies has been substantial and steady over the past decades. Figure 1.2 shows the history of confirmed best laboratory-cell efficiencies. The highest-efficiency research-cell was achieved in 2011 in a multi-junction concentrator at 43.5%. Other research-cell efficiencies range from 15% to 25% for crystalline silicon cells, about 10% to 20% for thin film, and 10.1% and 11.4% for the emerging PV technologies organic cells and dye-sensitized cells, respectively. In any case, the active areas of research and development for all PV technologies are mainly focused on further increasing module efficiencies and decreasing production costs, reducing at the same time the consumption of raw materials and making easier the scale-up of the processing to larger areas.

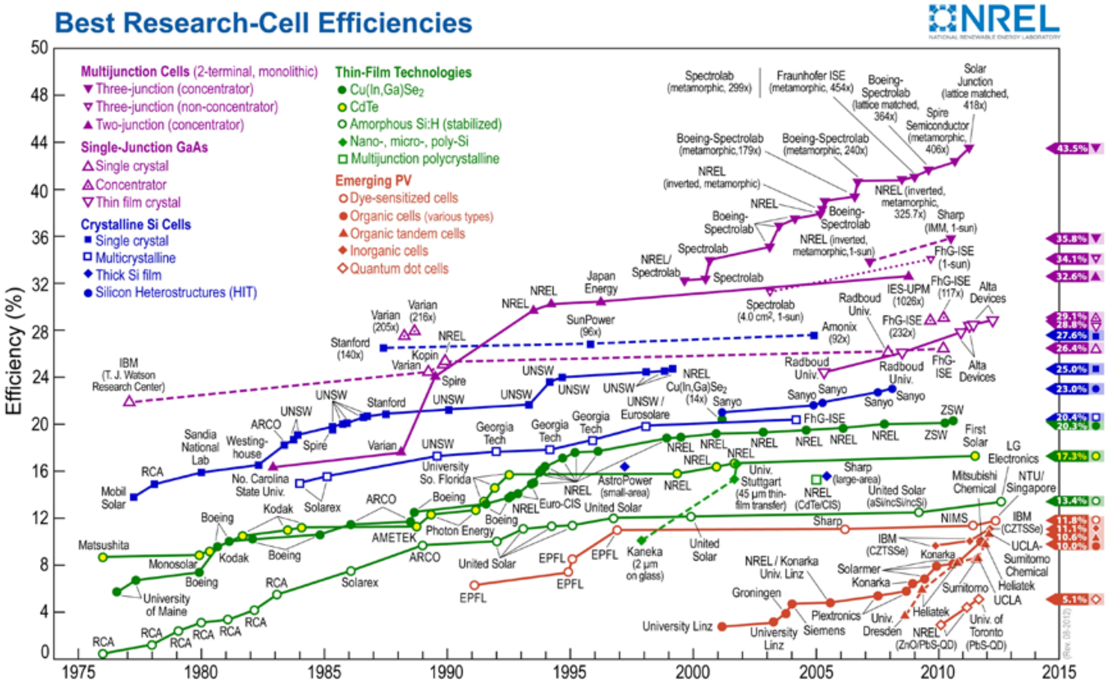

Figure 1.2. Efficiency evolution of best research cells by technology type. This table identifies those cells that have been measured under standard conditions and confirmed at one of the world’s accepted centres for standard solar-cell measurements. Source: NREL, 2012.

- **Crystalline silicon solar cells**

Despite the recent progress obtained with alternative materials, PV market is still dominated by crystalline silicon (c-Si) solar cells, especially due to the wide abundance of Si, its low cost and non-toxicity. In 2010, the market share of c-Si based solar cells was equal to 86% [4]. This means that technical progress can be taken to market faster than in any other photovoltaic technology. Although the basic design of crystalline devices has remained essentially the same for 20 years, this vast growth of the photovoltaic market is directly related to the fact that silicon fulfils the physical requirements for application in solar cells due to its natural semiconducting properties, the major and dominant presence of more efficient and reliable c-Si modules and the low capital costs related to the manufacturing and processing of silicon solar cells.

Following in the direction of improving the efficiency of silicon solar cells, new high efficiency technologies were invented and currently are being developed and introduced into the market. The 25% laboratory world record efficiency on c-Si with the so-called PERL (passivated emitter rear locally diffused) structure was published by Green and co-workers from the University of New South Wales in 1999 [9]. Similarly, the high-efficiency “point contact” technology from SunPower exhibits an impressive performance of 24.2% [10] on production size wafer. However, these larger values of conversion efficiency are reached using a sophisticated c-Si cell structure, involving numerous and complicated steps, that inevitably make increase the costs, which is not suitable for industrial demands (simple, high-throughput and reproducible processes).

In order to provide large-scale low-cost power production, silicon solar cells must break from the thick wafers and expensive high temperature process as a way to cost reduction in cell processing. Cheaper substrates such as multicrystalline Si (mc-Si), metallurgical and ribbon silicon constitute an alternative for monocrystalline silicon. c-Si substrates alone account for 25% to 45% of the cost of the solar cell fabrication [11]. Indeed, silicon solar cell industry uses much more silicon than necessary.

Instead of reducing the quality of the silicon, a more immediate cost reduction can be achieved by using thinner wafers. Despite the fact that nowadays’ wafers are cut from silicon ingots with a thickness around 250 µm, thinner wafers far below 100 µm should be enough for absorbing sun light in Si solar cells combining light trapping schemes. However, in this case, back surface passivation is a special relevant parameter due to the higher surface-volume ratio since thickness of the silicon wafer is decreased [12].

Thermally grown oxide at temperatures around 1000°C is the state-of-the-art surface passivation layer for n-type wafers and also provides good surface passivation for a wide range of p-type c-Si resistivities [13-17], being used in the record-efficiency PERL c-Si solar cell [9, 18]. The surface passivation of the as-grown thermal oxide is moderate, but can be significantly improved by subsequent annealing in a forming gas (H_2 in N_2). However, best results are obtained by the so-called alneal scheme, where a sacrificial layer of aluminium is evaporated on the film prior to annealing [19]. However, for a number of reasons, the high-temperature processing has some problems, including:

- the need for a very clean production equipment and a thorough cleaning of the samples due to the risk of contamination and diffusion of unwanted impurities into the bulk;
- long fabrication times (several hours at 1000°C) and the thin wafers' tendency to bow after being exposed at such a high temperatures;
- thermal degradation of lower quality silicon material (e.g. multicrystalline silicon [20, 21]);
- potentially higher costs due to a high thermal budget and long processing times.

Therefore considerable effort is put in the development of low temperature surface passivation schemes both at the front and back side of devices that do not show the limitations of thermal oxide.

1.3. State of the art in surface passivation

As it will be seen hereinafter, the rear side of the solar cell should exhibit good internal reflection to further use the long wavelength light, as well as good electrical contact between layers to minimise device series resistance. Besides, excellent surface passivation to reduce recombination losses and thus contribute to conversion efficiency enhancement is needed.

To this end, several surface passivation approaches have been developed and the choice of a particular one depends on the doping type of silicon substrate, the quality of the same, the economic constraints and it also depends on its use: front or rear surface passivation.

1.3.1. High-temperature approach

An economic mean to reduce surface recombination is the use of an aluminium back surface field (Al-BSF) to create a lightly-heavily doped junction p/p^+ at the rear side of the cell. In practice, the most effective technique to create it consists in the deposition of an aluminium film, usually by means of screen-printing of aluminium-based paste onto the rear of the cell. A subsequent firing step alloys the aluminium into the silicon creating a (p^+) layer, where an AlSi compact alloy and a phase-mixed AlSi/Al_2O_3 layer also coexist [22]. The alloying process is typically performed at 800-900°C and as a consequence of the high-temperature processing and subsequent cooling cycle, solar cells with Al-BSF contacts suffer from wafer bowing. Moreover, a moderate surface recombination velocity is provided [23]. Although the properties of Al-BSF are especially indicated for industrial solar cells (simple process providing good contact), its performance is insufficient to reach very-high efficient devices.

Apart from aluminium doping of rear c-Si surface, high-temperature back surface fields are also fabricated using boron or phosphorous diffusion (depending on the doping type of the substrate) to create the p/p^+ or n/n^+ junctions, respectively. p-type high-efficiency silicon solar cells incorporating a local boron-BSF have shown very high conversion efficiencies up to about 25% [9]. However, the fabrication of diffused contacts requires again high diffusion temperatures about 1000°C resulting in a number of possible problems more or less already stated: high energy consumption and potentially higher costs in silicon solar cell fabrication; contamination risk of the bulk material by diffusion of unwanted impurities; thermal degradation of lower quality silicon materials; and material stress due to fabrication process temperature gradient.

1.3.2. Low-temperature approach

For the above-mentioned reasons, low-temperature passivation schemes are preferable. Promising candidates such as hydrogenated amorphous silicon nitride (a-SiN_X:H) [24, 25], amorphous silicon oxides (a-SiO_X:H) [26-28], amorphous silicon carbide (a-SiC_X:H) [29-31], aluminium oxide (Al_2O_3) [32, 33], as well as hydrogenated amorphous silicon (a-Si:H) [34-37] have been investigated.

1.3.2.1. Hydrogenated amorphous silicon nitride

Hydrogenated amorphous silicon nitride (a-SiN_X:H) films deposited by plasma-enhanced chemical vapour deposition (PECVD) at temperatures below 400°C are one of the most extensively used low-temperature passivation alternatives to thermal oxide. Excellent surface recombination velocities for high- and low-resistivity silicon wafers of 1 and 20 cm/s, respectively, have been reported in both n- and p-type c-Si [38, 39].

Silicon nitride mainly passivates by field-effect, thanks to a high positive fixed charge density in the film as well as its contribution to the reduction of defects at the interface. Nonetheless, the large density of positive fixed charges within the SiN_X may induce an inversion layer at the rear of p-type c-Si solar cells, producing a detrimental parasitic shunting, which leads to a significant loss in the short-circuit current density [40].

Another strategy that improves the performance of silicon nitride lowering its positive fixed charge density is the combination of such layers in a stack with SiO_2 [41, 42] or hydrogenated amorphous silicon [43]. Silicon nitride films can also be used as antireflection coatings at the front side of devices.

1.3.2.2. Hydrogenated amorphous silicon oxide

The introduction of oxygen with additional hydrogen into amorphous silicon is used to deposit wide optical band gap materials for solar cells. a-SiO_X:H features high quality surface passivation, high transparency and assures an abrupt interface with the c-Si surface [26, 28]. As reported in [44] an excellent effective lifetime of 4.1 ms on n-type c-Si has been achieved, compared to 1.7 ms achieved with (i)a-Si:H films. High-transparent intrinsic a-SiO_X:H films have been used as buffer layers on heterojunction solar cells structures, combined with wide-gap high conductive µc-Si:H for use as emitter and BSF [44, 45].

1.3.2.3. Hydrogenated amorphous silicon carbide

Amorphous silicon carbide is produced from the decomposition of silane and methane (CH_4) and it can be phosphorus or boron doped using phosphine or diborane gases. Its passivation effectivness is based, as in the case of silicon nitride, on the reduction of interface state density and the field effect passivation due to the fixed charge density at the interface [30].

Martín et al. investigated the surface passivation provided by amorphous silicon carbide (a-SiC_X:H) films and excellent passivation properties were reported. SRVs as low as 30 cm/s for 3.3 Ωcm p-type wafers with intrinsic a-SiC_X:H layers were published. Results were further improved to 11 cm/s using phosphorous-doped films [46]. However, passivation quality was found to be dependent on the doping concentration of base material. Using a-SiC_X:H material as passivation layer at the rear side of c-Si solar cells resulted in conversion efficiencies over 20% [47].

1.3.2.4. Aluminium oxide

Recently, another interesting option is being investigated: the use of dielectric alumina (Al_2O_3) as a surface passivation layer. With a refractive index of ~1.65 and no significant absorption in the visible part of the solar spectrum, Al_2O_3 is well suited to improve the optical quality at the front or the back of the solar cell. Some works [48, 49] have shown that Al_2O_3 films grown by thermal Atomic Layer Deposition (ALD) provide a good level of rear surface passivation on low-resistivity p-type c-Si due to its high negative fixed charge density, and independently confirmed efficiencies above 20% have been obtained [50]. However, due to the very low deposition rates of thermal ALD technique alumina films fabricated at a high deposition rates have been investigated [33, 51]. Surface recombination values (< 2 cm/s) comparable to that obtained by thermal ALD have been obtained.

1.3.2.5. Hydrogenated amorphous silicon

Low-temperature passivation scheme resulting in outstanding surface recombination velocities is achieved by hydrogenated amorphous silicon (a-Si:H) [35, 36, 52], deposited in the temperature range of 200-250°C. Amorphous silicon is able to passivate all silicon doping types and levels and can be used to form both the emitter and the BSF. The good surface passivation by a-Si:H can mainly be attributed to the excellent electrical quality of the interface between c-Si and the a-Si:H film [34, 53]. Additionally, field-effect passivation of doped layers plays a role as a result of the amphoteric nature of the silicon dangling bond defects. Recently, extremely low surface recombination velocities (1-3 cm/s) on relatively thick a-Si:H obtained by various deposition techniques have been reported [54].

Since the fixed charge density in high quality intrinsic a-Si:H films is very low, no parasitic shunting occurs in the case of a-Si:H passivation on the rear side of diffused emitter c-Si solar cells. Thus, a-Si:H does not only yield an excellent level of surface passivation on crystalline silicon solar cells with a diffused emitter [55], but is also of prime importance for a-Si:H/c-Si heterojunction solar cells [56].

Despite all these promising features, a-Si:H does not withstand temperatures higher than 400°C, which makes this material incompatible with some of the current device processing technologies. Moreover, when applied at the front side, only very thin a-Si:H layers can be tolerated due to their high blue light absorption.

All things considered, it becomes obvious that the choice of the best passivation layer is strongly influenced by the device structure and by the fabrication process sequence. Regarding the use of hydrogenated amorphous silicon, the most common approach is the amorphous/crystalline silicon heterojunction (HJ), which benefits from wafer-based c-Si and thin-film technologies. Instead of high temperature treatment in diffusion junction, HJ devices uses a-Si:H to form the heterojunction with c-Si. In this area, impressive results have been achieved by Sanyo Electric [1] with the so-called a-Si/c-Si Heterojunction with Intrinsic Thin layer (HIT) solar cell [57]. HJ concept has shown great interests and has been studied extensively in recent years due to its advantages of low cost, solar cell processing at low temperature and potential for thinner wafer, while still keeping high efficiency and high stability.

1.4. a-Si:H/c-Si heterojunction solar cells

The study of a-Si:H/c-Si heterojunctions and its application in solar cells started a long time ago and it still attracts growing attention since Sanyo demonstrated the high efficiency silicon solar cell based on this structure [58]. The first HJs were studied in 1974 by Fuhs and co-workers [59]. Then, few years later, intrinsic a-Si:H films were found to passivate c-Si surfaces remarkably well, and in 1983 the first heterojunction solar cell was fabricated [60, 61]. The potential of this technology was definitely demonstrated by Sanyo

---

[1] In 2010, Japan's Panasonic Corporation acquired remaining shares of Sanyo Electric. However, the affiliation Sanyo is still being used within the photovoltaic community.

in 1992 with the structure denominated heterojunction with intrinsic thin layer (HIT) [58, 62] and has been successively developed to date. Nowadays, Sanyo is the only company producing HJ solar cells and it is also the market leader in mass production of HIT modules. At a laboratory scale, since 2011 they hold the world record efficiency of 23.7% on 100.4 cm^2 (98 μm-thick substrate) with an open-circuit voltage of 745 mV, a short-circuit current density of 39.4 mA/cm^2 and a FF equals to 80.9% [63, 64]. Moreover, Sanyo has also achieved very high efficiencies in mass production: 20% efficiency at the cell level, and 18.3% at the module level [65, 66].

The key of the success of these devices is the introduction of the thin buffer layer of undoped a-Si:H between doped emitter and wafer to reduce the interface state density, decrease surface recombination and lower emitter saturation current [67]. The HIT concept has also been applied to low temperature back surface field (BSF) contacts, creating a symmetrical bifacial structure, fabricated on CZ n-type wafers.

From a processing perspective, a-Si:H/c-Si heterojunctions have several advantages over a conventional c-Si homojunction, including: (1) good passivation properties, leading to high open-circuit voltages and high efficiency; (2) low processing temperatures which prevents bulk quality degradation in low-quality silicon materials [68] and enables technological development on thin substrates too; and (3) better temperature coefficient compared to traditional diffused cells [69, 70]. Moreover, only a small number of process steps are needed to fabricate the device. Thus, research and development of HJs can increase the solar cell efficiency using simple, high-throughput mass-production compatible processes.

Motivated by the excellent results largely demonstrated by Sanyo, HJ technology recently emerged on a global scale, where many other research groups battle to enhance conversion efficiencies [69, 71-75] and an increasing number of industrial partners are considering commercialization, as the Sanyo's most important patents expired in 2010. Figure 1.3 condenses the main reported results on HJ devices.

In Asia, apart from Sanyo, efficiencies of 22.7% have been obtained by Kaneka [76]. Besides, Hyundai Heavy Industries reached a 21.1% in 220 cm^2 cells. Likewise, at a laboratory scale, AIST and Tokyo Institute of Technology in Japan [45, 77-79], the Sungkyunkwan University of Korea [80] and the Institute of Electrical Engineering at the Chinese Academy of Sciences in China [81], are studying heterojunction devices.

In the USA, the National Renewable Energy Laboratory (NREL) reported the highest efficiency on p-type c-Si wafers (19.3%) [82]. Wang et al. used hot-wire CVD (HWCVD) instead of PECVD to deposit a-Si:H. They studied the deposition temperature effect on the cell performance [83] and found low temperature is crucial for achieving high open-circuit voltage.

In Europe, Roth & Rau obtained V_{OC} values up to 735 mV and conversion efficiencies of 21.9% on 4 cm^2 and 20.3% on 149 cm^2 [69], using RF PECVD. At EPFL Neuchâtel, a conversion efficiency of 21.8% and a V_{OC} of 726 mV on 4 cm^2 solar cells have been obtained on textured substrates using very high frequency (VHF) PECVD [84]. The Helmholtz-Zentrum Berlin (HZB) has reached high efficiencies of 17.4% on p-type c-Si and 19.8% on n-type c-Si wafers with pyramidal surface texturization [85] on 1 cm^2 wafers.

The National Institute of Solar Energy (INES), where this thesis has been developed, is conducting research on a-Si:H/c-Si heterojunction solar cells since 2006. Notably, INES has reached one of the highest efficiencies in Europe on large area 148 cm^2 n-type c-Si wafers and solar cells with up to 20.4% and 720 mV of V_{OC} (21% and 732 mV on 105 cm^2) have been reported [72]. This performance has been possible thanks to the equipment loaned recently by JUSUNG Engineering to INES.

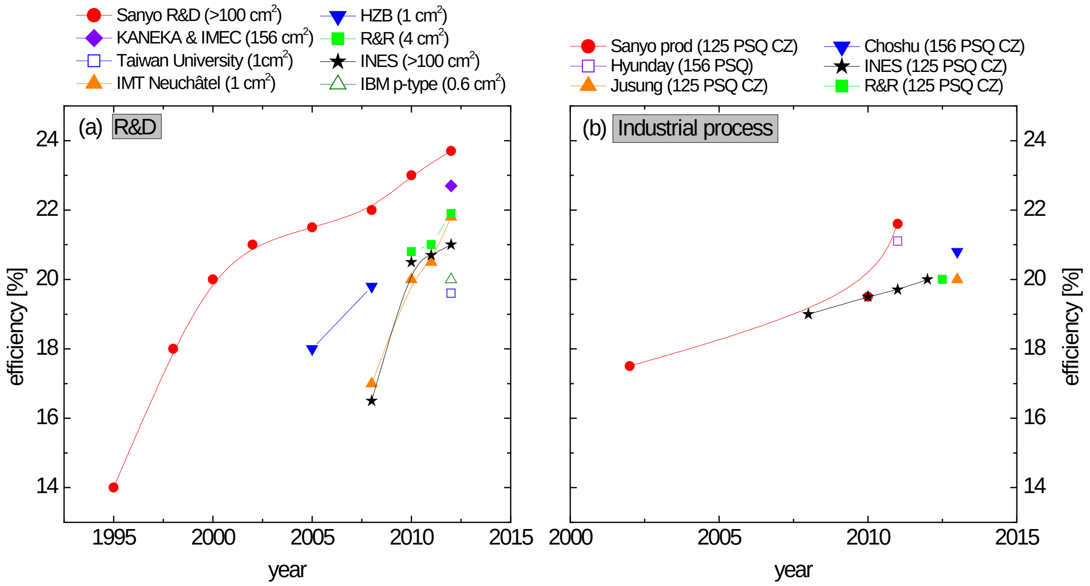

Figure 1.3. Reported efficiencies of HJ solar cells by different research groups (a) and industrial companies (b).

Finally, it is worth to remark that a recent interest has risen for HJ cells with interdigitated back contact (IBC) structure. The absorption in the front TCO and a-Si:H layer can be avoided having both contacts at the rear side of the device. Being introduced in 2007 [86], its efficiency attains lower results than in conventional HJ [72, 87]. However, this new technology has a theoretically great potential, being able to overcome the efficiency results of IBC cells with homojunction contacts [88], through a fabrication process involving less patterning steps.

For a review of the current status of HJ photovoltaic technology, the interested reader is referred to [56, 89].

1.5. Structure and fabrication process of heterojunction solar cells at INES

In this section, the structure of the solar cells studied in this thesis is described. HJ solar cells are made through a rather simple manufacturing process, where the different deposition steps are made at temperatures lower than 220°C. Moreover, there is no need of patterning since layers cover the entire device surface, the one behind the other one, which allows an industrial process. At INES, heterojunction solar cells are the result of teamwork, where several fields of expertise are involved.

The base material of the cell consists of 125 pseudo square high quality FZ n-type monocrystalline silicon wafer, with a thickness around 200 µm and a resistivity of 1-5 Ωcm (n-doped material has been chosen since higher conversion efficiencies than in p-type material can be achieved and light induced degradation phenomena can be avoided). The ⟨100⟩ oriented c-Si wafers are preliminary randomly textured by a classical alkaline wet process [90, 91], revealing Si ⟨111⟩ faceted square-based pyramids during the etching (see Figure 1.4(a)). This texture both reduces external reflection and improves internal reflection, allowing to increase the attainable current of the cell [92, 93], as it is shown in Figure 1.4(b). During the etching, special attention has to be paid in order to properly remove the wire-saw damage (~10 µm) since incomplete removal can directly impact on V_{OC} [89].

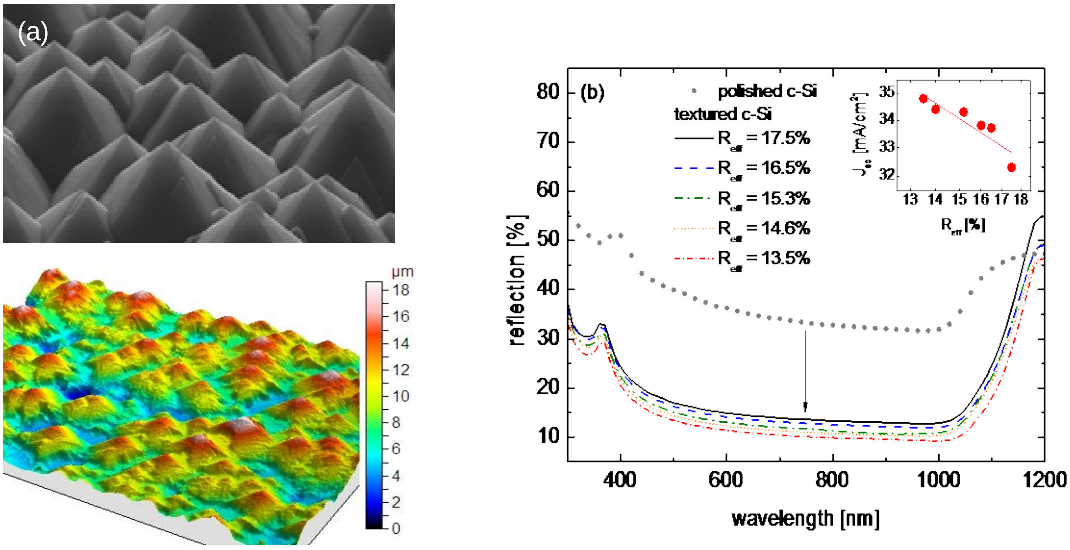

Figure 1.4. (a) SEM micrograph of randomly textured c-Si surface. (b) Reflectivity measurements for different texturing processes on 200 µm c-Si wafers. The 280 µm-thick polished c-Si sample is plotted for comparison. In the inset, a correlation between reflectivity of samples and short-circuit current density measured on the HJ cell is given.

Prior to the a-Si:H deposition, a multistep RCA clean is applied followed by a short dip in diluted hydrofluoric acid (HF) to remove the native oxide on the c-Si surfaces. It has been widely demonstrated that well-controlled surfaces are required to obtain high-quality passivation [94-96]. However, the duration of the initial phase of oxidation of H-terminated silicon surfaces is found to be relatively short. Consequently, a fast subsequent transfer of cleaned surfaces to film deposition systems is of significant importance.

Thus, samples are introduced in the JUSUNG cluster equipped with a load lock, two parallel-plate plasma-enhanced chemical vapour deposition chambers (RF, 13.56 MHz), two magnetron sputtering systems: Indium Tin Oxide (ITO) and Aluminium, and one metalorganic chemical vapour deposition at low-pressure (LP-MOCVD) chamber for Boron-doped Zinc Oxide (ZnO:B) depositions. Figure 1.5 shows a schematic view of the multi-chamber cluster tool (length: 6 m; width: 5 m), which is able to process 9 cells at the same time.

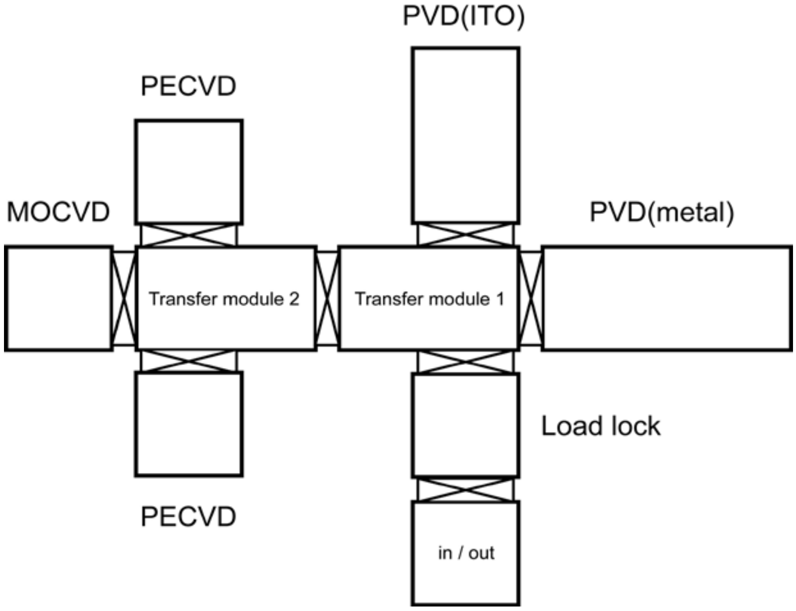

Figure 1.5. Schematic view of the multi-chamber deposition tool used in this thesis.

a-Si:H layers are deposited at front and back sides of the solar cell by PECVD with silane (SiH_4) diluted in H_2 as precursor gases, at 200°C. As it has been mentioned before, for a high-efficiency HJ device, high-quality surface passivation is required. Thus, a stack of layers is used in order to improve the passivation and to create the adequate electrical field.

Undoped a-Si:H passivates the c-Si surface mainly by hydrogenation of silicon dangling bonds, leading to a reduction of the interface defect density [97]. For a good passivation quality, deposition conditions are optimised and controlled in order to carry out a low-damage plasma deposition process. Besides, silicon epitaxial growth has to be avoided, obtaining an atomically sharp interface between the substrate and the a-Si:H film, where no crystalline material is deposited [78, 83] .

Boron-doped (p)a-Si:H is deposited by decomposition of silane and hydrogen-diluted diborane (B_2H_6, 0.5% in H_2). Phosphorous-doped (n)a-Si:H is obtained from a gas mixture of SiH_4 and hydrogen-diluted phosphine (PH_3, 1% in H_2). These doped films are required to form the emitter and BSF, respectively. The emitter layer forms the p/n junction in the cell, which creates the desired band bending in the c-Si wafer close to the a-Si:H/c-Si interface and thereby enables charge separation. The back surface field (BSF) repels minority charge carriers from the back side of the cell reducing this way recombination losses at the rear surface of the c-Si wafer.

In order to be able to collect the photogenerated current, on top of the emitter layer it is necessary to add a transparent conducting oxide (TCO), in our case, 90 nm-thick indium tin oxide deposited by DC magnetron sputtering from a ceramic ITO target containing 90 wt.% of In_2O_3 and 10 wt.% of SnO_2 (during the course of this work, a target containing 95 wt.% of In_2O_3 and 5 wt.% of SnO_2 has also been tested). Deposition is done on a dynamic way, so that the carrier speed of the substrate holder controls the desired thickness of the layer. This antireflection coating enables a good lateral conduction ($\rho < 10^{-3}$ Ωcm) to reduce series resistance losses. On the back side, 200 nm of ZnO:B layer are deposited by metalorganic chemical vapour deposition at low-pressure. Both TCOs are deposited at 180°C.

Finally, 500 nm of sputtered Al on the whole rear surface forms the back contact of the cell and a low-temperature silver paste is deposited through an optimized designed grid by screen printing on the front side. To this end, a compromise between grid lay-out and conductivity/transparency of the TCO has to be found, since lower sheet resistance enables a wider metal grid spacing [98] which reduces shadowing losses (therefore, larger J_{SC}) and consumption of silver paste, as well. Besides, fabricating narrow and tall metal lines to further reduce resistive and shadow losses at the front of HJ solar cells will be a challenge to be faced [99].

Since no masks are used during the fabrication process, an adapted laser scribing and edge isolation step is done to avoid any shunt in the cell. A schematic overview of the solar cell is given in Figure 1.6.

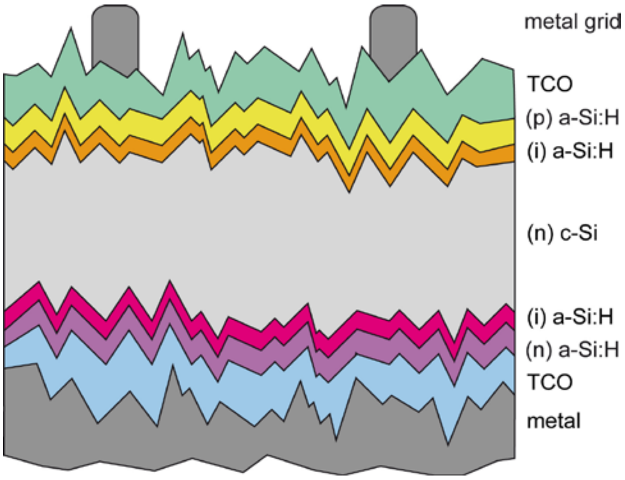

Figure 1.6. Schematic diagram of a standard heterojunction solar cell fabricated in this thesis.

1.6. Specific research objectives: back side of heterojunction solar cells

Back side (BS) of heterojunction solar cells plays an important role on device's results especially from an electrical point of view. While on the front side (FS) of the cells we need to find the compromise between optical and electrical properties on amorphous and TCO layers, at the BS some constraints in terms of optical properties disappear since back-side layers can only profit the long wavelength light.

The increase in J_{SC} owing to the optimisation of the back side of the device is weak and difficult to quantify. However, its impact will be more important as the thickness of the c-Si wafer will be diminished. Due to the difficulty to decorrelate the back side effects from the whole device and due to the fact that there is not a direct impact on the p/n junction, the BS of HJ solar cells has not been widely studied by other research groups.

Nevertheless, this back side is a key part of the solar cell to obtain high efficiencies and therefore it has to carry out certain conditions for the appropriate performance of the cell. Solar cell back side specifications concern amorphous layers and the back contact, usually comprising a rear side TCO and metallic contacts.

As presented in Table 1.1, the different layers and resultant interfaces used at the back side of HJ devices differently impact on the characteristic parameters used to evaluate the efficiency of solar cells. The BS of devices has a weak impact on J_{SC}, since the absorption of light is not predominant. Then, J_{SC} is mainly affected by the front side of the cell (UV absorption) and the optical confinement at the textured c-Si substrate. By contrast, the V_{OC} of the device is very sensitive to the a-Si:H/c-Si interface and to the amorphous layers themselves. The set of all layers and interfaces of the back side determine FF values, as it is especially affected by the series resistance.

Table 1.1. Qualitative impact of the different layers and interfaces used at the back side of a standard HJ device on the solar cell characteristic parameters (- none, × low, ×× medium, and ××× strong).

layer / interface	J_{SC}	V_{OC}	FF
c-Si	×××	××	×
interface c-Si/a-Si:H	-	×××	×
back a-Si:H	-	××	×
interface a-Si:H/TCO	×	×	×
back TCO	×	×	×
interface TCO/metal	×	-	××
back metal	×	-	××

BS amorphous layers have to properly passivate c-Si to avoid recombination of minority carriers before being collected. Thus, a very low defect state density at the heterointerface together with a strong electrical field is desired [67, 100]. Combining these two different passivation mechanisms in a single layer is extremely difficult because of the very low conduction properties of low defective intrinsic a-Si:H layers. To increase the layer’s conductivity, some doping can be introduced on them. However, defect density will also be increased [101, 102]. This fact leads to a tricky compromise between passivation properties (structural and morphological) and conduction properties (electrical) that will enable improved V_{OC} and FF. To this end, as it will be discussed later in this work, the inclusion of a thin intrinsic amorphous silicon layer at the back side will be advantageous for high efficiency devices. In this case, intrinsic a-Si:H applied to the rear side of HJ solar cells should have an enhanced dark conductivity (σ_d) no matter the photoconductivity (σ_{ph}) since there is no light-activated conduction at the back side of the solar cell.

When decreasing the thickness of c-Si substrate as an approach to cost reduction, high quality a-Si:H layers will be needed. In this case, the optical thickness of the solar cell will be increased beyond its real thickness and the relative importance of rear surface recombination will increase. Analogously, the role of the back contact in HJ solar cells will become more critical with thinner wafers, being the light trapping a key issue to be assessed. Then, in order to increase the attainable current in the cell an ideal back reflector should be ensured, and it should accomplish with maximum reflection (perfect mirror), low near infrared absorption of films, increased light path within the solar cell, and surface roughness in the corresponding spectral region. In this thesis, substrates thicknesses around 200 µm have been used and therefore these will not be the prevailing concerns when optimising the BS.

The back contact can be ensured by a metal layer deposited on top of the rear side a-Si:H [103, 104]. However, in this case, efficiencies are limited well below 16%, since the interface with the amorphous layer is not optimised. To overcome this drawback the use of a back TCO has been introduced, which apart from enhancing the contact between a-Si:H and metal layers in monofacial devices (TCO covered by a full metal sheet), also enables the use of bifacial (a metallic grid electrode partially covers the TCO) structures.

The TCO properties that should be accomplished differ when this layer is used in bifacial or monofacial HJ devices. Back side TCO in bifacial structures, like fot the front side, has to fulfil high transparency and high electrical conductivity. On the one hand, it assures the lateral collection of charges to the device terminals, which is not easily permitted due to the poor conductivity of a-Si:H layers. On the other hand, it also works as an antireflection coating in order to reduce reflectance losses due to the high refractive index of silicon. Therefore, its thickness is adapted and it is often limited to 80-100 nm.

By contrast, the transparency and conductivity criteria for the monofacial back TCO layer take into consideration the following: (i) short wavelengths are not able to reach the back TCO at all, because they are absorbed during the first transit of the light through the solar cell. Therefore, the transparency of the back TCO layer in the short spectral range is not a critical point [105]. (ii) Lateral transport constraints do not govern layer design when the TCO is used in full rear metallisation HJ solar cells. In this case, back side TCO is mainly used for contacting and optical purposes hence being as transparent as possible without incurring in contact resistance losses [56]. This way, V_{OC} and FF will be improved.

In order to guarantee the device integration into modules, the metal used at the rear side contacts and the other layers should be suitable for device encapsulation, providing good adhesion between the solar cell and the rear surface of the PV module. Moreover, the rear surface of the HJ module should have a low thermal resistance and it must prevent the entry of water and water vapour to avoid corrosion of metal contacts and interconnects, and degradation of the TCO layer, which is very sensitive to humidity. In the case of bifacial modules (bifacial cells), the encapsulant should be optically transparent in order to also profit from the rear reflected and diffuse light.

1.7. Aim of this work

In this thesis, research on n-type a-Si:H/c-Si heterojunction solar cells developed at the *Institut National de l’Energie Solaire* (INES) is presented. Technological and physical aspects of HJ devices are reviewed, with the focus on the comprehension of the back side role. After giving an introduction to the fundamental background on solar cells such as the device physics and band diagram analysis (section 2), an extensive work to optimise amorphous layers used at the rear side of our devices as well as back contact films is addressed.

In section 3, the influence of PECVD process parameters on the properties of amorphous layers is investigated with the aim of enhancing their electrical characteristics. Through the development and implementation of high-quality intrinsic and n-doped a-Si:H films on HJ solar cells, the needed requirements at the back side of devices are established. A comparison between different BSFs with and without the inclusion of a buffer layer is presented and resulting solar cell output characteristics are discussed. Various material characterisation techniques are used (some of them performed at the *Laboratoire de Génie Électrique de Paris*), and numerical simulation tools are applied to give more insight into the observed tendencies of the studied samples.

In section 4, a discussion on the back contact of HJ solar cells is presented. A new back TCO approach based on boron-doped zinc oxide (ZnO:B) layers is studied. Then, this part of the work focuses on the deposition of ZnO thin films by LPCVD. In order to properly understand the obtained results, the basic properties of ZnO are presented. With the aim of developing high-quality ZnO:B layers well-adapted to their use in HJ devices, different deposition parameters are studied, and their influence on solar cells is assessed. Moreover, post-deposition treatments are investigated as a way to enhance ZnO characteristics.

In section 5, diverse technological issues related to the fabrication of heterojunction solar cells are presented. The effects of eventual deposition system failures on the solar cell performance are discussed, and the key development aspects towards record-efficiency heterojunction devices fabricated at INES are given. Besides, HJ solar cell module integration is presented, in which different tests varying the back side design are investigated. Finally, this thesis concludes with a summary of the main results and gives some prospects for future studies.

2. Main aspects of the back side of amorphous/crystalline silicon heterojunction solar cells physics

As previously said, the back side plays an important role on the characteristic parameters of HJ solar cells. In order to obtain high V_{OC} values a good passivation scheme both at the emitter and at the back side of devices is required. Good rear surface passivation will act to repel one type of charge carriers and thus it will contribute to lower the carrier recombination in the device.

This section presents and clarifies the most relevant background information required to properly interpret the results presented in the following chapters. Here the basic recombination mechanisms for electrons and holes in crystalline silicon will be introduced, and a review of surface passivation strategies will be also covered. Besides, discussion on fundamentals of solar cells, energy band diagrams and optical concerns focused on the rear side will be given.

2.1. n/n$^+$ junction: recombination and passivation

Recombination and passivation mechanisms at the rear n/n$^+$ junction of n-type HJ devices have been little studied. Generally, they are based on the same principles as the front side, and therefore the same objectives are pursued. Most of the back side physics issues are common with the emitter structure; however, since no p/n junction exists at the BS, the characterisation of recombination does not consider the emitter saturation current density J_{0e}. As it will be seen, recombination and passivation quality at the n/n$^+$ rear junction will be given by the effective lifetime measurement.

2.1.1. Basics of carrier recombination mechanisms in crystalline silicon

The definition of passivation with respect to c-Si surfaces is the reduction of the rate at which electrons in the conduction band (charge carriers) drop to fill a hole in the valence band. This annihilation process is also known as carrier recombination. In n-type material, the rate at which these electrons and holes are annihilated, i.e. the recombination rate, is defined by the relation:

$$U = \frac{\Delta p}{\tau} \tag{2.1}$$

where Δp is the excess minority carrier density and τ is the lifetime of such carriers.

Recombination in a semiconductor can occur by multiple ways both in the bulk and at the surfaces. Bulk recombination has been extensively addressed in previous works [12, 106, 107]. Thus, in this thesis, only the basic equations are presented, illustrated by plots of the fundamental recombination processes in bulk silicon material. For surface recombination, theoretical foundations will be discussed.

The different recombination paths in the bulk and at the surface may occur simultaneously within the semiconductor. The recombination rate of some of the processes might be negligible, while others may contribute to a higher extent.

2.1.1.1. Bulk recombination

In bulk c-Si there are three recombination pathways considered to limit the bulk lifetime, τ_b: 1) radiative recombination τ_{rad}, 2) Auger recombination τ_{Aug}, and 3) recombination through defects (Shockley-Read-Hall (SRH) recombination, τ_{SRH}).

Between these three fundamental recombination processes present in semiconductors, two of them are intrinsic and therefore, unavoidable (radiative and Auger recombination). The third one (SRH) is related to the presence of defects and is an extrinsic process, related to crystal defects. Then, the net carrier recombination lifetime in the bulk can be expressed as:

$$\frac{1}{\tau_b} = \frac{1}{\tau_{rad}} + \frac{1}{\tau_{Aug}} + \frac{1}{\tau_{SRH}} \tag{2.2}$$

The individual recombination processes are discussed in the following sections.

- **Radiative recombination**

Radiative recombination is the inverse process of photogeneration. An electron from the conduction band makes a transition into its ground-state in the valence band, with the emission of photon to release its excess energy (see Figure 2.1). It depends directly on the availability of electrons and holes and it is given by [108]:

$$U_{rad} = Bnp \tag{2.3}$$

where B is the coefficient of radiative recombination. For silicon, $B \sim 10^{-15}$ cm^3/s at room temperature, although this value may change depending on the reference source [109, 110].

As c-Si is an indirect band gap semiconductor, the process must be assisted by a phonon to simultaneously conserve energy and momentum, and therefore such a four-particle process has a low probability of occurring [111].

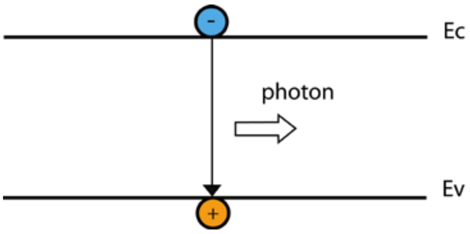

Figure 2.1. Radiative recombination mechanism.

Under illumination, the electron and hole concentrations can be written as $n = n_0 + \Delta n$ and $p = p_0 + \Delta p$, where p_0 (n_0) is the equilibrium hole (electron) concentration, and Δn (Δp) is the minority excess photogenerated carrier concentration. Considering the case for an n-type material, $n_0 = N_d$ and $p_0 = n_i^2/N_d << \Delta p$, with N_d the doping concentration of c-Si and n_i the instrinsic carrier concentration. Assuming an injection level where both excess carrier concentrations are equal ($\Delta n = \Delta p$), the radiative recombination rate can be then written as:

$$U_{rad} = B(N_d + \Delta p)\Delta p \tag{2.4}$$

Accordingly to equation (2.1) the radiative recombination lifetime can be expressed as:

$$\tau_{rad} = \frac{1}{B(N_d + \Delta p)} \tag{2.5}$$

Depending on the photogenerated carrier concentration this expression can be simplified (at low injection level $\Delta p << N_d$, whereas at high injection level $\Delta p >> N_d$). In general, at least one other recombination mechanism will be dominant over radiative processes at any given injection-level in silicon wafers.

- **Auger recombination**

Auger recombination is the reverse of impact ionization, in which an electron or a hole with high kinetic energy collides with another electron out of its bond, thereby creating a free electron and a free hole. In the reverse process, the energy set free during recombination is transferred to an electron or a hole, which subsequently releases its excess energy in the form of heat (thermalisation) [112]. Figure 2.2 illustrates the process of Auger recombination in which three particles partake.

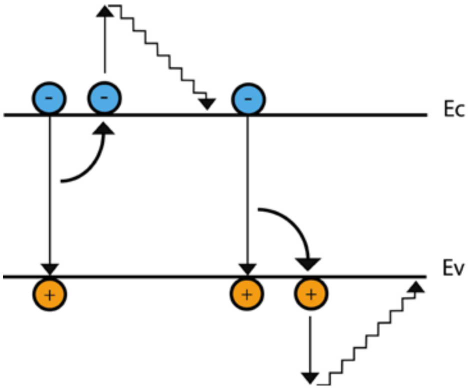

Figure 2.2. Auger recombination mechanism.

Unlike radiative recombination, where an electron and a hole recombine emitting a photon, in Auger recombination the excess energy lifts a third electron/hole to a higher/lower conduction/valence band level, respectively. The particle relaxes inside its band to its equilibrium state by emitting or absorbing phonons.

The Auger recombination rate is then proportional to the probability that an electron-hole-electron (eeh) or an electron-hole-hole (ehh) interaction occurs and depends on the concentration of involved carriers (excess carrier density and the doping concentration) [113, 114]. The rates at which both processes occur are given by:

$$U_{Aug,eeh} = C_n\left(n^2p - n_0{}^2p_0\right) \tag{2.6}$$

$$U_{Aug,ehh} = C_p\left(np^2 - n_0p_0{}^2\right) \tag{2.7}$$

Assuming that $n_0{}^2p_0$ and $n_0p_0{}^2$ are negligible [106], the total Auger recombination rate can be expressed as:

$$U_{Aug} = U_{Aug,eeh} + U_{Aug,ehh} = C_n n^2 p + C_p n p^2 \tag{2.8}$$

where C_n and C_p denote the Auger coefficients for electrons and holes.

From this expression and equation (2.1) the Auger lifetime in n-type c-Si can be defined as follows, considering $n_0 = N_d$, $p_0 << \Delta p$, and $\Delta n = \Delta p$:

$$\tau_{Aug} = \frac{1}{C_n\left(N_d + \Delta p\right)^2 + C_p\left(N_d + \Delta p\right)\Delta p} \tag{2.9}$$

Under low-injection conditions, τ_{Aug} is constant and inversely proportional to the doping concentration of the c-Si:

$$\tau_{Aug} = \frac{1}{C_n N_d^{2}} \tag{2.10}$$

By contrast, at high-injection τ_{aug} can be expressed as:

$$\tau_{Aug} = \frac{1}{C_a \Delta p^{2}} \tag{2.11}$$

where $C_a = C_n + C_p$ is the ambipolar Auger coefficient.

Although recombination rates can be described by similar empirical factors as does the factor B for the radiative recombination, the relationship in Auger mechanisms cannot be easily pinned down. For low injection conditions, Coulomb interaction between charge carriers induces higher Auger recombination rates [112], whereas at high injection this effect is diminished. The Auger lifetime is strongly influenced by Coulomb forces and the possible influence of other processes, preventing a simple description of this phenomenon. Hence, various models based on the Coulomb-enhanced effect have been suggested [113-115] for all doping densities at any injection level. However, they tend to diverge from experimental data. Up to now, the most complete description for the Auger recombination rate for both low and high injection levels, doping type and doping level has been proposed by Kerr and Cuevas (for extended details see [116]).

- **Recombination through defects**

Imperfections in the crystalline silicon due to impurities, or crystallographic defects, such as vacancies and dislocations, produce a determined number of states within the band gap that act as carrier traps for free electrons or holes. A free carrier trapped in the defect releases its excess energy by a phonon emission process, and can be either emitted again to its original band or recombine with an oppositely charged carrier (Figure 2.3). While the first process does not contribute to carrier recombination, the second one is a dominant mechanism in indirect band gap semiconductors.

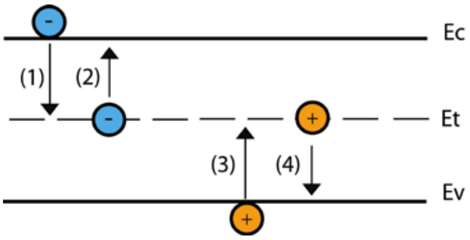

Figure 2.3. Possible interactions between a defect positioned at E_t and a charge carrier: (1) capture of an electron, (2) emission of an electron, (3) capture of a hole and (4) emission of a hole.

The recombination rate was first calculated by Shockley, Read and Hall in 1952 [117, 118] and is therefore often referred to as Shockley-Read-Hall (SRH) recombination. Their statistical model uses the density of localised states per unit of volume (density of recombination centres) N_t, the capture cross sections for electrons (σ_n) and holes (σ_p), which represents the efficiency of the defect to capture electrons and holes, and the energy level of the recombination centre E_t. Then, the following expression for the net SRH recombination rate can be found:

$$U_{SRH} = \frac{\nu_{th} N_t \left(np - n_i^2\right)}{\dfrac{n + n_1}{\sigma_p} + \dfrac{p + p_1}{\sigma_n}} \tag{2.12}$$

being ν_{th} the thermal velocity of the charge carriers (here, considered to be equal for electrons and holes), and n_i the instrinsic carrier concentration. The statistical factors n_1 and p_1 are the electron and hole densities when the Fermi level coincides with the recombination centre energy E_t:

$$n_1 = N_c e^{\left(\frac{E_t - E_c}{k_B T}\right)}, \qquad p_1 = N_v e^{\left(\frac{E_v - E_t}{k_B T}\right)} \tag{2.13}$$

where N_C and N_V are the effective densities of states at the conduction and valence band edges, respectively.

Using equation (2.1), and assuming the charge neutrality condition ($\Delta n = \Delta p$), SRH lifetime can be expressed as follows:

$$\tau_{SRH} = \frac{\tau_{p0}\left(n_0 + n_1 + \Delta p\right) + \tau_{n0}\left(p_0 + p_1 + \Delta p\right)}{p_0 + n_0 + \Delta p} \tag{2.14}$$

with τ_{n0} and τ_{p0} the capture time constants for electrons and holes defined as:

$$\tau_{n0} = \frac{1}{\sigma_n v_{th} N_t}, \qquad \tau_{p0} = \frac{1}{\sigma_p v_{th} N_t} \tag{2.15}$$

This expression shows that τ_{SRH} is in general a function of the excess carrier concentration. In the case of similar characteristic lifetimes τ_{n0} and τ_{p0}, recombination rate is higher when $n_1 \approx p_1$. This takes place when the localised state lies near the middle of the c-Si band gap. Therefore, mid-gap trap states are very effective recombination centres. Under the assumption of low-injection conditions and $\Delta p \ll n_1, p_1$, τ_{SRH} in n-type c-Si can be simplified to:

$$\tau_{SRH} = \tau_{p0}\left(1 + \frac{n_1}{N_d}\right) + \tau_{n0}\frac{p_1}{N_d} \tag{2.16}$$

At high-injection ($\Delta p \gg N_d$), equation (2.14) can be expressed as follows. As it can be seen, τ_{SRH} does not depend on the energy level of the recombination centre and is also independent of the doping concentration.

$$\tau_{SRH} = \tau_{p0} + \tau_{n0} \tag{2.17}$$

SRH recombination is especially important at the c-Si surface where the density of crystallographic defects is very high (see next section).

2.1.1.2. Surface recombination

c-Si surfaces are a recombination pathway due to the truncation of crystal lattice periodicity, which results in a high surface density of unsaturated bonds and other surface states that exist at energy levels within the forbidden gap of the crystal bulk. Surface recombination is a special case of SRH recombination in which the localised states occur at the surface. Unlike bulk SRH centres, these states do not usually occupy a single energy level, but rather form a set of states distributed across the band gap.

The surface recombination rate U_S via a single level surface state located at an energy E_t can be defined as follows [12]:

$$U_S = \frac{n_s p_s - n_i^2}{\dfrac{n_s + n_1}{S_{p0}} + \dfrac{p_s + p_1}{S_{n0}}} \tag{2.18}$$

with, n_1 and p_1 defined as in equation (2.13, n_s (p_s) the density of electrons (holes) at the surface ($n_s = n_0 + \Delta n_s$ and $p_s = p_0 + \Delta p_s$), N_{st} the density of defects per unit area, and S_{n0} and S_{p0} the surface recombination velocities of electrons and holes, defined as $S_{n0} = \nu_{th} N_{st} \sigma_n$ and $S_{p0} = \nu_{th} N_{st} \sigma_p$.

At low-injection level, equation (2.18) can be simplified for an n-type c-Si considering that $n_0 = N_d >> p_0$, and $p_1 >> p_0$ (with $\Delta n_s = \Delta p_s$):

$$U_S = \frac{S_{p0}}{1 + \frac{1}{N_d}\left(n_1 + \frac{S_{p0}}{S_{n0}} p_1\right)} \Delta p_s \tag{2.19}$$

At high-injection conditions, equation (2.18) turns into:

$$U_S = \frac{S_{n0} S_{p0}}{S_{n0} + S_{p0}} \Delta p_s \tag{2.20}$$

Analogously to equation (2.1), surface recombination can be characterised by a surface recombination velocity S, instead of a recombination lifetime, defined as:

$$U_s = S \Delta p_s \tag{2.21}$$

where U_S [$cm^{-2}s^{-1}$] denotes the surface recombination rate and Δp_S [cm^{-3}] is the excess minority carrier density at the surface.

Unlike bulk recombination via defects, in surface recombination an electric field at the semiconductor surface is usually found. Owing to the fact that the electric field creates large differences between the density of electrons and holes at the surface, Δn_S is far away from Δp_S. Hence, an effective surface recombination velocity can be defined:

$$U_s = S_{eff} \Delta p \tag{2.22}$$

where $\Delta p = \Delta n$ is the minority carrier density at the limit of the space charge region created at the surface, which can be measured easier than Δp_S varying the illumination level.

2.1.2. Effective lifetime and surface recombination velocity

The different recombination paths in the bulk and at the surface may occur simultaneously within the semiconductor. The recombination rate of some of the processes might be negligible, while others may contribute to a higher extent. From the definitions for the bulk lifetime and the surface recombination velocity, we can define the effective carrier lifetime as reciprocal sum of bulk and surface lifetimes:

$$\frac{1}{\tau_{eff}} = \frac{1}{\tau_b} + \frac{1}{\tau_s} = \frac{1}{\tau_b} + \frac{S_{front}}{W} + \frac{S_{back}}{W} \tag{2.23}$$

S_{front} [cm/s] and S_{back} [cm/s] denote the front and back surface recombination velocities respectively and W [cm] is the wafer thickness.

Equation (2.23) only holds when the bulk lifetime is high enough to allow photogenerated carriers to reach both surfaces, and when the surface recombination is sufficiently low to avoid transport-limited profiles near the surfaces [119, 120]. Generally, this can be assumed to occur if τ_{eff} is greater than 100 µs [121]. Throughout this work, high-quality float zone material (FZ) has been used as well as high-quality passivation layers, thereby assuring the assumption of the preceding conditions. Finally, considering that the front and rear surfaces are identical and the photogeneration of carriers is homogeneous, equation (2.23) can be simplified as follows:

$$\frac{1}{\tau_{eff}} \approx \frac{1}{\tau_b} + \frac{2 \cdot S_{eff}}{W} \tag{2.24}$$

From the experimental data and assuming an infinite bulk lifetime, the upper limit of the effective surface recombination velocity will be calculated according to:

$$S_{eff} \leq \frac{W}{2\tau_{eff}} \tag{2.25}$$

2.1.3. Surface passivation techniques

The high number of defects at the bare silicon surfaces makes surface recombination the dominant mechanism in silicon wafers. The reduction of such surface recombination is achieved by surface passivation. In thinner silicon wafers surface passivation becomes even more important for the development of high-efficiency solar cells, since photogenerated carriers will easier reach the rear surface of devices.

Generally, surface passivation is ascribed to two strategies: that of reducing interface defect density (D_{it}), namely chemical passivation, and the reduction of either electron or hole concentrations (or both) at the surface, i.e. field effect passivation. Reducing the defect density requires the surface bonding valence states to be positioned outside the c-

Si band gap, which can be achieved by Si-O, Si-N, Si-H, and localised Si-Si bonds. The surface carrier concentration can be reduced by an induced electric field thanks to a passivation layer.

2.1.3.1. Field effect passivation

Since both an electron and a hole are required for the recombination process, surface recombination rate in c-Si is maximised when the concentration of electrons and holes is equal. If respective concentrations are unbalanced, the recombination rate will be strongly reduced. Based on this fact, field effect passivation reduces the electron or hole density at the surface, inducing a band bending at the silicon surface through the creation of an electric field which provides an energetic barrier to charge accumulation at the interface.

The electron (hole) concentration at the surface can be reduced by depositing a fixed negative (positive) charged film or introducing a doping profile within the semiconductor. Silicon nitride (SiN_x) [24, 25] or aluminium oxide (Al_2O_3) [32] have been studied as dielectric films storing a high charge carrier density. However, because of the presence of a large fixed charge, the effectiveness of passivation depends on the silicon doping type and level. Thermally grown silicon dioxide with a relatively low charge density can also be used by applying an external voltage or an electrostatic charge at the surface to provide the field effect [122].

The field effect passivation scheme can either be applied at the front or rear side of c-Si, creating a p/n junction with opposite doping types or lightly-heavily doped junctions with dopants of the same polarity as the bulk (p/p^+ or n/n^+). In the latter case, passivation is referred to as back surface field since it is often used for the rear surface passivation of solar cells.

2.1.3.2. Chemical passivation: saturation of defects

Chemical passivation allows saturating the dangling bonds present at the c-Si surface properly, and consequently the number of recombination centres can be decreased. This strategy is usually related to a passivating layer grown over the c-Si surface which decreases the density of defects N_{st}. Although, the reduction of the capture cross sections σ_p and σ_n would have the same effect, it is generally believed that these parameters are intrinsically related to the type of defect and, hence, cannot be varied.

Surface passivation by dangling bond saturation can be achieved by growing an oxide film at high temperatures or by depositing passivating films with the addition of molecular hydrogen as a precursor gas. This is the case of a-Si:H, that can also give additional field effect passivation by further growth of doped layers.

Besides, cleaning steps before deposition of the passivating film are above all very important to reduce defect density at the c-Si surface. In most chemical cleaning methods, a dipping into diluted HF solution prior to depositions eliminates the native oxide at the substrate and terminates surface dangling bonds by atomic hydrogen. Other cleaning approaches are based on dry methods, usually consisting on a plasma and etching gas exposure [123].

In many practical cases, the above-mentioned techniques occur at the same time, reducing the interface state density and additionally providing a field-effect passivation. An overview of the most relevant materials and techniques for c-Si surface passivation has been presented in section 1.3.2, emphasizing the rear surface approaches.

2.2. n/n$^+$ band energy diagram analysis

Once the main surface passivation techniques for c-Si have been introduced, in the following paragraphs a detailed analysis of the rear n/n$^+$ junction behaviour is given. In order to give more insight on the physical aspects at this back junction, computer assisted modelling based on the simulation software AFORS-HET [124] and a home-developed simulation code based on Silvaco Atlas 2D finite element commercial tool [125] have been used.

In n type c-Si wafers, rear passivation leads to an n/n$^+$ junction which establishes the so-called BSF. In homojunction devices, the rear band bending mainly depends on the doping concentration of the n$^+$ region. As can be seen in Figure 2.4, if a lightly doped BSF is used almost flat bands are obtained. On the contrary, if higher dopings are achieved, the electron transport at the conduction band is enhanced. However, in any case, holes are not prevented from reaching the n/n+ junction, and therefore recombination mechanisms can limit the potential of the homojunction BSF.

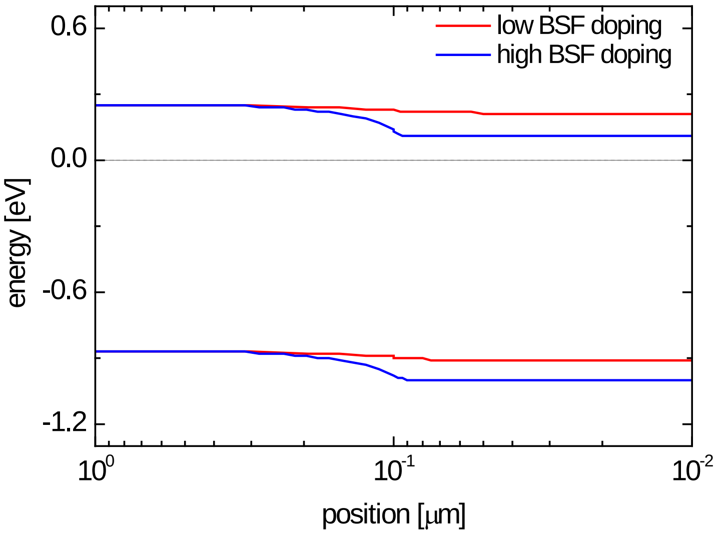

Figure 2.4. Band diagram at the n/n$^+$ homojunction obtained from AFORS-HET numerical device simulator. Two differently doped n$^+$ regions have been tested.

Device operation can be greatly improved by using heterojunctions instead of usual homojunctions. Due to the difference of electron affinity and band gap of amorphous and crystalline materials, the energy band diagram (after Anderson's model) is characterised by the presence of discontinuities in both the conduction-band edge and valence band-edge, which will allow the selective control of carrier transport. At the n/n$^+$ junction these offsets provide a barrier that favours the collection of electrons and repulses holes from the rear electrode. However, this band bending can be significantly modified depending on the properties of the amorphous material, which will then have an impact on the solar cell's BSF operation, and therefore on the performance of the final device.

In this section a short overview of the band line-up at the n/n$^+$ junction is given, and the impact of varying the properties of amorphous silicon is discussed. As a simplified approximation, no defect density at the rear heterointerface has been accounted for, since as it can be seen in Figure 2.5, simulations of the n/n$^+$ junction with an (n) layer with low D_{it} lead to small differences on the band bending in (n)c-Si ($\Delta\varphi_{c\text{-}Si} \sim 9$ mV) compared to the use of layers with higher D_{it}.

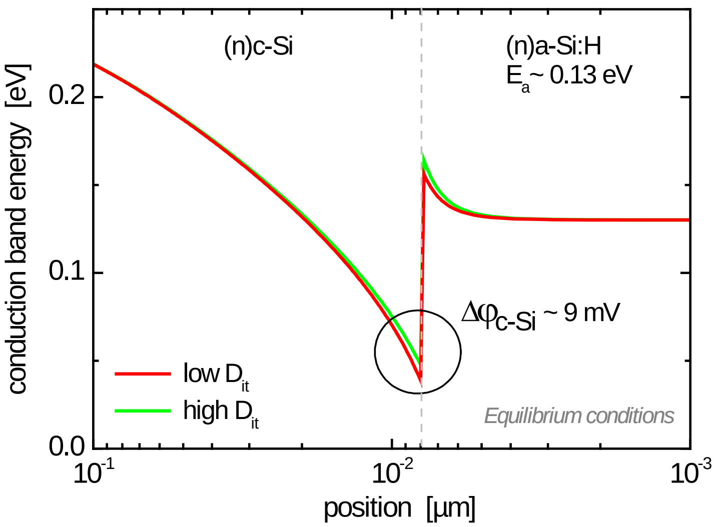

Figure 2.5. Conduction band bending of an n/n^+ heterojunction with varying D_{it} at the amorphous/crystalline interface. Low and high D_{it} values corresponds, respectively, to 1×10^9 and 1.2×10^{12} cm^{-2}.

In Figure 2.6, results of band energy numerical simulations for two different n/n^+ junctions are presented, where the activation energy (E_a), at the n^+ region have been modified. In Figure 2.6(a), a highly doped (n^+) layer characterised by a small E_a has been used. In this case, the (n^+) conduction band energy lies below that of the c-Si. Consequently, the spike at the conduction band is quite reduced and the electrons' transport across the junction is provided through thermionic emission and tunnelling-mediated mechanisms. At the valence band offset, holes are effectively screened, diminishing the carrier recombination probability.

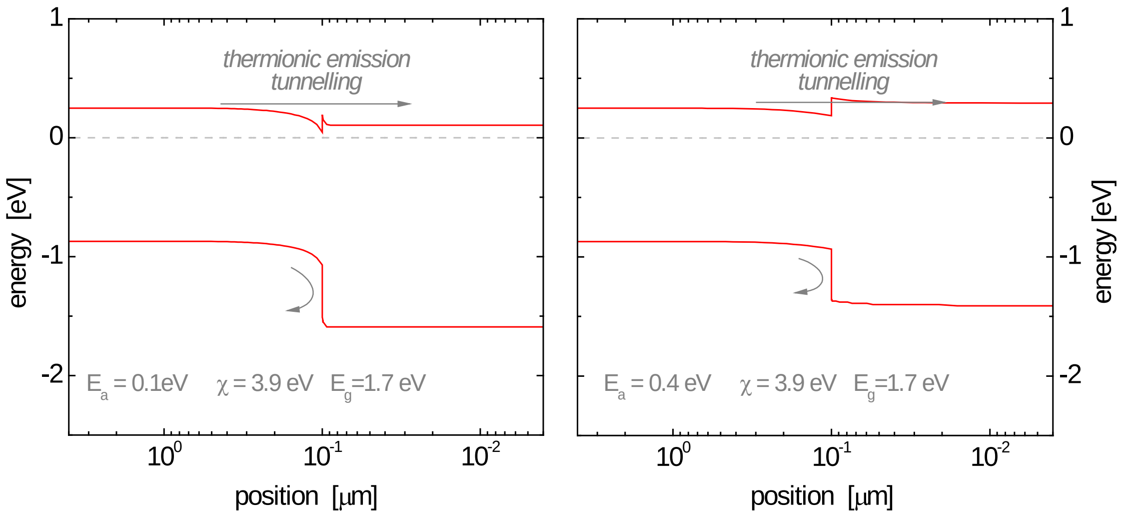

Figure 2.6. Band diagram of two different n/n$^+$ heterojunctions as calculated with the AFORS-HET simulation tool. E_a of the (n$^+$) region has been modified.

If a less doped (n$^+$) layer is used, and E_a is increased (Figure 2.6(b)), the band bending is modified in a way in which both thermionic emission and tunnelling mechanisms are hampered, since the spike at the conduction band becomes larger. Here, the passing of electrons is not as evident as in Figure 2.6(a). Besides, the barrier at the valence band is smaller, which could be a drawback to prevent holes reaching the (n$^+$) region.

Then, in view of results presented in Figure 2.6, it will be preferred to use (n$^+$) layers with lower activation energies in order to minimise the barrier for electrons at the conduction band and enlarge the valence band mismatch. Thereby, the electron charge transport will be enhanced at the same time as holes will be effectively repulsed.

If a different band gap of the (n$^+$) material (leading to different conduction and valence band offsets) is used in simulations, the band bending is accordingly modified. In Figure 2.7(a) the same activation energy as in Figure 2.6(a) is used. Again, the (n$^+$) conduction band energy lies below that of the c-Si. However, in this case due to the lower electron affinity used in the calculations, the conduction band offset is more pronounced, and tunnelling processes through the spike are also involved. As the material's gap is higher, the offset at the valence band is larger, which increases the screening of holes towards the n base material.

In Figure 2.7(b) a higher E_a is used for simulations (i.e. less doping in the layer). As it can be seen, the bending in the (n$^+$) material extends over a larger region, which makes tunnelling-mediated paths a less provable mechanism for electron transport. Moreover, as the valence band barrier is smaller the loss of holes may increase, which renders the case presented in Figure 2.7(b) less favourable.

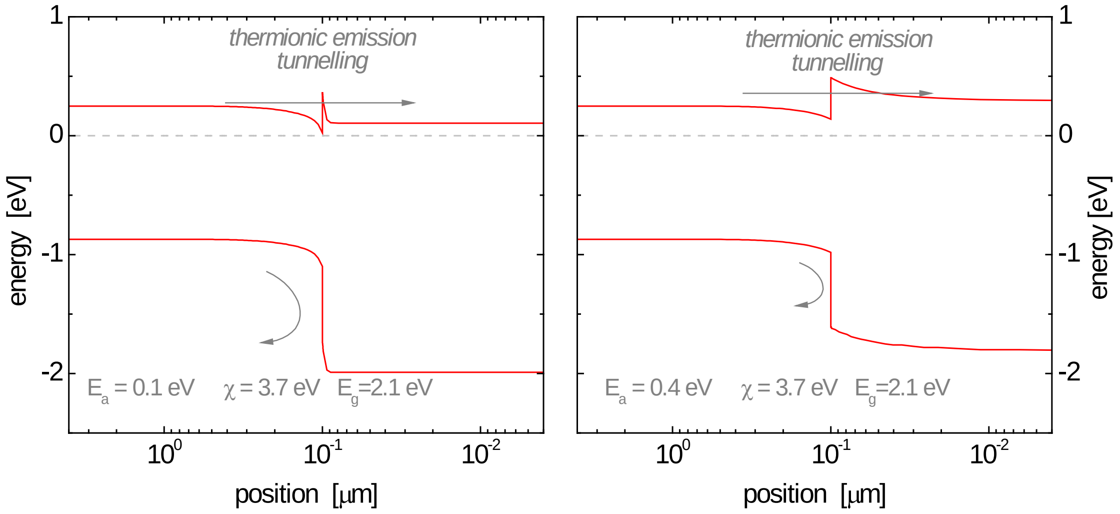

Figure 2.7. Band diagram of two different n/n$^+$ heterojunctions as calculated with the AFORS-HET simulation tool. E_g of the (n$^+$) region has been modified compared to Figure 2.6.

According to these results, for a high performing n/n$^+$ heterojunction, here the use of materials with low activation energy and high band gap will be preferred. Thereby, the charge transport in the conduction band will be enhanced, and a strong barrier at the valence band will be created to effectively repulse holes. Consequently, recombination mechanisms will also be minimised.

2.3. The solar cell and the impact of the BS on device characteristics

Silicon heterojunction device structure uses c-Si absorber layer. However, the p/n junction is no longer achieved by contact of opposite doping types within a crystal lattice as it is been done in homojunction solar cells. Rather, the junction is made through deposition of thin a-Si:H film doped with the opposite polarity to that of the absorber. Then, the heterojunction is done between crystalline and amorphous phases, which have a band gap energy difference of approximately 0.6 eV.

2.3.1. Current density and open-circuit voltage

The effects of the p/n junction can be described with the diode equation, an expression for the current density at the junction as a function of voltage. When a load is present, a potential difference develops between the terminals of the cell. A current which acts in the opposite direction to the photocurrent is generated and the net current is reduced from its short circuit value. This called dark current density (J_{dark}) varies like:

$$J_{dark} = J_0\left[\exp\left(\frac{qV}{n_d k_B T}\right)-1\right] \tag{2.26}$$

where J_0 is the saturation current density, q is the charge of an electron, n_d is the diode ideality factor, k is the Boltzmann's constant and T is the temperature.

As inferred from equation (2.26), the p/n junction diode admits a much larger dark current under forward bias ($V > 0$) than under reverse bias ($V < 0$). As early reviewed, the behaviour of the device is strongly affected by the recombination properties of the material. Generated minority carriers need to diffuse to the junction to be collected and thereby, be able to contribute to the current. Therefore, diffusion length L_{diff} [cm] being characterised by the diffusion coefficient D [cm^2/s] and the lifetime τ according to $L_{diff} = \sqrt{D\tau}$, is a valuable indication of recombination properties of material (and it is taken into account in the calculation of J_0). In order to extract the charge carriers, L_{diff} should be in the order of wafer thickness, W.

Under typical illumination conditions, photons with energy larger than the band gap are absorbed creating electron and hole pairs which are separated in the space charge region with electrons being attracted to the n-type region (positively charged) and vice versa for holes (p-type region). If an external circuit is connected with the front contact held at voltage V, dark current is shifted by the value of the photogenerated current (J_{ph}):

$$J = J_0\left[\exp\left(\frac{qV}{n_d k_B T}\right)-1\right]-J_{ph} \tag{2.27}$$

where J_{ph} can be calculated using the approximation $J_{ph} = qG(d_{depl} + L_n + L_p)$, being L_n and L_p the diffusion lengths of the minority carriers in their respective regions and d_{depl} the width of the depletion region [107].

The sign convention for current in photovoltaics is such that the current is positive, which is the opposite of the usual convention for electronic devices. Thus, from now on, the net current density in the cell will be presented as $J = J_{ph} - J_{dark}$.

When the contacts of the cell are isolated, the potential difference is maximised, thus obtaining the open circuit voltage (V_{OC}) as apparent in equation (2.28):

$$V_{oc} = \frac{n_d k_B T}{q}\ln\left[\frac{J_{ph}}{J_0}+1\right] \tag{2.28}$$

Maximising V_{OC} requires minimising the saturation current, which can be achieved maintaining high carrier lifetimes, hence the importance of surface passivation.

2.3.2. Fill factor and efficiency

Conversion efficiency of a solar cell is defined as the ratio of its electric power density delivered to the incoming light density that strikes the cell, which usually corresponds to the internationally accepted standard test condition (reference air mass AM1.5, sunlight normalized to 1000 W/m^2, temperature kept at 25°C). Conversion efficiency is determined by measuring the photocurrent as a function of the cell voltage using the formula:

$$\eta = \frac{J_{sc} V_{oc} FF}{P_s} \qquad (2.29)$$

where J_{SC} is the short-circuit current density (flowing through the device when the voltage is zero); V_{OC} is the open circuit voltage (voltage between the terminals of the device when the current is zero); P_S is the incident solar power density (1000 W/m^2); and FF the fill factor defined as the electric power produced at the maximum power point of the J(V) curve divided by the product $J_{SC} \cdot V_{OC}$, as it can be seen in Figure 2.8.

$$FF = \frac{J_{mp} V_{mp}}{J_{sc} V_{oc}} \qquad (2.30)$$

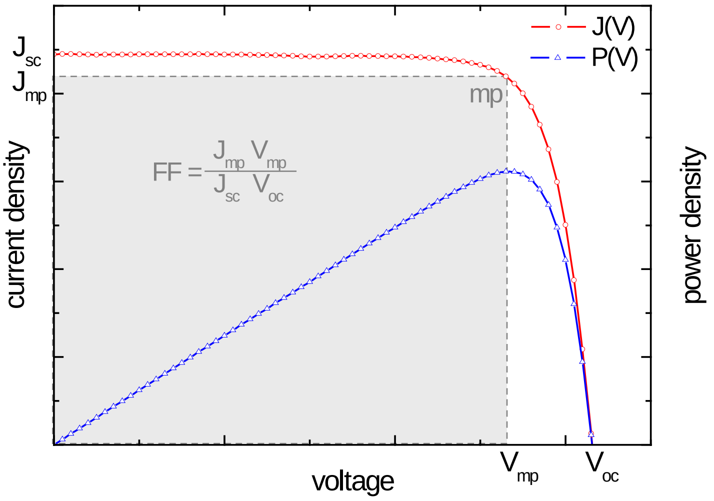

Figure 2.8. J(V) characteristic of a solar cell under illumination.

2.3.3. Equivalent circuit of heterojunction solar cells

The most commonly accepted model describing solar cells has been used for our HJ devices. It is based on the well-known two-diode model, which schematically describes the equivalent circuit diagram for a solar cell as depicted in Figure 2.9.

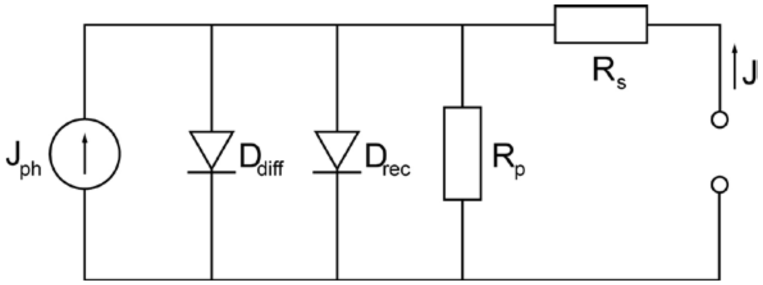

Figure 2.9. Equivalent circuit for two-diode model of a real solar cell including series and shunt resistances.

The current-voltage characteristic of the two-diode model can be expressed as [107]:

$$J = J_{01}\left[\exp\left(\frac{V - R_s J}{n_1 kT}\right) - 1\right] + J_{02}\left[\exp\left(\frac{V - R_s J}{n_2 kT}\right) - 1\right] + \frac{V - R_s J}{R_p} - J_{ph} \qquad (2.31)$$

In Figure 2.10(a) the impact of the two-diode model parameters on the dark J(V) characteristic of the solar cell is shown. The solar cell is characterised by a first diode with an ideality factor n_1 and a current saturation J_{01}. It is the main diode giving information about diffusion transport occurring at the p/n junction at high-forward bias. Therefore, it principally impacts the V_{OC} parameter. In Figure 2.10(b), experimental dark J(V) curves corresponding to two differently doped BSF are presented. The lower V_{OC}s obtained with the BSF1 sample correspond to higher J_{01} values. Ideality factor n_1, typically lies between 1 and 2.

At moderate forward bias, the second diode becomes especially important on heterojunction solar cells. Diverse charge transport paths within the structure can arise, such as emission process, recombination or tunnelling effect. Saturation current density J_{02}, gives an idea of phenomena in the space charge region (recombination and tunnelling), hence having an impact on mainly FF (although its effects can also be seen in the V_{OC}); the smaller J_{02}, the better FF. The ideality factor n_2 typically lies above 2.5 in HJ devices.

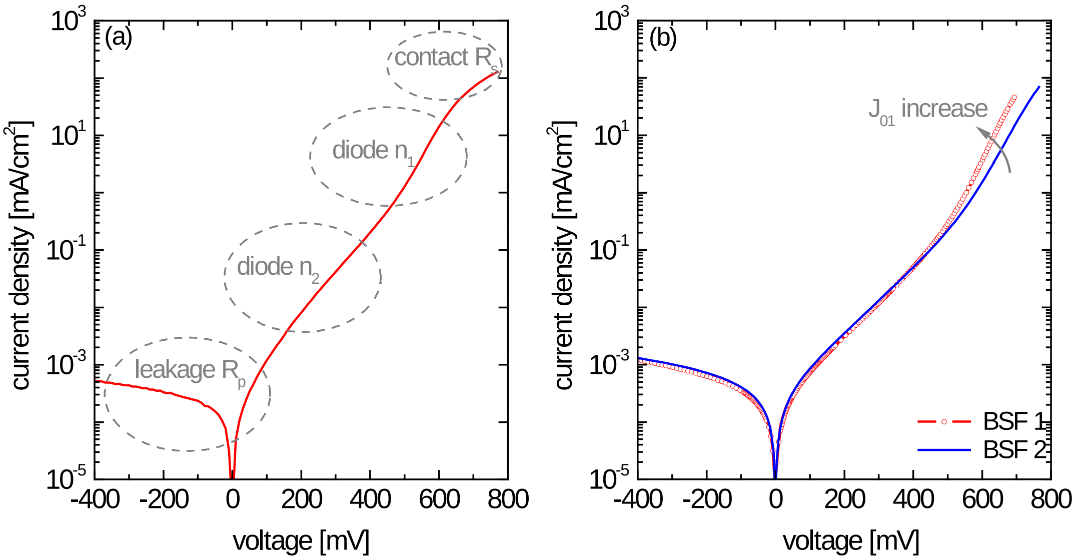

Figure 2.10. Experimental dark current-voltage characteristic showing the influence of the two-diode model parameters.

R_S and R_P are the parasitic series and parallel resistances, respectively. The series resistance arises from the bulk resistance of the silicon wafer, the resistance of the metallic contacts of the front and back surface, the contact resistance between layers and metallic contacts and further circuit resistances from connections and terminals. If, for example the a-Si:H BSF is not sufficiently doped the charge transport will be hindered and consequently R_S will increase. Its impact on the J(V) curves is indicated in Figure 2.11(a) and (b). The parallel resistance is mainly caused by leakage across the p/n junction due to non-idealities and impurities near the junction, which cause partial shorting of the junction, particularly near the edges of the cell. Under reverse bias and at very low forward bias, parallel resistance prevails, as observed in Figure 2.10. If, for instance the edge isolation is not properly done the front emitter and the rear of the cell will be contacted, leading to a decrease in R_P, which impacts the J(V) characteristics as presented in Figure 2.11(c) and (d). Both types of parasitic resistances primarily reduce the value of the fill factor. In turn, for an efficient solar cell R_S should be as small as possible, and R_P as large as possible (in the MΩcm^2 range).

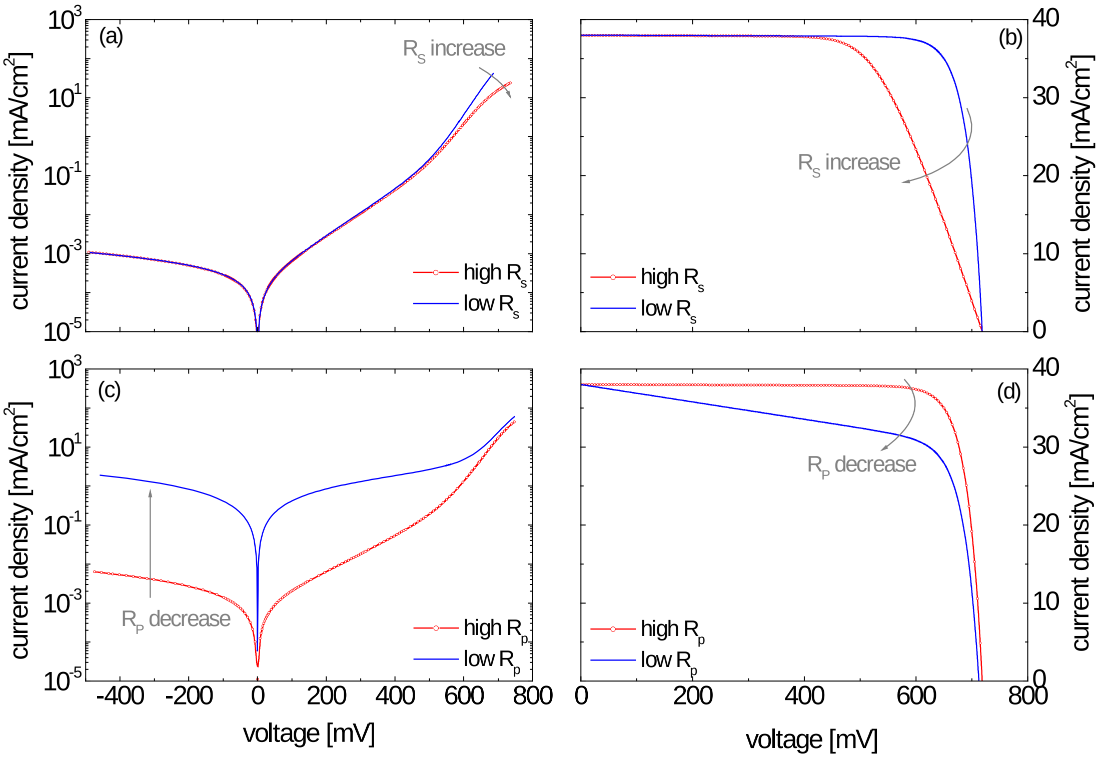

Figure 2.11. Experimental J(V) curves at dark and under illumination for different series (a, b), and parallel (c, d) resistance values.

2.4. Band diagram analysis and carrier transport at the rear side of HJ solar cells

The amorphous/crystalline heterojunction results from the contact between these two materials, which have a different energy band gap (E_g) of approximately 0.6 eV ($E_{g,\text{ c-Si}}$ = 1.12 eV and $E_{g,\text{ a-Si:H}}$ = 1.75 eV at 300 K). According to the Anderson's model [126], which is the most widely used to represent the band diagram of the HJ cells, the difference of band gaps and electron affinities entails the presence of band offsets at the conduction and valence band edges (ΔE_C, ΔE_V respectively).

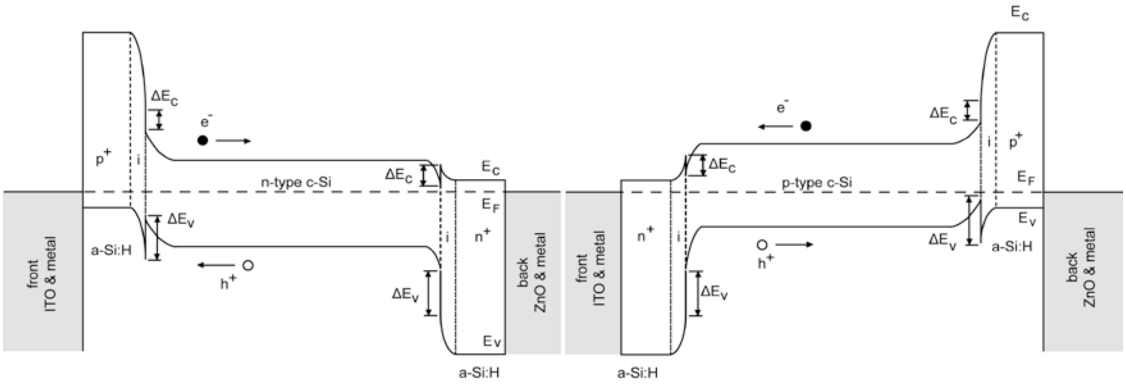

Figure 2.12. Schematic band diagram of a silicon heterojunction cell based on (a) n-type and (b) p-type c-Si.

The discontinuity in the conduction-band edge equals the difference in electron affinities ($\chi_{c\text{-}Si} = 4.05$ eV and $\chi_{a\text{-}Si:H} = 3.9$ eV), and the discontinuity in the valence-band edge depends on the difference in both electron affinities and band gaps. Thus, the band offset between a-Si:H and c-Si at the valence band, is larger than that at the conduction band [127]. Besides, the band bending held up on the amorphous silicon side is comparably flat to that on c-Si, where most of the overall band bending is supported [128].

In Figure 2.12 a schematic overview of the band diagram of a-Si:H/c-Si HJ cells is given. In the case of n-type based devices, holes are collected at the front side of the solar cell. The large valence band offset on the front side leads to a potential barrier in which minority carrier holes can be trapped, thus limiting efficient photogenerated carrier transport. However, tunnel transport mechanisms can assist trapped holes crossing this potential barrier to get the (p)a-Si:H emitter [129].

On the back side, the small offset at the edge of conduction band does not prevent electron collection at the metal electrode. Moreover, the pronounced ΔE_V sets a strong barrier for holes that are effectively screened, thus preventing recombination mechanisms at the rear side.

The insertion of the thin intrinsic a-Si:H layer containing less defect states than doped a-Si:H provides a remarkable improvement in c-Si surface passivation, although it can also suppress the trap assisted tunnelling which in turn can somehow be a useful contribution for the conduction of majority carriers [130]. Actually, tunnelling can be useful to improve FF values.

A way to create a larger barrier for minority carriers (holes) is the further doping of rear side a-Si:H, bringing the Fermi level closer to the conduction band edge. Besides, as it has been discussed in section 2.2, the height of the valence band offset can also slightly be increased enlarging E_g by the introduction of oxygen or carbon into the layer (a-Si:H-based alloys, such as a-SiC$_X$:H and a-SiO$_X$:H) [44]. However, this mechanism may lead to a reduction of the passivation efficiency due to defects in the layer.

In Figure 2.12(b), the band line-up of a p-based heterojunction is also presented. In this case, electrons are collected on the front side and holes on the back side. The fact that silicon solar cells are more efficient on n-type c-Si wafers than on p-type can predominantly be ascribed to the inherent asymmetry of the conduction and valence band offsets. The less favourable band offsets created in (n)a-Si:H/(p)c-Si heterojunction is believed to reduce performance compared to its oppositely doped counterpart [85]. Although carrier collection is more efficient than for n-based HJ (smaller ΔE_C), the expected built-in voltage is also smaller, thus leading reduced V_{OC}s [130]. Besides, minority charge carriers are also less effectively screened from the back side and the large offset in the valence band between (p)c-Si and (p)a-Si:H often hinders the majority carriers (holes) from flowing to the back terminal.

Nevertheless, p-type wafers are also being used on HJ solar cells fabrication, since they are more easily found on the market than n-type wafers, and several groups [82, 129, 131-134] have already demonstrated performing results on p-type, although conversion efficiencies are still lower than those achieved on n-type wafers.

As briefly reviewed in the preceding paragraphs, in order to enhance the carrier transport at the rear side of HJ solar cells a compromise between band line-up and carrier transport is necessary. Minimal dangling bond density in (i)a-Si:H, fine-tuning of tunnelling mechanisms and maximised band bending (high-quality wide-gap a-Si:H layers) are desired. The accomplishment of all these conditions is subject to the technological aspects of the a-Si:H deposition technique. Thus, an extensive work of development of high-quality back surface field schemes and subsequent assessment on their performance has been conducted. To this end, a deep study of the influence of the deposition parameters of PECVD-grown amorphous layers and their impact on HJ solar cells is presented in the following chapter.

2.5. Back side optical considerations

As it has been previously said, optical issues concerning the back side of HJ solar cells are clearly determined by the way layers at the front side behave. The a-Si:H and TCO films at the front of silicon heterojunction solar cells absorb light parasitically. As presented in Figure 2.13, the a-Si:H stack at the front of the cell is very absorbing at short wavelengths (< 600 nm), which is characterised by the increased extinction coefficient. Moreover, ITO absorbs both in the UV and also in the IR due to excitation of free carriers. Then, all of the short wavelength losses and some of the IR losses occur at the front of the cell, thus governing the attainable J_{SC} of the cell. For this reason it can be considered that the back side of solar cells will not play a decisive role on the optical losses of the device.

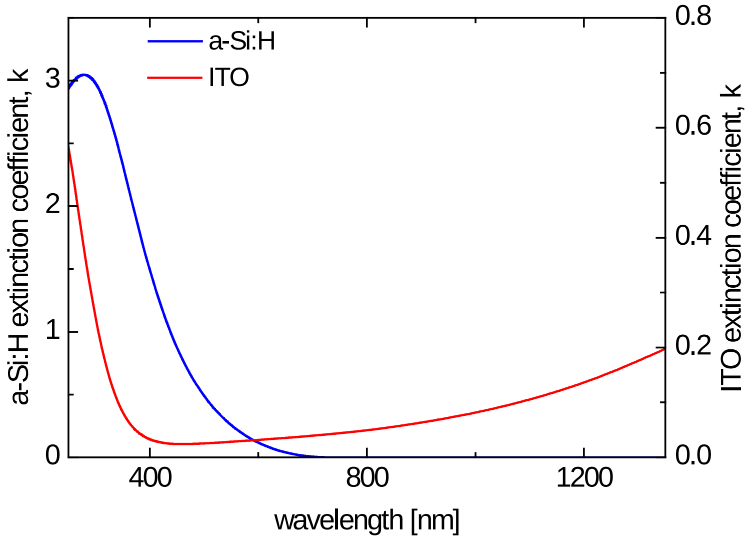

Figure 2.13. Extinction coefficient obtained by spectroscopic ellipsometry for (p)a-Si:H and TCO films.

Figure 2.14 shows the reflectivity of various solar cells with identical front side and different rear side configurations. In the long wavelength range, differences have been observed whether ITO, ZnO or no TCO is used at the back contact. The maximum contribution of photons of wavelength λ to the short-circuit current density has been calculated using equation (2.32) [135].

$$J_{sc}(\lambda)\big|_{max} = IQE(\lambda)P_s(\lambda)\frac{q}{hc}\lambda(1-R(\lambda)) \qquad (2.32)$$

where $P_S(\lambda)$ is the incident illumination power of photons at a given wavelength, hc/q = 1239,84 Vnm, R(λ) stands for the reflection at the cell surface and IQE(λ) denotes the internal quantum efficiency of a standard HJ solar cell considered to be equal in all of the cases.

Indeed, the differences in R(λ) induced by the various back side configurations occur at wavelengths higher than the gap of c-Si, where photons weakly interact with the semiconductor. Therefore, no J_{SC} changes in the IR region have been obtained. Integrating $J_{SC}(\lambda)$ over the whole spectral region, leads to almost equal short-circuit current densities in all the devices herein presented (see Figure 2.14). This highlights the fact that the rear side does not remarkably contribute in the optical behaviour of our devices.

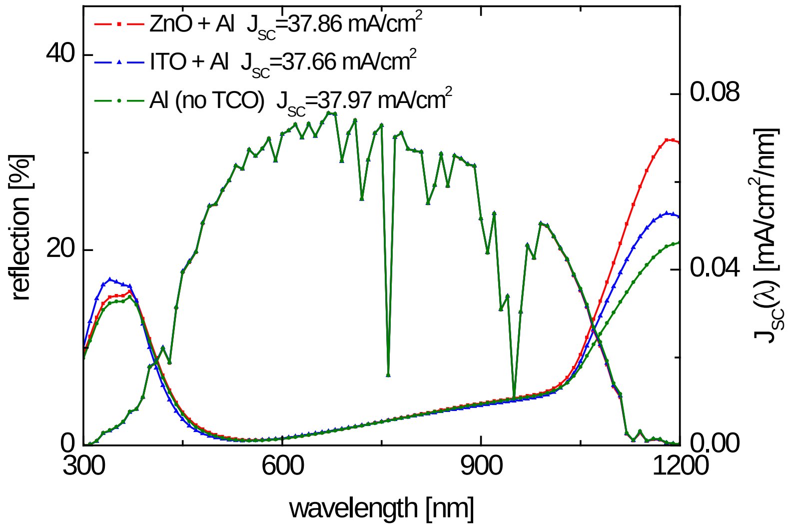

Figure 2.14. Reflection and short-circuit current density per wavelength unit for three different devices with various rear configurations. The $J_{SC}(\lambda)$ curves for all samples are superimposed.

Despite all this, the current trend towards wafer thickness reduction can not be dismissed. When using thinner wafers not only rear side passivation quality becomes even more important, but also the optical performance of devices gets more relevant. Light trapping schemes and improvements at the back of the cell which allow long wavelength light to undergo multiples internal reflections without leaving the cell will contribute to J_{SC} and lead to enhanced performances. However, this will not be a major concern of the present work, since wafers around 200 µm have been used.

3. Amorphous silicon layers applied to back side of HJ devices

Hydrogenated amorphous silicon has demonstrated to be a high performing material in a-Si:H/c-Si heterojunction solar cells, leading to conversion efficiencies over 23% [64]. Intrinsic and doped layers applied to the emitter of devices have been widely studied and their influence on the solar cell conversion efficiencies has been reported. By contrast, little research has been done on amorphous silicon at the rear side of HJ cells, since its impact on the overall device performance depends on the front side events, and therefore it is difficult to quantify. Nevertheless, this amorphous back side is a key part of the solar cell and plays a valuable role to obtain high efficiencies.

In the present chapter, some fundamental aspects of amorphous silicon on which the analysis of experimental data is based will be introduced. The experimental set-up used for the deposition and characterization of studied amorphous layers will be briefly described. Moreover, the technological steps taken in order to optimise the properties of (n)a-Si:H layers will be detailed. Finally, optimised amorphous layers will be used at the BSF of heterojunction solar cells and their effects on the device will be investigated. The fundamental parameters and the main requirements at the BSF to achieve high efficiencies will be assessed.

3.1. Properties of hydrogenated amorphous silicon

In single crystal silicon each atom is covalently bonded to four neighbouring atoms through equal bonding lengths and angles. A unit cell can be defined, from which the crystal lattice is identically reproduced by stacking it one next to each other. A regular atomic arrangement results in a structure with a long range order that differs from that of hydrogenated amorphous silicon, as illustrated in Figure 3.1. Though most silicon atoms are four-fold coordinated, a-Si:H does not exhibit a structural order over a long range due to small deviations in bond lengths and angles. The larger deviations lead to weak bonds that can easily be broken, resulting in defect formation within the atomic network. In a-Si:H, defects are mainly silicon atoms that are covalently bonded to only three silicon atoms and have one unpaired electron [136]. These unsaturated bonds are the so-called dangling bonds.

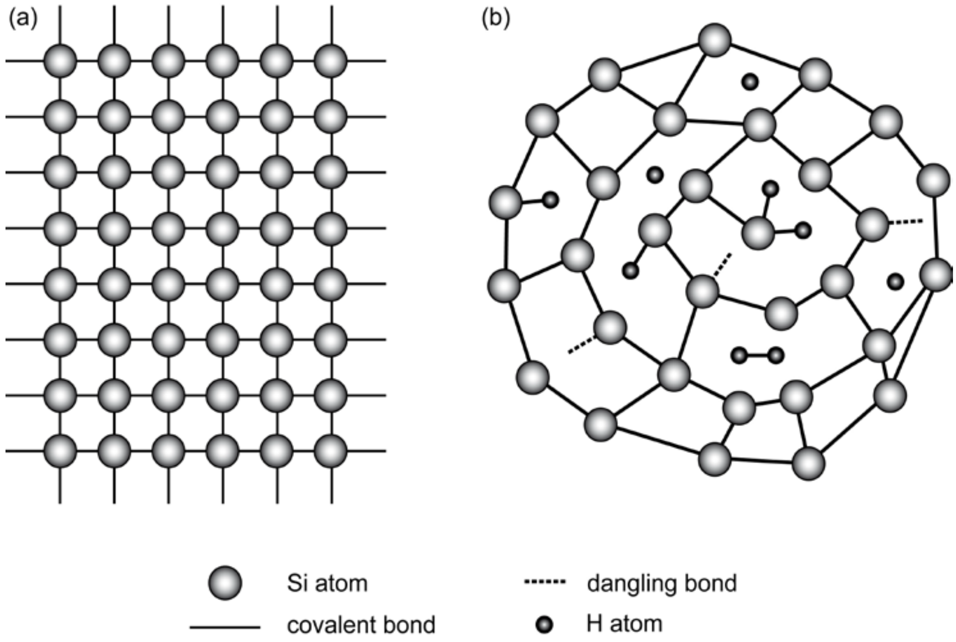

Figure 3.1. Schematic view of the atomic structure of (a) single crystal silicon and (b) hydrogenated amorphous silicon.

In pure a-Si, a large concentration of defects in the amorphous atomic structure is found (about 10^{21} defects per cm^3). However, these defects can be reduced by the incorporation of hydrogen into the atomic network. Additional hydrogen passivates most of the silicon dangling bonds, lowering defect density down to 10^{16} cm^{-3} [137]. Besides, it has been demonstrated that incorporation of hydrogen into the a-Si network allows a better integration of dopant atoms [138] which are essential for photovoltaic applications.

In order to understand the optical and electrical properties of a-Si:H, a proper description of the density of states (DOS) distribution is of great importance. In Figure 3.2 the corresponding model for the density of states introduced by Davis and Mott [139] is shown. For an ideal silicon crystal, the valence band (VB) and the conduction band (CB) are separated by a well-defined band gap (E_g), where there are no allowed energy states in it. Contrary to this, the energy states of the valence and conduction bands in a-Si:H spread into the band gap throughout the band tail states near the band edges. In addition, between the band tails lie allowed energy states introduced by defects (defect states related to dangling bonds), represented by two Gaussian distributions.

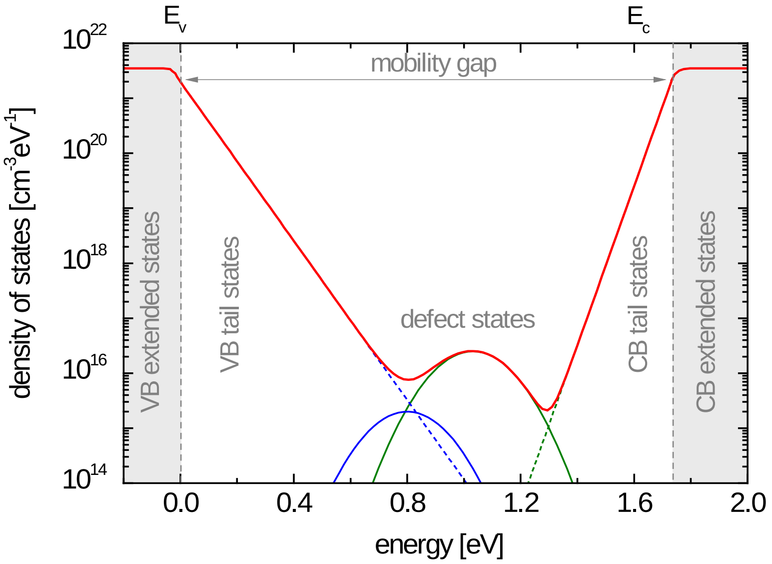

Figure 3.2. Standard model of density of states in hydrogenated amorphous silicon. The shaded areas indicate extended states in the bands, which have tails of localised states with an exponential distribution. Within mobility gap, two Gaussian distributions of states represent defect states related to dangling bonds.

A continuous distribution of density of states characterises a-Si:H, and no properly defined band gap between E_V and E_C can be settled. In general, the band edge is considered to be the energy that separates localised states from extended ones in the DOS distribution. The band edges are correspondingly termed the conduction and valence band mobility edges, and define the mobility gap (E_μ) which is commonly considered to be 0.1 to 0.2 eV larger than the optical band gap [137].

The states above the conduction band mobility edge and below the valence band mobility edge are extended, and are populated with electrons and holes, respectively. The localised states within the mobility gap consist of the tail states and the defect states, and can be different in nature. CB tail states are acceptor-like states and VB tail states are donor-like states, whereas dangling bond states (“D-centres”) are amphoteric. Dangling bonds can be in three different charge states: positive (D^+) when they are not occupied by electrons, neutral (D^0) when occupied by one electron or negative (D^-) when occupied by two electrons [136]. Therefore, for this kind of defects, charge state transitions between the +/0 (donor-type) and 0/- (acceptor-type) are possible, and define two energy levels that characterise the centres of the two Gaussian distributions, separated by the correlation energy U. In the case of a-Si:H it is considered to be positive and in the order of 0.2 eV.

A more advanced description of defect states distribution in a-Si:H is the defect-pool model [140, 141] which accounts for the break of weak Si-Si bonds as the source of defect-forming reactions, where hydrogen is thought to play an important role by breaking and reforming Si-H bonds. The main idea behind the defect-pool model is that the concentration of dangling bond states depends on the formation energy of the dangling bonds. Moreover, the formation energy of a dangling bond depends on charge state of the dangling bond and thereby on the position of the Fermi level. For n-type material, where E_F gets closer to the E_C, the dangling bond distribution is shifted towards the lower part of the gap and defect concentration increases. On the contrary, as the Fermi level gets closer to the valence band (p-type material), dangling bond distribution is shifted towards E_C.

3.2. Experimental details for PECVD a-Si:H

In the following paragraphs the deposition technique used to fabricate a-Si:H layers is presented. Details on the sample preparation, and the characterisation techniques used to determine the properties of studied layers are given.

3.2.1. PECVD set-up

Deposition of amorphous silicon layers, whether they are intended to be used as passivation layer, emitter or BSF, or for material characterisation has been carried out in a five-chamber cluster tool, equipped with two parallel-plate capacitively coupled PECVD reactors operating at 13.56 MHz, as depicted in Figure 3.3. In this technique the plasma provides a source of energy to excite and decompose the gaseous precursors (SiH_4, H_2 and hydrogen-diluted PH_3 in the case of (n) layers) due to multiple collisions between high-energetic electrons, and generates radical and ions species in the chamber. The deposition of an a-Si:H film is achieved by attaching these reactive particles of dissociated silane molecules to the surface of the growing film. Then, the film growth in a PECVD process consists of a gas diffusion, electron impact dissociation, gas-phase chemical reaction, radical diffusion and deposition. Detailed analysis of the process involved in the growth of amorphous silicon go beyond the scope of this work and can be found elsewhere [137, 142, 143].

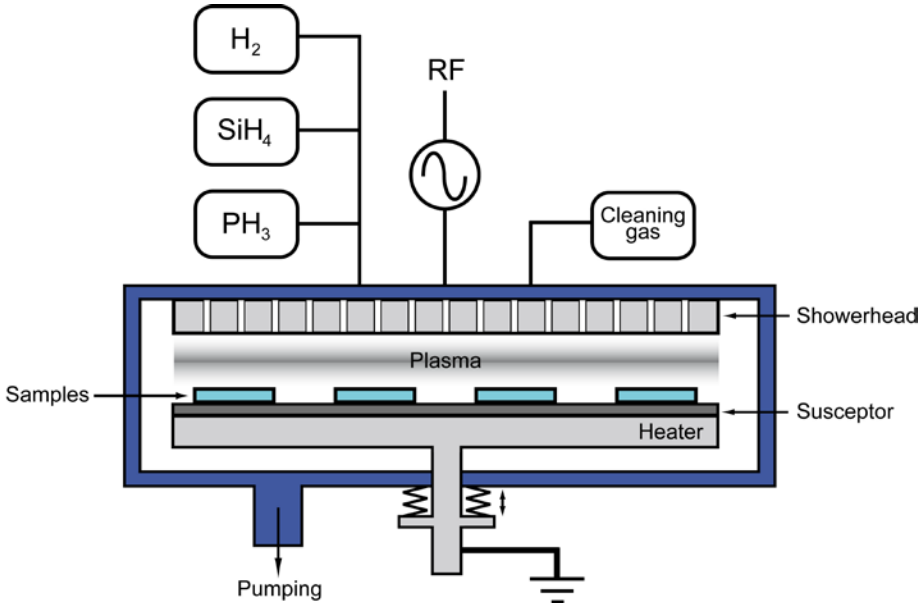

Figure 3.3. Schematic illustration of the PECVD system used at INES.

Initially, all doped amorphous layers were performed inside the same PECVD reactor, named ‘PM1’ as defined in Figure 1.5. Top quality intrinsic layers were grown in a different reactor (‘PM3’ as indicated in Figure 1.5). Thus, at the beginning of this thesis buffer and phosphorous-doped layers were deposited in the same chamber as the boron-doped films, using appropriate cleaning schemes of the ‘PM1’ reactor after each deposition. However, in the course of this work, we realised that cross-contamination problems affected the quality of our a-Si:H films. In order to improve the layers’ passivation, technical modifications were incorporated on the cluster tool. p- and n-type a-Si:H depositions together with their associated buffer films were split, being processed in two specifically dedicated chambers: ‘PM1’ for (p) layers and ‘PM3’ for the (n) ones.

Then, unless otherwise indicated, all of the intrinsic and n-doped films analysed and reported on in this thesis have been processed inside the same PECVD chamber (the other one being reserved for p-doped layers). The substrates placed on a tray of 60×60 cm^2 are heated at 200°C to achieve optimum film quality, since thermally activated surface diffusion of adsorbed radicals favours the film’s growth.

3.2.2. Sample preparation and standard characterisation techniques

Depending on the characterisation to be performed on samples, a-Si:H films have been deposited on Corning glass or polished c-Si wafers. Deposition parameters have been carefully adjusted in order to enhance the quality of deposited layers, minimizing process-induced damage during thin-film growth (see section 3.4).

Samples fabricated for passivation purposes were deposited on FZ n-type c-Si polished wafers (⟨100⟩; 300 µm; 1-5 Ωcm). After cleaning the samples in a wet chemical HF bath, a-Si:H was deposited sequentially on both surfaces. Single intrinsic or n-doped 10 nm-thick precursors as well as samples with an (i) a-Si:H buffer layer between the wafer and the (n)a-Si:H were fabricated. To determine the passivation quality of films, a symmetric a-SiH/c-Si/a-Si:H structure equally treated on both sides, was used.

The quality of the (n)a-Si:H/(n)c-Si heterointerface was determined by Quasi-Steady-State Photoconductance (QSSPC) measurements, performed with a WCT-120 Sinton instrument, in both QSS and transient modes. The QSSPC technique allows the contactless characterisation of solar cell precursors [144]. From this measurement, the effective lifetime τ_{eff} (limited by surface recombination as defined in section 2.1.2) can be determined as a function of the excess minority carrier density. Furthermore, this technique also allows the estimation of the implied open-circuit voltage of solar cell precursors according to:

$$V_{oc,impl} = \frac{k_B T}{q} \ln\left(\frac{(N_d + \Delta p)\Delta p}{n_i^2} \right) \tag{3.1}$$

where kT/q and n_i^2 are constants already fixed in the system calculations, and N_d is determined from the c-Si resistivity specified by the user. More details on this technique can be found elsewhere [106, 122].

The thickness and microstructure of layers were estimated by Spectroscopic Ellipsometry (SE), fitting the experimental data using the widely known Tauc-Lorentz Model [145] and the surface roughness layer of the Bruggemann's approach, as it has been further detailed in [129]. The model describes the energy dependence of the imaginary part of the dielectric function ε_2 using the equation (3.2).

$$\varepsilon_2(E) = \frac{AE_0C(E - E_g)^2}{(E^2 - E_0^2)^2 + C^2E^2} \cdot \frac{1}{E} \qquad E > E_g \tag{3.2}$$

where E_0 is the peak transition energy, E the energy, E_g the optical gap (Tauc's gap), C a broadening parameter related to the film disorder, and A a parameter related to the film density.

Secondary Ion Mass Spectrometry (SIMS) was mainly used to detect the phosphorous concentration of (n) layers. Fourier-Transform InfraRed spectroscopy (FTIR) acquisitions were also performed to determine the type of bonds between silicon and hydrogen atoms within the amorphous material. Both analysis allowed to correlate structural features with optical and electrical properties of a-Si:H layers.

The output characteristics of complete HJ devices were determined using a solar simulator, with illumination calibrated to the AM1.5 spectrum (1000 W/cm^2) and sample temperature maintained at 25°C according to standard test conditions. Besides, Suns-V_{OC} measurements were also performed [146]. This technique directly measures V_{OC} as a function of the light intensity, typically from a few suns to just below 0.1 suns. The measurement results in a contactless pseudo J(V) curve, which is independent of series resistive losses. Then, Suns-V_{OC} allows to identify a pseudo FF (pFF), which is only limited by recombination and shunting phenomena.

3.3. Advanced electrical characterisation

The electrical properties of samples were evaluated on 100 nm-thick a-Si:H layers deposited on Corning glass with temperature dependent conductivity measurements. The conductivity of a-Si:H is often determined to evaluate the electronic transport properties of thin film samples. Measurements performed both at dark and under optical bias give information about the material quality. The experimental determination of σ is done through current-voltage characteristic measurements, using a coplanar electrode configuration providing an ohmic contact. Layers under study are deposited on a highly resistive Corning glass, and should be thick enough (~ 100 nm) to minimise the potential effect of glass/a-Si:H and a-Si:H/air interfaces on the measured properties.

Preventing any light, dark conductivity (σ_d) can be determined according to:

$$\sigma_d = \frac{I}{V}\frac{\omega}{\ell d} \tag{3.3}$$

where V is the applied voltage, I the measured current, ℓ the length of electrodes, d the film thickness and ω the distance between electrodes.

The dark conductivity of a-Si:H is thermally activated, and can be described by [137]:

$$\sigma_d(T) = \sigma_0 \exp\left[-\frac{(E_{TR} - E_F)}{k_B T}\right] \tag{3.4}$$

where E_{TR} is defined as the average energy of the conducting electrons, σ_0 denotes the conductivity prefactor ($\sigma_0 = N(E_C)q\mu k_B T$).

E_{TR} coincides with the conduction band edge (E_C) if an abrupt mobility edge applies to the material. However, in a-Si:H other transport mechanisms arise from the existence of localised states for which the energy lies deep in the band, well away from the mobility edge. Thus, conduction may also take place by hopping at the band tails and at the Fermi level. These transport mechanisms are weak and temperature dependent, tending to dominate at very low temperatures.

Based on the assumption that no hopping mechanisms exist, extended state conduction takes place. Therefore, the activation energy (E_a), typically defined as E_C-E_F for an n-type material, can be determined by the Arrhenius plot obtained from the temperature dependent dark conductivity measurements, according to equation (3.4). Nonetheless, the linear relationship between log(σ(T)) and 1/T lays as an approximation since the mobility, and thus the conductivity prefactor σ_0, is weakly temperature dependent.

If the same samples as used for the dark conductivity measurements are illuminated with appropriate light, the photoconductivity (σ_{ph}) can be determined, which gives an indication of the material's photo-response and its suitability to be used as a photoactive layer. Photoconduction takes into account generation, transport and recombination of excess photogenerated majority carriers, and can be expressed as in equation (3.5), assuming that generation and recombination are balanced in thermal equilibrium [137]:

$$\sigma_{ph} = q\mu\Delta n = q\mu\tau G \tag{3.5}$$

where Δn is the density of photogenerated majority carriers (electrons), μ their mobility, τ their lifetime and G the optical generation rate of carriers.

Photoconductivity allows the determination of the mobility-lifetime product $\mu\tau$, a useful figure of merit characterising the quality of charge carriers that dominate the transport in a-Si:H (electrons in n-type a-Si:H). Using geometry factors of samples, $\mu\tau$ can be expressed as follows [147]:

$$\mu\tau = \frac{I_{ph}\omega}{qV\ell\Phi_0(1-e^{-\alpha d})} \tag{3.6}$$

where I_{ph} is the measured photocurrent, ω the distance between electrodes, V the applied voltage, ℓ the length of electrodes, Φ_0 the illumination intensity measured in photons per unit area per second, α the absorption coefficient of the material and d the film thickness.

Temperature dependent conductivity measurements were carried out placing the samples into a cryostat pumped down to 10^{-5} mbar. Samples were heated from the ambient to 450 K, and then cooled down to 110 K. To perform the photoconductivity measurement, a monochromatic light at $\lambda = 660$ nm with incident photon flux in the range of 10^{14}-10^{15} photons/($cm^{-2}s^{-1}$) was used. Figure 3.4 shows an example of the Arrhenius plot of dark and light conductivity for two differently n-doped samples. Activation energy has been determined from the slope of the linear portion of the dark conductivity plot and μτ has been deduced from the photoconductivity result at 300 K.

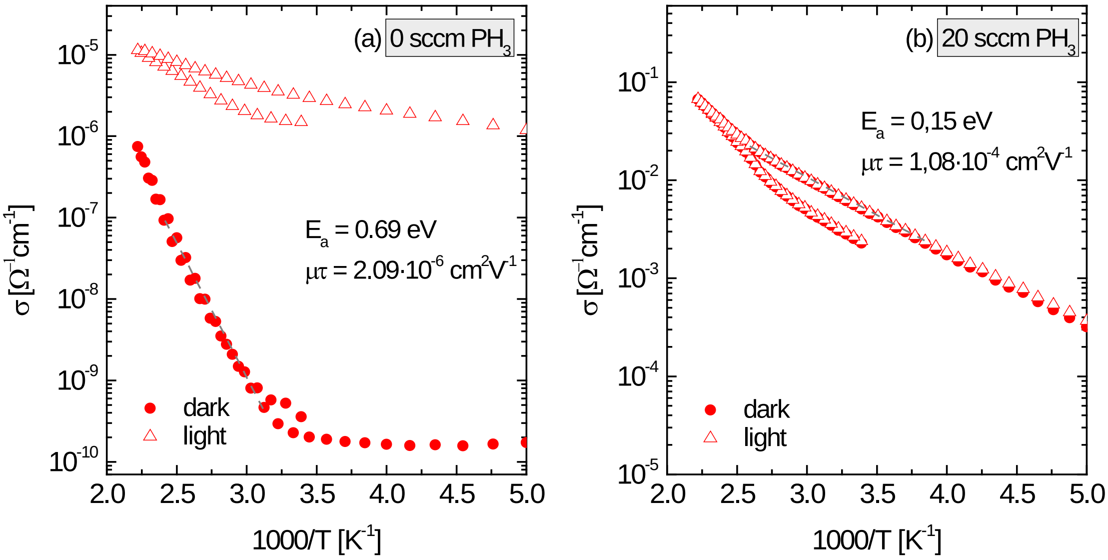

Figure 3.4. Arrhenius plot of conductivity at dark and under optical bias for (a) intrinsic and (b) doped a-Si:H layers. Activation energy and mobility-lifetime product at 300 K are also given.

Comparing results in Figure 3.4, the doping effect on the conductivity as well as photoconduction features of samples are evidenced. Undoped a-Si:H is photosensitive, whereas the doped layer exhibits the same light and dark conductivity, due to electronically active impurities introduced. Activation energy in the intrinsic layer (E_a = 0.69 eV) reflects slight n-type behaviour (typical values for undoped a-Si:H stay around 0.8 eV), which is usually originated from the dissymmetric valence and conduction band tail states. In the doped a-Si:H samples, E_a is much lower, indicating that the Fermi level is shifted towards the conduction band edge due to a higher doping level. A higher mobility-lifetime product is also observed for the doped sample.

In addition to temperature dependent conductivity measurements, High-Frequency Modulated PhotoCurrent (MPC-HF) technique was used to determine the density of states of photosensitive (i) a-Si:H layers. In this technique, a spectroscopy of the defects comprised between the majority carriers band edge and the Fermi level is performed by varying the temperature, and the frequency of the light excitation (here a monochromatic light at λ = 650 nm was used, uniformly absorbed within the thickness of the sample). From this measurement, a relative DOS reflected by N(E)c/μ, N(E) being the DOS at energy E, c the capture coefficient and μ the carrier mobility, can be directly deduced from the photocurrent modulus and its phase shift with the excitation according to [148]. For these electrical characterizations, the samples were placed into a cryostat pumped down to 10^{-5} mbar, and temperature was varied from 450 K to 110 K.

3.4. Influence of deposition parameters

a-Si:H layer properties and resulting passivation quality are sensitive to deposition conditions. Therefore, a deposition parameter survey has been performed in order to identify the process conditions leading to enhanced performing layers applied to the BSF of heterojunction solar cells. The study has been mainly focused in the achievement of high implied V_{OC}. The parameters studied are as follows: deposition pressure (p_{dep}), inter-electrode distance (d_e), PH_3 concentration and hydrogen dilution ratio (H_2/SiH_4). The impact of c-Si substrate orientation has been also analysed, since as it has been reported [35, 149], depending on the grain orientation the growth of a-Si:H can turn into epitaxial layers.

3.4.1. Process pressure

Deposition pressure has been varied from 0.8 T to 2.0 T with a fixed inter-electrode distance at 23 mm. The process temperature has been set at 200°C and the deposition time has been duly adjusted in all samples in order to obtain similar thicknesses (around 10 nm) in all cases. The pressure effects have been studied over a wide range of PH_3 flow rates. In this sample series, in order to keep the total amount of gases constant during layers' deposition, the hydrogen content in the gas mixture has been adjusted as the doping content has been increased.

Figure 3.5 shows the variation of the passivation quality of layers deposited at different process pressures. It can be seen that the maximum implied V_{OC} is not obtained at the same doping for all process conditions. When increasing the pressure, the highest value of implied V_{OC} is moved to lower concentrations of PH_3. On the contrary, at lower pressures (0.8 T) better passivating conditions are shifted towards higher PH_3 flow rates. This can be explained through a better incorporation of the doping content into the film with regard to deposition conditions. Better passivation layers are obtained with a low defect density of states but enough field effect due to the active doping.

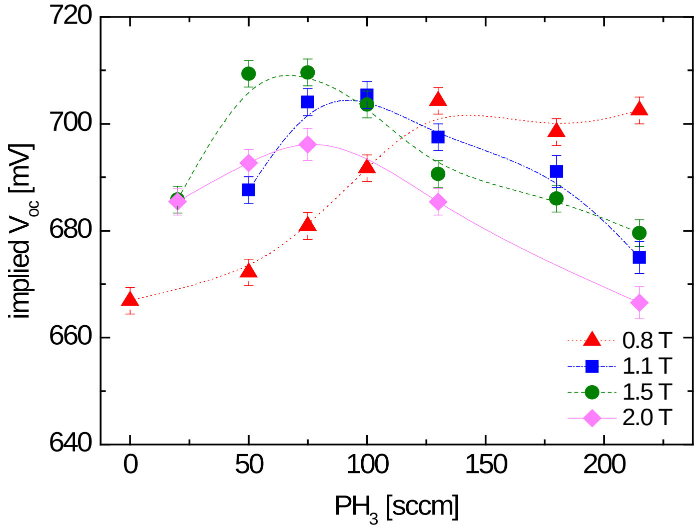

Figure 3.5. Implied V_{OC} at 1 sun as a function of PH_3 flow rate for different process pressures: 0.8 T, 1.1 T, 1.5 T and 2.0 T; inter-electrode distance has been fixed at 23 mm.

Although higher pressures lead to better performing layers in the low doping range, further increasing the pressure leads to detrimental effects on the passivation quality of the films, as it is observed at 2.0 T. Based on results obtained in Figure 3.5, a pressure of 1.5 T seems the most adequate to fabricate lightly doped (n)a-Si:H films, whereas 0.8 T of pressure is suitable for heavily doped ones.

In order to study the effects of a further decrease in process pressure, p_{dep} has been fixed at 0.5 T. A comparison between both deposition conditions is presented in Figure 3.6, where it can be seen that implied V_{OC} of layers deposited at 0.5 T is degraded over the whole range of explored PH_3 flow rates.

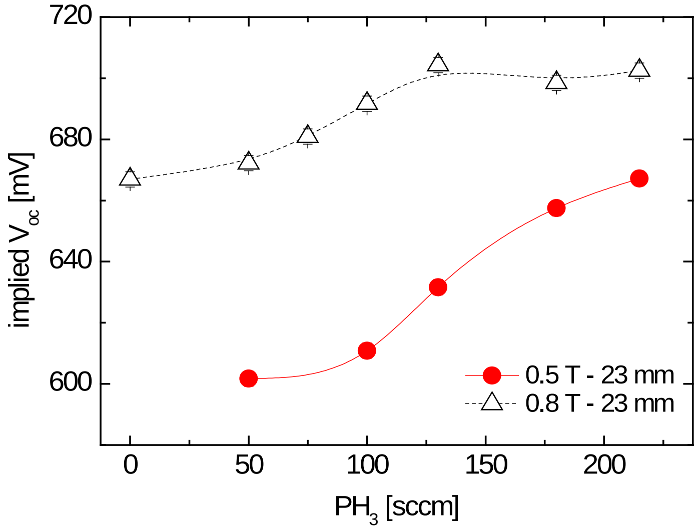

Figure 3.6. Implied V_{OC} at 1 sun as a function of PH_3 flow rate for (n)a-Si:H layers deposited at 0.5 T of pressure. The tendency at 0.8 T is given for comparison. In both cases, inter-electrode distance has been fixed at 23 mm.

Figure 3.7 shows the imaginary part of the pseudo-dielectric function of layers deposited at 0.5 T. SE measurements show that films grown at such a low pressure regime result in epitaxial structures no matter the doping concentration. The a-Si:H spectrum shows a peak centred around 3.6 eV, whereas c-Si spectrum has two peaks placed at 3.4 eV and 4.2 eV (other peaks at lower energies correspond to thickness-related interferences). Epitaxed layers have an intermediate spectrum with a soft peak tending to 4.2 eV. As clearly seen in Figure 3.7, a decrease in the crystalline fraction content in the layers is observed when increasing PH_3 flow rate, since the characteristic c-Si peak at 4.2 eV becomes less pronounced and changes towards the a-Si:H spectrum. This tendency is well correlated with V_{OC} results shown in Figure 3.6, and it has been already reported in [78]; the smaller the crystallinity, the better the passivation quality of the layers, since for the improvement of the a-Si:H/c-Si passivation an atomically sharp interface is necessary.

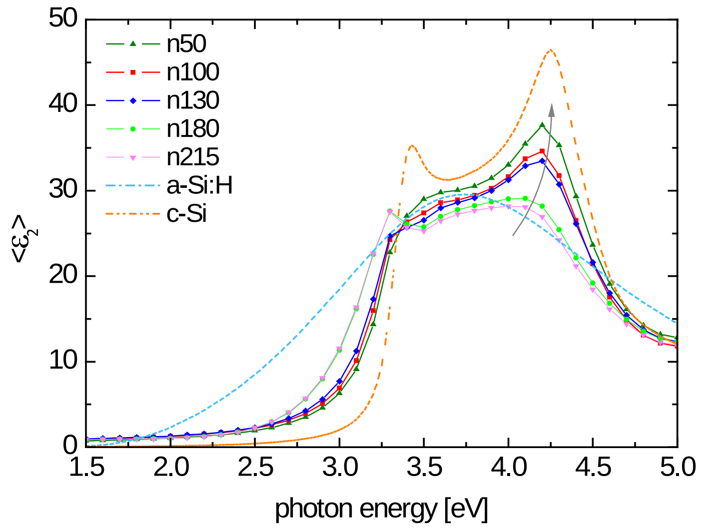

Figure 3.7. Imaginary part of the pseudo-dielectric function of various n-doped a-Si:H films deposited at 0.5 T. The amorphous and crystalline silicon spectra are given for comparison.

An extended analysis on the epitaxial behaviour of (n)a-Si:H films grown at pressures between 0.5 and 0.8 T has evidenced that the amorphous content of n layers may vary depending on the PH_3 flow rate as well as p_{dep}. As presented in Figure 3.8(a) the crystalline fraction of 50 sccm doped a-Si:H layers lowers as the process pressure increases. Similarly, the crystalline content in 215 sccm of PH_3 layers (Figure 3.8(b)) tends to decrease at higher pressures, although these layers are basically amorphous. Comparing Figure 3.8(a) and (b), it can be observed that the crystalline content on films deposited at lower PH_3 flow rate is higher than that at 215 sccm. Then, additional PH_3 content turns the microstructure of samples more amorphous. Above 0.8 T, no crystalline fraction is observed, so complete amorphous layers are deposited.

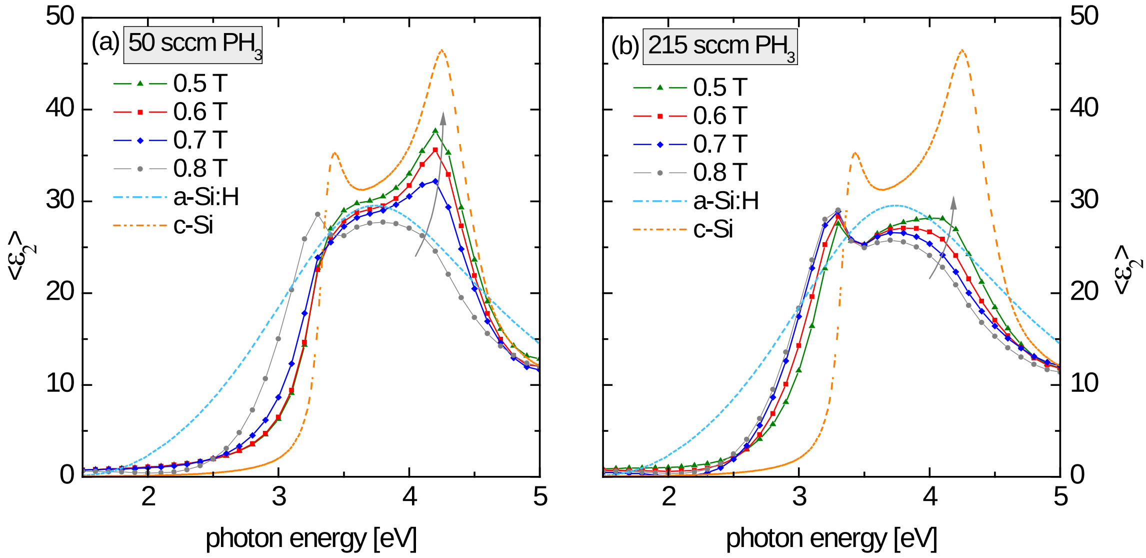

Figure 3.8. Imaginary part of the pseudo-dielectric function of (a) 50 sccm and (b) 215 sccm of PH_3 deposited layers with varying process pressure.

Thus, in view of these results a pressure of 0.8 T will be suitable when depositing (n) layers at highly doped ratios since completely amorphous films with high implied V_{OC}s will be obtained. On the contrary, a p_{dep} around 1.5 T is optimal at low PH_3 flow rates in order to obtain high quality passivating layers.

3.4.2. Inter-electrode distance

The distance between the parallel electrodes (d_e) affects the emerging network of amorphous deposited layers, and has to be therefore precisely adjusted. Thus, various inter-electrode distances have been tested at the intermediate pressure of 1.1 T. Resulting QSSPC measured implied V_{OC}s are shown in Figure 3.9.

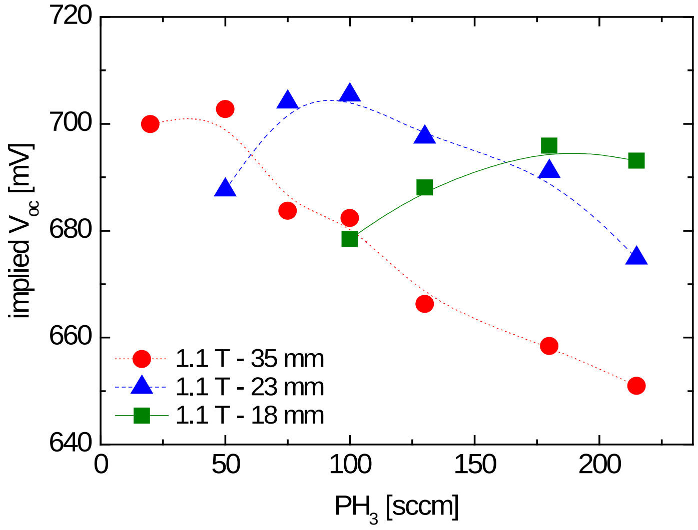

Figure 3.9. Implied V_{OC} at 1 sun as a function of PH_3 flow rate for different inter-electrode distances: 35 mm, 23 mm and 18 mm. Deposition pressure has been fixed at 1.1 T.

Similarly to what has been observed when increasing the deposition pressure, a larger d_e results in a better implied V_{OC} for lower doping rates. For the smallest inter-electrode distance (d_e = 18 mm), the higher PH_3 contents are favoured over the lower ones. However, at this deposition condition, the plasma was found to be instable, since randomly blinkings were observed during the process. Thus, although smaller spacing is usually desirable for a uniform deposition, it is sometimes insufficient to maintain the plasma.

According to the fact that larger d_e further enhance the passivation at lower doping, the effect of increasing the distance between parallel electrodes has been tested on (n)a-Si:H layers deposited at the 1.5 T in order to see if even better results can be obtained. Indeed, as shown in Figure 3.10, higher implied V_{OC} are obtained at even lower doping contents when d_e is increased from 23 mm to 35 mm.

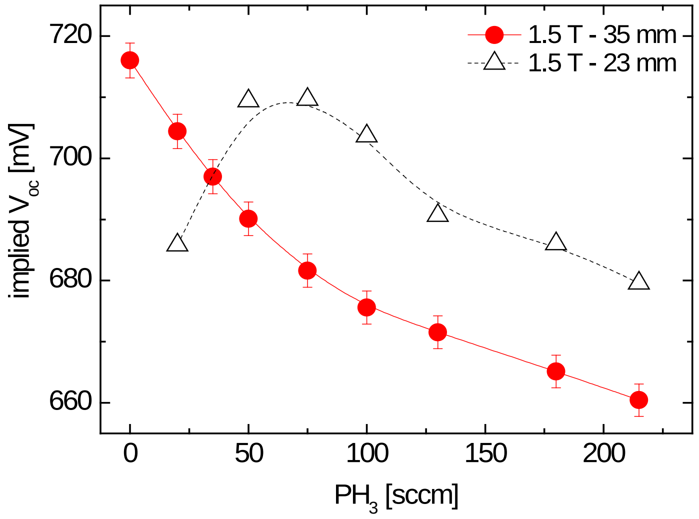

Figure 3.10. Implied V_{OC} at 1 sun as a function of PH_3 flow rate for various (n)a-Si:H layers deposited at 1.5 T and two different inter-electrode distance: 35 mm and 23 mm.

Based on these results, it can be concluded that a pressure of 1.5 T and an inter-electrode distance of 35 mm lead to enhanced V_{OC} on undoped and lightly doped (n)a-Si:H layers. Therefore these will be the deposition conditions to be used at low PH_3 flow rates.

Concerning the influence of inter-electrode distance variation in 0.8 T deposited layers, in Figure 3.9 it has been highlighted that a distance of 23 mm enables better passivation at higher doping compared to results obtained at larger d_e (35 mm). Besides, it has been found that a further decrease in d_e (18 mm) creates some plasma instabilities, which has to be avoided in order to obtain repeatable results. Based on this, and considering that p_{dep}=0.8 T favours enhanced V_{OC}s at higher doping (see Figure 3.5), it seems natural not to increase d_e beyond 23 mm, nor to decrease it at lower distances where it might be difficult to maintain the plasma. Therefore, 23 mm of spacing between electrodes has been set for films grown at low pressure. p_{dep} = 0.8 T and d_e = 23 mm are found to be optimised conditions leading to enhanced implied V_{OC} when higher PH_3 flow rates are used.

As it has been verified by SE measurements, inter-electrode distance does not have an effect on the crystalline fraction of the grown samples. Therefore, no epitaxial layers at any of the studied conditions (23 mm and 35 mm) have been obtained.

3.4.3. PH_3 concentration

As already mentioned, during the course of this work the PECVD cluster design was modified, since some limitations were identified due to the fact that all doped amorphous layers were grown inside the same ‘PM1’ chamber (see Figure 1.5). Indeed, the former technical specifications had a great impact on the achievable results, thus limiting the quality of films. Below, the influence of the (n) doping content on the passivation quality will be discussed regarding the deposition’s chamber used (‘PM1’ before chamber splitting; ‘PM3’ after chamber splitting).

Undoped layers deposited inside the same reactor where boron-doped layers were also grown (‘PM1’; see open column at 0 sccm of PH_3 in Figure 3.11), were of lesser quality compared to that deposited after chambers splitting (‘PM3’; see solid column). Before this cluster modification, a little quantity of PH_3 doping had to be introduced into the intrinsic a-Si:H in order to obtain high performing layers, since in spite of the chamber cleaning performed between depositions of different doping types, a small residual boron content was found to be present in that layer. Introducing a small quantity of PH_3 compensated the detrimental effects of unintended boron doping, hence the good implied V_{OC} obtained at 1 sccm of PH_3. As per results obtained in Figure 3.11, this technological problem was solved once p-doped layers where performed in a specifically dedicated reactor, different from that used for undoped and n-doped a-Si:H.

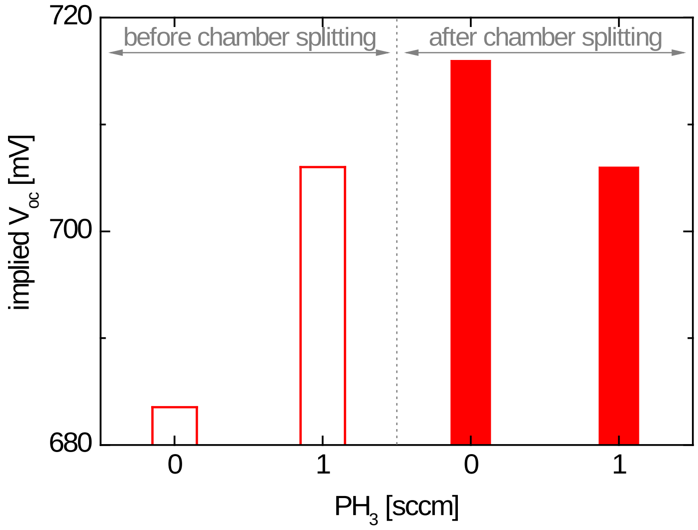

Figure 3.11. Imlpied V_{OC} comparison between layers with identical deposition parameters (p_{dep} = 1.5 T; d_e = 35 mm) grown inside the same reactor where boron-doped layers were also grown (‘PM1’, before chamber splitting) or inside ‘PM3’ chamber, specifically dedicated for (n) layers (after chamber splitting).

MPC-HF measurements performed on this improved intrinsic layer (deposited inside ‘PM3’) yield a DOS of $N(E) \sim 2.5\times10^{16}$ $cm^{-3}eV^{-1}$ for E_C-E = 0.5 eV (considering generalised values for the electron capture coefficient, $c_n = 4\times10^{-8}$ cm^3s^{-1} and mobility, $\mu_n = 10$ $cm^2V^{-1}s^{-1}$), which is typical of device grade a-Si:H. The good quality of our (i)a-

Si:H layers is also reflected in the high mobility-lifetime product of 2.1×10^{-6} cm^2V^{-1} obtained from steady-state photoconductivity measurements (with incident photon flux in the range of 10^{14}-10^{15} photons/($cm^{-2}s^{-1}$) at λ = 660 nm), which is also common for intrinsic amorphous layers ($\mu\tau$ values above 10^{-7} cm^2V^{-1} are required for device-quality material).

Once the adequacy of chamber's splitting has been verified, the influence of the PH_3 content on the properties of resulting layers has been analysed varying the n-doping level of a-Si:H from 0 up to 215 sccm of PH_3. Deposition pressure and inter-electrode distance have been fixed at 1.5 T and 35 mm, respectively. Figure 3.12(a) shows how the passivation quality of these (n) samples is deteriorated as the doping concentration increases. In order to extract relevant interface parameters, lifetime measurements have been fitted using the recombination model for a-Si:H/c-Si heterostructures developed by C. Leendertz et al. in [150]. Compared to other attempts to deduce interface parameters [34, 53], the used model allows for the definition of arbitrary interface defect distributions, and the charge states of the defects depending on the quasi-Fermi level positions are also considered. However, band bending is not computed in the model, although field effect passivation mechanism is accounted for via an effective interface fixed charge. Then, the interface density of defects and the interface charge density have been determined using capture cross sections $\sigma_p^0 = \sigma_n^0 = \sigma^{uncharged} = 1\times10^{-17}$ cm^2 and $\sigma_p^+ = \sigma_n = \sigma^{charged} = 10\sigma^{uncharged}$, with a Gaussian dangling bond distribution centred at mid-gap (width: 0.18 eV, correlation energy: 0.15 eV) [151].

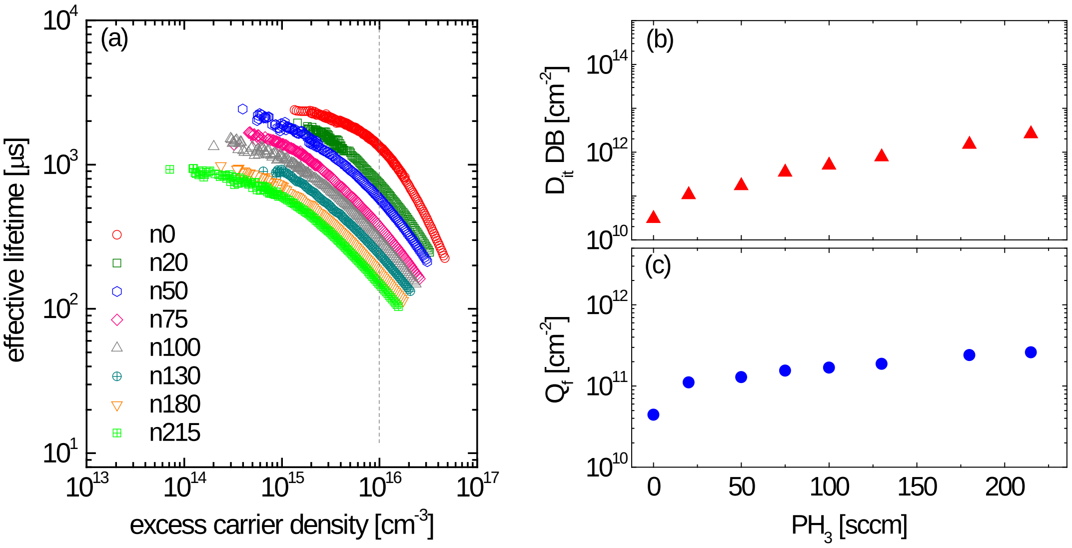

Figure 3.12. (a) Lifetime measurements for samples with varying doping content, deposited at p_{dep} = 1.5 T and d_e = 35 mm. (b), (c) Parameters extracted from lifetime data

as a function of PH_3 doping: concentration of Gaussian distributed defects (D_{it} DB) and effective fixed charge density (Q_f).

The parameters extracted from the model are presented in Figure 3.12(b). As the doping content of the layer increases, interface defect density becomes higher, indicating that defect passivation is less effective. Accordingly, the fixed charge increases in the highly doped layers, which is somehow related to the band bending and therefore, to the field-effect passivation. The undoped sample exhibits the smallest D_{it} and Q_f, while the 215 sccm-doped layer exhibits the highest values, which are almost equal to those of the sample deposited at 180 sccm of PH_3. The rather similar results obtained in these two differently doped samples (215 sccm and 180 sccm) suggest that not all the phosphorous amount is actively incorporated into the layer, but a certain quantity of the total content does not play an active role in the carriers' conduction, thus creating defects at high doping concentrations. Passivation quality of samples results from a compromise between interface defect density and effective fixed charge.

In Figure 3.13 the activation energy of the dark conductivity is compared with the total phosphorous concentration of the layers measured by SIMS, which steadily increases when the PH_3 flow rate is also increased. As it can be noticed from the E_a results, the undoped layer exhibits slight n-type behaviour. Indeed, the activation energy E_a of our (i) layer is found at 0.69 eV, which is slightly lower than typical values of undoped a-Si:H that are commonly in the range 0.7-1 eV. At this point, it is worth reminding that the same chamber ('PM3') is used for the deposition of both (i) and (n)a-Si:H layers, so that residual n-type doping might be found.

Up to 50 sccm of PH_3 flow rate, the activation energy becomes smaller due to the doping of a-Si:H. Above 50 sccm, the activation energy increases. This fact is attributed to the creation of defects at high doping concentration, in agreement with results presented in Figure 3.12(b). Thus, the (n) layers doped up to 50 sccm of PH_3 will be better for passivation purposes than those deposited at higher PH_3 flow rates. When increasing active doping concentration of (n)a-Si:H, band bending at the a-Si:H/c-Si heterointerface increases, which is favourable for better charge carrier collection. However, as reported in [101], the number of gap states in the a-Si:H layers and interface states slightly increase with heavily doped layers.

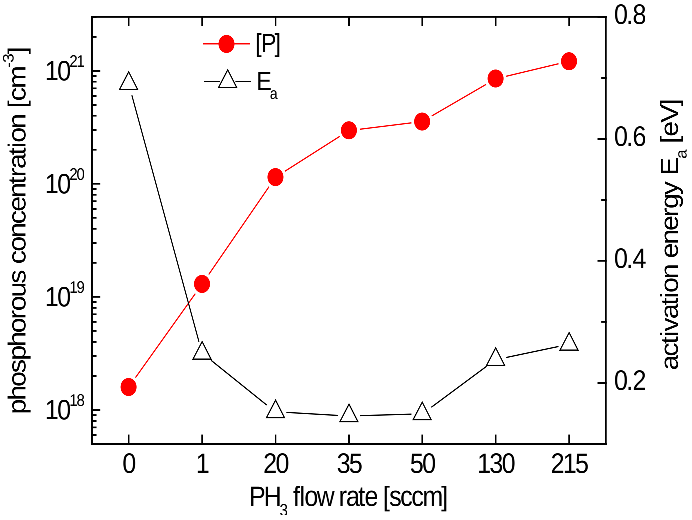

Figure 3.13. Total phosphorous concentration on (n) doped layers calculated from SIMS depth profile of 10 nm-thick samples compared with its corresponding activation energy calculated from temperature dependent conductivity measurements.

To further discuss on the influence of varying PH_3 on a-Si:H layers, the silicon-hydrogen bond content of samples deposited at the optimised condition of p_{dep} = 1.5 T and d_e = 35 mm (1.5 T-35 mm) has been analysed. In addition, analysis of films at p_{dep} = 0.8 T and d_e = 23 mm (0.8 T-23 mm) has also been performed. In Figure 3.14 the structure and hydrogen bonding of a-Si:H films is related to their passivation properties in terms of implied V_{OC}. From FTIR measurements performed on bulk a-Si:H films deposited onto c-Si, it can be concluded that low dihydride ($Si\text{-}H_2$) percentage within the layer is associated with high-quality material. According to [35] monohydride bonding is preferred since a low void fraction is present in the material. As shown in Figure 3.14, the larger the monohydride (Si-H) fraction, the better the implied V_{OC} of layers. As the doping level of (n) layers is increased, the hydrogen content in the gas mixture is adjusted in order to keep the total amount of gases constant during layers' deposition. Passivation quality of different samples decreases, indicating that the increasing ratio between the hydrogen diluted within the phosphine and the pure hydrogen introduced in the reactor creates more porous layers. Lower values of V_{OC} are obtained, correlated with higher $Si\text{-}H_2$ values. Regarding results at 0.8 T and 23 mm, only highly doped layers have been analysed, since these process conditions will only be used with high PH_3 flow rates, as already discussed in previous sections.

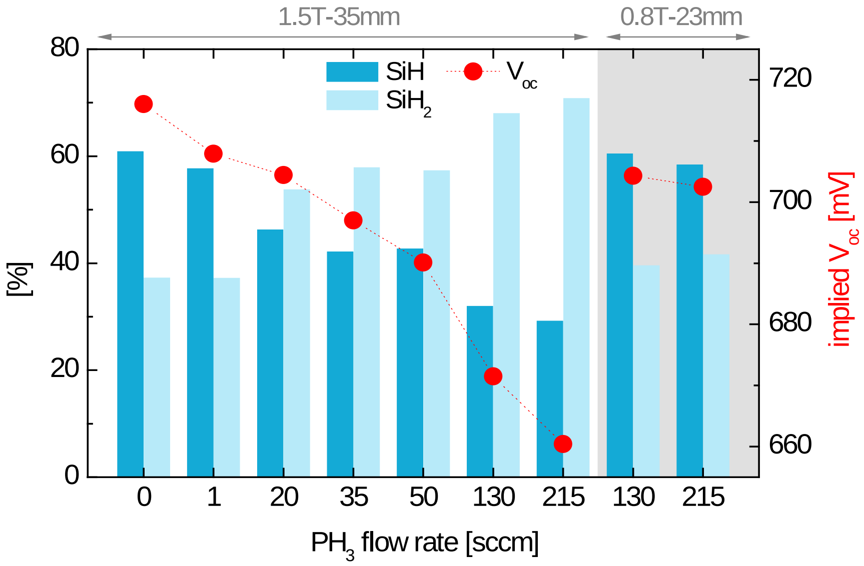

Figure 3.14. Fourier-transform infrared spectroscopy measurements performed on different (n)a-Si:H layers. Implied open-circuit voltage measured by QSSPC at 1 sun is also shown for 10 nm-thick layers.

The PH_3 doping content of a-Si:H deposited at 1.5 T clearly influences the properties of layers. Their passivation quality is found to steady degrade with the increasing doping content, and it is found to be strongly linked to hydrogen bondings created during film's growth. The corresponding activation energies determined by temperature dependent dark conductivity measurements have been well correlated with the total phosphorous concentration present in layers as well as their concentration of interface defects. Highly doped layers are more defective, and consequently Fermi level is moved away from conduction band. Based on this result, depending on the layer's requirements wanted, special attention will be paid when choosing the optimal doping.

3.4.4. Hydrogen dilution ratio

As it has been discussed in the preceding section, the passivation quality of films is found to be dependent on the hydrogen alloying. Based on this, the hydrogen dilution during PECVD a-Si:H deposition (characterised by the hydrogen to silane ratio, $R = H_2/SiH_4$) has been varied in order to investigate whether even better implied V_{OC}s can be obtained at a fixed PH_3 doping level. Since deposition rate is found to decline as the hydrogen dilution is increased, the process time has been duly adjusted in order to obtain 10 nm of thickness in all studied samples. Figure 3.15 presents the V_{OC} changes as a function of H_2 ratio for various representative process conditions.

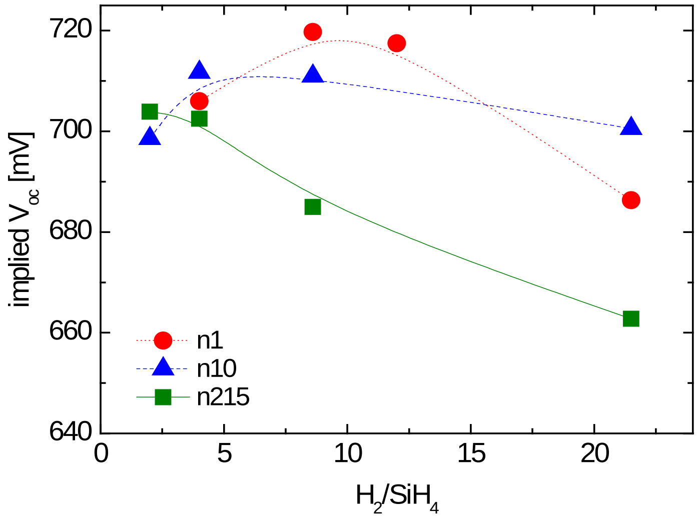

Figure 3.15. Implied V_{OC} at 1 sun as a function of hydrogen dilution ratio for three different (n)a-Si:H samples doped with 1 sccm (n1), 10 sccm (n10), and 215 sccm (n215) of PH_3.

For each of the layers tested, an optimised H_2/SiH_4 ratio interval leading to enhanced V_{OC} is found. Thus, the a-Si:H layer doped with 1 sccm of PH_3 allows for 720 mV of implied V_{OC} when a ratio of 8.6 is used. In the case of 10 sccm-doped samples similar results have been obtained in the ratio range between 4 and 8.6. When a higher doping level is used (215 sccm-doped sample), low ratios clearly favour enhanced V_{OC}s. As can be observed in Figure 3.15, at any doping content the higher ratios degrade the passivation quality of films.

The recombination model for a-Si:H/c-Si heterostructures [150] already introduced in section 3.4.3 has been used to extract the interface density of defects and the fixed charge density of layers deposited with different hydrogen ratios. Table 3.1 shows the results for n0 and n1 samples at R8.6 and 21.5. At the higher ratio, Q_f slightly increases in both samples, which should lead to an enhancement of the implied V_{OC}. On the contrary, V_{OC} remarkably decreases according to the increase of D_{it} at the H_2/SiH_4 ratio of 21.5.

Table 3.1. Concentration of Gaussian distributed defects (D_{it} DB) and effective fixed charge (Q_f) at the interface for n1 and n10 samples at different ratios.

sample	H_2/SiH_4	D_{it} DB [cm^{-2}]	Q_f [cm^{-2}]
n1	8.6	5.0×10^{10}	1.5×10^{11}
	21.5	8.8×10^{11}	2.7×10^{11}
n10	8.6	5.7×10^{10}	1.0×10^{11}
	21.5	3.8×10^{11}	2.5×10^{11}

Dark conductivity at 300 K and activation energy determined for the samples doped at 1 and 10 sccm of PH_3 are presented in Figure 3.16 (no measurements have been performed on n215 samples deposited at higher ratios as they are found to be not enough performing). Opposite tendencies between differently n doped layers are obtained when augmenting the hydrogen ratio. In the case of the 10 sccm-doped sample, σ_d lowers and E_a moves away from the conduction band, which is in good agreement with passivation results shown in Figure 3.15. Being the PH_3 flow rate unchanged, the varying dilution ratio may induce some differences on doping incorporation. Hence, at higher ratios more defects are created on the material. Contrary to this, σ_d of the 1 sccm (n) layer increases and accordingly E_a becomes smaller. Surprisingly, the more conductive layer (obtained at R = 21.5) does not coincide with the best passivating one (R = 8.6).

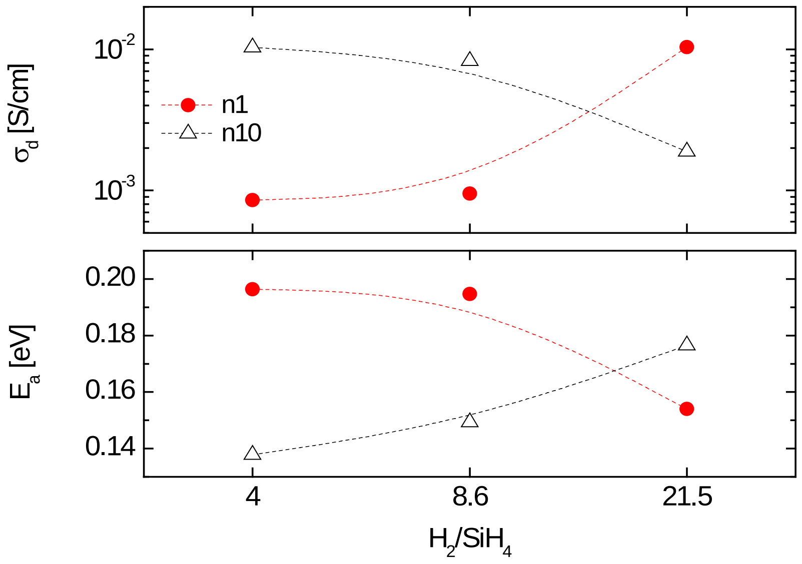

Figure 3.16. Dark conductivity at 300 K and activation energy as a function of hydrogen dilution ratio for a-Si:H layers deposited at 1 sccm and 10 sccm of PH_3.

The quantity of hydrogen during the growth of samples has been varied. Accordingly, monohydride and dihydride bonds might have been modified, being a critical parameter for passivation quality as it has been previously reported in Figure 3.14. From FTIR measurements shown in Figure 3.17(a), it can be seen that the content of monohydride bonds for the n1 samples increases with the H_2/SiH_4 ratio, matching up with a higher implied V_{OC} between R4 and R8.6. However, the ratio at 21.5 presents a disrupting behaviour: the higher content of Si-H bonds is detected, though it has the smallest V_{OC}. Regarding results for layers doped at 10 sccm (Figure 3.17(b)), decreased monohydride content at R21.5 certainly coincides with a lower V_{OC}.

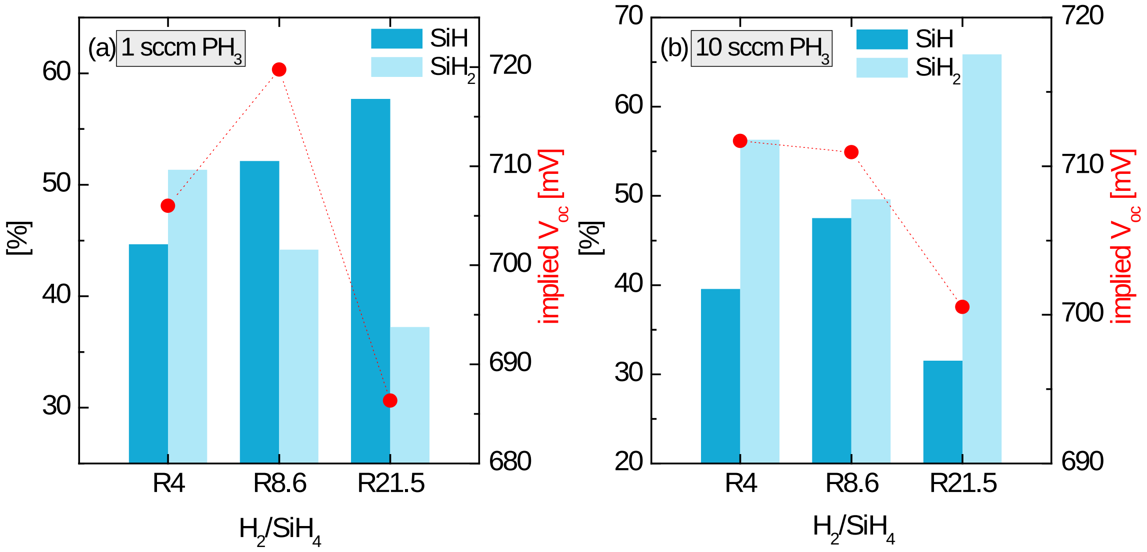

Figure 3.17. Mono- and dihydride bonds determined from FTIR spectroscopy measurements performed on (n)a-Si:H films doped with (a) 1 sccm and (b) 10 sccm of PH_3 deposited at various hydrogen dilution ratios. Corresponding implied V_{OC}s for 10 nm thick layers is also shown.

Comparing Figure 3.17 and Figure 3.16, it can be seen that the increase in monohydride bonds in the n1 sample is correlated with the observed decrease in the E_a. Similarly, the sample doped at 10 sccm has a smaller content of Si-H bonds when the E_a raises between the ratios 8.6 and 21.5. However, the trend for the n1 layer deposited at R21.5 still remains unexplainable.

As presented in Figure 3.18, further analysis of SE measurements show that the peak transition energy in the 1 sccm sample tends to slightly increase and get closer to that of the c-Si when increasing the hydrogen dilution ratio from 4 to 21.5. Although no evident epitaxial structure is present at R = 21.5, this tendency to crystallinity could explain the disagreement between FTIR measurements, passivation and dark conductivity results, since an increase in the crystalline fraction can enhance the charge carriers conduction, but can also lead to detrimental surface passivation. Concerning the sample doped with 10 sccm of PH_3, no changes on the amorphous content of the layer have been observed between different H_2/SiH_4 ratios.

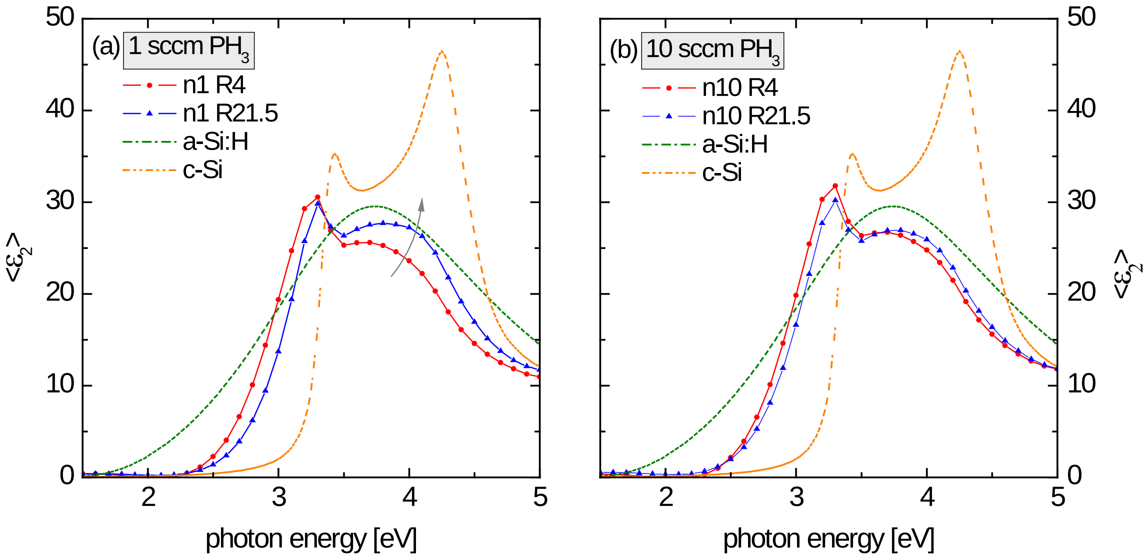

Figure 3.18. Imaginary part of the pseudo-dielectric function of n1 and n10 a-Si:H layers, deposited at two different H_2/SiH_4 ratios: R = 4 and R = 21.5.

The pronounced loss in V_{OC} for layers doped at 215 sccm deposited at low pressure and high hydrogen dilution is also related to changes on the material structure, since an increase on the crystalline fraction is observed at R21.5. In spite of the fact that in section 3.4.1 no epitaxial structures were obtained at pressures of 0.8 T and 1.5 T, it has been found that the H_2/SiH_4 ratio can play an important role on their microstructure. Hydrogen dilution during PECVD a-Si:H deposition is found to be an effective way to vary the material properties of the resulting film, enabling enhanced passivation performance.

3.4.5. Influence of c-Si wafer orientation

So far, the influence of different deposition parameters on a-Si:H quality has been examined without paying much attention to the substrate. Here the surface passivation quality of (n)a-Si:H layers has been examined on FZ n-type c-Si ⟨100⟩ and ⟨111⟩ oriented wafers (1-5 Ωcm), since the nature of the sample can certainly influence the growth process. Indeed, depending on the grain orientation of c-Si, the growth of a-Si:H can turn into epitaxial layers [35], thus deteriorating the surface passivation quality of the deposited layer.

Figure 3.19 presents the changes of V_{OC} for various a-Si:H layers deposited on ⟨100⟩ and ⟨111⟩ wafers. Only significant doping contents have been tested. As it can be clearly seen, the measured V_{OC} exhibits a pronounced Si surface orientation dependence. The values of V_{OC} decrease on ⟨111⟩ wafers for layers deposited at high pressure, whereas V_{OC} increases on ⟨111⟩ wafers for the highly doped a-Si:H deposited at low pressure.

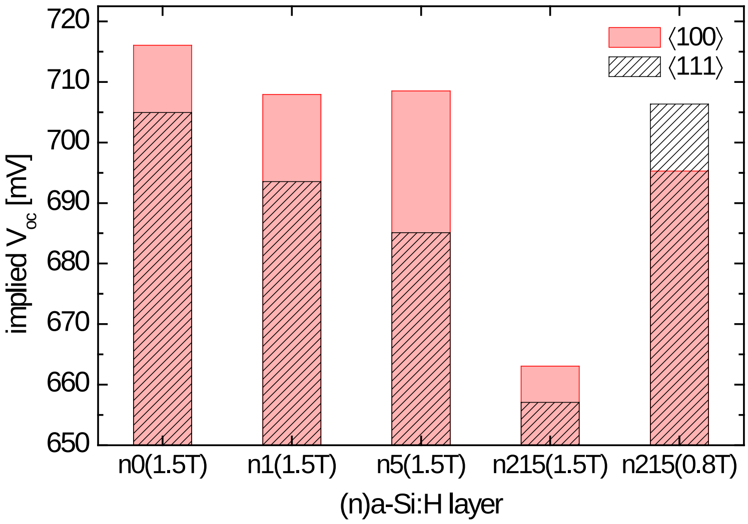

Figure 3.19. Implied V_{OC} at 1 sun for various (n)a-Si:H samples deposited on ⟨100⟩ and ⟨111⟩ oriented n-type wafers.

SE measurements indicate that the decreased passivation quality regarding different c-Si orientation can not be attributed to epitaxial growth of films. In Figure 3.20(a), no changes on the crystalline content of layers deposited on both ⟨100⟩ and ⟨111⟩ wafers can be inferred from the plot of the imaginary part of the pseudo-dielectric function. As an attempt to explain this behaviour, FTIR spectroscopic measurements have been done on samples in order to investigate the influence of crystalline orientation on predominant bonds in a-Si:H network. Results presented in Figure 3.20(b) do not show significant differences between Si-H and Si-H_2 regarding the c-Si orientation. Layers deposited on ⟨111⟩ c-Si, have a bit less monohydride bonds in benefit of little more dihydride bonds. However, these slight differences can not explain the variation on passivation results between ⟨100⟩ and ⟨111⟩ oriented wafers.

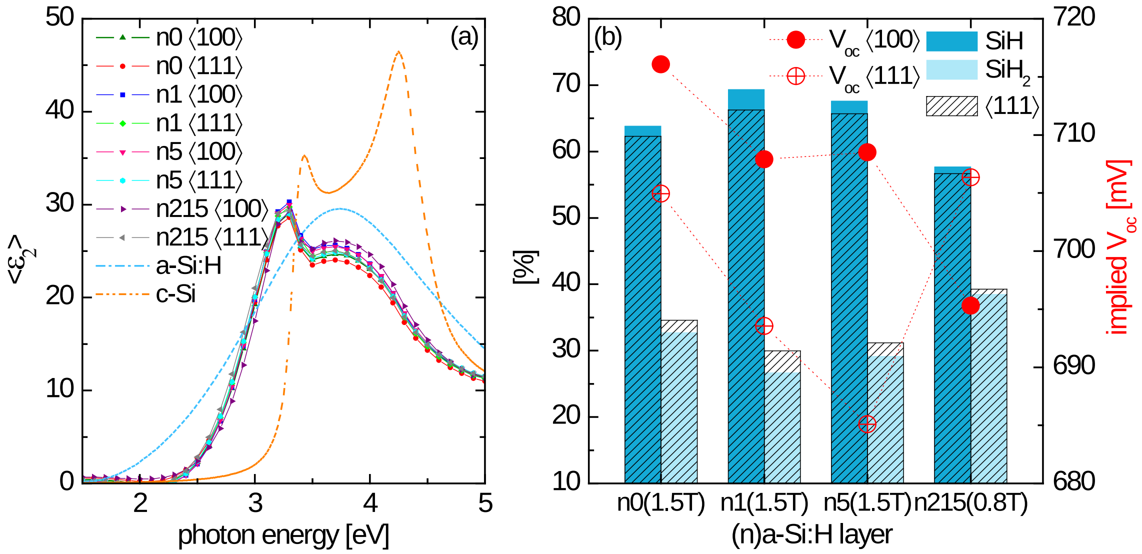

Figure 3.20. (a) Imaginary part of the pseudo-dielectric function of (n)a-Si:H layers deposited on ⟨100⟩ and ⟨111⟩ oriented wafers. (b) Mono-and dihydride bonds determined from FTIR spectroscopy measurements for (n) layers deposited on ⟨100⟩ and ⟨111⟩ oriented wafers. Corresponding implied V_{OC} of layers is also shown.

From SE and FTIR measurements it has been proved that no remarkable differences in the bulk of a-Si:H layers can explain the differences observed on implied V_{OC}s induced by the orientation of c-Si. Then, it is supposed that depending on the crystalline silicon network orientation, a different distribution of defects at the a-Si/c-Si heterointerface is created which may vary depending on the deposition parameters fixed during the films' growth.

Lifetime measurements of representative samples have been fitted using the recombination model for a-Si:H/c-Si heterostructures [150] introduced in section 3.4.3. Interface density of defects and the fixed charge density of layers deposited both on ⟨100⟩ and ⟨111⟩ substrates are shown in Figure 3.21. As it can be observed, Q_f increases on layers deposited on ⟨111⟩ oriented wafers no matter the deposition conditions used. On the contrary, D_{it} increases in layers deposited at high pressure (n0 and n1), whereas it decreases in low-pressure deposited one (n215). These results indicate that D_{it} is the main limiting factor in V_{OC}, as both parameters follow the same tendency. This way, the assumption of a varying distribution of defects on differently oriented wafers depending on process conditions of a-Si:H layers is reinforced.

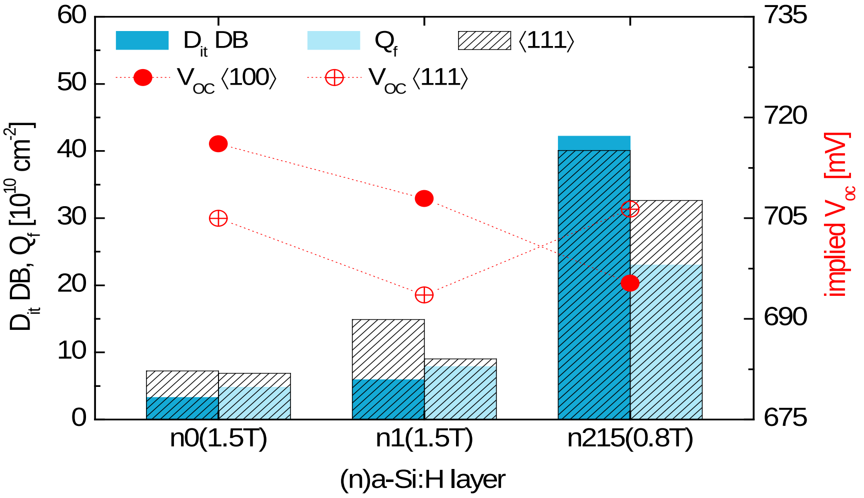

Figure 3.21. Concentration of Gaussian distributed defects (D_{it} DB) and effective fixed charge density (Q_f) at the interface, extracted from lifetime data of various layers deposited on ⟨100⟩ and ⟨111⟩ oriented c-Si wafers. Implied V_{OC} is shown for comparison.

3.5. Integration of (n)a-Si:H single layers at the BSF of HJ devices

For a-Si:H layers applied to BSF of HJ devices, passivation and electrical conduction becomes critical. The use of a-Si:H on thin-film solar cells requires low dark conductivity values as an indication of the absence of electronically active impurities. Moreover, photoconductivity is expected to reach high values indicating reasonably low recombination of the photogenerated carriers [137, 147]. Contrary to this, a-Si:H applied to the rear side of HJ devices should have an enhanced σ_d no matter the σ_{ph}, since there is no light-activated conduction at the back side of the solar cell. Besides, low defect state density is also required to enhance passivation properties. Then, since dark conductivity of good quality (low defective) intrinsic layers is very low, the only way to reduce series resistance is by doping them, which thus also introduces defects.

Therefore, to accomplish the passivation requirements needed at the back surface field, an optimal gas phase doping concentration has to be found, in which the Fermi energy in the rear (n)a-Si:H layers is close enough to the conduction band and the defect state density remains sufficiently low. If the a-Si:H/c-Si interface is not properly passivated, the open-circuit voltage of the HJ solar cell will be limited to values far below from those defined by the front band bending [152].

In order to understand the role of the (n) layer BSF as well as to evaluate its impact on complete devices, silicon heterojunction solar cells with a single amorphous layer BSF were fabricated according to the process described in section 1.5. The (n) doping level of the rear a-Si:H was varied from 0 up to 215 sccm of PH_3, and p_{dep} and d_e were kept at

1.5 T and 35 mm, respectively. An extensive characterisation of these layers has been presented in section 3.4.3, and will be of capital importance to understand results herein presented. The front side of each device was kept identical, and consisted of an optimised (i)/(p)a-Si:H stack followed by ITO deposition and a silver screen printed grid. The solar cells characteristics as a function of the doping content of the 12 nm-thick rear a-Si:H layer are presented in Figure 3.22.

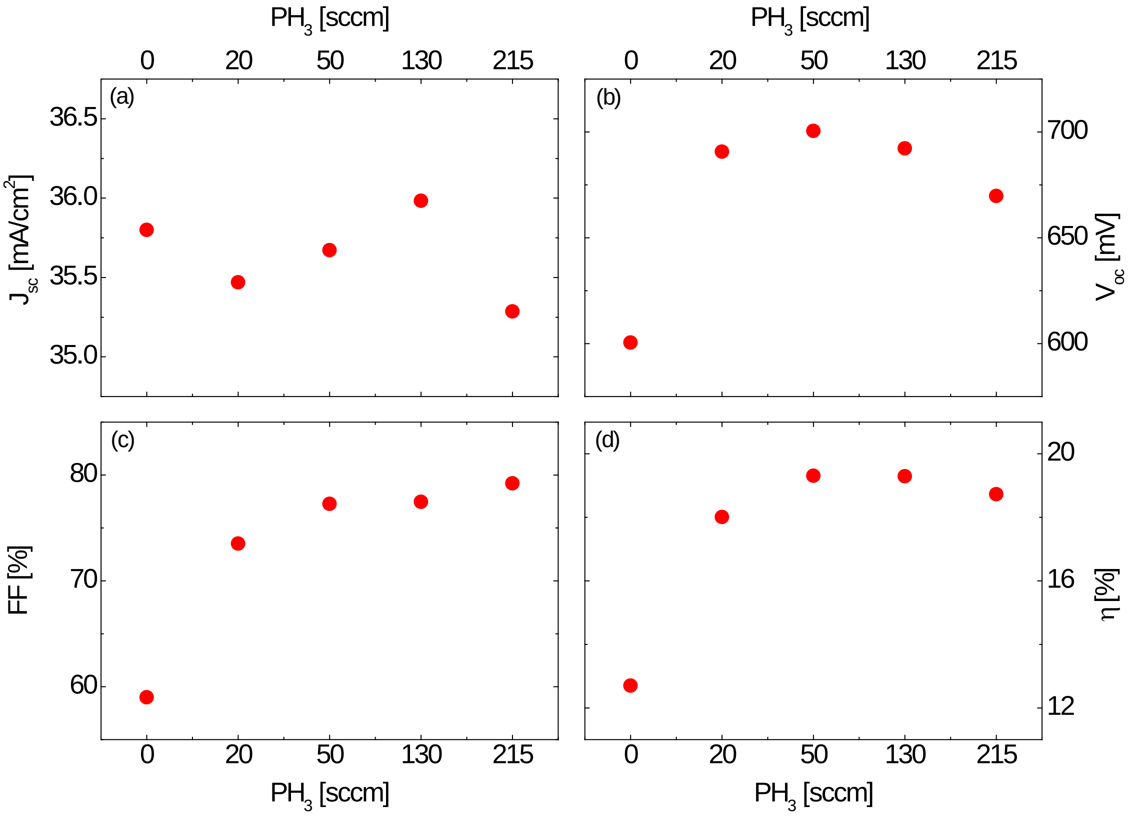

Figure 3.22. Output characteristics of HJ solar cells as a function of BSF (n)a-Si:H doping. Each data point represents the average value of three cells.

As it can be observed, differences in J_{SC} have been obtained. Experimentally it has been found that reflectivity of textured wafers, absorption of front side deposited layers, as well as the front metal grid shadowing in our solar cells remarkably influences the attainable short-circuit current density (see Figure 3.23). In this thesis, for a given series of samples, c-Si substrates issued from the same texture batch have been used to fabricate the devices. Therefore, it can be assumed that similar reflectivities between wafers are obtained. Moreover, identical layers have been used at the solar cell's emitter. Then, neither the layers' thickness nor their absorption is found to substantially fluctuate. Based on this little variability on J_{SC} results will be induced by the above mentioned parameters. However, electrode screen-printing process certainly induces changes on the front side shadow, and consequently the J_{SC} of samples may vary. As presented in Figure 3.23(b), an increase of 1% in shadowing results in a decrease of ~ 0.53 mA/cm^2 in J_{SC}. The shadowing measured in the studied solar cells ranges from 6 to 7%, which may certainly be the reason of the obtained ΔJ_{SC}.

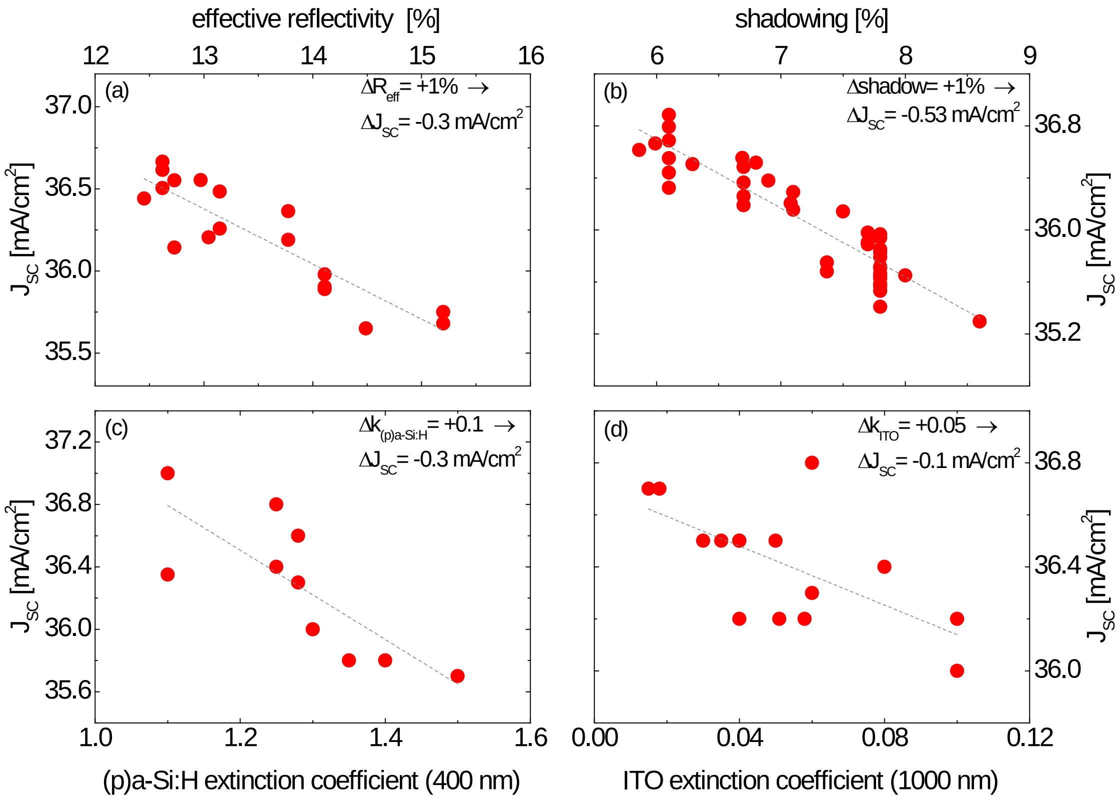

Figure 3.23. Influence on the J_{SC} of HJ solar cells induced by (a) the effective reflectivity of textured c-Si substrates, (b) the front metal grid shadowing of devices, and (c) and (d) the extinction coefficient of front side (p)a-Si:H and ITO layers, respectively.

Supported by results presented in Figure 3.13 it can be seen that the V_{OC} trend is well correlated with E_a results presented in section 3.4.3. In the sample with the intrinsic single BSF (n0), the lower V_{OC} is obtained coinciding with the higher E_a, whereas the n50 sample exhibits the higher V_{OC} and the lower E_a. In agreement with the increase of the activation energy above 50 sccm of PH_3 (Figure 3.13), the V_{OC} of n130 and n215 samples diminishes.

The increased D_{it} in the 215 sccm n-doped layer (Figure 3.12(b)) does not have a detrimental effect in FF results. The large quantity of fixed charges induces the right field effect and compensates recombination mechanisms at the BSF. As expected, undoped or lightly doped layers used at the rear side of the solar cells do not introduce enough doping content in order to create a sufficient band bending, hindering in this way the charge transport towards the rear side of the cell.

The software AFORS-HET has been used to simulate the band energy diagram of devices with 0 sccm-, and 215 sccm-doped BSF. Results are presented in Figure 3.24(a). Indeed, the high E_a in the n0 sample creates a band bending in the wrong sense, establishing a barrier for electrons. Accordingly, the experimental J(V) curve of n0 device shows a typical S-shape (see Figure 3.24(b)), which besides exhibiting a severe R_S due to low n0 layer conductivity, also indicates the insufficient rear band bending created in the solar cell. When activation energy is small enough (as in n215 sample), the band line-up at the n/n$^+$ junction leads to the right bending and consequently good values of V_{OC} and FF can be obtained. In the BSF with the 215 sccm-doped layer, additional tunnelling-mediated transport paths through the conduction band offset are also activated, which might be the reason of the highest FF obtained.

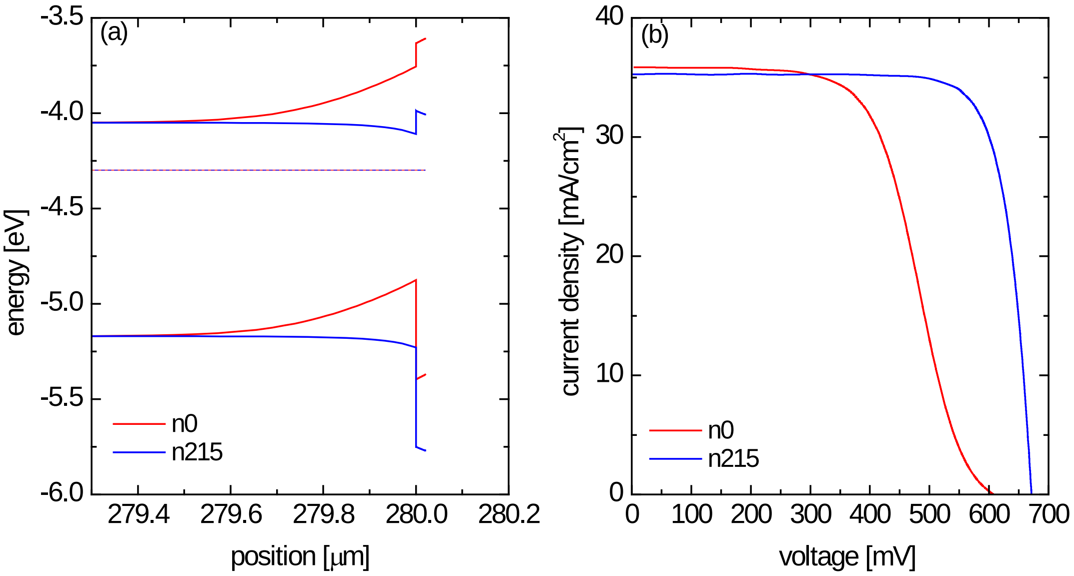

Figure 3.24. (a) Simulatated band energy diagram of the n/n$^+$ junction BSF doped with 0 sccm (n0), and 215 sccm (n215). (b) Experimental J(V) characteristics of HJ solar cells using the n0 and n215 single layer a-Si:H BSF.

Then, when using a single (n)a-Si:H layer on the rear side of HJ, a highly doped BSF with sufficiently small E_a is necessary to create the appropriate band bending to be able to collect the charges. Even with an optimised emitter, it has been found that if there is not enough electrical field and therefore band bending induced at the rear side, lower V_{OC}s and FFs will be obtained on final devices. As it has been demonstrated, when using a single layer BSF, the field effect induced by higher doping content prevails over optimised defect density at the n/n$^+$ heterointerface.

3.6. Integration of (n)a-Si:H double-layer stacks at the BSF of HJ devices

In order to achieve high efficiency HJ silicon solar cells, a very low defect state density at the heterointerface together with a strong electrical field to collect carriers and provoke enough band bending is required on both sides of the device [67]. As shown before, combining these two different passivation mechanisms in a single layer is extremely difficult because of the very low conduction properties of low defective intrinsic a-Si:H layers. Besides, when enhancing conductivity by increasing the doping on a-Si:H layers, defect density is also increased (being still more critical on boron-doped layers) [101, 102]. Therefore, it seems necessary to introduce a double-layer stack or a gradient layer to combine both mechanisms [56, 89] and assure high V_{OC} combined with high FF.

Besides, it has to be taken into account that depositing a double layer at the back side of the HJ solar cell allows a more flexible deposition process where different parameters can be used in order to find the better conditions leading to a low thin-film deposition's damage. In this respect, as reported in section 3.4.1, best passivation results at low PH_3 flow rates have been obtained at higher pressures, whereas low pressure is found to be more performing at increased doping rates. Therefore, an a-Si:H stack combining a lightly-doped (low defective) high-pressure-deposited layer followed by a highly-doped low-pressure-deposited one will be used. From here on, when referring to this double-layered back side configuration, it has to be taken into account that process pressure used for the first and second layer deposition are 1.5 T and 0.8 T, respectively.

In Figure 3.25, the experimental lifetime data measured by QSSPC of two different optimised double-layer a-Si:H stacks are depicted. Corresponding lifetime curves of single layers used to create the stack are also presented. As it can be seen, effective surface recombination velocity of n215 layer is boosted when a thin lightly doped layer is previously deposited on c-Si.

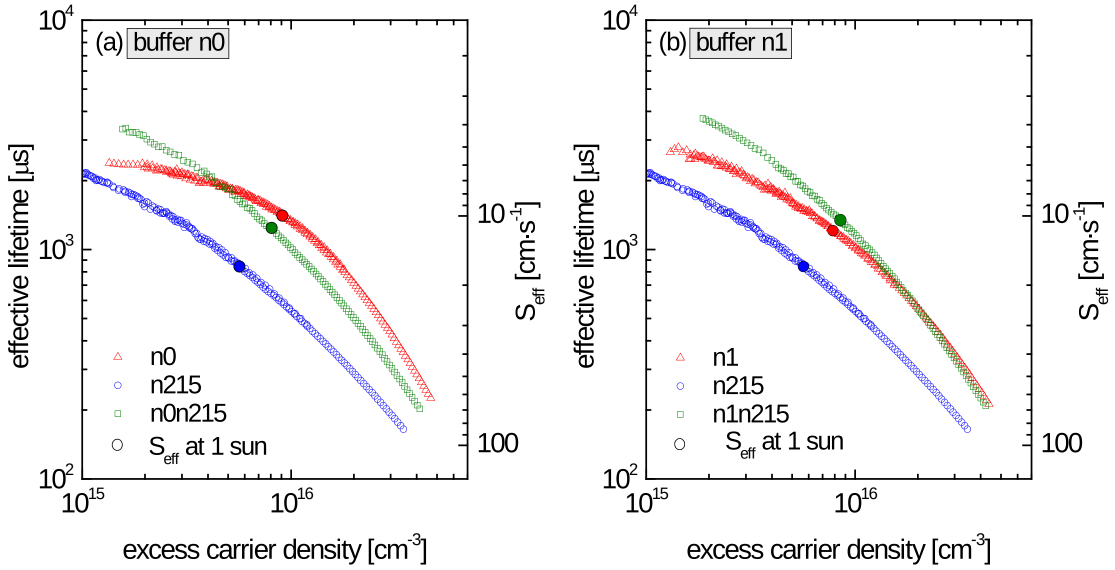

Figure 3.25. Effective lifetime measurements from QSSPC on two different stacks using (a) intrinsic, and (b) 1 sccm PH_3 doped a-Si:H buffer layer (n0 and n1, respectively). The upper limit of the effective surface recombination velocity (S_{eff}) of (n) layers has been calculated; circles show the effective recombination velocity measured at 1 sun.

By fitting lifetime measurements with the recombination model for a-Si:H/c-Si heterostructures [150], the interface density of defects and the fixed charge density have been determined (the same model parameters as in section 3.4.3 have been used). Indeed, as presented in Figure 3.26 both density of defects and fixed charge in n215 layer are maximum. By contrast, the D_{it} and Q_f of n0 and n1 samples are rather smaller. When these layers are used to create the stack, D_{it} is remarkably reduced compared to that of n215 sample and Q_f is still high to ensure enough field effect passivation. Double-layer stacks take advantage of both passivation mechanisms (low D_{it} and high field effect), and implied V_{OC}s of 712 mV (in the n0n215 stack) and 715 mV (in the n1n215 stack) can be achieved compared to the 696 mV of the n215 single layer.

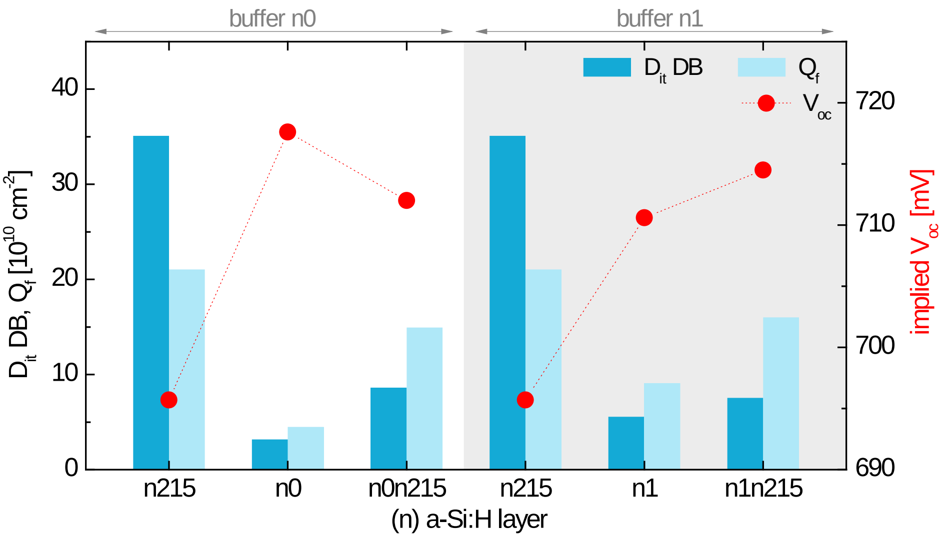

Figure 3.26. Concentration of Gaussian distributed defects (D_{it} DB) and effective fixed charge density (Q_f) at the interface, extracted from lifetime data of different single and stacked (n) layers. The left part of the figure corresponds to the double-layer stack made with an intrinsic buffer layer (n0), whereas at the right part results using a lightly-doped buffer layer (n1) are presented. Implied V_{OC} is also shown.

The addition of a thin undoped or lightly doped layer between the c-Si and the heavily n-doped layer not only enhances defect state density of the film with the higher doping level, but also maintains the electrical field passivation. Nevertheless, it is obvious that the effectiveness of stack in the BSF of devices will be subject to characteristics of single layers used.

In the following paragraphs the influence of varying properties of the intermediate layer (from now on referred to as buffer layer), as well as the heavily n-doped layer (from now on referred to as (n^+) layer) used at the BSF of HJ devices have been evaluated on the solar cell. Thus, the doping of a-Si:H films, their thickness and the hydrogen dilution ratio used during their deposition process have been analysed.

Device modelling will be used when necessary in order to give more insight on the observed tendencies in studied samples. Because of the presence of two distinct layers at the amorphous BSF, if otherwise indicated the modelling approach used herein lies on a home-developed simulation code, using a 2D finite element commercial tool [125]. Besides classical drift-diffusion resolution, it allows complete solar cell simulation in operating conditions (1 sun illumination), and accounts for the amphoteric nature of amorphous silicon defects and single-state midgap interface traps at heterojunctions. More details on this approach can be found elsewhere [153].

3.6.1. Buffer layer doping influence

The PH_3 content of the buffer layer grown on the back side of c-Si surface has been varied from 0 (intrinsic layer) to 20 sccm. An (n^+) layer, consisting of 215 sccm-doped a-Si:H deposited at $p_{dep} = 0.8$ T has been used to complete the double-layer stack BSF. Table 3.2 summarises some of the relevant properties of layers under study. Besides, simulation analysis of these (n) layers has been performed in order to accurately describe a-Si:H properties that will contribute to model HJ devices. Corresponding details and results can be found in appendix A.

Table 3.2. Optical gap, dark conductivity at 300 K and activation energy of (n)a-Si:H layers.

doping [sccm]	deposition pressure [T]	E_g [eV]	σ_d [S·cm^{-1}]	E_a [eV]
0	1.5	1.738	2.26×10^{-10}	0.69
1	1.5	1.733	2.51×10^{-4}	0.24
5	1.5	1.732	1.51×10^{-3}	0.20
20	1.5	1.731	5.60×10^{-3}	0.15
215	0.8	1.648	1.52×10^{-2}	0.13

The impact of a-Si:H doping level on a-Si:H/c-Si interface quality has been investigated by means of QSSPC measurements together with proper modelling. In Figure 3.27 effective lifetime results obtained on 10nm-thick single layer precursors to be used on solar cells are depicted.

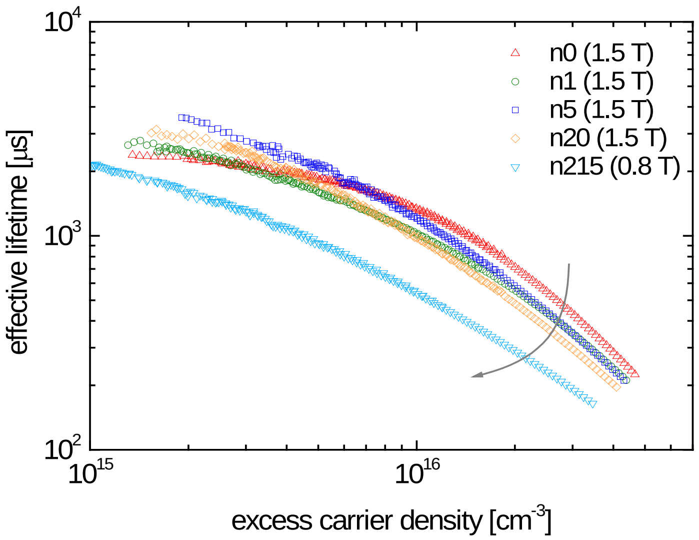

Figure 3.27. Effective lifetime as a function of excess carrier density in the bulk c-Si of double-sided (n) a-Si:H/c-Si samples with different a-Si:H doping levels. Curves are obtained using both QSS and transient results.

Good passivation properties on a-Si:H layers have been obtained, even for the highly-defective n215 layer deposited at low pressure. The changes of the curves with the doping in a-Si:H can be well understood in the light of the two main passivation mechanisms (field effect and interface defect passivation) as described in [151]. At high excess carrier density the effective lifetime decreases (as indicated by the arrow in Figure 3.27) when increasing layers doping, which is due to an increase in interface defect density. Interestingly, this is well correlated with the a-Si:H bulk defect concentration in our layers (see Table A.1 in appendix A), which is in agreement with the idea developed by T.F. Schulze et al. suggesting that the interface defects map with the bulk defect density in a-Si:H [154].

From Figure 3.27 the change in the shape of the curve between the n0 sample and other samples at lower excess carrier density can also be observed, which is characteristic of an improved field-effect passivation with doped layers. Thus, the effective surface recombination velocity S_{eff} comes out from both field effect passivation and interface quality (described by surface recombination velocities S_{n0} and S_{p0}).

In order to disentangle these two phenomena, a QSSPC model based on a self-consistent resolution of Poisson, continuity and Boltzmann equations (i.e. drift-diffusion model) has been used. This model accounts for Shockley-Read-Hall (SRH) bulk recombination in c-Si and at the interface through a single level at midgap (interface defect density D_{it}), and Auger recombination in c-Si [116]. For each double-sided a-Si:H/c-Si precursor, infinite lifetime in FZ c-Si has been assumed. For modelling's simplicity, only single and monovalent defect states have been considered at midgap, which can reasonably account for the more widely accepted Gaussian distributed dangling bond defects if the capture cross sections are chosen equal to that of the charged dangling bonds. Thus, capture cross sections $\sigma_n = \sigma_p$ have been set at 10^{-16} cm^2 [151]. Corresponding values of S_{n0} and S_{p0} are also indicated. Finally, field effect passivation has been accounted for thanks to the a-Si:H layers description obtained from conductivity measurements, and D_{it} has been extracted from the comparison between calculated and experimental QSSPC curves. Figure 3.28 shows two examples of such QSSPC lifetime curves exhibiting an excellent agreement between modelling and experimental results.

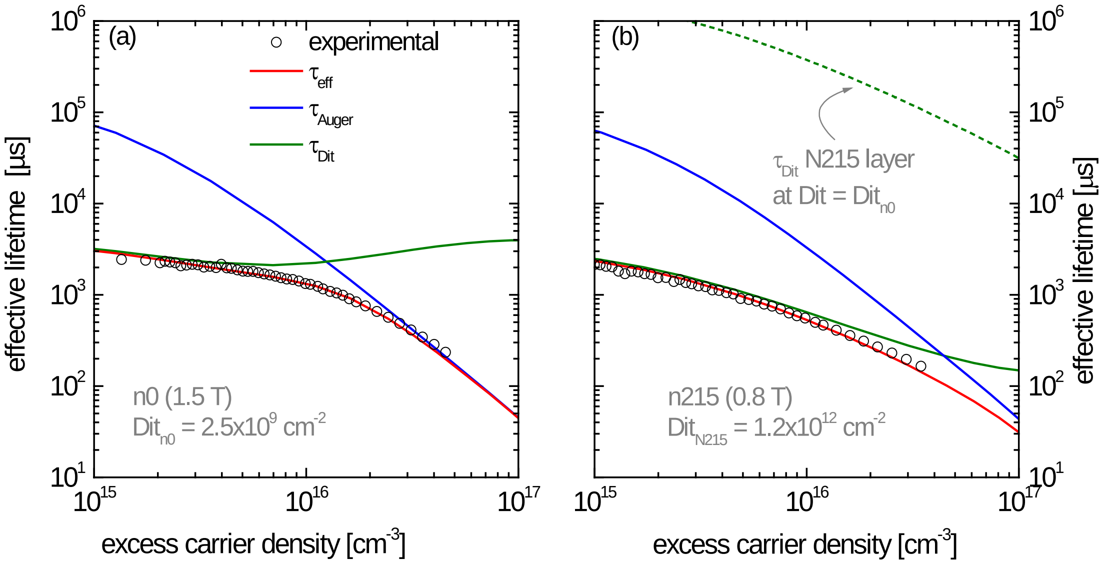

Figure 3.28. Effective lifetime of (a) undoped (n0), and (b) 215 sccm-doped (n215) a-Si:H samples. Solid lines represent QSSPC simulation results with appropriate n0 and n215 interface parameters. Dashed line illustrates passivation properties of a virtual highly-doped a-Si:H layer with low D_{it}, in which the overall τ_{eff} is Auger-limited.

It can be observed that for the undoped a-Si:H layer the effective lifetime is limited by recombination via D_{it} at low injection level, whereas Auger recombination dominates at high injection conditions. For doped layers, the recombination via interface defects is still influencing the lifetime even at high excess carrier densities. The compromise between field effect passivation and interface defect density is also clearly revealed in the n215 layer. Simulations have been performed considering passivation layers with low activation energy (i.e. high field effect, n215 case), together with a very low D_{it} (n0/c-Si interface case). Theoretical advantage of highly doped passivation layer is clearly demonstrated: in this case, minority carriers are pushed away from the interface and lifetime can be drastically increased. Unfortunately, highly-doped a-Si:H layers lead to defective interfaces, overlapping this theoretical benefit. Interface parameters extracted from modelling are summarised in Table 3.3.

Table 3.3. Interface defect densities (D_{it}) and surface recombination velocities (S_{n0}, S_{p0}) extracted from QSSPC measurements on different (n)a-Si:H samples.

doping [sccm]	deposition pressure [T]	D_{it} [cm^{-2}]	S_{n0} [cm·s^{-1}]	S_{p0} [cm·s^{-1}]
0	1.5	2.0×10^{10}	21.6	26
1	1.5	2.4×10^{11}	259.2	312
5	1.5	1.6×10^{11}	172.8	208
20	1.5	1.6×10^{12}	1728	2080
215	0.8	9.6×10^{12}	10368	12480

3.6.1.1. Solar cells results

Using the same front side (p)a-Si:H emitter structure, HJ solar cells with some of the studied (n) layers were fabricated on (n)c-Si. Five different back heterostructures were proposed as indicated in Figure 3.29. A comparison of the obtained performances is shown in Figure 3.30.

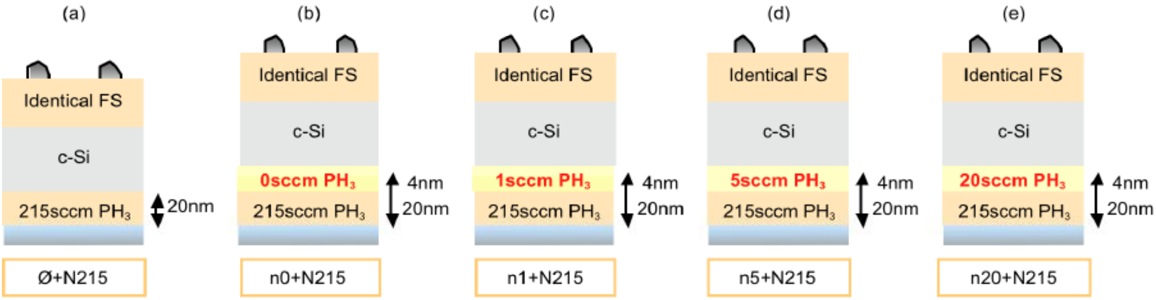

Figure 3.29. Illustration of the 5 studied configurations: (a) 20 nm of single heavily (n)a-Si:H layer; (b) 4 nm of intrinsic layer followed by a 20 nm thick (n)a-Si:H layer; (c) 4 nm-thick lightly-doped layer (1 sccm PH$_3$) plus 20 nm of (n)a-Si:H layer; (d) 4 nm of a 5 sccm doped (n) layer followed by a 20 nm thick (n)a-Si:H layer and (e) 4 nm thick 20 sccm doped layer plus 20 nm of (n)a-Si:H layer.

The short-circuit current density obtained by the different structures is notably the same, as the front side of each device has not been modified; small differences can be observed due to subsequent technological steps such as the spreading area of grid electrode, which may cause some optical losses. However, it is worth mentioning that a further increase of the a-Si:H layer doping level used at the BSF could result in a decrease of J$_{SC}$ that is slightly affected by recombination.

It can also be seen that the BSF with a single highly doped layer (Ø+N215) exhibits the lowest open circuit voltage as the defect density in the layer is considerably high. By contrast, the presence of an intermediate undoped or lightly doped a-Si:H layer leads to lower interface defect density which is reflected in the enhanced V$_{oc}$ results. A maximum value of V$_{OC}$ is obtained with the intrinsic BSF (n0+N215). Adding some doping to the intermediate layer lowers the V$_{OC}$ since D$_{it}$ increases, and so does recombination at this interface. As it can be clearly seen in Figure 3.30, the V$_{OC}$ trend governs efficiency results.

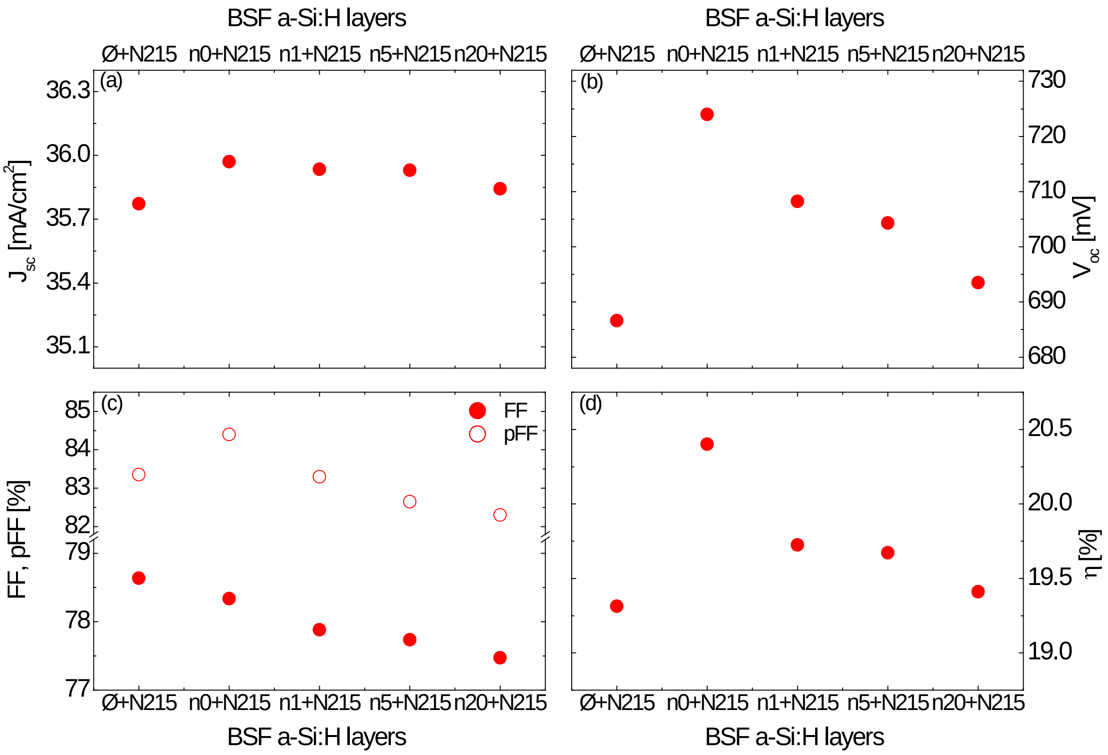

Figure 3.30. Solar cell characteristics as a function of a-Si:H layers used at the BSF. (a) Short-circuit current density; (b) open-circuit voltage; (c) fill factor and pseudo-FF; and (d) efficiency. Each data point represents the average value of three cells.

Taking into account the results obtained on electrical properties of (n) type a-Si:H layers, an increase in FF is expected when increasing (n) a-Si:H doping level and thus conductivity (decrease in series resistance, R_s). However, the opposite behaviour is observed in Figure 3.30: FF slightly decreases although the conductivity measured of the single a-Si:H films used as intermediate layers on the BSF stacks increases. Series resistance of devices calculated according to [155] is shown in Figure 3.31. Conductivity measurements performed on (n) single layers used at the BSF are also shown for comparison. From Figure 3.30(c) and Figure 3.31 it can be seen that decreasing FF is well correlated with increasing R_S.

Having the same grid electrode resistance (line resistance) and identical layers except for the intermediate a-Si:H layer at the BSF, the changes measured in devices' series resistance (as depicted in Figure 3.31) can only be attributed to the electrical behaviour of the rear buffer layer, that is: (i) the layer conductivity or (ii) the interfaces surrounding this buffer layer (the a-Si:H/c-Si heterointerface or the interface created between the lightly-doped/heavily-doped layers of the a-Si:H stack).

Analysing single layer conductivity results, the opposite tendency is observed with global series resistance. Thus, it could be said that bulk conductivity measured on (n)a-

Si:H thick layers deposited on glass may not be representative of the real conductivity of the thin (4 nm) intermediate layer used on the BSF of HJ solar cells. Thus, interfaces are playing the main role on the electrical behaviour of the BSF. Moreover, it has to be considered that the highest FF is obtained with the lowest R_S and it corresponds to the single layer BSF (Ø+N215), where only the a-Si:H/c-Si interface has to be considered. In this back side configuration, the c-Si is passivated through a heavily-doped, highly-defective a-Si:H layer.

In order to elucidate which is the critical interface in our devices, we have performed complementary Suns-V_{OC} measurements that will give some insight on the BSF behaviour of our heterojunction solar cells. Comparing the FF and the pseudo FF (pFF) taken from the Suns-V_{OC} measurements (see Figure 3.30(c)) it can be observed that the highest pFF corresponds to the back heterostructure with the intrinsic intermediate layer (n0+N215). In that case, the density of states, as previous measurements and simulation have demonstrated, is the lowest one. Regarding the Ø+N215 back side configuration, the higher FF is obtained, although it has a lower pFF comparable to that of the n1+N215. As expected, these results evidence two different phenomena driving the FF: interface defects and series resistance. It is worth mentioning that the fabricated cells have very high shunt resistances, so differences in pFF are mainly attributed to recombination aspects [146].

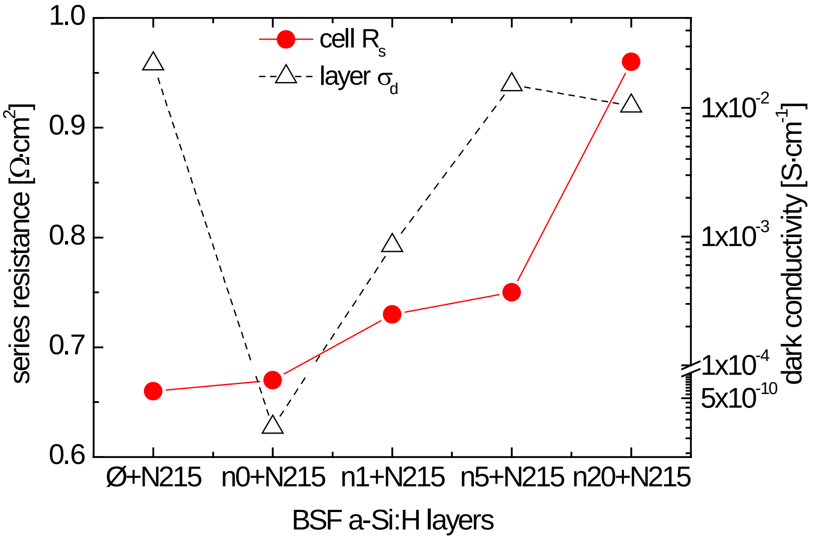

Figure 3.31. Series resistance of HJ solar cells and conductivity of intermediate layer used at the back side of devices. Conductivity measurements have been performed on (n) doped 100 nm-thick single layers deposited on glass at a PH_3 flow rate equal to the doping used in the stack's buffer layer (0, 1, 5 and 20 sccm). Conductivity of Ø+N215 makes reference to the layer doped at 215 sccm of PH_3.

From Figure 3.30(c) and Figure 3.31 it can be stated that interface defects are more important on pFF behaviour when the use of the intermediate a-Si:H layer is introduced, compared to the single BSF. For that reason, limiting factors of the FF are mainly occurring at the interface between the two amorphous layers of the stack. Taking into account the fabrication process of our HJ solar cells it might be suggested that an accumulation of O_2 impurities on the surface of the intermediate amorphous layer can come out, due to the short-time air exposure of this layer prior to the N215 deposition. This fact could explain the opposite trend between FF and conductivity that has been obtained in this work.

Unlike these results, in the analysis of the doping influence of a single layer BSF presented in section 3.5, the FF of the different n-doped 12 nm-thick layers follows the layers' conductivity trend. Thus, when the conductivity is too low and the series resistance is too high, there is not enough field effect to promote carriers collection and consequently, FF is degraded. By contrast, when the (n) doping content on the single layer is sufficiently high, conductivity is enhanced and R_S does not interfere on FF results. In the case of using a single layer BSF, the conductivity of (n) films (and their E_a) seems to be an important mechanism to consider on the overall device performance. The cause of this can be the fact that it does not exist the additional defect-rich interface created when using a double amorphous layer BSF. Then, when using stacks at the back side of HJ solar cells, thorough care will have to be taken when depositing the a-Si:H layers.

As already mentioned, for device optimization not only the conductivity and the passivation of the layers is important, but some unexpected tendencies may arise as a result of the interaction between the different materials used to form the HJ. To date, there is not too much work done on this subject. Therefore, simulation analysis will be used to try to shed new light that contributes to increase the comprehension of the BSF conduction mechanisms in HJ solar cells.

3.6.1.2. Solar cells modelling

Complete solar cell simulations in operating conditions have been performed, based on the a-Si:H layers and interfaces description previously obtained from single layer measurements. Given the number of additional experiments which have been required for a complete analysis of (n) layer properties, comparable accuracy in solar cell description is not expected since there are many other parameters influencing device performances, such as (p)a-Si:H, TCO properties, process induced damage, metal grid shadow variability…

For the sake of objectivity, the modelling approach used in this work is not able to reproduce quantitatively solar cell parameters (J_{SC}, V_{OC} and FF) as a function of back side n-doped amorphous layers. Besides (n)a-Si:H analysis performed in this work, standard literature parameters have been considered for front/back side TCO, c-Si substrate and front (i)/(p)a-Si:H layers [156]. Output simulation results allow to determine band diagram and potential profiles, together with electron/hole recombination rates profiles. Herein, simulations have focused on N215, n0+N215, n1+N215 and n20+N215 cases. Figure 3.32 represents conduction band bending at the back side interface for each configuration.

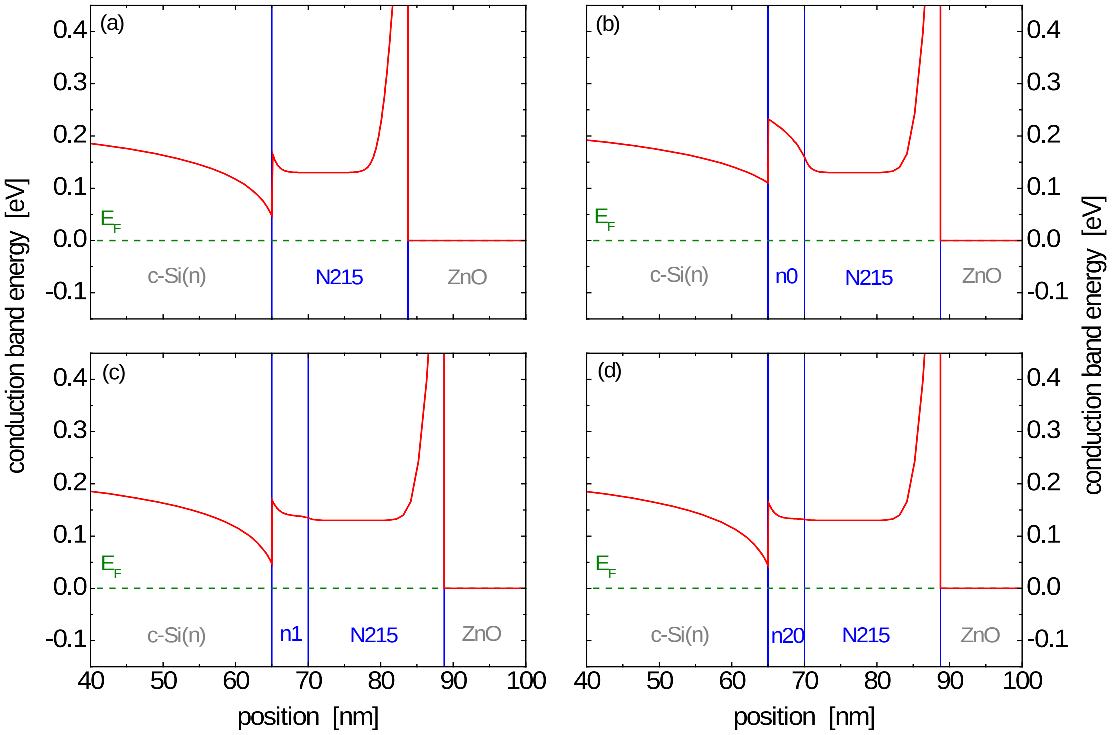

Figure 3.32. Conduction band energy variation of (a) N215, (b) n0+N215, (c) n1+N215 and (d) n20+N215. Simulations have been performed in dark conditions at zero-bias (i.e. equilibrium conditions, no Fermi level splitting).

As expected, an important a-Si:H potential barrier limits electron conduction from a-Si:H layers to back side TCO. a-Si:H and ZnO work functions mismatch explains the presence of a potential drop in the less conductive layer ($\Phi_{a\text{-}Si:H} = E_a + \chi_{a\text{-}Si:H}$ ~ 0.13+3.93 eV vs. $\Phi_{ZnO} = 4.55$ eV). In our simulation procedure, direct tunnelling transport is accounted within Wentzel Kramers Brillouin (WKB) model [157] in order to keep computational burden into reasonable limits. However, it is worth mentioning that trap-assisted tunnelling is the most probable transport mechanism. Thus, electrostatic optimization of this interface (work functions mismatch, a-Si:H/TCO properties, a-Si:H trap-assisted transport) needs further investigation in order to reduce this potential barrier and reach higher FF values.

Figure 3.33 represents the band bending at the back interface (total bend bending on both sides of the BSF HJ (n)c-Si+(n)a-Si:H and band bending in (n)c-Si alone), according to the different a-Si:H intermediate layer configurations. Thanks to the proper modelling of interface lifetime and D_{it} extraction, our simulation results show tendencies in line with V_{OC} experimental data and the total band bending appears directly correlated to interface quality. In particular, n0+N215 configuration exhibits excellent passivation properties (S_{n0} = 21.6 cm/s) leading to a V_{OC} value higher than 720 mV.

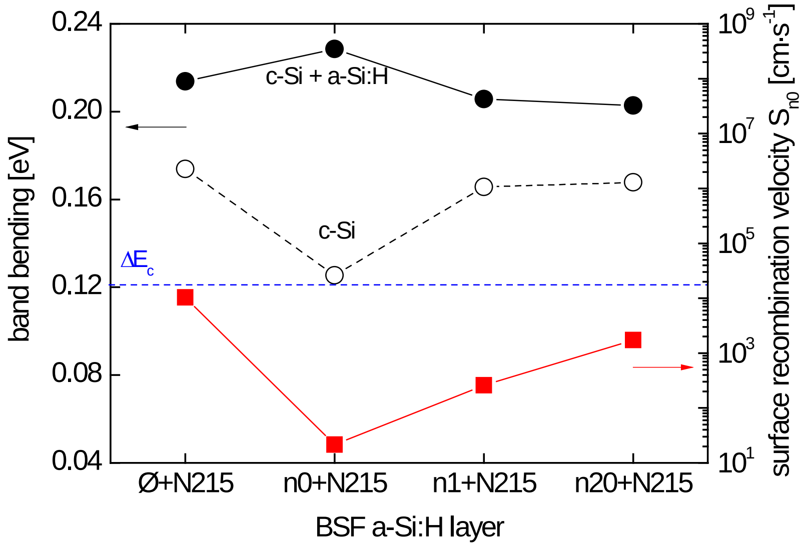

Figure 3.33. Band bending in c-Si and sum of the band bending in both c-Si and a-Si:H (c-Si+a-Si:H) at the BSF (n) a-Si:H/ (n) c-Si heterojunction for the Ø+N215, n0+N215, n1+N215 and n20+N215 configurations. Surface recombination velocity is also shown for comparison purposes.

For each case, buffer layer conductivity is a determining factor of voltage drop asymmetry in c-Si and a-Si:H. Increasing the doping level of the buffer layer induces a lower band bending in a-Si:H, and accordingly, higher field effect in c-Si. However, this last point is not consistent with measurements and experimental FF values showed in Figure 3.31. Lower a-Si:H stack resistance was to be hoped when increasing buffer layer doping level; this would have induced both better film conductivity and a lower a-Si:H potential barrier seen by electrons coming from c-Si substrate (see for instance c-Si potential drop compared with ΔE_C in Figure 3.33). Measurements performed in this study show an important increase of cell resistivity when increasing buffer layer doping, which is inconsistent with our assumptions. Further analysis of (n)a-Si:H interfaces are expected to help explaining this phenomenon.

3.6.2. Buffer layer thickness influence

Based on results obtained in the preceding section, where the undoped a-Si:H layer exhibited enhanced performances amongst other buffer doping tested, here the influence of the thickness of this intrinsic buffer layer is analysed. Thus, 1 nm-, 4 nm-, and 10 nm-thick (i)a-Si:H (p_{dep} = 1.5 T) films have been grown on textured c-Si substrates, followed by 20 nm of (n^+) layer deposition consisting of 215 sccm-doped a-Si:H deposited at p_{dep} = 0.8 T. Devices with no intrinsic layer (i.e. 0 nm) have also been fabricated in order to compare single layer and double-layer stack BSF. Front side emitter and other rear-side layers are identical in all devices.

Figure 3.34 shows the obtained solar cell parameters. The insertion of the high-quality (i)a-Si:H layer reduces surface recombination velocity at the rear a-Si:H/c-Si heterointerface, thus improving the junction properties. V_{OC} is notably improved with increasing (i) layer thickness. Nevertheless, samples with the thickest (i) layer show a large decrease in FF, being mainly attributed to an increase in series resistance, as can be seen in the inset of Figure 3.34(c).

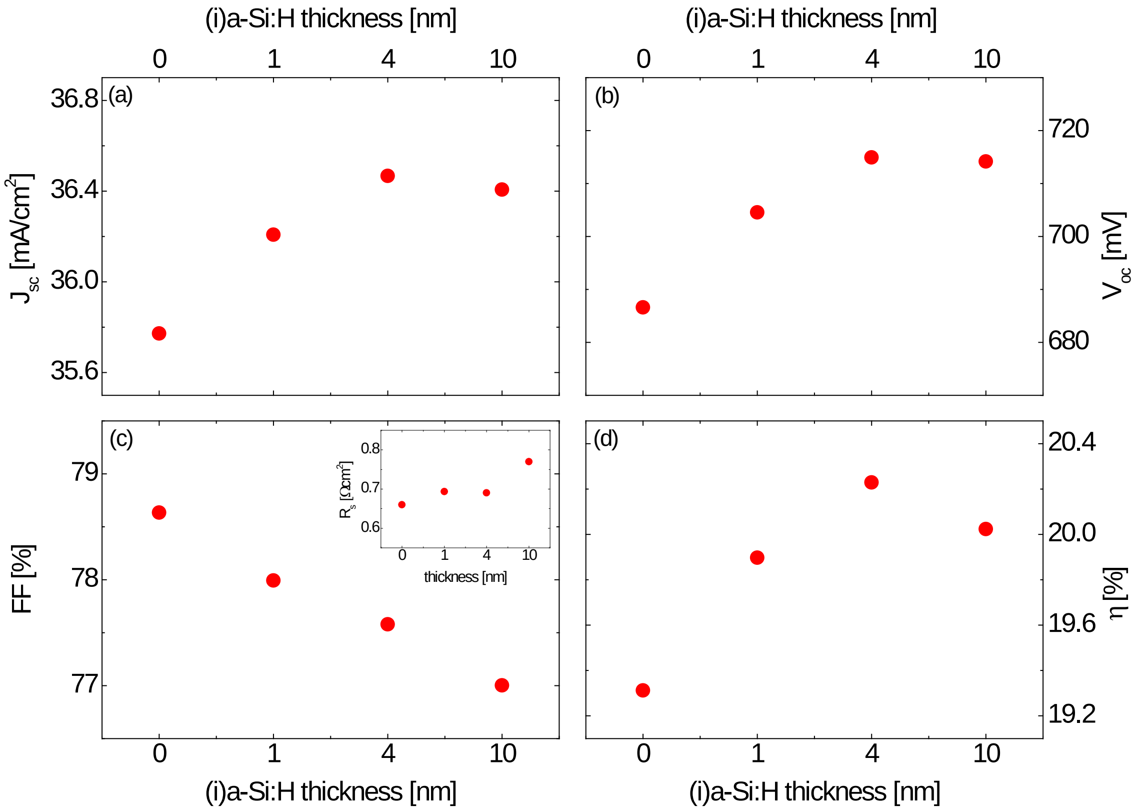

Figure 3.34. Solar cell characteristics as a function of (i)a-Si:H thickness used at the BSF. (a) Short-circuit current; (b) open-circuit voltage; (c) fill factor and R_S; and (d) efficiency. Each data point represents the average value of three cells.

In the case of using the (n)a-Si:H layer directly in contact with the c-Si (buffer layer thickness equal to 0), the FF is maximised due to the higher conductivity of the 215 sccm-doped (n^+) layer (reduced overall R_s in the device). However, this BSF configuration results in degraded efficiencies due to poor defect passivation. When (i)a-Si:H layer is used, overall cell efficiency is maximised for layers being thick enough to properly passivate c-Si. Here, an optimum (i) layer thickness of 4 nm on textured wafers has been found.

Regarding cells' current, when the thickness of the (i) layer emitter is varied, a decrease in J_{SC} is expected to occur due to increased short-wavelength absorption (see Figure 3.23) and low conductivity of (i)a-Si:H. On the contrary, at the rear side negligible absorption in the a-Si:H layers can be assumed. Here, the observed changes in J_{SC} mainly stand for the fact that wafers used for the fabrication of devices with no buffer layer (thickness equals to 0) have not been textured on the same wet bench as the one used for the other substrates. Then, a different effective reflectivity is obtained. Besides, shadowing variability has been detected between devices.

Fitting QSSPC experimental measurements performed on solar cells after a-Si:H growth and before TCO depositions has allowed determining interface defect density D_{it}, using the model introduced in section 3.6.1. Good agreement between experimental and fitted data is obtained. As can be seen in Figure 3.35(a) effective lifetime at mid injection level is limited by recombination via D_{it}, whereas Auger recombination dominates at high injection conditions. In Figure 3.35(b) interface defect density of devices extracted from QSSPC data modelling are presented. As expected, D_{it} increases with decreasing thickness of (i) layer, which is in good agreement with V_{OC} results presented in Figure 3.34.

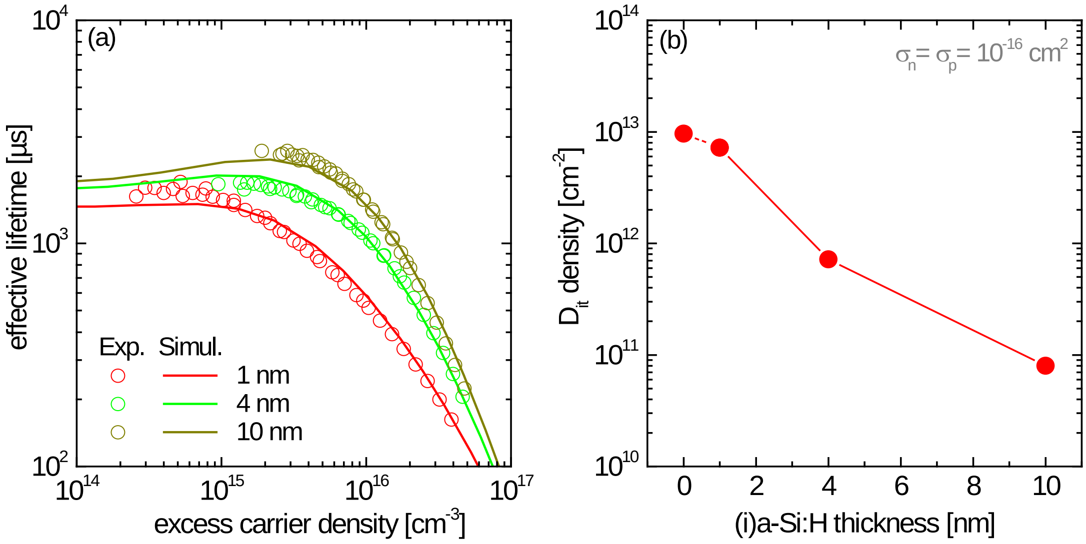

Figure 3.35. (a) Effective lifetime for solar cell samples with varying rear (i)a-Si:H thickness (symbols) and simulated lifetime curves fitted to experimental data (lines). (b)

Interface defect density of samples. The D_{it} corresponding to sample with no intrinsic layer (thickness equal to 0) is also given.

Solar cell simulations have allowed the determination of the band diagram and band bending (φ) at the back side of devices. Results are presented in Figure 3.36. The higher FFs obtained with thinner samples are good correlated with band bending at the a-Si:H/c-Si interface. The minority-carrier transport is enhanced on thinner (i) layers due to lower film resistivity, and also because of easiest thermionic and tunnelling transport, since $\varphi_{c\text{-}Si} > \Delta E_C$. By contrast, in the case of thicker BSF configurations (where $\varphi_{c\text{-}Si} < \Delta E_C$) thermionic and tunnelling transport mechanisms are hampered. Therefore, a degradation of the FF is observed.

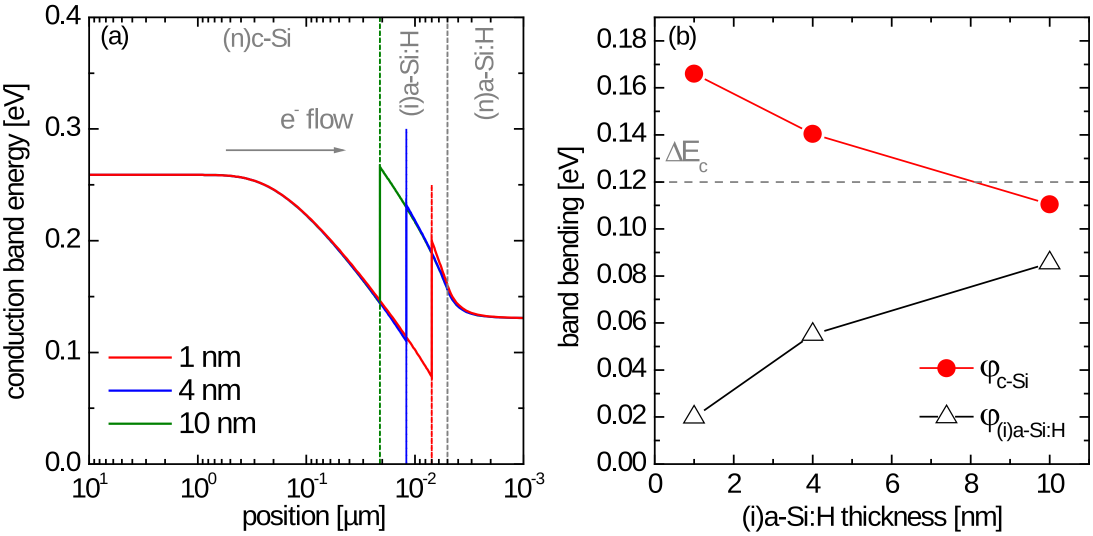

Figure 3.36. (a) Conduction band energy at the rear side of solar cells when different buffer layer thicknesses are used (simulations have been performed in dark conditions at zero-bias). (b) Band bending in c-Si and a-Si:H at the (n)a-Si:H/(n)c-Si heterointerface.

3.6.3. N^+ doping influence

As presented in section 3.4.1, an optimum of deposition pressure at 0.8 T leading to enhanced passivation properties of (n)a-Si:H layers with high PH_3 flow rates has been found. However, few differences on V_{OC} results are observed above 130 sccm of PH_3 (see Figure 3.5). With the aim of determining an optimal (n^+) doping to be used at the BSF, HJ solar cells have been fabricated using 4 nm of (i) buffer layer followed by 20 nm of 130 sccm-, 215 sccm- or 300 sccm-doped (n)a-Si:H layers. Front side emitter and other rear-side layers have been kept identical in all devices.

In Figure 3.37(a), the dark conductivity at 300 K and the activation energy of (n) single layers being used as a double-layer stack BSF are presented. Better conduction properties are obtained with the (n) layer doped at 215 sccm. Accordingly, E_a is smaller, indicating that the Fermi level lies closer to the conduction band compared to the other layers. From modelling calculations introduced in appendix A, the acceptor defect density N_{def} and donor doping level N_D have been determined (see Figure 3.37(b)).

For each case, N_{def} has been calculated from equation (A.1) (considering two Gaussian distributions of localised states and constant band tails) and N_D has been set in accordance with experimental E_a. When increasing the PH_3 flow rate from 130 to 300 sccm, higher N_{def} is observed, which is consistent with doping-induced defect creation. In parallel, active doping increases with (n^+) PH_3 addition in a non-linear way; at high doping level, active phosphorous concentration tends to saturate. For this reason, the best defect density/doping level compromise is obtained with the layer doped at 215 sccm, which thus exhibits the smallest E_a.

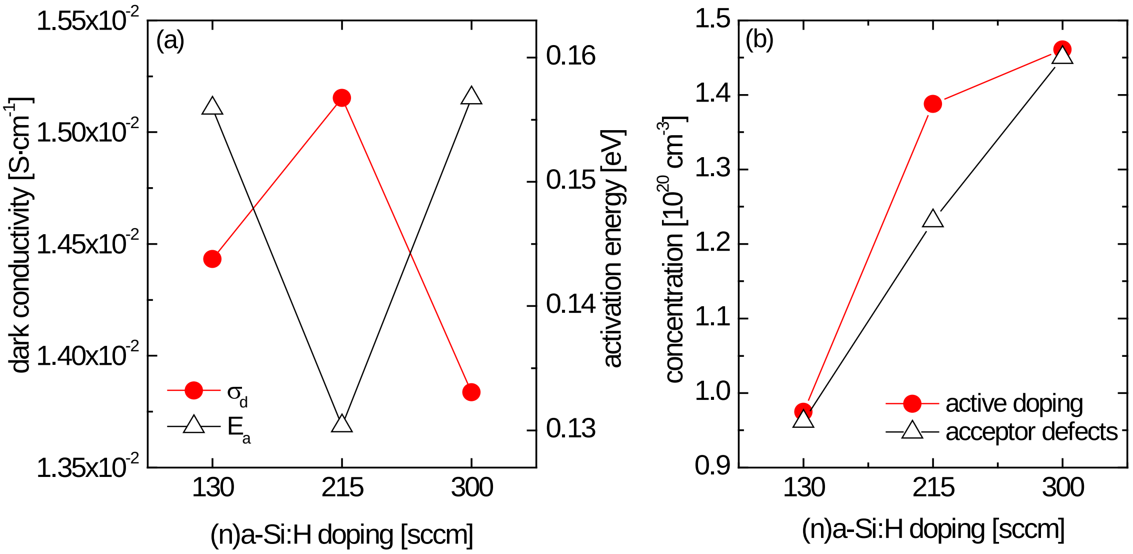

Figure 3.37. (a) Dark conductivity at 300 K and activation energy, and (b) defect density and donor doping concentration for highly doped (n)a-Si:H layers.

The output solar cell characteristics obtained with the different BSF configurations tested are given in Figure 3.38. Small differences in V_{OC} are observed in devices with 130 sccm- and 215 sccm-doped (n^+) layers. However, a remarkable decrease is obtained in the case of (n)a-Si:H at 300 sccm (ΔV_{OC} = -25 mV). Due to the higher defect density of this n300 layer (Figure 3.37(b)), a certain fall in V_{OC} was expected, although such a substantial decrease can not only be owed to N_{def}.

The same tendency is obtained in FF results, where the value at 300 sccm sharply drops about 5% compared to the 215 sccm-sample. Accordingly, as can be seen in the inset of Figure 3.38(c), the overall series resistance rather increases in the 300 sccm-doped layer, which can partly explain the FF degradation. Nevertheless, such different results obtained in the case of the most heavily-doped double-layer BSF constitute an unexpected trend that must be carefully considered.

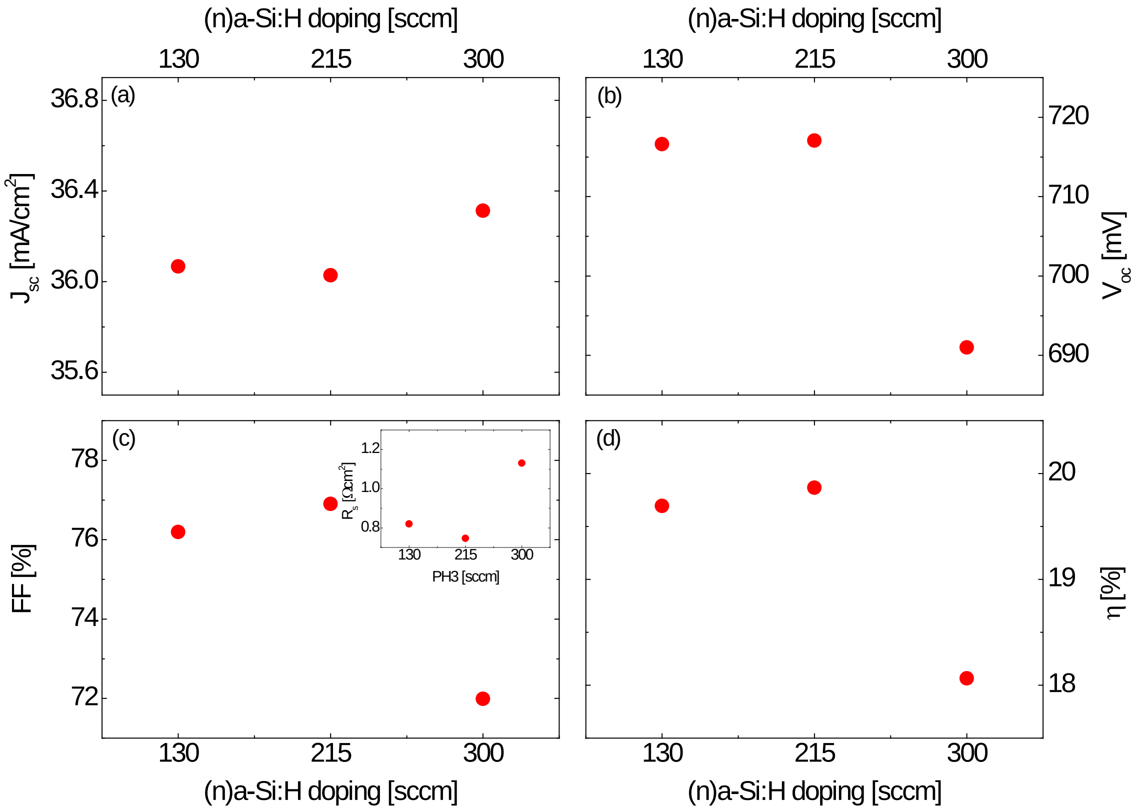

Figure 3.38. Solar cell characteristics as a function of the (n)a-Si:H layer PH_3 flow rate used at the BSF. (a) Short-circuit current; (b) open-circuit voltage; (c) fill factor and series resistance; and (d) efficiency. Each data point represents the average value of three cells.

Fitting QSSPC experimental measurements performed on solar cells prior to TCO deposition and metallisation has allowed determining interface defect density using the model introduced in section 3.6.1. Results presented in Figure 3.39(a), show a very slight increase in D_{it} as a function of (n)a-Si:H doping, that can not entirely explain the degradation in solar cell output characteristics (a drop around 25 mV is observed on V_{OC} results of solar cells with the (n^+) layer at 300 sccm). Conduction band diagram at the rear a-Si:H/c-Si interface (Figure 3.39(b)) has been also determined performing solar cell simulations. The small differences observed in FF between the use of (n^+) layers at 130 or 215 sccm are in good agreement with the obtained band bending. However, characterisation and modelling performed so far are not able to provide a clear explanation for that drop in V_{OC}, FF and η at 300 sccm-doped (n) layer.

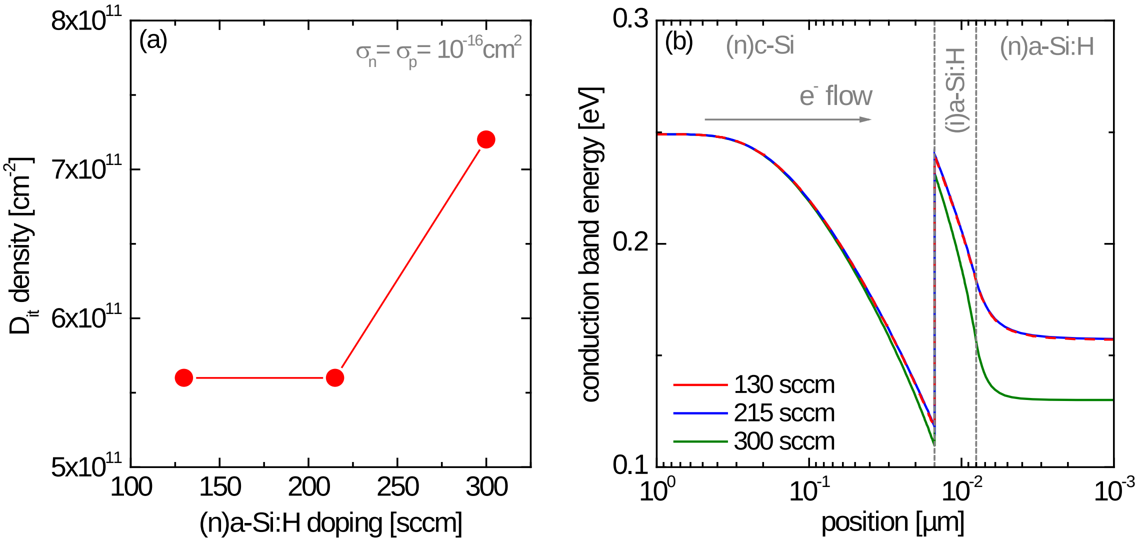

Figure 3.39. (a) Interface defect density determined from modelling of QSSPC experimental data for various (n) layer dopings, measurements have been performed on solar cells prior to TCO deposition and metallisation.(b) Conduction band energy at the rear side of solar cells when different (n) layer dopings are used (simulations have been performed in dark conditions at zero-bias).

In order to identify eventual problems occurred during solar cell fabrication, SIMS analyses have been performed on each differently doped reference sample (the same for SE measurements). Depth profiles for phosphorous, hydrogen and oxygen concentrations ([P], [H] and [O], respectively) are presented in Figure 3.40. In accordance with the PH_3 flow rate introduced into the PECVD chamber during (n) layers depositions, the [P] slightly increases. As the hydrogen content has not been varied, the [H] remains almost unchanged in any of the samples, although a small signal increase near the (i)/(n)a-Si:H interface is detected. By contrast, a pronounced [O] peak is found in all samples at the (i)/(n) interface (considered its magnitude, here the [H] peak can be neglected). Curiously, the better solar cell efficiency is obtained with the (n^+) BSF layer exhibiting less pronounced oxygen peak (doped at 215 sccm), whereas the layer with the higher [O] at the (i)/(n^+) interface (doped at 300 sccm) coincides with the one resulting in poorer device performance. Then, a problem that occurred between buffer layer and (n^+) layer deposition is evidenced, being the most probable reason of detrimental results on 300 sccm BSF-doped devices. Indeed, during the fabrication of this solar cell batch the (n^+) layer deposition was unexpectedly delayed due to some PECVD technical problems, and samples were subject to atmosphere exposure.

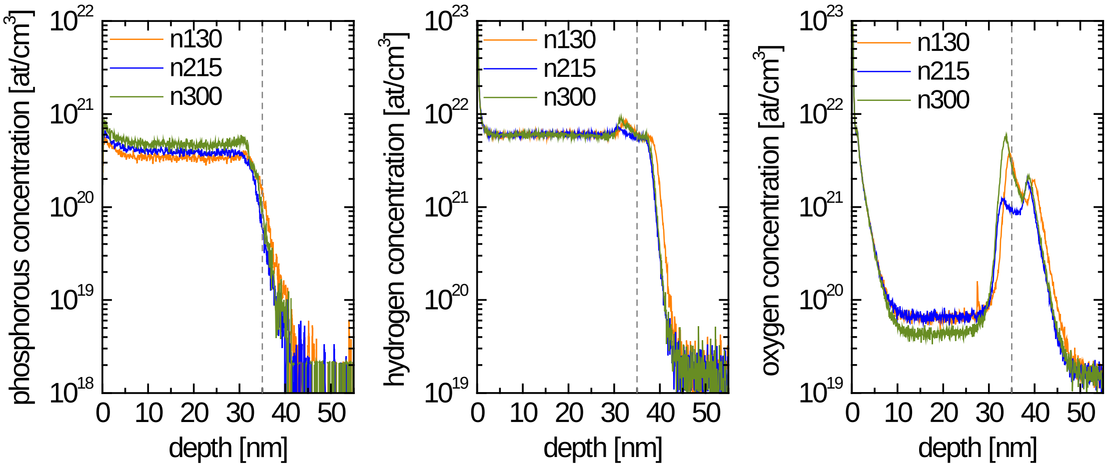

Figure 3.40. SIMS analysis depth profiles for P, H and O of 130 sccm-, 215 sccm-, and 300 sccm-doped (n) layers used at the BSF of HJ.

The increased [O] peak found in the 300 sccm-doped sample is considered to act as a high recombining layer, thus hindering the transport of carriers. In order to study the impact of this event on the energy band diagram, simulations have been performed introducing a virtually highly-defective thin layer at the interface between the buffer and the 300 sccm (n) layer. Obtained results should only be considered as a qualitative tendency of what might be happening at the n/n$^+$ junction under the influence of this [O] peak, and not as a physical fact. As represented in Figure 3.41, the band diagram at the junction is distorted. So much so that band bending is modified in a way in which charge carriers face a kind of barrier that renders difficult their transport compared to the ideal case without any additional defective layer. Based on this event, the significant drop in FF and V_{OC} results of 300 sccm (n$^+$) layer can be reasoned out.

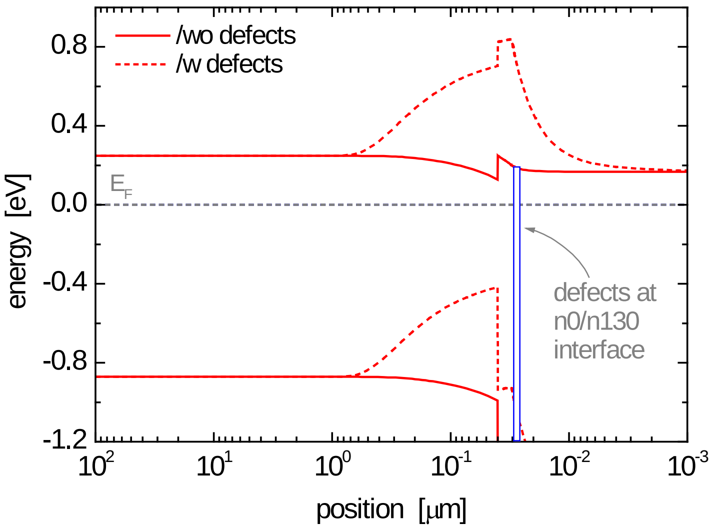

Figure 3.41. Energy band diagram of the (n)c-Si/(i)/(n300)a-Si:H sample, where a virtually high-defective layer of 1 nm has been introduced at the (i)/(n^+) interface in order to simulate the influence of [O] peak (represented by dashed lines).

3.6.4. Buffer layer and N^+ layer hydrogen dilution

Considering the importance of the hydrogen content on the layers' properties, the impact of varying hydrogen dilution on the BSF buffer layer has been studied. For that purpose, HJ solar cells with the same front side schema have been fabricated, and the H_2/SiH_4 ratio during the growth of 4 nm intrinsic layer has been adjusted to 4, 8.6, and 21.5. Subsequently, 20 nm of (n)a-Si:H with 215 sccm of PH_3 has been deposited. Output solar cell results are shown in Figure 3.42.

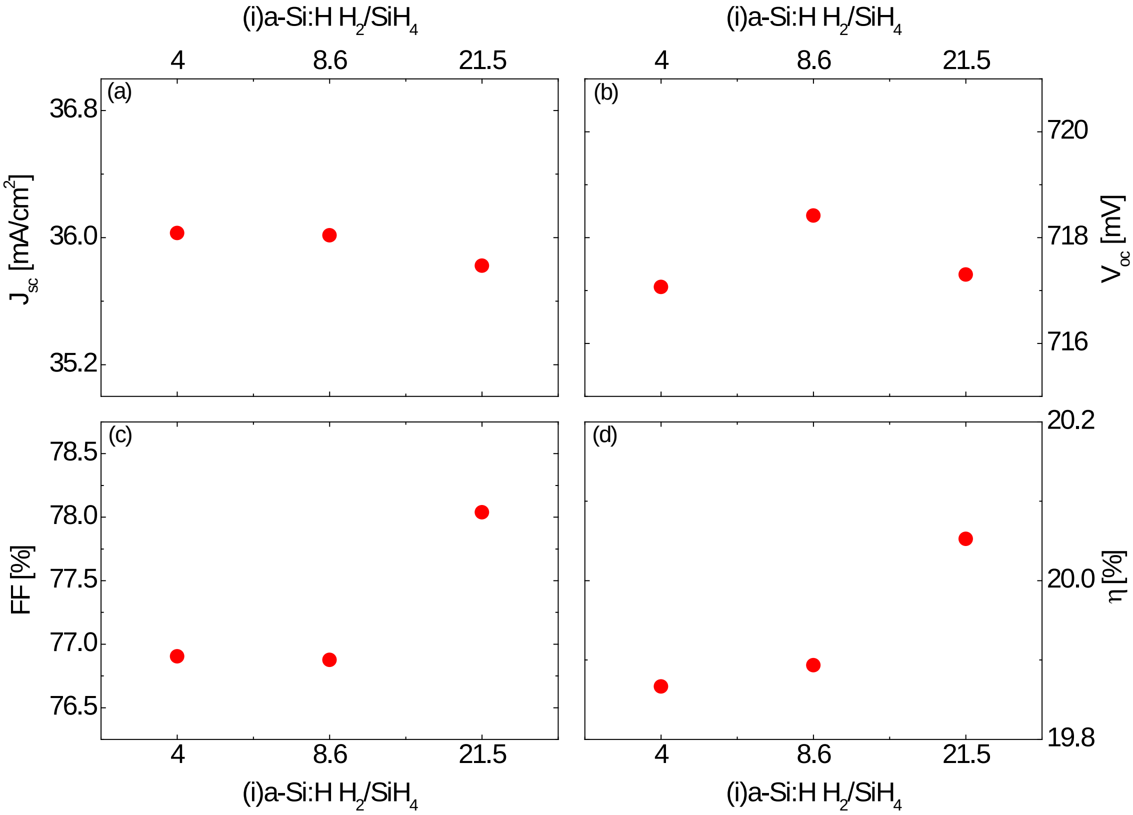

Figure 3.42. Solar cell characteristics as a function of the H_2/SiH_4 ratio used during intrinsic buffer layer growth used at the BSF. (a) Short-circuit current; (b) open-circuit voltage; (c) fill factor; and (d) efficiency. Each data point represents the average value of three cells.

In section 3.4.4, the passivation trend obtained on heterojunction precursors (see Figure 3.15) tended to decrease at higher hydrogen dilutions. Particularly, the implied V_{OC} obtained on 10 nm-thick 1 sccm-doped layers remarkably diminished about 30 mV when increasing H_2/SiH_4 ratio from 8.6 to 21.5. Assuming a similar behaviour on intrinsic layer, in Figure 3.42(a) it can be seen that when using these layers on HJ solar cells, the impact of hydrogen dilution on the open-circuit voltage of devices is not so evident. Only slight differences can be appreciated, though the average value at R = 8.6 is still higher. With regard to Figure 3.42(b) it can also be seen that small variations are obtained: the difference between highest and lowest average values does not exceed 1.2% in FF and 0.2% in η. Surprisingly, solar cells with the buffer layer at R = 21.5 are somewhat the best performing ones. This result suggests that passivation properties of 10 nm-thick layers differ from that on 4 nm-thick ones, since the incorporation of excess hydrogen is done otherwise in thinner layers.

Similarly, the influence of hydrogen dilution on the BSF (n^+) layer has been studied. Heterojunction solar cells have been fabricated with 4 nm of buffer layer followed by 20 nm of (n)a-Si:H doped at 215 sccm with hydrogen dilution equal to 4, 8.6 and 21.5. Emitter and other rear side layers have been unchanged. Again, only slight differences on V_{OC}, FF and η are observed in Figure 3.43, although in this case results are better correlated with single layer passivation trend presented in Figure 3.15. Solar cell conversion efficiency and FF decrease about 0.5% and 0.8% as the H_2/SiH_4 ratio is increased.

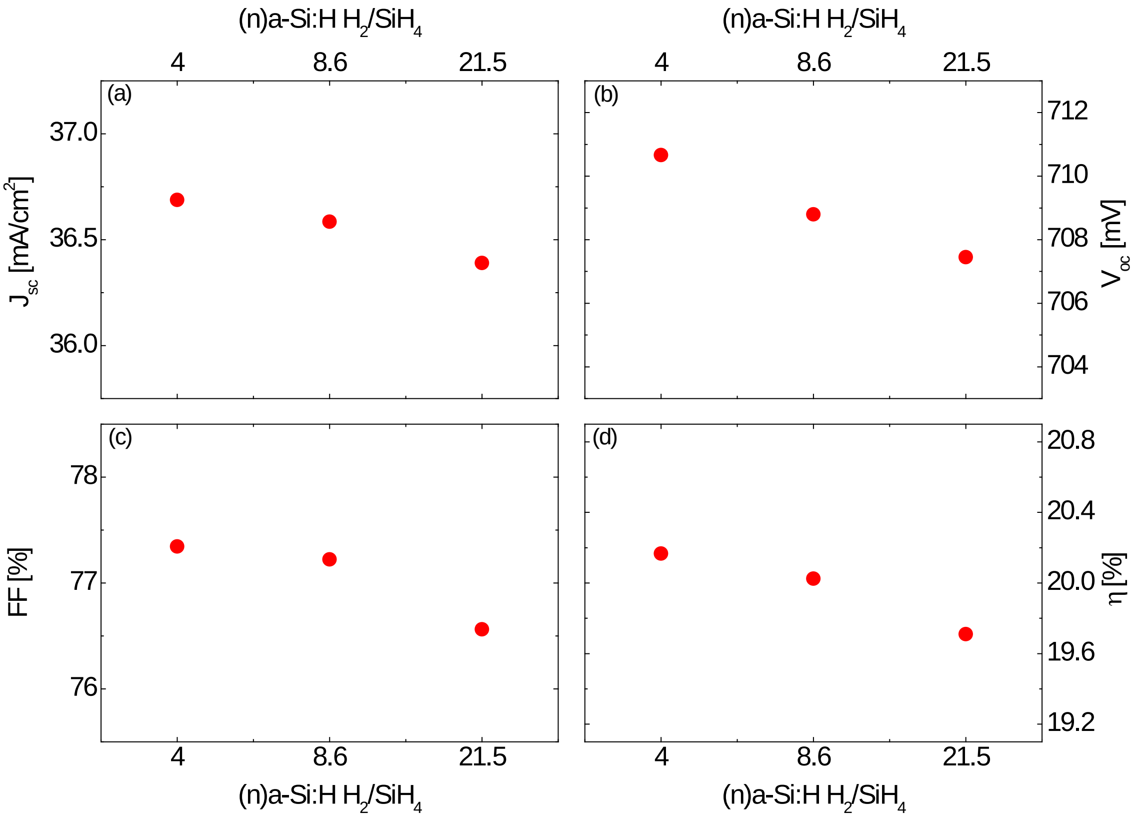

Figure 3.43. Solar cell characteristics as a function of the H_2/SiH_4 ratio used during intrinsic buffer layer growth used at the BSF. (a) Short-circuit current; (b) open-circuit

voltage; (c) fill factor; and (d) efficiency. Each data point represents the average value of three cells.

Series resistance of devices presented in Figure 3.42 and Figure 3.43 has been calculated and no significant differences have been obtained between different layers tested, which is in good agreement with FF values. Results obtained on both buffer layer and (n^+) layer with varying hydrogen dilution clearly indicate that changes introduced on a-Si:H layers used at the rear side of the solar cells are far from having a pronounced influence in the overall device performance. Moreover, expected tendencies as per characterisations performed on single layer precursors may vary, since thicknesses used on solar cells differ from the ones used for characterisation purposes, and the interaction with adjoining layers may also determine performance results.

3.6.5. N^+ layer thickness

The thickness of the (n^+) layer (doped at 215 sccm) has been varied in order to identify possible trends on solar cell conversion efficiency. Thus, 10 nm, 20 nm and 30 nm have been tested, keeping unchanged other layers. As can be seen in Table 3.4, V_{OC} results range from 710 to 713 mV when increasing the thickness; FF values are around 77.6% ($\Delta FF_{max\text{-}min}$ = 0.2%); and conversion efficiency stays at 19.6% at any thickness. For the studied samples no differences have been identified, contrary to what has been presented in section 3.6.2 for intrinsic buffer layer thickness. Based on these results, it has been evidenced that (n^+) layer thickness is a parameter of second order, which has a little influence on the overall device performance.

Table 3.4. Solar cell parameters of devices with various (n^+) layer thicknesses.

n^+ thickness [nm]	J_{SC} [mA/cm^2]	V_{OC} [mV]	FF [%]	η [%]
10	35.3	710	77.6	19.5
20	35.4	713	77.6	19.6
30	35.5	712	77.4	19.6

In a future approach, thinner (n^+) samples or even thicker ones (although the latter will be less interesting from an industrialisation point of view) should be tested in order to verify if this parameter can really have an impact on solar cell output characteristics. Besides, it will also be interesting to investigate the influence of the (n^+) layer thickness when different TCO layers are used at the rear back contact. The band bending at the interface with the amorphous layer and the TCO may vary, and in this case the effects of using different n^+ layer thickness can be different than that obtained here.

4. Back contact of heterojunction solar cells

In this chapter, a discussion on the back contact of HJ solar cells is presented. Different alternative schemas exist and resulting efficiencies have been already demonstrated by different groups. Low temperature back contact in HJ solar cells can be ensured by a metal (usually, Ag or Al) layer directly deposited on c-Si [158]. However, since no back surface field is created in these structures, attainable V_{OC} is rather low. If amorphous layers are used, recombination losses at the rear side of devices are minimised. Then, in this case, the back electrode is deposited on top of the rear side a-Si:H [103, 104]. However, the insertion of a TCO layer is also commonly used in cells with full rear metallisation [72]. Indeed, better efficiencies have been demonstrated with this back TCO/metal contact structure. As in the front TCO, sputtered indium tin oxide is also the most extended choice at the rear contact. However, in this thesis a new back TCO approach based on boron-doped zinc oxide (ZnO:B) layers has been studied. The use of ZnO:B will not be extended to the front side since, as it will be presented later on, some stability constraints have been evidenced.

Here, the structural, electrical and optical properties of ZnO layers deposited by low pressure chemical vapour deposition (LPCVD) are described. Different deposition parameters have been studied with the aim of developing ZnO:B layers with similar or even better optoelectronic properties as compared to the reference ITO. Besides, different post-deposition treatments have been also investigated.

Research has focused on film properties relevant for their application as rear side TCO material in HJ solar cells. Thus, such layers have been tested on the back contact of heterojunction devices and the impact on the conversion efficiency has been studied.

During the course of this thesis, a number of adjustments on the deposition system have been made resulting in changes in film properties under the same deposition conditions. Therefore, the following results are presented in a way where variability linked to deposition settings is excluded. Deposition conditions between samples of the same series have been kept.

4.1. Transparent conductive oxides in HJ solar cells: Why ZnO:B?

Transparent conductive oxides (TCO) layers constitute a major aspect of heterojunction solar cells, being used either as a front electrode or as a part of the back-side reflector. Due to the low conductivity of the a-Si:H layer, a conducting and transparent film is needed for efficient charge carrier collection, since the metal grid alone is not sufficient for that purpose. Besides, TCO is also of prime importance for light trapping and reduced reflectance losses, especially when used on the front side.

This peculiar combination of physical properties is only achievable if material has a sufficiently large energy band gap (typically > 3.3 eV) so that absorption due to band-to-band transitions is limited to the UV [159], as well as a relatively high concentration of free carriers in its conduction band. Nevertheless, the accomplishment of both requirements is not evident, since high carrier concentration (N) causes absorption in the infrared spectra. Thus, a careful balance between electrical conductivity and optical transmittance is required [160].

When the TCO is used at the rear side of heterojunction solar cells with full rear metallisation some of these constraints disappear, although optical and contacting properties still remain important (see section 1.5).

Nowadays, the choice of TCO materials is vast and varied. The majority of known TCOs are n-type semiconductors where charge carriers at the conduction band arise either from defects in the material or from extrinsic dopants. However, p-type materials have also been reported [161, 162], although these TCO layers have relatively lower conductivities and lower transmittance. Then, n-type TCO materials are widely extended on PV applications. Indium tin oxide is the most commonly used for silicon heterojunction solar cells, owing to the excellent compromise on its optoelectronic properties. Low resistivity values can be achieved thanks to its relatively high free carrier concentration ($N > 2\times10^{20}$ cm^{-3}), although parasitic absorption in the IR range is still a limiting factor for high short-circuit current devices [56].

As a consequence of the relative scarcity of indium as well as the widespread use of ITO in most thin-film transparent electrode applications, its cost has risen [163]. Therefore, in the last few years zinc oxide (ZnO) has gained increasing attention as a promising low-cost alternative. Although the electrical and optical properties of the ZnO are widely known [164], it should be mentioned that to date little research has been done on the implementation of ZnO films as the back-side TCO of a-Si:H/c-Si HJ solar cells.

Undoped ZnO is an n-type transparent material, the conductivity of which results from oxygen vacancies or interstitial zinc atoms [165]. Nonetheless, in order to enable the use of ZnO layers as a TCO with enhanced electrical properties, higher conductivities can be obtained by doping them with donor elements such as aluminium (ZnO:Al) or boron (ZnO:B), amongst others [105, 166-168]. Boron- or aluminium-doped zinc oxides are favoured materials due to their performance advantages, in that they can provide a low sheet resistance, high transparency extending out to the infrared or the possibility to produce material with a roughness that will provide light scattering over the range of the solar spectrum [105].

However, ZnO properties may drastically vary depending on the deposition technique used. Magnetron sputtering yields to flat ZnO:Al films [166, 169-171] that can be subsequently textured through an etching process to further enhance optical properties. However, this post-etching step could result in a drawback when up-scaling to industrialization. On the other hand, low pressure MOCVD (i.e. LPCVD) leads to as-grown rough ZnO:B surfaces when the appropriate deposition conditions are chosen [168, 172, 173]. Besides, LPCVD technique allows lower temperature processing compared to high-pressure regime depositions (atmospheric pressure CVD, APCVD), and it also provides excellent conformal coverage of textured substrates [174], which is entirely beneficial to HJ technology.

The cost-effective large scale production of ZnO:B films on the one hand and the development of such films with improved properties on the other hand are the main reasons that have aimed the inclusion of such film as an alternative TCO material in HJ solar cells. Therefore, a deposition parameter survey has been done in order to find optimised ZnO:B layers, suitable for the rear contact of our devices.

4.2. Fabrication of ZnO:B layers by low pressure CVD

After having introduced in the previous sections the interests in using ZnO:B layers at the back contact of heterojunction solar cells, here the experimental details for the fabrication of this material are given. Low pressure CVD zinc oxide has particular features that determine their characteristics. In order to provide the background necessary to comprehend the discussion in the following chapters, fundamental physical properties of ZnO layers are summarised. Finally, a deposition parameter survey is presented, where the influence of the various conditions studied on the ZnO properties is discussed. In addition, heterojunction solar cells with different ZnO layers are analysed and the effects of varying ZnO properties is assessed.

4.2.1. Relevant properties of ZnO films

Zinc oxide crystallizes in the hexagonal wurzite structure. APCVD and sputtered ZnO layers are highly oriented with the c-axis perpendicular to the substrate, resulting in this case, in polycrystalline films with smooth surfaces. Contrary to this, for thick LPCVD layers a strong preferentially oriented growth is observed within the plane $(11\bar{2}0)$, parallel to the substrate [175]. Columnar grains are formed and extended up to the surface of ZnO films, resulting in crystallite facets forming a pyramidal-like rough surface. Because of such pyramidal structure, ZnO layers exhibit an as-grown surface texture, which in some cases can scatter the light that enters into the solar cells. However, as it will be explained below, the structure of relatively thin ZnO films is composed of small grains, generally with no clear preferential orientation.

The characteristic polycrystalline structure leads to a vast amount of grain boundaries that constitute crystallographically disturbed regions leading to electronic defects at the band gap of semiconductors. In these regions, as depicted in Figure 4.1, energetic barriers of height Φ_b are created, whose periodicity is given by the mean grain size. The maximum value of Φ_b is given by equation (4.1), when the trap density (N_t) at the grain boundaries is considered to be lower than the carrier concentration within a grain of length L ($N_t < NL$; reasonable assumption in heavily n-doped TCO) [176].

$$\phi_b = \frac{q^2 N_t^2}{8\varepsilon\varepsilon_0 N} \tag{4.1}$$

where q is the elementary charge, N_t is the charge carrier trap density, N is the carrier concentration in the bulk of the grain, ε is the dielectric permittivity of the material and ε_0 the vacuum dielectric permittivity.

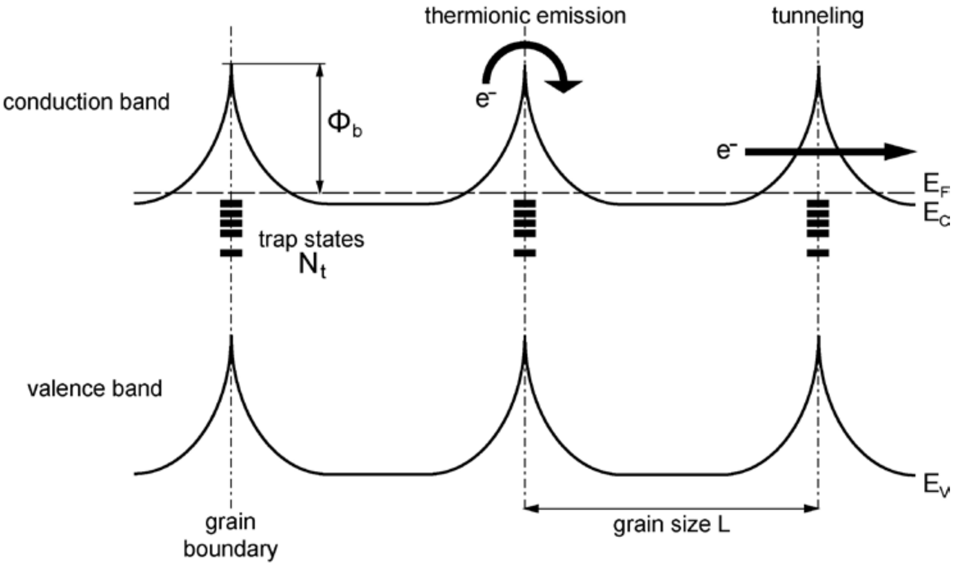

Figure 4.1. Schematic band energy diagram of polycrystalline TCO with grains of length L and energetic barriers of height Φ_b at the grain boundaries. Transport mechanisms across the barrier are indicated. Adapted from [177].

The transport paths for electrons across the grain barriers are based on both thermionic emission over the barrier, and tunnelling of the barriers when high carrier concentrations in the grains narrow the width of Φ_b [108]. However, electron transport within the TCO is governed by various scattering mechanisms [160]. According to Matthiesen's rule each of them separately contributes to the overall mobility following the relation:

$$\frac{1}{\mu} = \sum_{i=1}^{n} \frac{1}{\mu_i} \tag{4.2}$$

where μ_i is the mobility due to each scattering mechanism.

Mobility is diminished as scattering phenomena become more important. Scattering caused by the discontinuity presented by grain boundaries hinders the carrier transport through the space charge region at the potential barrier, and therefore it contributes to mobility degradation. Likewise, ionised or neutral impurities within the crystallites can also result in an increase in carrier scattering. The presence of extrinsic dopant atoms or defects such as interstitial zinc atoms and vacancies interacts with free carriers, causing the deflection of electrons. Besides, phonon scattering events can also contribute to mobility degradation at the crystallites due to the interaction of electrons with an electric field induced by lattice vibrations of bonds [178].

Then, in a polycrystalline material such as LPCVD ZnO films, the contribution of grain boundaries (μ_b), dislocations (μ_d) and crystallites themselves (μ_{cr}) should be considered for the overall mobility calculation:

$$\mu_{Hall}^{-1} = \mu^{-1} = \mu_{cr}^{-1} + \mu_b^{-1} + \mu_d^{-1} \tag{4.3}$$

The resistivity (ρ) of ZnO films is related to the charge carrier density N and the carrier mobility μ by the relation:

$$\rho = \frac{1}{N\mu q} \tag{4.4}$$

In practice, the resistivity of TCOs cannot be decreased by simultaneously increasing the carrier density and the mobility. Usually, mobility is observed to saturate and even start to reduce as the carrier density is increased indicating dominant scattering by ionised impurities. Besides, at high carrier concentrations transmission in the near infrared (NIR) region reduces due to absorption by free carriers (FCA). Then resistivity may be decreased without increasing NIR absorption by rather increasing μ.

4.2.2. Low-pressure chemical vapour deposition system

As already been mentioned, chemical vapour deposition (CVD) is a particularly interesting technology not only because it gives rise to high-quality films but also because it is applicable to large-scale production. Generally, chemical reactions take place at temperatures higher than that advisable in HJ devices [167, 179]. However, this drawback can be overcome if both low pressure and metal-organic precursors are used during deposition, leading to the technique called low-pressure metal-organic chemical vapour deposition (LP-MOCVD, from now on LPCVD or MOCVD will be used indistinctively). In this case, deposition temperatures can be reduced well below 250°C and parasitic pre-reactions in the gas phase are minimised [175].

In the LPCVD method ZnO deposition occurs as a result of chemical reactions of vapour-phase precursors on the substrate, which are delivered into the growth zone by the carrier gas. The reactions take place in a reactor where a necessary temperature profile is created in the gas flow direction. In the particular case of the LPCVD ZnO:B films used in this thesis, diethylzinc ($(C_2H_5)_2Zn$ or DEZ) and water (H_2O) are used as precursor gases in combination with a separate source of argon as a carrier gas; diborane (B_2H_6) is used as the doping gas.

The hydrolysis reaction that leads to the formation of ZnO from DEZ and water vapour is described as follows:

$$(C_2H_5)_2Zn + H_2O \rightarrow ZnO + 2C_2H_6 \qquad (4.5)$$

However, chemical kinetics taking place in the reactor is notably more complex; many intermediate reactions occur and they strongly depend on the deposition conditions and also on the reactor configuration [180].

When diborane is incorporated into the process, it is decomposed and the ion B^{3+} is incorporated in the ZnO crystal. Nonetheless, due to the low deposition temperatures used (<200°C), the hydrogen inclusion during the film growth cannot be avoided. Hence, not only boron ions are incorporated, but also boron compounds [181]. In Figure 4.2 a schematic view of the vertical injection LPCVD system used at INES is shown.

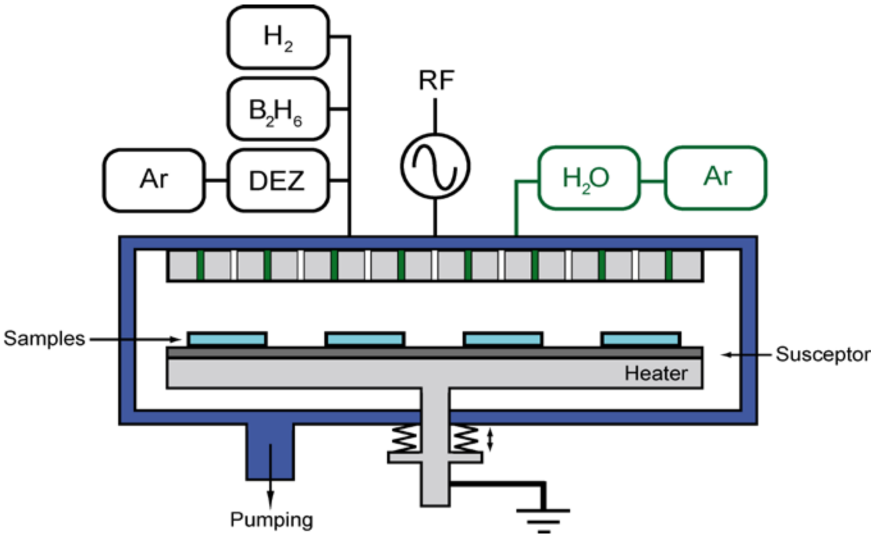

Figure 4.2. Schematic illustration of the LPCVD system used at INES.

Mass-flow controllers fix the flow of reactants introduced into the vacuum chamber. In order to prevent condensation throughout the gas lines, temperature is kept at 50°C and gases are only evaporated once inside the reactor. The gas inlet into the chamber is done through a shower where the different precursors come into contact. To avoid any premature reaction in the showerhead a temperature profile is also assured. Finally, process pressure is limited by the total amount of gases used during the reaction and the aperture of a butterfly valve (deposition pressure is usually fixed at 0.4 T). The reactor design makes also possible to vary the distance between the samples tray and the gas inlet.

The MOCVD system is part of the five-chamber deposition cluster, where samples can be processed on a tray of 60×60 cm^2. The deposition area inside the chamber is heated through a hot plate (heater) where temperature can be set from the ambient to temperatures exceeding 250°C. However, the real temperature during the ZnO:B cannot be controlled in-situ. Therefore it might be possible that deposition temperature differs from the one set. Because of the fact that temperature plays an important role during the CVD process, eight thermocouples have been used to measure the real temperature on the sample tray under two different pressure conditions: (a) primary vacuum, no gas has been introduced inside the reactor, and (b) argon is introduced till reaching a pressure of 1 T. Figure 4.3 shows the temperature uniformity deduced from eight measured points. Unfortunately, the disruptive functioning of a ninth thermocouple did not allow the collection of an extra temperature point.

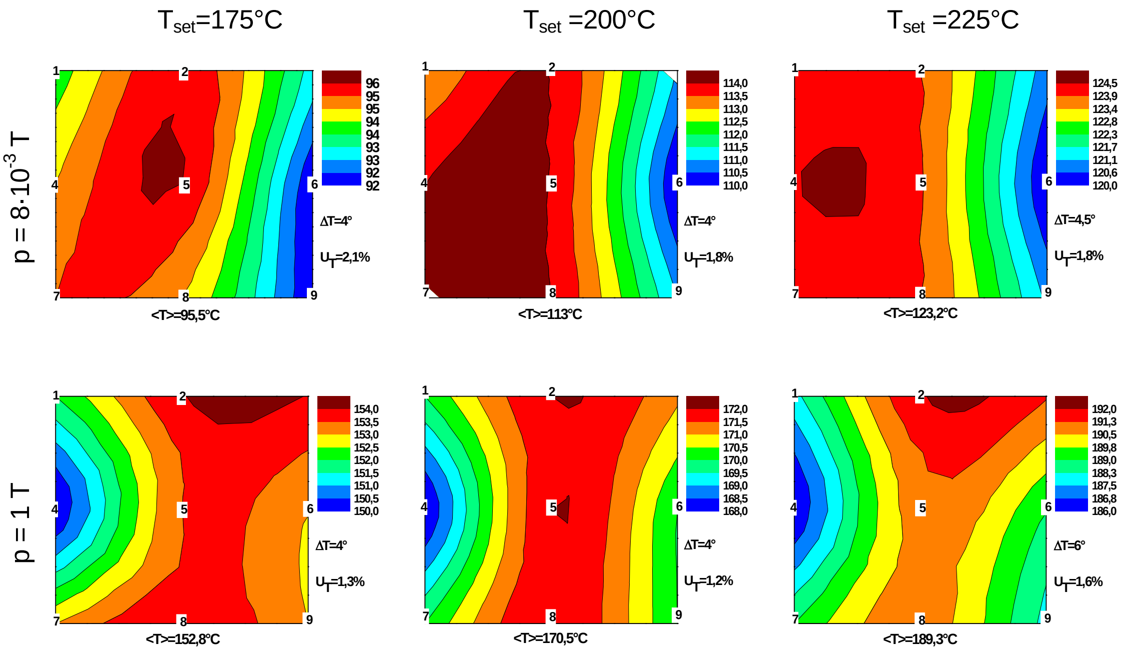

Figure 4.3. Thermal distribution on the ZnO:B tray under two different pressures inside the MOCVD reactor and three fixed temperatures of the hot plate.

The temperature non-uniformity in all six conditions does not exceed 2.1% and a mean deviation of 4°C is found in most cases. Moreover it has been found that an increase in the process pressure leads to a better thermal contact, thus reducing the difference between fixed and real temperatures. As observed in Figure 4.3, when the heater temperature is fixed at 200°C, the real mean temperature of the tray differs from almost 100°C at extremely low pressure, compared to 30°C at 1 T. Then, in the latter case the amount of gas and the pressure fixed inside the chamber contribute to thermal transfer, since it has to be considered as well that the MOCVD chamber walls are also heated at 80°C for uniformity reasons.

As presented in Figure 4.4 the substrate tray temperature strongly depends on the system pressure. Between 0.1 and 1 T, the difference between the fixed temperature at the heater and the effective temperature measured in the substrate tray may exceed 40°C. However, in this case reactor walls are not heated. Hence, results herein presented are only indicative, though it can be expected that if an external heating to the chamber is applied (in this case, 80°C) thermal stabilisation will be reached at lower pressures. Then, even if the temperature variation in the range of MOCVD studied pressures will be smaller than that in Figure 4.4, it will be difficult to foresee the real temperature held during the deposition process.

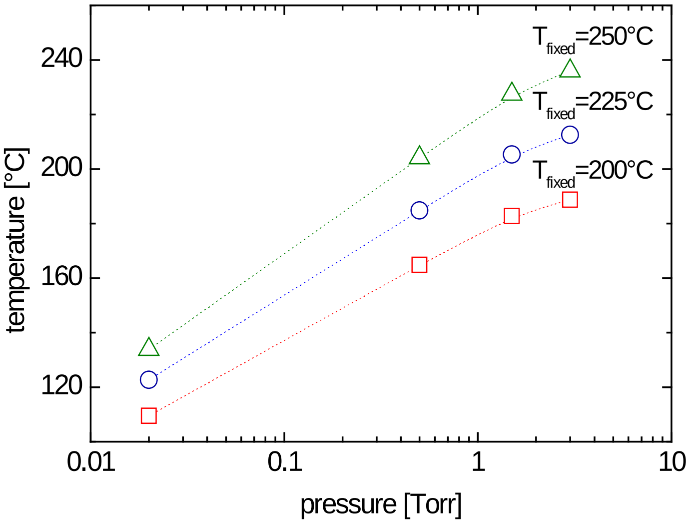

Figure 4.4. Mean temperatures measured on the sample tray as a function of the fixed pressure in a CVD reactor with a configuration similar to the one that is used in the MOCVD system. Three different heater temperatures have been tested (200°C, 225°C and 250°C).

4.2.3. Influence of deposition parameters

As inferred from the above-mentioned details regarding the MOCVD system, different deposition parameters can be independently controlled, thus leading to ZnO:B layers with diverse material properties. Within the scope of this work, the following parameters have been studied: diborane to DEZ gas flow ratio, water vapour to DEZ gas flow ratio, deposition time and heater temperature. The distance between the substrate and the gas inlet has also been varied between three different positions (large, small and short) and no significant changes have been obtained. Thus, the influence of this deposition parameter will not be further discussed.

ZnO:B films have been deposited on glass substrates (Corning Eagle XG) and n-type c-Si for characterising morphological, optical and electrical properties of the material. Process pressure in all sample series has been fixed at 0.4 T and the heater temperature has been set at 180°C, if otherwise not specified. Layer thickness has been determined by spectroscopic ellipsometry measurements. The optical transmittance, both total and diffuse (TT and DT, respectively), and reflectance (R) of the films have been measured using a spectrophotometer with an integrating sphere, in the visible and NIR wavelength range. The haze factor, which quantifies the light scattering capacity of the ZnO layers, has been defined as the DT/TT ratio measured at 1000 nm. Electrical resistivity, carrier concentration and mobility have been estimated at room temperature by Hall effect measurements and sheet resistance has been evaluated by using a four point probe. X-ray diffraction (XRD) measurements and transmission electron microscopy (TEM) cross-sections have been performed to characterize the crystallographic orientation and the microstructure of the ZnO layers. Finally, morphology of ZnO samples has been observed by scanning electron microscopy (SEM).

4.2.3.1. Diborane to DEZ gas flow ratio

In order to observe the effect of boron incorporation into the zinc oxide layers, a doping series has been deposited at 180°C. The doping level has been controlled increasing the diborane to DEZ gas flow ratio. The sample thickness has been fixed around 250 nm and other deposition parameters have been kept constant. In this case, the growth rate has not varied significantly with the introduction of B_2H_6.

Figure 4.5 shows the electrical properties of boron-doped ZnO layers as a function of the doping level B_2H_6/DEZ. As expected, the introduction of active boron atoms increases the free carrier density in the layers. The enhancement of the carrier concentration with B_2H_6 results from the extrinsic donors due to boron substitution at the Zn site and/or the boron interstitial in the ZnO lattice [168]. Accordingly, Hall mobility increases reaching a maximum at a doping level of 0.1. However, a degradation in μ is observed at higher ratios.

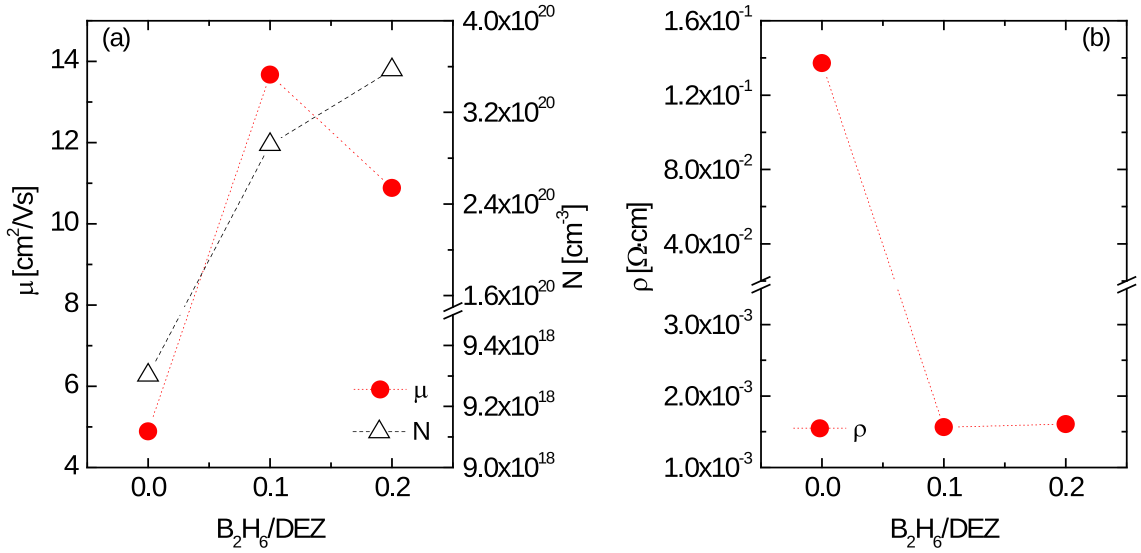

Figure 4.5. Electrical properties of ZnO:B layers deposited at different doping levels. Hall mobility, carrier concentration and resistivity are shown for a sample series deposited at 0.4 T.

SEM micrographs of undoped and doped ZnO layers presented in Figure 4.6, show that the surface grain size of ZnO:B films is reduced when the doping ratio is increased, augmenting in this way the density of grain boundaries in the material. Therefore, mobility degradation observed in Figure 4.5 can be attributed to increased grain boundary scattering events.

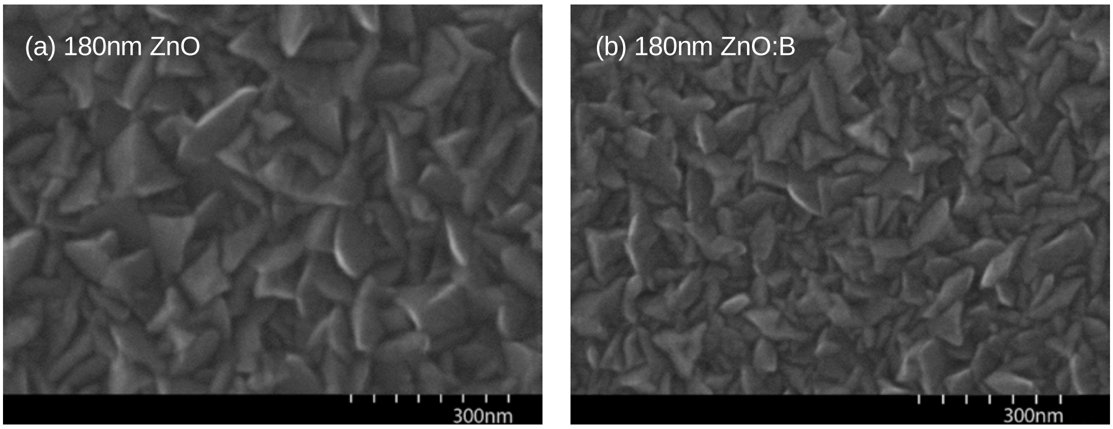

Figure 4.6. SEM surface micrographs of 180 nm-thick ZnO:B layers deposited at (a) B_2H_6/DEZ = 0 (undoped) and (b) B_2H_6/DEZ = 0.2.

However, the decrease in the average mobility can not only be influenced by the individual contribution at the grain boundaries, but also at the crystallites. Too much boron doping can increase the presence of ionised or neutral impurities within the ZnO, raising the deflection of electrons in grains. Despite this, it has been seen that carrier concentration of samples steadily increases in the studied B_2H_6/DEZ ratio range. Other works [35, 37] have reported a stabilisation of N values at higher diborane ratios, being attributed to the saturation of the active boron doping concentration into the layer. The additional introduction of boron atoms does not yield to a higher electronically active doping, but provokes a high level of defects that can degrade the doping efficiency.

For the doping range herein studied, this effect is not yet seen, which may suggest that mobility related to impurity scattering is not remarkably influencing overall mobility degradation. The increase in μ for very low doping levels (B_2H_6/DEZ < 0.1) as well as the boron-induced morphological changes in samples indicate that in this case, electron scattering by grain boundaries is the main limiting mechanism in μ. Thus, fine tuning of the dopant content within the layer is able to reduce the potential barrier height when impurities remain under a certain critical threshold [180].

In Figure 4.5(b) it can be seen that with the increase of the doping level, the resistivity is lowered by two orders of magnitude achieving a value around 1.5×10^{-3} Ωcm, which is low enough to enable ZnO:B to act as a TCO layer in HJ solar cells. This result indicates that boron ions have been successfully incorporated in ZnO films, which contributes to the decrease of the samples resistivity. However, a further increase of the doping does not yield a further decrease of the resistivity; beyond B_2H_6/DEZ = 0.1, ρ remains constant since variations in N and μ are compensated. Doping levels exceeding 0.2 have not been explored. Nonetheless, it should be expected that for higher doping contents resistivity increases again as a consequence of an impurity excess.

Total and diffuse transmittance measurements have been performed on this sample series and no significant change has been observed with increasing B_2H_6 flow rate. In Figure 4.7, no DT exists at the studied sample thickness, and a small drop of TT in the NIR wavelength range (λ > 1000 nm) is visible. Usually, this reduction of transmittance can be attributed to free carrier absorption, which becomes higher when the free carrier concentration increases due to raised doping ratio [160, 182]. Total transmittance in all samples stays over 80%.

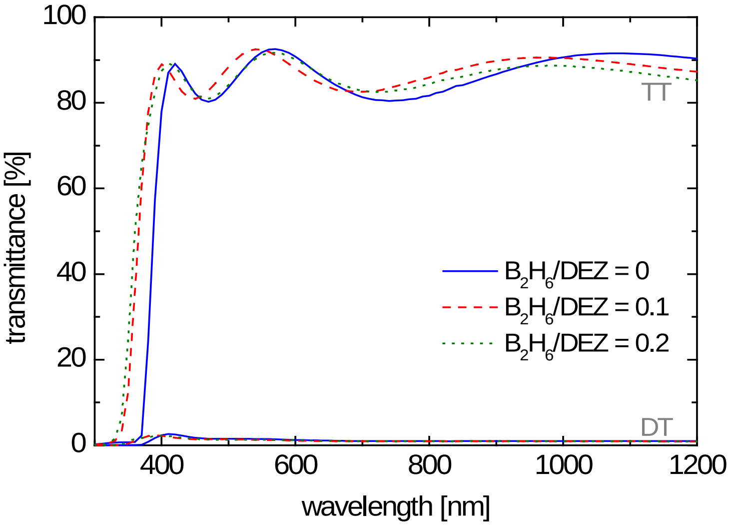

Figure 4.7. Total and diffuse transmittance for samples deposited on glass with different doping ratios.

For this series of samples, best electrical properties are found at a diborane to DEZ gas flow ratio equal to 0.1, where mobility is maximised, carrier concentration is enhanced and resistivity is lowered to the order of 10^{-3} Ωcm, which agrees with the state-of-the-art values for LPCVD films deposited at low temperatures.

4.2.3.2. Water vapour to DEZ gas flow ratio

The water introduced into the reaction enables the hydrolysis of DEZ. As reported in [175] the water to DEZ gas flow ratio influences the absorption of ZnO films. Moreover, it has been specified that the H_2O/DEZ ratio has to be kept higher than 1 to obtain layers with sufficient optical transparency.

Therefore, keeping the B_2H_6 and DEZ gas flows constant, H_2O flow rate has been increased. Thus, the H_2O/DEZ ratio has been varied from 0.125 to 1.5, to study their influence on film's properties. The doping ratio (B_2H_6/DEZ) has been set at 0.1, the optimised condition found in the preceding section. To minimize the influence of thickness variation on the properties of the ZnO:B films, the deposition time for all samples has been duly adjusted to obtain similar thicknesses around 250 nm. Deposition rate is found to decrease when increasing the quantity of water vapour introduced in the reactor, as observed in Figure 4.8.

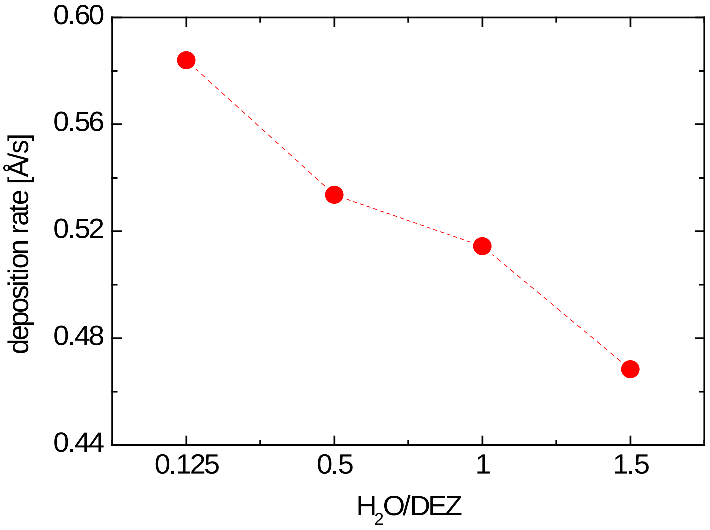

Figure 4.8. Growth rate in dependence of H_2O/DEZ gas flow ratio for LPCVD ZnO:B films deposited at 180°C and 0.4 T. All samples have a thickness around 250 nm.

The electrical properties of the ZnO:B films of this series are represented in Figure 4.9. Hall mobility and carrier concentration slightly decrease as the H_2O/DEZ ratio becomes higher. Consequently resistivity ρ increases. This behaviour might suggest that further increasing the quantity of H_2O do not improve the incorporation of effective doping within the ZnO:B layer, and therefore a little decrease in N is observed between H_2O/DEZ = 0.125 and 1. The raising quantity of hydrogen introduced within the layer could probably inhibit the doping effect of boron atoms. Besides, it might be also possible that higher H_2O/DEZ ratios lead to a modification of the zinc oxide morphology (i.e. grain size), thus reducing the carriers' mobility. Similar results have been obtained in [175] for H_2O/DEZ ratios higher than 1. However, no explanations about water-induced electrical changes are provided.

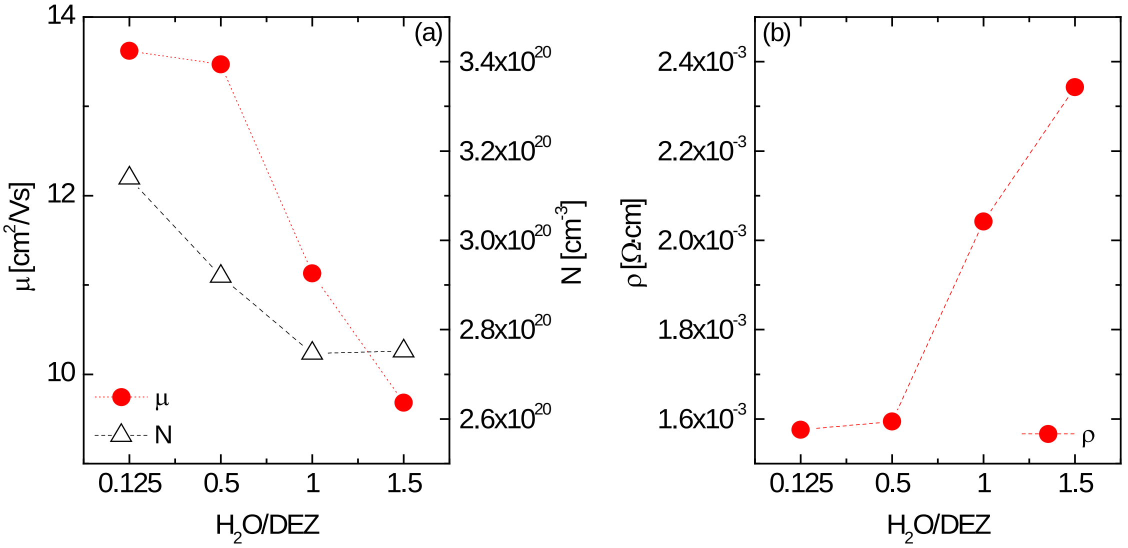

Figure 4.9 Variation of electrical properties as a function of H_2O/DEZ gas flow ratio: (a) Hall mobility and carrier density; (b) resistivity. In all samples, thickness and other deposition parameters have been kept constant.

For this sample series, best electrical properties are found at the lowest H_2O/DEZ ratio equal to 0.125. Nonetheless, it will be interesting to explore the properties of samples deposited at even lower ratios.

Total and diffuse transmittance measurements have been performed and no change has been observed with increasing H_2O flow, at the studied sample thickness. Contrary to [175], enhanced ZnO:B layers have been deposited here using an excess of DEZ compared to H_2O, which in our case has lead to TCO layers with sufficient optical quality to be used in HJ solar cells. Therefore, in the light of the better results obtained at lower ratios (Figure 4.9), it would be interesting to explore the properties of samples deposited at even lower ratios in order to verify if such degradation of the optical transparency is found under the deposition parameters herein used. Moreover, further experiments should be done in order to find other high-quality ZnO:B deposition conditions with less consumption of DEZ, which would be beneficial from an industrialisation point of view.

4.2.3.3. Increasing thickness

Optimised boron-doped zinc oxide layers have been grown, increasing the deposition time (t_{dep}). Consequently, the thickness of the samples has been modified according to Figure 4.10. The film growth is almost linearly dependent on t_{dep}, although somewhere below 600 nm a slight exponential increase of the thickness is observed. In agreement with [175, 180] an incubation phase during the growth of the first hundreds of nanometres takes place. At this stage nuclei are formed on the substrate, giving rise to an initial layer with small crystallites that will later continue its growth forming columnar grains that will extend up to the surface of the ZnO:B film.

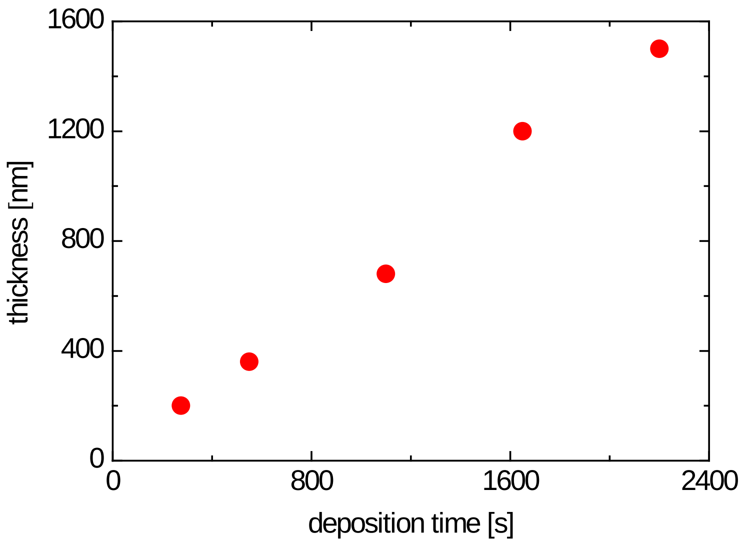

Figure 4.10. Thickness variation of ZnO:B layers as a function of LPCVD deposition time. Other deposition parameters have been set constant.

SEM micrographs of the cross-section of some of the ZnO:B samples having different thicknesses, as well as their respective XRD patterns are shown in Figure 4.11. The upper ends of the columnar grains appear at the zinc oxide surface as pyramids. For the studied thickness range, SEM images show that the grain size slightly increases with the film thickness, hence the as-deposited rough ZnO surface grown by LPCVD, which may efficiently scatter the light that enters into the solar cell. However, as will be seen hereinafter, thicker layers (> 1μm) are needed to profit from this light-scattering capacity. In [175] 2 μm-thick ZnO films result in pyramids with a basis size of almost 400 nm.

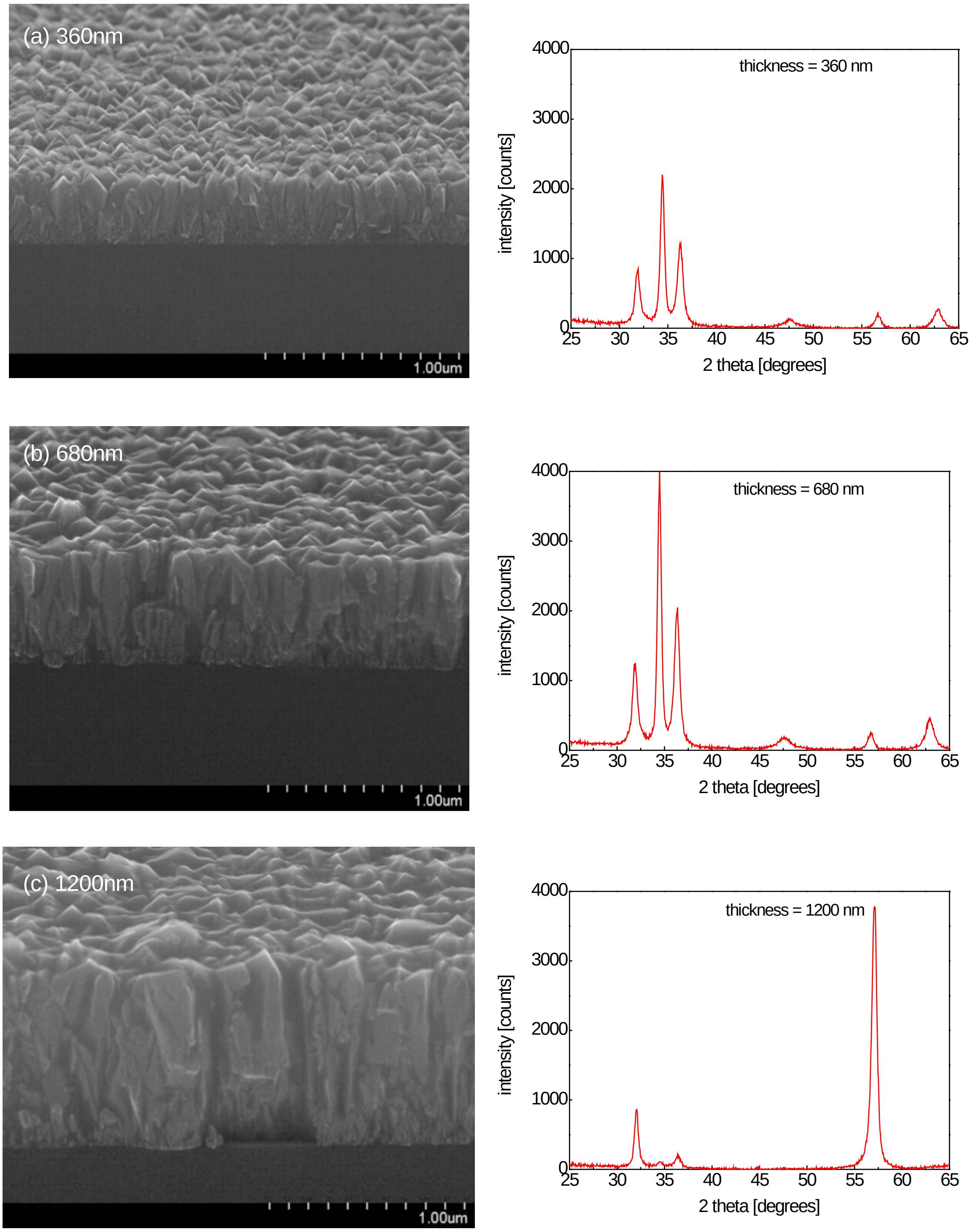

Figure 4.11. SEM micrographs of a cross-section of various ZnO:B layers with different thicknesses. X-Ray diffraction of the same layers is also shown.

The zinc oxide layers at 360 nm and 680 nm of thickness are mainly oriented along three directions perpendicular to the $(10\bar{1}0)$, (0002) and $(10\bar{1}1)$ crystallographic planes. In these cases, polycrystalline ZnO:B structure has no preferential growth orientation.

However, at a thickness of 1.2 µm, the grains start to be preferentially oriented along a single crystallographic direction, which is perpendicular to the $(11\bar{2}0)$ planes. This suggests that the growth of zinc oxide is done with the c-axis, parallel to the substrate, and a pyramidal texture growth surface can be formed. This preferential orientation is typical for rough ZnO:B films growth by LPCVD [172, 183].

The TT and DT of the samples are presented in Figure 4.12(a). As it can be observed, the total transmittance stays over 80% in the range of 400-1200 nm for samples with a layer thickness below 1.2 µm. Besides, diffuse transmittance is slightly enhanced as the thickness is increased. Only thin layers with thicknesses below 680 nm posses a DT almost equal to 0, indicating that no scattering of the light is possible. This is also reflected by the haze factor presented in Figure 4.12(b), which increases for the thicker layers mainly in the visible range of the spectra, since beyond 700 nm DT is almost unvaried.

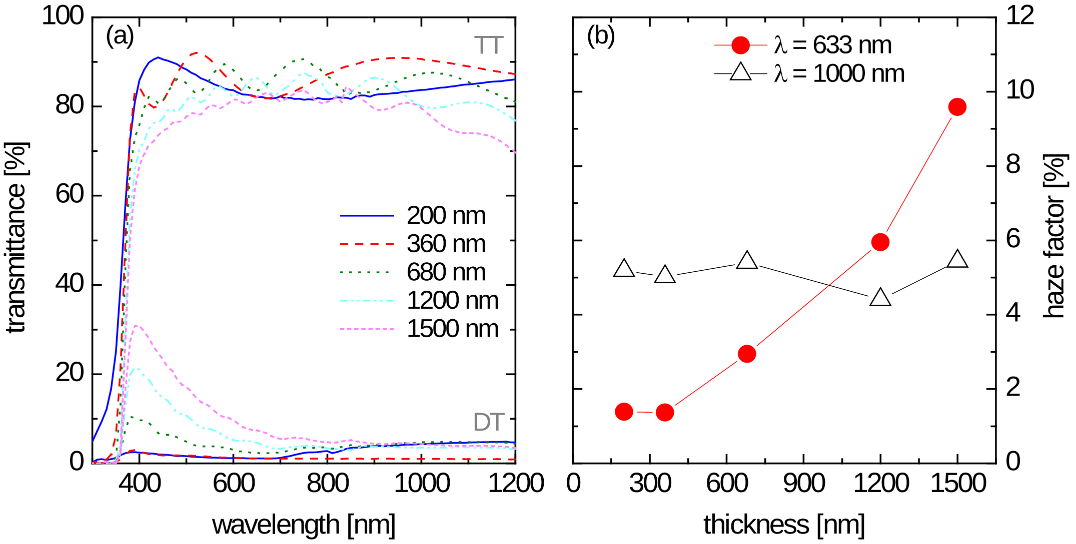

Figure 4.12. (a) Total and diffuse transmittance of ZnO:B in function of the film thickness. (b) Haze factor values in function of the thickness of ZnO:B deposited under the same conditions.

Higher light-scattering capacity is due to rougher ZnO surfaces as a consequence of an increase in the pyramidal grain size of the material with the thickness of the layer. Compared to [173] the studied samples are not thick enough to effectively diffuse the light. Furthermore, light-scattering ZnO:B layers (th > 1.5 µm) will hardly be considered a feasible option to be implemented in our HJ solar cells due to economic and production time constraints.

With regards to the variation in the electrical properties with the film thickness, Figure 4.13 shows the Hall measurement of the obtained films. Both mobility and carrier concentration, increase with film thickness. However, Hall mobility begins to decrease after reaching a maximum of 22 $cm^2V^{-1}s^{-1}$ with a relatively high carrier concentration of 3.8×10^{20} cm^{-3}. The increase in mobility can be attributed to the larger grain size, which reduces the contribution of electron scattering induced by grain boundaries. The decrease in mobility at higher carrier concentrations highlights the role of impurity scattering. The net effect is a decrease of the film resistivity, determined both by N and μ.

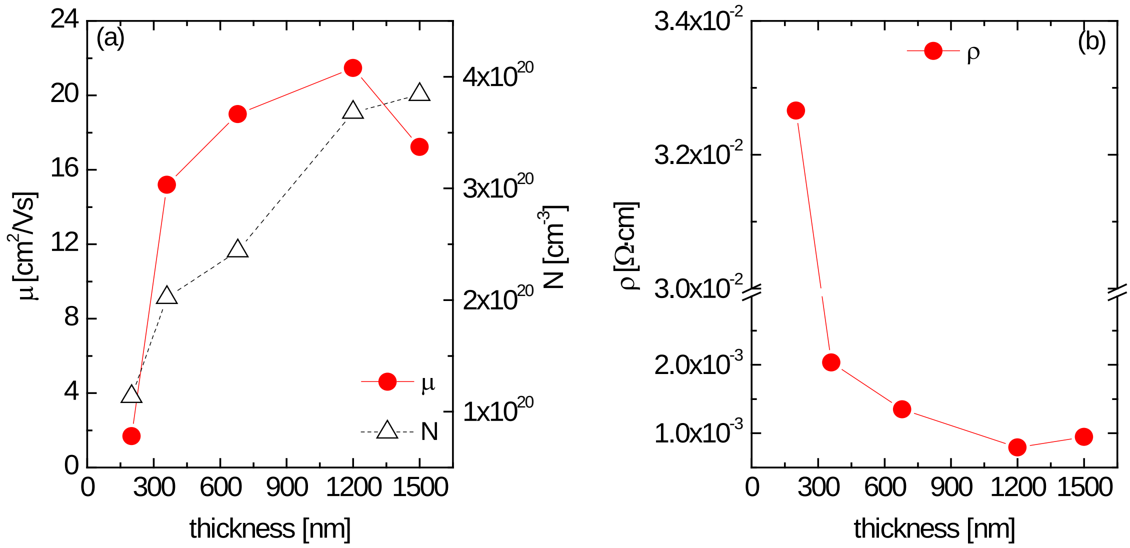

Figure 4.13. (a) Mobility μ, and carrier concentration N, and (b) resistivity ρ for boron-doped ZnO layers in dependence on their thickness.

The influence of the ZnO:B layer thickness has been tested on solar cells. Then, complete HJ devices have been fabricated, where only the deposition time during ZnO:B processing has been varied. Output solar cell parameters obtained for thicknesses ranging from 40 nm to 1.5 µm are shown in Figure 4.14.

The short-circuit current density and FF tend to lower as the TCO thickness is increased. However, no clear correlation with overall device R_S has been found. Indeed, a decrease of the film resistivity is obtained for thicker layers as it has been shown in Figure 4.13. Analysing Suns-V_{OC} measurements, constant pFF values have been obtained (Figure 4.14(c)). Therefore, J_{SC} and FF decreasing trend might be attributed to an increase in charge carrier recombination in thicker layers.

As presented in Figure 4.13, both mobility and carrier concentration increase with film thickness. However, mobility begins to decrease in ZnO:B layers with relatively high carrier concentration. Interestingly, a similar trend is obtained in V_{OC} results. Regarding conversion efficiency, a maximum value has been determined at 340 nm of ZnO:B layer, indicating that a good compromise between films resistance and device recombination mechanisms is obtained.

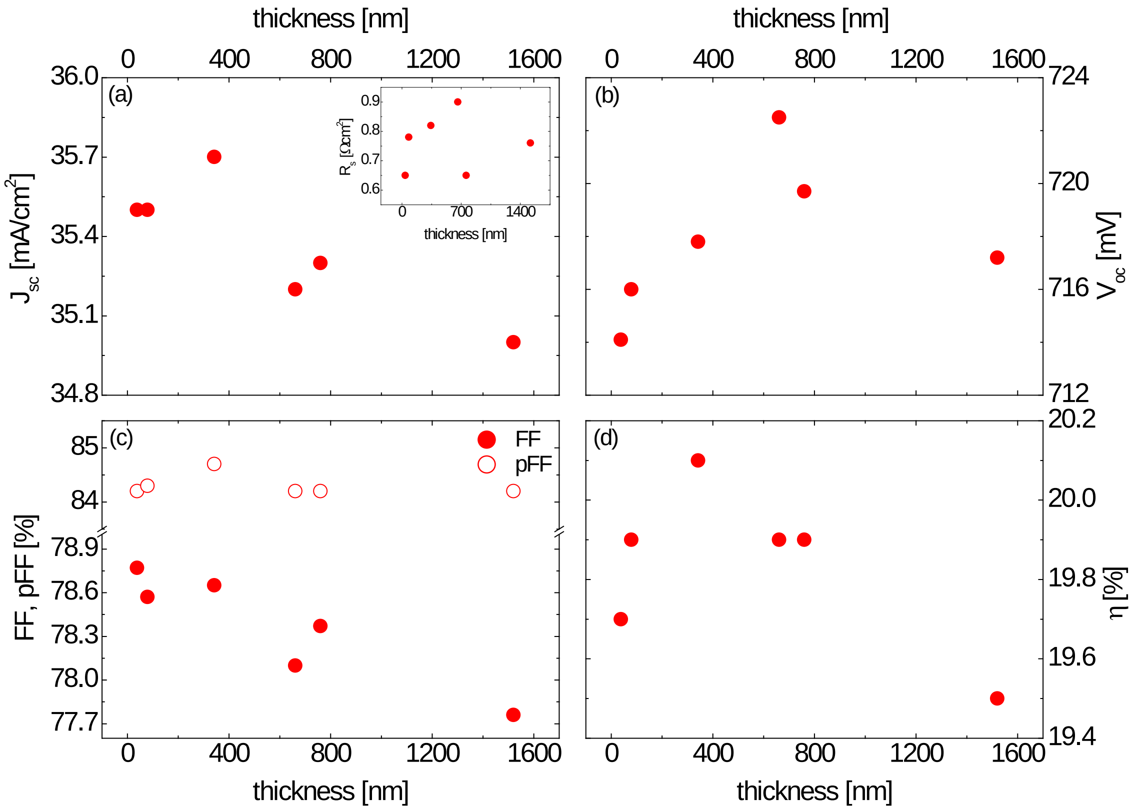

Figure 4.14. Solar cell characteristics with varying ZnO:B layer thickness. Open symbols in figure (c) correspond to pseudo-FF values determined from Suns-V_{OC} measurements. Each data point represents the average value of three cells.

4.2.3.4. Heater temperature variation

Temperature is one of the most sensitive parameters in ZnO:B grown by LPCVD. It has been reported that higher temperatures improve the overall crystal structure enhancing the electron mobility [172, 183]. However, considering the use of these ZnO layers into HJ devices, high temperatures are restricted, since a-Si:H layers are detrimentally affected.

Then, in this section the properties of ZnO:B films deposited at heater temperatures ranging from 120°C to 200°C are studied. Other deposition parameters have been kept constant and deposition time has been duly adjusted in order to obtain layer thicknesses around 250 nm.

It has been found that the films growth rate is strongly influenced by the temperature used during the deposition. At higher temperatures more thermal energy is available, and therefore chemical reactions taking place at the growth surface are boosted [172]. In Figure 4.15, it is shown how the deposition rate increases with the temperature.

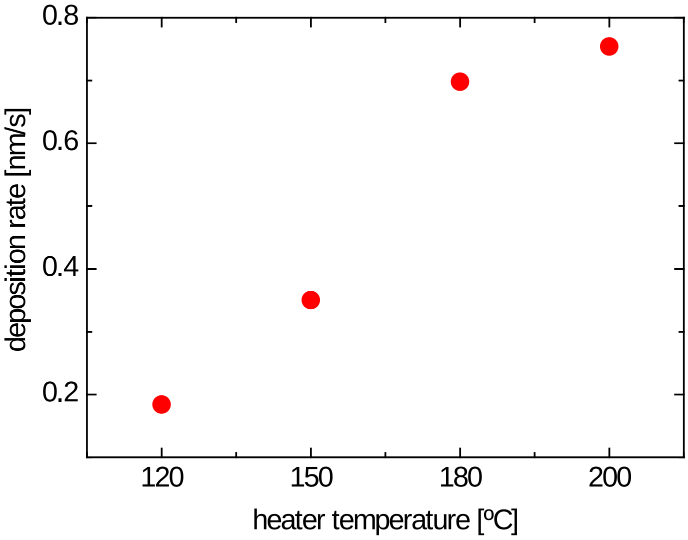

Figure 4.15. Deposition rate of ZnO:B as a function of the heater temperature.

As mentioned before, the crystalline structure of the film also depends on the deposition temperature. Thus, the surface roughness and the electrical properties are affected when changing the temperature. Total transmittance measurements have not shown any significant temperature dependence. Being the thickness of deposited samples not thick enough to see any light-scattering effect, the analysis of the diffuse transmittance has been dismissed in this study.

The electrical properties of boron-doped ZnO layers as a function of substrate temperature are shown in Figure 4.16. It is clear that mobility and carrier concentration are strongly dependent on the heater temperature. An increase in both parameters is observed, especially up to 180°C. Accordingly, resistivity is rapidly decreased from 3.96×10^{-1} to 7.51×10^{-3} Ωcm when the heater temperature is raised from 120°C to 150°C. Afterwards, resistivity tends to be constant at higher temperatures.

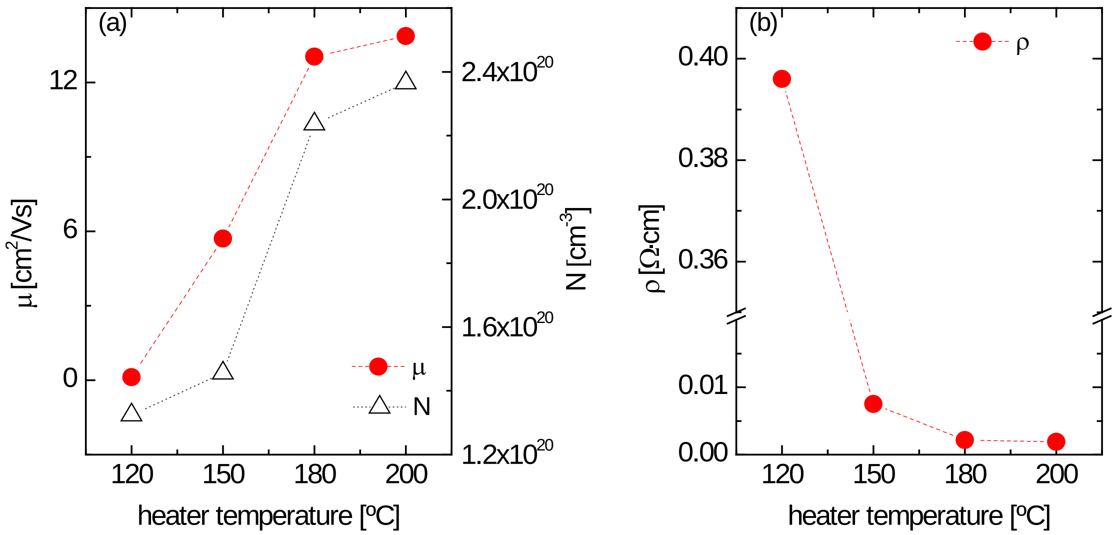

Figure 4.16. Electrical properties of boron-doped ZnO as a function of substrate temperature. Mobility, carrier concentration and resistivity are given.

This behaviour might be related to the change of the crystal orientation or grain structure. Thus, the microstructure and morphological characteristics of the studied films have been evaluated. SEM micrographs of films are shown in Figure 4.17, together with their corresponding XRD spectra. As observed, the average grain size tends to become larger with increasing substrate temperature (there is a clear transition between 120°C and 150°C). At 120°C the surface morphology of the film is characterised by granular crystallites. This sample has pronounced preferential orientation along the (0002) direction, suggesting that the grains have a c-axis perpendicular to the substrate surface. Increasing the temperature to 150°C, the film shows a textured morphology. Here, the $(10\bar{1}0)$ and $(11\bar{2}0)$ reflection peaks are dominant, as it has been observed with quite thicker ZnO:B layers deposited at higher pressures [183]. This is in contradiction with what is shown in [172], where only a single XRD peak corresponding to the $(11\bar{2}0)$ crystallographic planes significantly appears. These observed discrepancies could be attributed to the different thickness of the studied layers and also to the fact that in this work there are not the adapted means to measure the real temperature at the substrate tray during deposition. Therefore, the temperature uncertainty makes difficult the results comparison. Further increasing the temperature does not show clear differences in the main growth directions, although a $(10\bar{1}1)$ peak appears with slight intensity in the samples at 180°C and 200°C. Here, the surface morphology remains stable.

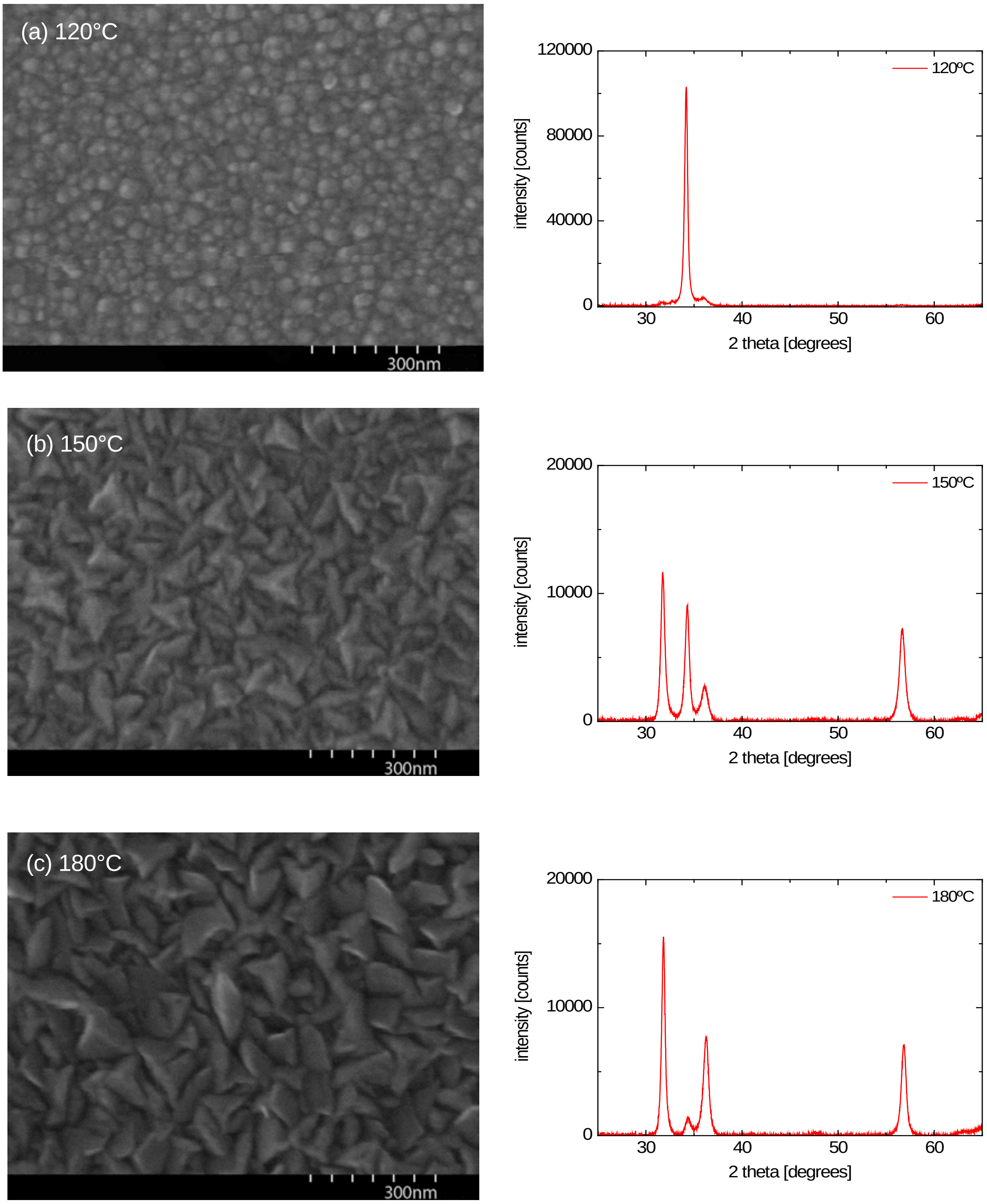
(a) 120°C
300nm
120000
80000
40000
0
intensity [counts]
30
40
50
60
2 theta [degrees]
120ºC
(b) 150°C
300nm
20000
10000
0
intensity [counts]
30
40
50
60
2 theta [degrees]
150ºC
(c) 180°C
300nm
20000
10000
0
intensity [counts]
30
40
50
60
2 theta [degrees]
180ºC

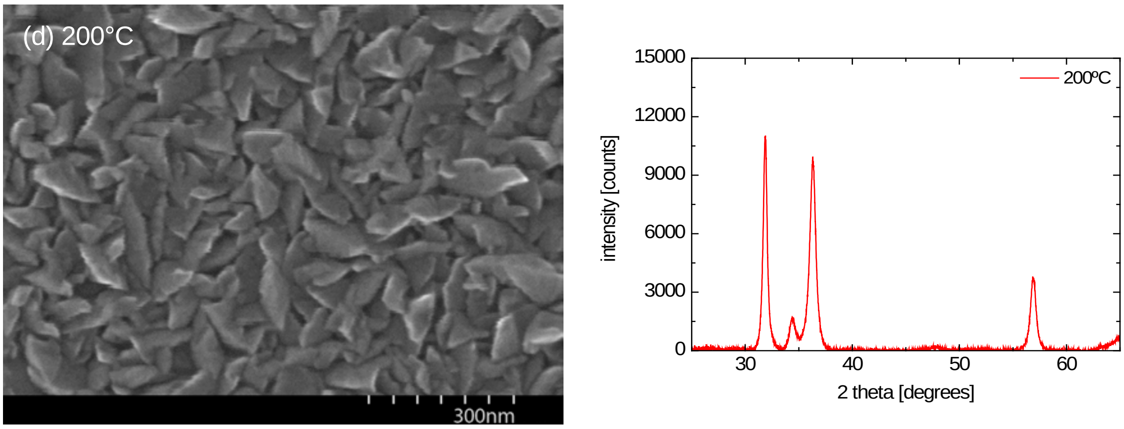

Figure 4.17. Surface morphology of the ZnO:B films deposited with various heater temperature: (a) 120°C, (b) 150°C, (c) 180°C and (d) 200°C. Corresponding XRD patterns are also shown.

The root mean square values of the roughness (S_{rms}) of the ZnO:B layers surface as determined by AFM images are shown in Figure 4.18. S_{rms} increases with the temperature, reinforcing what has already been observed through the SEM images: with increasing temperature, the crystallites gradually become a bit larger and the height of pyramids emerging out of the surface are slightly higher.

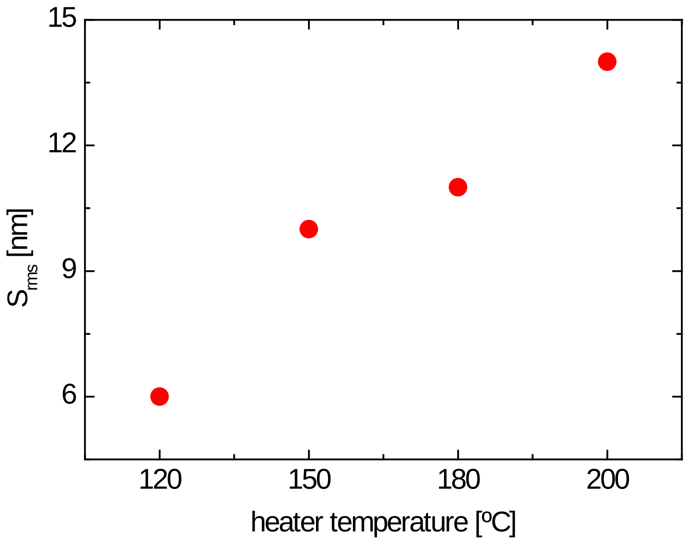

Figure 4.18. Surface roughness of ZnO:B layers in function of the heater temperature used during their deposition.

The same temperature study has been performed on samples with equal thicknesses deposited at a lower distance to the gas-inlet. Again, a complete electrical, structural and morphological analysis has been conducted. The same tendencies as detailed above have been obtained. However, at this shorter distance, the 200°C deposition has lead to a non-uniform sample with R_{sq} ranging from 50 to 160 Ω/sq on the same sample. This suggests that chemical reactions have not taken place under suitable conditions.

4.3. Post-H-plasma treatment

Post-hydrogen-plasma treatments are found to be beneficial for the enhancement of the electrical and optical properties of ZnO films. Some works [184-187] have reported on this effect, showing that both carrier concentration and mobility are increased after hydrogen plasma treatment, and therefore, resistivity of films is decreased.

Here, the influence of a post-H-plasma treatment has been analysed on ZnO samples with different thicknesses (80 nm and 250 nm) and doping levels (undoped and B_2H_6/DEZ = 0.1). The reason for testing the post-H-plasma treatment on undoped samples accounts for an attempt to enhance the insufficient electrical conductivity on such highly transparent ZnO films where no doping has been introduced. Likewise, the H-plasma has been applied to thinner samples in order to improve the electrical properties on these cost-effective layers deposited through a more rapid process where less material consumption takes place.

To this end, the following process parameters have been explored: (i) pressure (from 0.5 T to 1 T), (ii) RF power (between 250 W and 500 W), (iii) distance between samples and gas inlet, and (iv) plasma duration. However, for most of the conditions tested no significant differences, except for the duration series, have been found. Therefore, in the following only the results on plasma duration will be presented.

During the plasma treatment time evaluation, the pressure and RF power were kept at 1 T and 300 W, respectively, and the heater temperature was maintained at 180°C. A H_2 flow rate of 2000 sccm was introduced into the chamber immediately after the ZnO film deposition. The treatment time was varied up to 180 seconds in order to assess the effect of the hydrogenation process duration on samples. Sheet resistance measurements before and after the H-plasma exposure are shown in Figure 4.19.

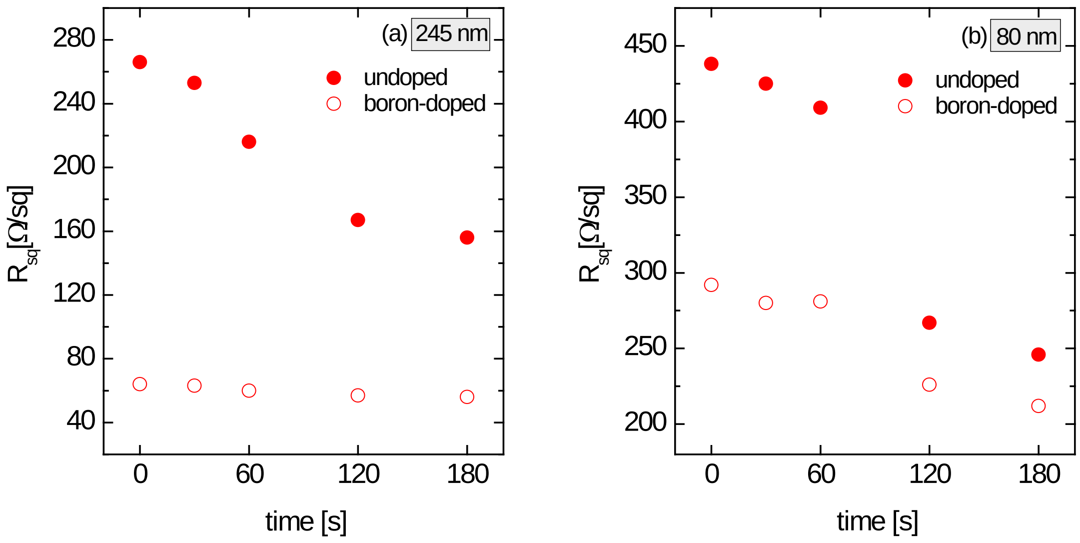

Figure 4.19. Variation in the sheet resistance (R_{sq}) as a function of post-H-plasma exposure time on undoped and boron-doped samples deposited at (a) 245 nm and (b) 80 nm of thickness. Non-treated samples results are given at a plasma exposure time equals to zero.

As clearly seen, the H-plasma exposure has a more pronounced effect in the more resistive samples, i.e. the undoped ZnO layers, where the R_{sq} is further reduced as the treatment duration increases. Thus, in the 80nm-thick samples, the R_{sq} of undoped ZnO layers is reduced by 190 Ω/sq when 180 seconds plasma is applied, whereas ZnO:B R_{sq} decreases by 80 Ω/sq under the same plasma conditions. The same behaviour is observed on thicker samples. However, in this case the R_{sq} of boron-doped samples remains unchanged irrespective of the exposure time, since the as-deposited resistivity of films is quite low to be further enhanced by a post-H-plasma exposure. On thinner samples, the sheet resistance of undoped layers is reduced below values corresponding to non-treated boron-doped films.

According to [188], this surface treatment allows the incorporation of hydrogen into the layer, which not only passivates most of the defects in the material, but also introduces interstitial hydrogen. For this reason electrical properties are enhanced, since as being proposed recently [189], hydrogen itself also plays the role of a shallow donor, increasing the carrier concentration and being the origin of the n-type conductivity of undoped ZnO. Therefore, the effect of hydrogen plasma is more evident and pronounced on the non-doped layers, than on boron-doped ones.

Based on these results, a post-hydrogen-plasma will be applied by default immediately after each ZnO deposition, since in any case this post-treatment will have a more or less pronounced positive effect. Depending on the ZnO layer to be deposited, the plasma exposure time will be duly adjusted to maximise its benefits on the electrical properties of the film. Thus, for the optimised process conditions of 250 nm-thick boron-doped ZnO layers, which have been obtained at a doping ratio of 0.1, 60 seconds of H-plasma will be enough to ensure enhanced film resistivity.

4.4. Stability analysis under atmosphere exposure

Polycrystalline ZnO layers are known to have unstable electrical properties in the long term, due to increased potential barriers induced by oxygen chemisorption at the grain boundaries [174]. Several research groups have discussed on humidity-induced degradation of zinc oxide electrical properties [190-192] for various deposition methods. For this reason stability behaviour of our LPCVD ZnO:B layers under atmosphere exposure at room temperature has been analysed [193], as these can strongly affect the performance of HJ solar cells.

Polycrystalline ZnO layers are known to have unstable electrical properties in the long term, regardless of the deposition method [174]. Several research groups have discussed on this effect, which is magnified when ZnO is exposed to damp heat atmospheres [190-192]. The absorption of water vapour at the grain boundaries (oxygen and hydrogen chemisorption) points to the most probable reason of the electrical properties degradation, since an increase of potential barriers is induced. The direct consequence of this phenomenon is that, for use in PV modules, specially designed encapsulation must be provided to protect the ZnO films in solar modules.

Aware of the strong impact that the degradation of ZnO can have in HJ solar cells performance, the stability behaviour of our LPCVD ZnO:B layers under atmosphere exposure and at room temperature has been analysed [193]. Indeed, a degradation of the electrical properties has been revealed even at no harsh conditions. Figure 4.20 shows the evolution of the relative variation of sheet resistance for various thicknesses of boron-doped and undoped ZnO layers depending on the elapsed time. As it can be seen, an increase in R_{sq} for all films tested has been found, although an abrupt deterioration especially on both thinner samples and undoped samples is evidenced.

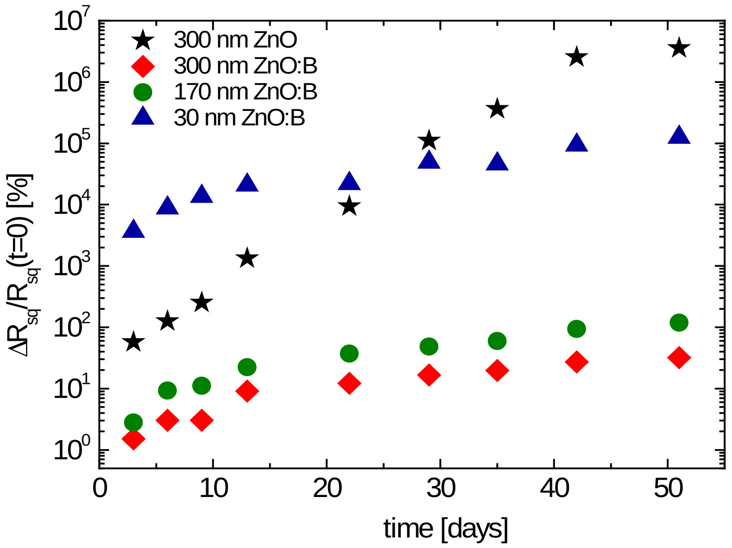

Figure 4.20. Relative variation in R_{sq} within time under ambient air exposure. Three different ZnO:B thicknesses and undoped ZnO samples are shown. The gas phase doping ratio ([B_2H_6/DEZ]) used during the ZnO deposition is equal to 0.1, except for undoped sample.

The sample without B_2H_6 is more sensitive to degradation, whereas doped layers show a smaller increase of the relative variation in R_{sq} within time. Similar observations have been published for thicker layers of ZnO:Al [194] and ZnO:H [195] stored in ambient air conditions and in a humid air atmosphere, respectively. In [190] the resistivity as a function of damp heat exposure for 2 µm ZnO:B shows that increasing the doping level in LPCVD films strongly enhances the stability against humid environment.

With regard to stability behaviour at different layer thickness, the 30 nm sample is extremely affected during the first three days increasing its resistivity by a factor up to 1000. Contrary to this, the electrical properties become more stable as thicker ZnO:B films are deposited, being even unchanged on 1000 nm-thick samples (consequently, results are not shown in Figure 4.20).

Ellipsometry measurements performed on samples show that all films are optically stable and no increase in roughness or oxide on the surface has been detected during this time. Additionally, X-ray photoelectron spectroscopy (XPS) analysis on 200 nm-thick ZnO:B prepared with the same conditions used for the samples shown in Figure 4.20 have been performed over eleven weeks. Zn/O signal ratio has been evaluated and no significant variation in composition has been found. Therefore, these results discard any surface oxidation, which might also be the reason of conductivity degradation due to a decreased number of oxygen vacancies on the surface of the material. On the contrary, these results strengthen the assumption that degradation phenomena take place at the grain boundaries of LPCVD ZnO:B, and arise from the fact that H atoms naturally present in the ZnO lattice (water vapour is used during LPCVD) diffuse towards grain boundaries, modifying this way the potential barriers.

Then, stability differences between samples with and without boron-doping can be attributed to an increase in trap states at the grain boundaries due to the interaction with in-diffused hydrogen. However, as doping is introduced on ZnO grains, this effect is restrained since the width and height of grain boundary potential barriers diminish [190, 195]. Thus, transport tunnelling mechanisms through potential barriers are boosted, resulting in more stable films. On the other hand, the stability enhancement observed on thicker films can be ascribed to a subsequent increase in grain size and thus, a reduction on grain boundaries as well (see section 4.2.3.3). Hence, the effect of grain boundary scattering is decreased and the capture of free carriers is lessened. For this reason, stability of electrical properties over time are more favourable on thicker ZnO:B layers.

To date, such unstable behaviour of relatively thin ZnO films at ambient conditions has not been reported. Although ZnO has been extensively developed for thin film silicon photovoltaics, its use applied to HJ solar cells is still innovative and not very well known. In order to comprehensively study the effects of electrical degradation of ZnO:B on a-Si:H/c-Si solar cells, 5×5 cm^2 devices with various front and back side configurations have been fabricated on double-side polished FZ n-type c-Si (⟨100⟩, 1-5 Ωcm). Metal grid electrodes on both sides of solar cells have been used when necessary to allow the contact of TCOs with the atmosphere. Details of the six different proposed heterostructures are given in Table 4.1.

Table 4.1. HJ solar cell configurations used in the analysis of ZnO:B stability over time on final device.

sample	FS TCO	thickness (nm)	BS TCO	thickness (nm)	BS electrode
ITO-ITO/grid	ITO	85	ITO	85	Ag grid
ITO-ZnO/grid	ITO	85	ZnO:B	300	Ag grid
ZnO-ZnO/grid	ZnO:B	1000	ZnO:B	300	Ag grid
ITO-ZnO/Al	ITO	85	ZnO:B	300	Al
ITO-ZnO/Ag	ITO	85	ZnO:B	300	Ag
ITO-ZnO/ITO/grid	ITO	85	ZnO:B + ITO	300 + 50	Ag grid

In Figure 4.21, the evolution of solar cells parameters within time can be seen for three devices with screen-printed grid electrodes on both sides. As it can be noticed, ZnO:B plays a clear role on solar cell degradation. Devices with ZnO:B on the back side present a gradual decrease of their conversion efficiency, down to 90% of the relative value after one month. Besides, the device with ZnO:B on both sides shows a higher drop on FF of up to 6%. On the contrary, the cell with ITO at the back side (HJ-ITO) is almost constant on its photovoltaic parameters and no significant change with respect to the uncertainty range of solar cell efficiency measurement is shown.

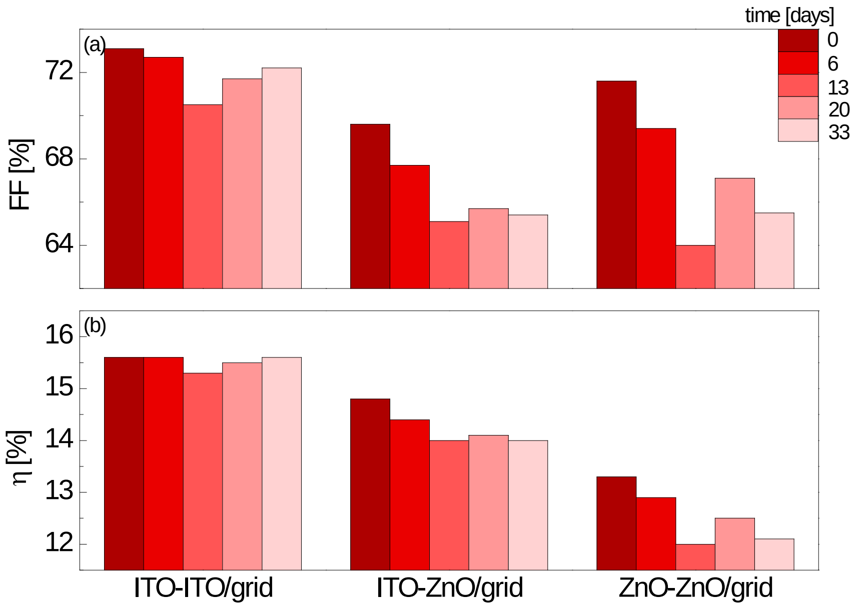

Figure 4.21. Evolution of fill factor (a) and efficiency (b) within time for various HJ solar cell configurations. Both front and back side TCOs are in contact with air.

It is important to remark that V_{OC} and J_{SC} were stable in any of the tested devices. Thus, changes on conversion efficiency are directly governed by FF variation. As it is well known, the FF is mainly limited by parallel (R_P) and series (R_S) resistance. Having all devices very high R_P values, variations in FF can be mainly attributed to R_S. Figure 4.22 shows the good correlation between calculated series resistance values as per [155] and experimental FF results. Consequently, it can be stated that electrical degradation of the ZnO:B directly damages the cells' series resistance and consequently fill factor and efficiency too.

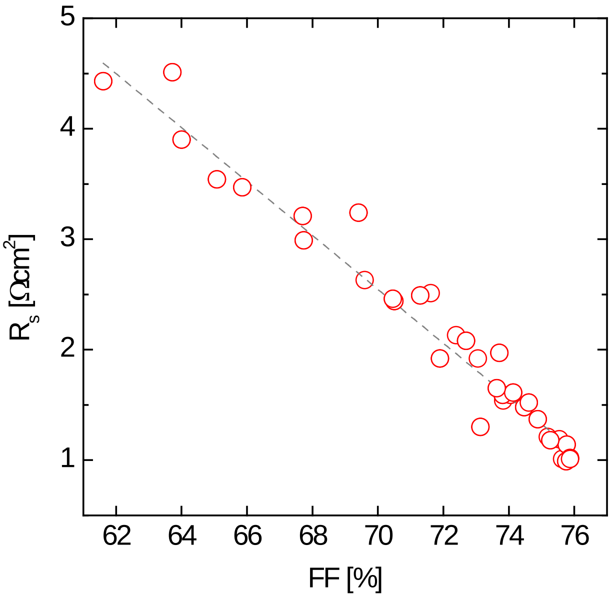

Figure 4.22. Correlation between series resistance and fill factor of solar cells under study measured within time.

A comparison analysis to further explore the ZnO:B induced degradation on solar cells has been conducted. Here, the ZnO:B used as a rear TCO has been shielded using 500nm full sheet aluminium or silver layer deposited by DC-magnetron sputtering and e-beam evaporation, respectively. Besides, a third configuration with 50 nm-thick ITO capping on ZnO:B layers has been tested. Results presented in Figure 4.23 show that all samples are found to be stable in time, contrary to what has been observed in Figure 4.20, where R_{sq} of ZnO:B layers degraded within time.

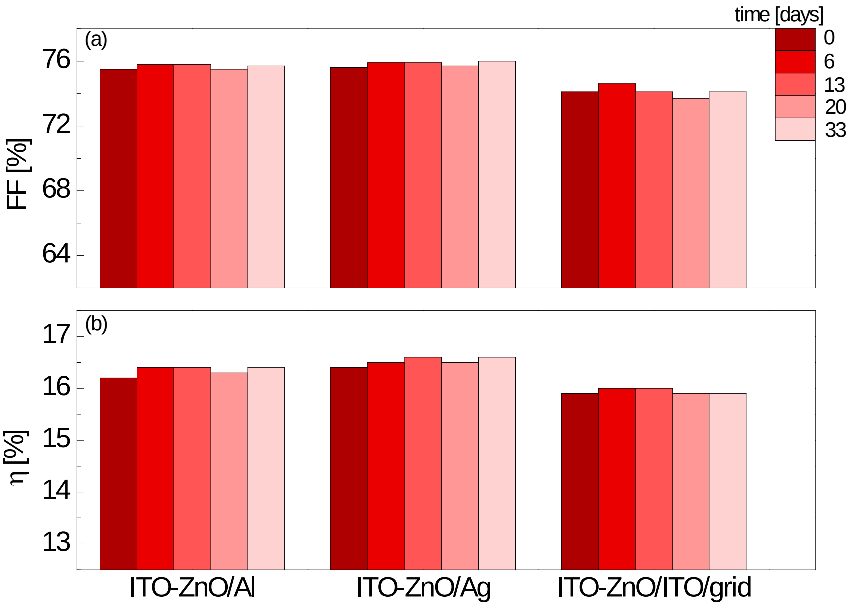

Figure 4.23. Evolution of fill factor (a) and efficiency (b) within time for various HJ solar cell configurations. Back side ZnO:B layers are capped and protected from atmosphere exposure.

To deeply understand ZnO:B conduction and degradation mechanisms on cell performance, a full sheet aluminium layer was deposited on the back side of designated “ITO-ZnO/grid” device after 4 weeks under air exposure. Surprisingly, device FF was found to recover up to its initial value, which suggests that vertical conduction is not affected by the degradation of the ZnO:B layer. Then, mechanisms inducing the degradation of ZnO films mainly affect the lateral conduction, which is consistent with the increase of the potential barrier and grain boundary scattering events on the ZnO polycrystalline structure due to intrinsic hydrogen in-diffusion. When the rear side ZnO:B is covered by a full size metal electrode, only vertical conduction on the charge collection is needed. In this case, performance of solar cells is kept stable within time.

In the light of these results, it can be concluded that our zinc oxide layers are suited to be applied at the back side of the solar cells only when a full sheet metallisation layer is afterwards deposited. By doing so, the lateral conduction on ZnO layers will not be required and only the vertical conduction on the material will be favoured. By contrast, ZnO layers will not be able to be used on a bifacial configuration or at the front side of the solar cell, since in this case a device performance degradation due to the intrinsic instability of the ZnO takes place.

4.5. Laser annealed ZnO: a novel approach for high-efficiency cost-effective HJ solar cells

Throughout preceding sections, boron-doped ZnO films have been developed, and enhanced electrical and optical properties comparable to that of ITO thin films have been obtained [171, 193, 196-198]. However, a problem of non-electrical stability of ZnO films has been revealed, resulting in the inadequacy to use these layers on a bifacial configuration or simply on the heterojunction font side TCO. Therefore, there is still significant room to improve on ZnO optoelectronic performance and stability from as-deposited material state in order to further enhance the solar cell efficiency and extend the use of zinc oxide on the heterojunction device even without being protected with a full sheet metallisation layer.

Among approaches to improve the TCOs performance and stability, thermal annealing treatments by laser processing appear to be advantageous when locally re-crystallising the TCO and thus enhancing the electrical and optical film properties [199]. For this reason attention has been put at investigating the effect of pulsed XeCl excimer laser annealing (ELA) at 308nm ($\tau = 150$ ns) on our LPCVD ZnO thin films. ZnO deposition conditions have been adjusted to prepare samples with various thicknesses (80 nm and 180 nm) and boron doping levels (B_2H_6/DEZ = 0 and 0.1), since from a cost-effective point of view, thinner samples appear to be more advisable for an industrialisation process and undoped layers are also advantageous from an optical approach as they exhibit higher transparency than doped material.

Zinc oxide layers have been grown on c-Si and subsequent laser treatment has been applied to them. Samples have been annealed varying the laser fluence from 0 to 2 J/cm^2 in order to identify different effects of the laser annealing depending on the as-deposited conditions of the ZnO films. Special attention has been paid to study the ZnO stability under ambient exposure after laser treatment.

Four point probe measurements have been used to characterise the material before and after the laser processing, as well as spectroscopic ellipsometry measurements. Spectrophotometer measurements have not been performed due to ZnO adherence problems on Corning glass arisen after laser annealing. The evaluation of the optical properties will be done analysing the changes induced on the refractive index (n) and the extinction coefficient (k) determined from ellipsometry measurements. The haze factor has not been evaluated since results obtained in section 4.2.3.3 indicate that no significant changes will be seen considering the thicknesses of the studied ZnO layers.

Results presented in Figure 4.24 show the variation of spectroscopic ellipsometry parameters and sheet resistivity (R_{sq}) of 180 nm-thick boron-doped ZnO layers irradiated at different laser energy densities. The point at 0 mJ/cm^2 corresponds to the reference ZnO without any thermal annealing. As can be observed in the graph, no variation on the sheet resistance occurs after the laser annealing. Only beyond 1000 mJ/cm^2 a detrimental effect on the film properties is observed, where the layer R_{sq} is increased. Besides, as clearly seen on the ε_2 plot, the microstructure of the material is modified depending on the energy density applied to the film.

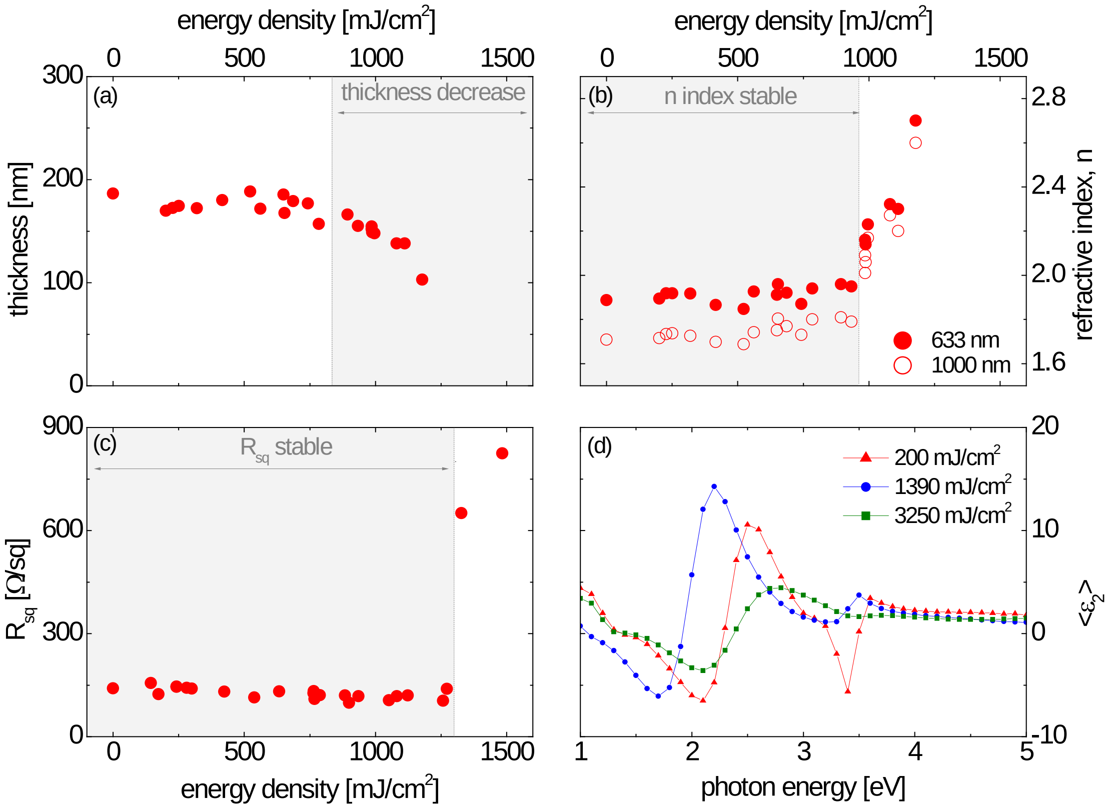

Figure 4.24. Spectroscopic ellipsometry parameters and sheet resistivity of 180 nm-thick boron-doped ZnO layers as a function of the energy density applied during laser annealing.

However, a different behaviour is observed when no boron doping is introduced into the 180nm-thick layer, as shown in Figure 4.25. Here, the laser treatment seems to have a more beneficial effect on samples. In the fluence range from 500 to 1200 mJ/cm^2, sheet resistivity sharply decreases from 500 to 100 Ω/sq. In the same interval, the quantity of ZnO present on the surface roughness layer used in the Tauc-Lorentz model increases around 850 mJ/cm^2, which indicates that the laser annealing has created a more compact surface layer. Film thickness remains constant on the optimised range of energy densities.

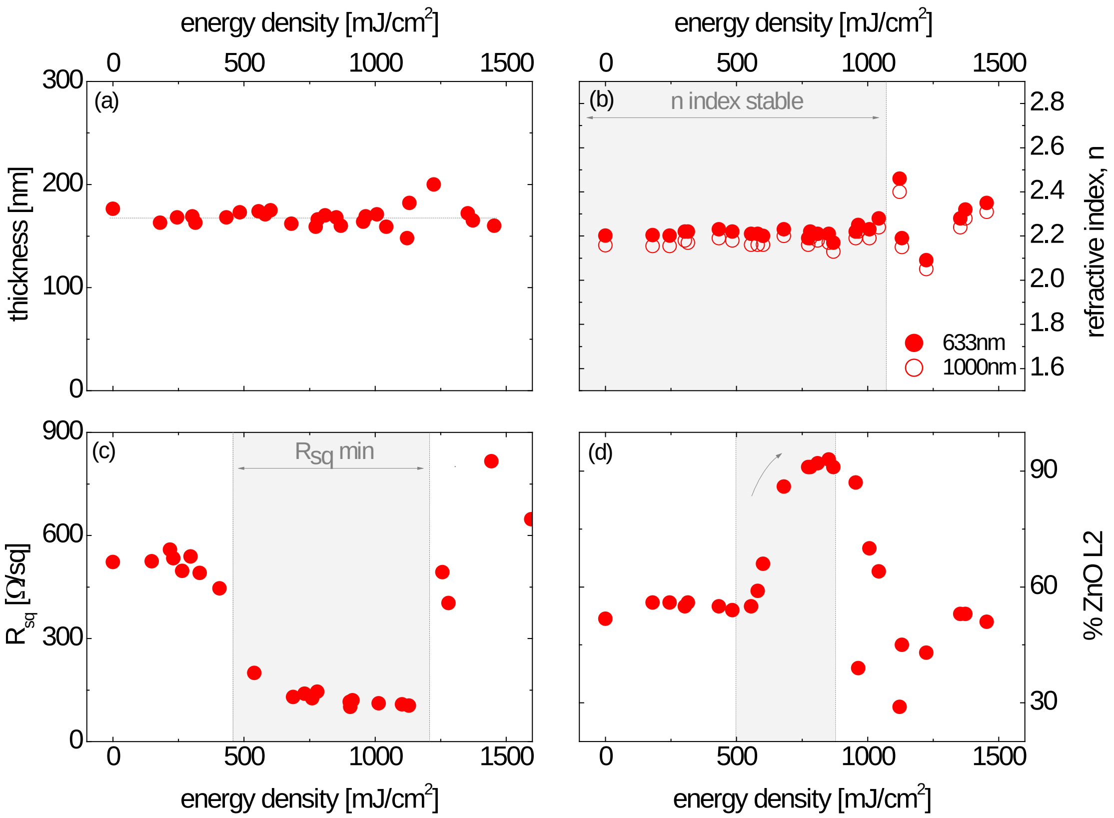

Figure 4.25. Spectroscopic ellipsometry parameters and sheet resistivity of 180 nm-thick undoped ZnO layers as a function of the energy density applied during laser annealing. The point at 0 mJ/cm^2 corresponds to the reference ZnO without any thermal annealing.

The same study has been performed on thinner layers (80 nm) in order to verify if the same behaviour as observed in the preceding thicker samples is also obtained. Moreover, focus has been put on the feasibility of obtaining better properties on thinner ZnO films, thanks to the laser annealing, which would be beneficial for more cost-effective HJ.

In the case of ZnO:B deposited at a thickness around 80nm, as can be seen in Figure 4.26(a), sheet resistances comparable to that of thicker ZnO:B samples (see Figure 4.24) are obtained when energy densities between 600 and 1000mJ/cm^2 are used. Similarly, as shown in Figure 4.26(b), the R_{sq} obtained on thinner undoped samples with laser fluences ranging from 500 to 1300 mJ/cm^2 are in the same level as those obtained in 180nm-thick layers (see Figure 4.25).

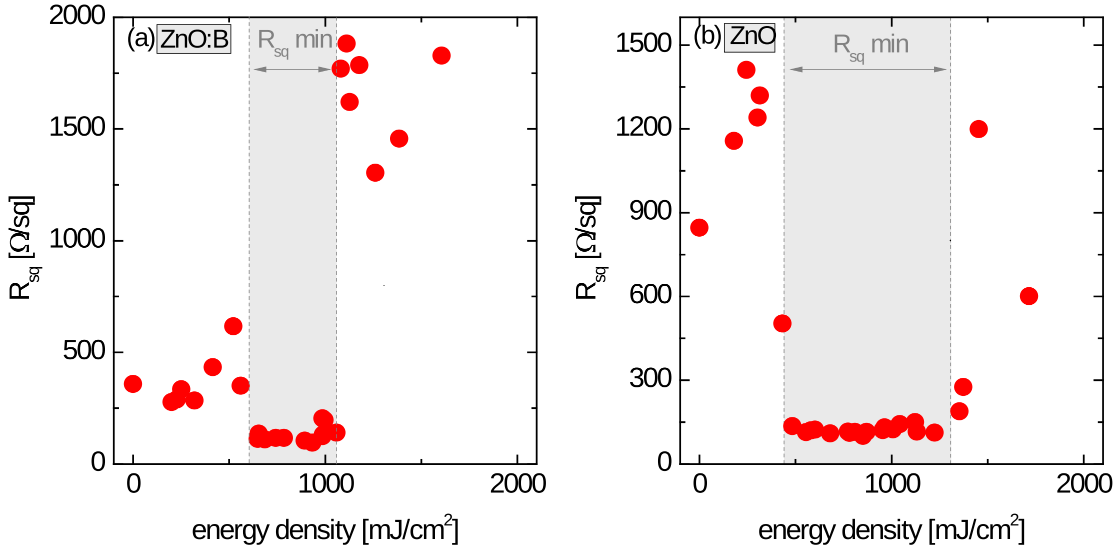

Figure 4.26. Sheet resistance of (a) boron-doped and (b) undoped 80 nm-thick ZnO films after undergoing laser annealing at varying fluences.

In all samples, a laser fluence interval, where the electrical properties are enhanced, has been identified. In general, energy densities between 500 and 1000 mJ/cm^2 lead to enhanced electrical properties with much lower resistivity than that of the reference. Surprisingly, similar R_{sq} values around 100 Ω/sq have been obtained after laser processing in all samples irrespective of thickness or doping on ZnO layers. This behaviour might be attributed to the fact that laser recrystallisation only takes place on the layer surface without altering bulk material properties. Thus, carriers' conduction is done through the layer surface without involving transport mechanisms at the grain boundaries.

After analysing the behaviour of the ZnO exposed at various laser fluences and considering that these layers are deposited onto (n)a-Si:H material in our HJ devices, ZnO/(n)a-Si:H/c-Si precursors have been fabricated to study the impact of the laser treatment on the passivation quality. The measured implied V_{OC} values for 4 selected energy densities are represented in Figure 4.27.

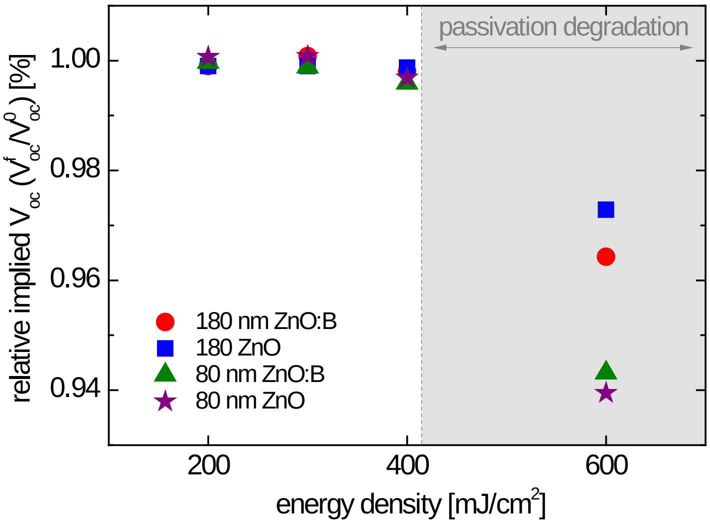

Figure 4.27. Variation of implied-V_{OC} values measured by the QSSPC technique on solar cells precursors as described in the inset for different laser fluences. A degradation of the passivation is observed for energies higher than 400 mJ/cm².

As it can be seen, no degradation of the passivation is detected when ZnO is irradiated at values lower than 400 mJ/cm^2. Above this threshold, amorphous silicon and the interface between the a-Si:H/c-Si are modified and an important loss of about 20 to 50 mV on implied V_{OC} values is occurred. This reduction of the passivation quality at 600 mJ/cm^2 becomes more pronounced for the thinner ZnO layers, suggesting that the TCO thickness is not enough to completely absorb the laser energy density and therefore, a-Si:H layers are degraded due to overheating. It is worth mentioning that energy fluences having no impact on c-Si passivation quality are not the ones with enhanced sheet resistances, but with similar electrical properties as the non laser-exposed samples. In general, it can be said that laser fluences leading to enhanced electrical properties (500 to 100 mJ/cm^2) will also result on degraded passivation structures.

To better understand the laser treatment effects on layer properties and passivation quality of ZnO/(n)a-Si:H/c-Si precursors, the morphological changes on ZnO films after laser annealing have been analysed. Two representative laser fluences belonging to each passivation regime found in Figure 4.27 have been chosen (300 and 600 mJ/cm^2). Corresponding SEM images of ZnO films' surface after undergoing the laser annealing are presented in Figure 4.28. As can be noted from Figure 4.28(a) and (c) there are no evident differences in films when both boron-doped and undoped layers have been irradiated at a fluence of 300 mJ/cm^2. The differences on grain size are mainly attributed to the use of boron doping, as it has been explained in section 4.2.3.1. However, when the laser energy density is further increased (600 mJ/cm^2) some cracks along the surface can be identified in the case of ZnO:B film (Figure 4.28(b)). This effect is magnified when no boron has been introduced into the layer. As shown in Figure 4.28(d), a dramatic change in the surface morphology is observed, where different domains separated by cracks are formed and a significant smoothing of the surface is evidenced. It should be noted that despite the surface damage associated with this fluence regime, the sample sheet resistance is not degraded (see Figure 4.25).

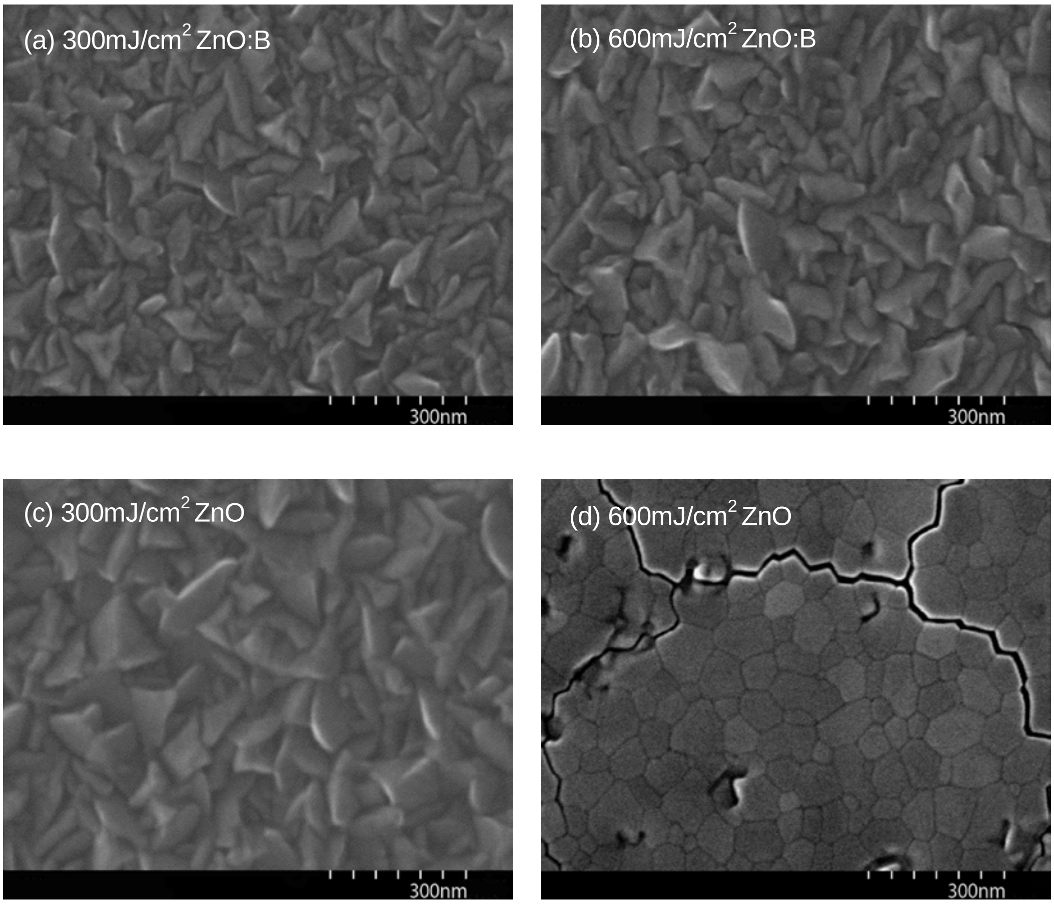

Figure 4.28. SEM images of surface of 180 nm-thick boron-doped and undoped ZnO films after undergoing laser annealing.

This can be attributed to a different interaction of the laser within the material when boron is introduced. Refractive index and extinction coefficient of both samples are shown in Figure 4.29, highlighting the higher absorption coefficient for the undoped ZnO at the applied laser wavelength. Therefore, in this case, the energy density is strongly absorbed in the material and the impact of the laser treatment is more powerful than in boron-doped samples.

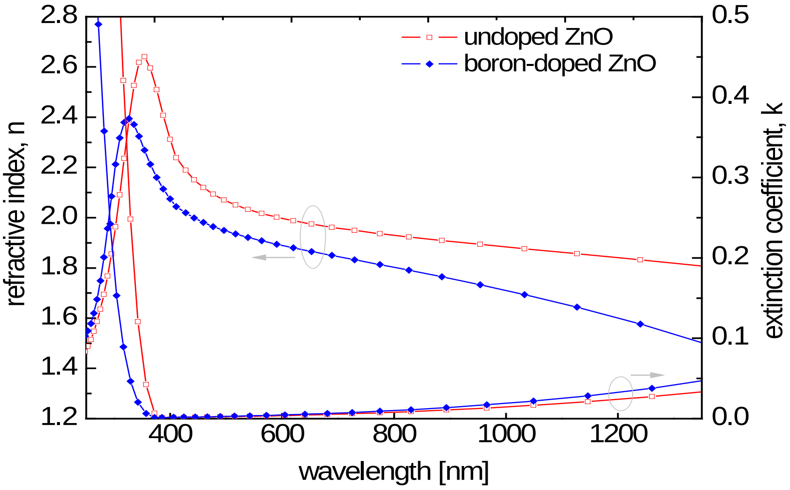

Figure 4.29. Refractive index and extinction coefficient modelled from spectroscopic ellipsometry measurements for undoped and boron-doped ZnO samples.

The same characterisation has been performed on the undoped and boron-doped 80 nm-thick samples and no morphological differences have been found between 300 and 600 mJ/cm^2 of laser energy density. Moreover, as presented in Figure 4.30, exposure at laser fluences of 600 mJ/cm^2 do not yield to cracked or smoothed layers, as it has been found in the thicker samples. For both boron-doped and undoped films, the surface remains stable after laser annealing, suggesting that a thickness of 80 nm is not enough to absorb the laser energy, and consequently the underlying n-doped a-Si:H film is affected by the laser. This assumption is in accordance with results shown in Figure 4.27, where a strong degradation of the c-Si passivation is found in the case of thinner samples, irrespective of doping content of the ZnO layer irradiated at 600 mJ/cm^2.

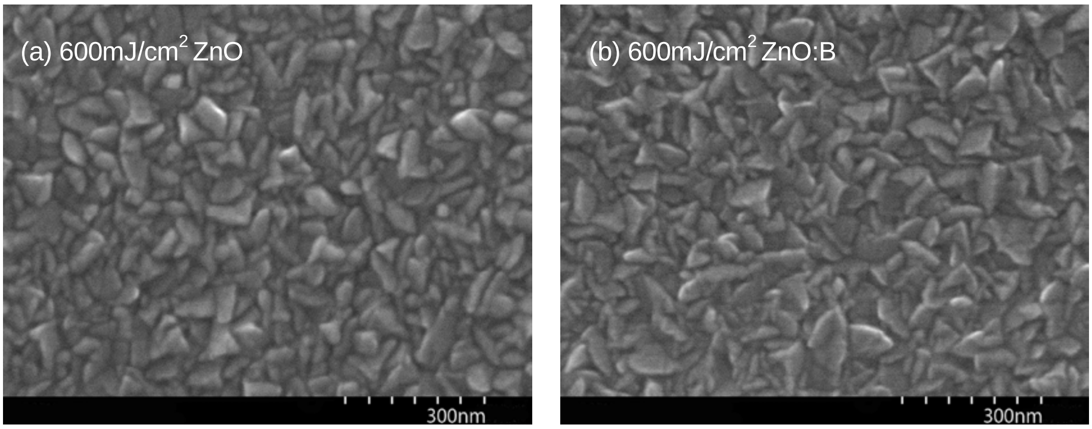

Figure 4.30. SEM images of surface of 80 nm-thick undoped and boron-doped ZnO films after undergoing laser annealing at 600 mJ/cm^2.

XRD measurements have been also performed on studied layers to see if any laser induced change occurs on the crystalline orientation of films. As presented in Figure 4.31, no differences have been found for the various ZnO thicknesses, doping levels and fluences analysed. Laser annealing does not modify ZnO bulk properties and no preferential crystallographic orientation is highlighted; the $(10\bar{1}0)$, $(10\bar{1}1)$ and $(11\bar{2}0)$ reflection peaks coexist in all samples.

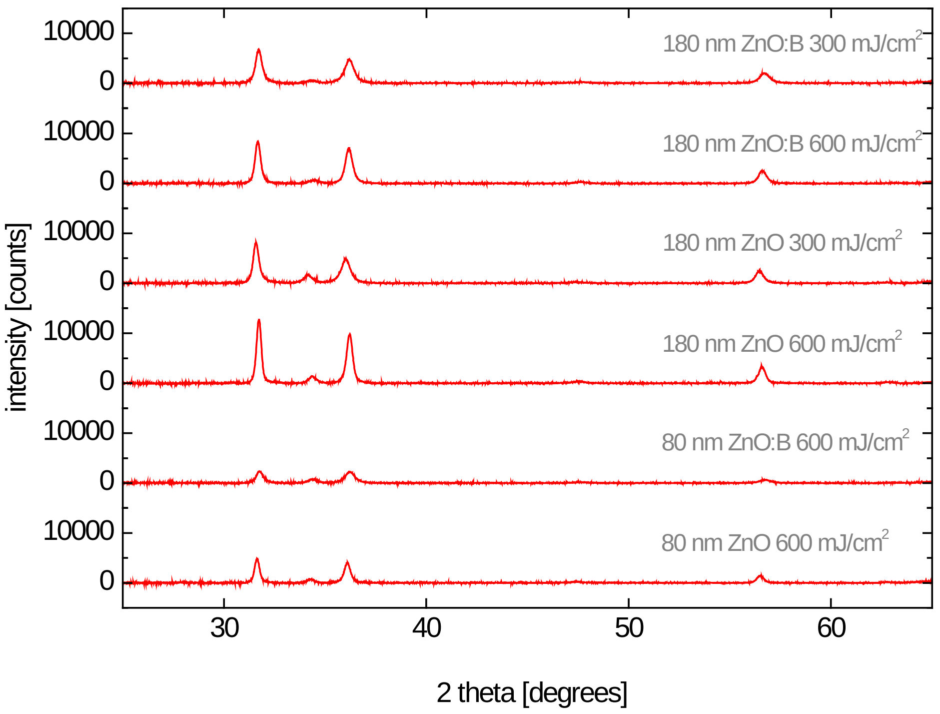

Figure 4.31. XRD patterns of 180 nm and 80 nm-thick undoped and boron-doped ZnO exposed to laser fluences of 300 and 600 mJ/cm^2.

In order to evaluate the laser annealing effect on the ZnO electrical properties degradation, a stability analysis under atmosphere exposure as a function of time has been carried out on laser annealed samples. Results presented in Figure 4.32 evidence that samples are also affected by degradation despite the laser post-treatment. Since annealing does not modify the ZnO bulk properties, grain boundaries in the material remain unchanged. Hence, the same degradation mechanisms reviewed in section 4.4 take place, which is supported by the fact that the same sheet resistance degradation trend is obtained for both laser-annealed and as-deposited samples. Similar results have been obtained on undoped material.

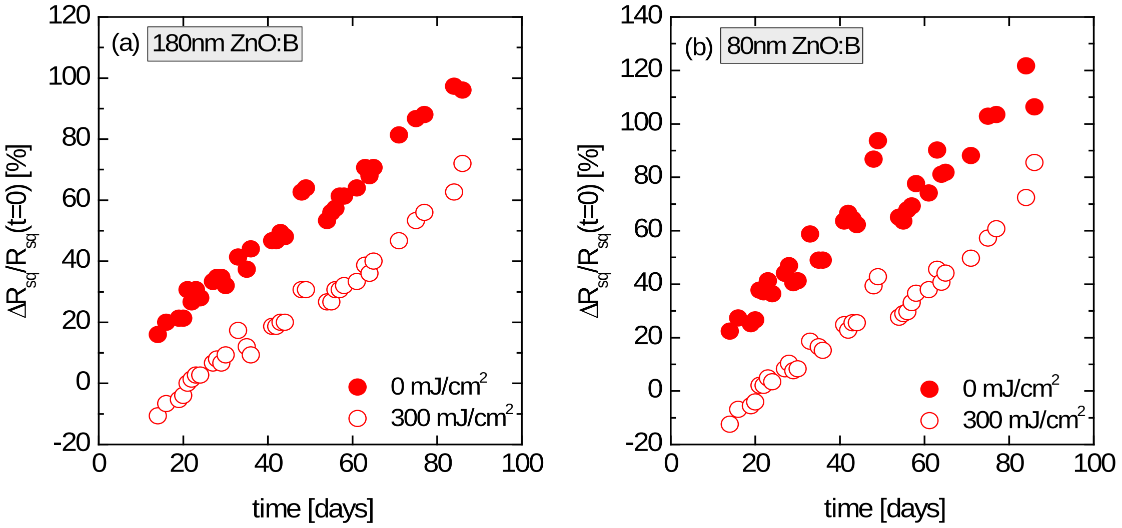

Figure 4.32. Relative variation in R_{sq} with time at ambient conditions for boron-doped laser-annealed samples with (a) 180 nm and (b) 80 nm of thickness. The evolution of non-treated samples deposited under the same conditions is also given for comparison.

Excimer laser annealing of ZnO samples with different thicknesses and boron doping concentrations leads to improved electrical properties under specific energy densities. Surface morphology of samples remains unchanged except for thicker samples exposed to high-fluence regime. Besides, crystalline orientation of films is the same in any of studied conditions. However, taking into account that laser annealed ZnO will be part of the back contact in heterojunction solar cells, in the fluence regime where electrical properties are enhanced, passivation quality of ZnO/a-Si:H/c-Si precursors is degraded. A threshold laser fluence of 400 mJ/cm^2 has been found from which passivation quality is lowered. However, laser annealing is found not to avoid electrical degradation of ZnO under this energy density. Therefore, ambient exposure ZnO stability still constitutes a problem for heterojunction solar cells, thus being inadvisable for their use in bifacial structures.

Based on these results, complete HJ devices on textured substrates have been fabricated and the ZnO surface has been irradiated with adapted laser fluences prior to deposition of the full rear side metal contact. In this case, 80 nm and 180 nm-thick boron-doped ZnO layers have been tested to verify the effect of laser treatment on solar cells. Corresponding performance results are presented in Table 4.2 (average values over 3 solar cells are given for each condition).

As it can be seen, current density and open-circuit voltage decreases with increasing exposure fluence. This effect is clearly observed when thinner zinc oxide layers are used, since as explained before passivation quality of (n)a-Si:H layers is affected by the laser annealing even at low fluences when ZnO:B layers are insufficiently thick. Focusing on results obtained on 180 nm-thick ZnO films, it can be noticed that there are no significant changes on performance parameters at low fluences compared to reference results without any laser processing. However, further increasing the laser fluence leads to device degradation, in accordance with results presented in Figure 4.27.

Table 4.2. Solar cell parameters for devices deposited with different ZnO:B thicknesses and irradiated at energy densities of 300 and 600 mJ/cm^2.

ZnO:B thickness [nm]	before laser annealing				energy density [mJ/cm^2]	after laser annealing			
	J_{SC} [mA/cm^2]	V_{OC} [mV]	FF [%]	η [%]		J_{SC} [mA/cm^2]	V_{OC} [mV]	FF [%]	η [%]
80	35.4	707	77.5	19.4	300	35.9	688	77.6	19.2
					600	31.5	577	79.5	14.5
180	35.3	709	77.2	19.4	300	35.7	705	77.6	19.5
					600	32.2	584	79.5	14.9

The series resistance is found to be unchanged at 0.5 Ωcm^2 in all devices, regardless of laser annealing. Interestingly, 600 mJ/cm^2 annealed devices exhibit higher fill factors at any of the ZnO:B thicknesses tested. Figure 4.33 compares FF and pFF of studied samples. Since very high shunt resistances are obtained, and series resistances are found to be equal between devices, changes in FF and pFF can mainly be attributed to recombination issues. Indeed, samples irradiated at 600 mJ/cm^2 exhibit lower pFF/FF ratio, which also supports the assumption that carriers' conduction at the rear side is enhanced (lesser recombination), and consequently FF is improved. Furthermore, these results are also in agreement with the enhanced R_{sq} values found for single ZnO layers irradiated at the laser fluence regime between 500 and 1000 mJ/cm^2.

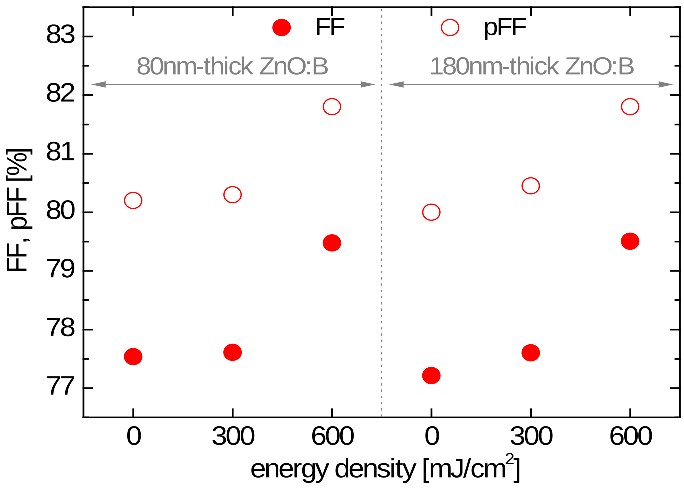

Figure 4.33. Fill factor and pseudo fill factor of HJ solar cells with different ZnO:B thicknesses and irradiated at energy densities of 300 and 600 mJ/cm^2.

Light J(V) characteristics illustrated in Figure 4.34 correspond to the thicker ZnO:B samples irradiated at 300 and 600 mJ/cm^2. A clear drop in J_{SC} and V_{OC} is observed and remarkably different dark J(V) curves are obtained. Higher laser fluences result in a modification of the first diode mainly impacting the V_{OC} parameter. As it can be seen in Figure 4.34(b), the voltage range where the impact of the R_S is visible lays away from the obtained V_{OC} value in the 600 mJ/cm^2 sample (584 mV). Therefore, a higher FF is obtained despite the low V_{OC}. The saturation current density of the second diode as well as R_P and R_S remains unchanged between different energy densities.

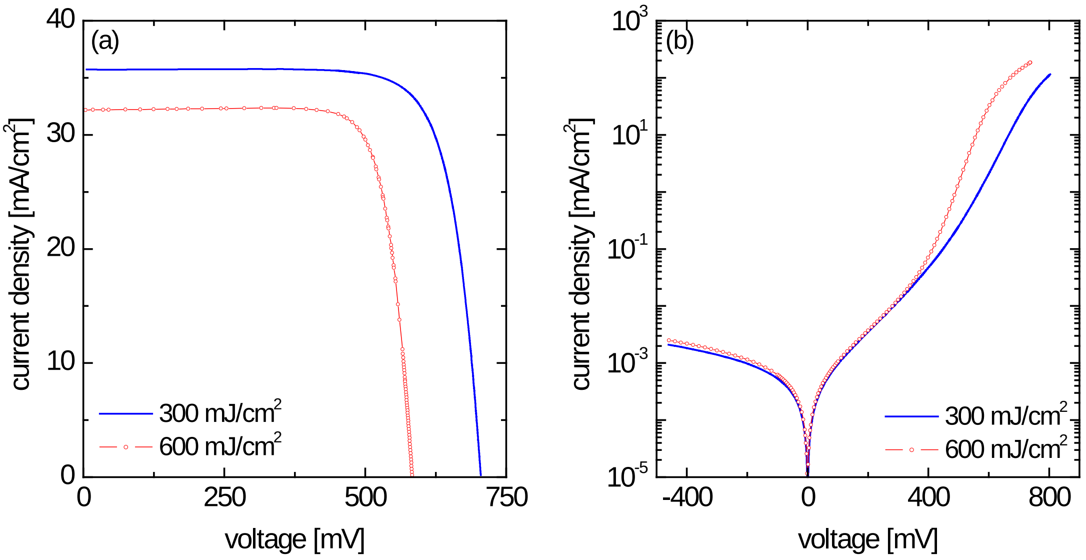

Figure 4.34. (a) Light and (b) dark J(V) characteristics of heterojunction solar cells with 300 and 600 mJ/cm^2 irradiated ZnO:B layers used as the back side TCO.

5. Solar cell and module integration

The work developed within this thesis, is part of a complex process where multiple steps take place in order to finish a complete HJ device. This chapter deals with diverse technological issues related to the fabrication of HJ solar cells. The importance of precisely controlling the technical aspects of the deposition process is discussed. Besides, record-efficiency HJ devices fabricated during this work are presented. Finally, the main aspects of HJ solar cell module integration are discussed, with the focus on different approaches concerning the back side.

5.1. Back-contact comparison

As it has been stated at the beginning of section 4, different choices at the back contact of HJ solar cells can be adopted. Within this work, the interest in using a-Si:H and ZnO:B layers prior to the deposition of the metal electrode has already been discussed. In order to demonstrate the potential of this configuration over other alternatives, HJ solar cells with different TCOs have been fabricated. Thus, the use of a back side ZnO layer is compared to the ITO option. Besides, samples with no TCO inclusion, in which the metal electrode is directly deposited on top of (n)a-Si:H layers have also been fabricated. The front side of devices has been unchanged, as well as the other rear components ((n)a-Si:H layers and aluminium contact).

Solar cell measurements are shown in Figure 5.1. If no TCO is used ('Ø' sample) solar cell characteristics are worse compared to that of ZnO:B or ITO samples. The V_{OC} notably diminishes, which suggests that recombination losses are greater since the contact between the metal and the amorphous layer is not optimum in this kind of structures. Moreover, as it can be seen in the inset of Figure 5.1(a), a higher series resistance is found in samples without a rear TCO, which also supports the idea of a low-quality back-contact. Accordingly, the FF decreases whereas the pseudo-FF remains unchanged. Consequently, conversion efficiency drops by almost 3%.

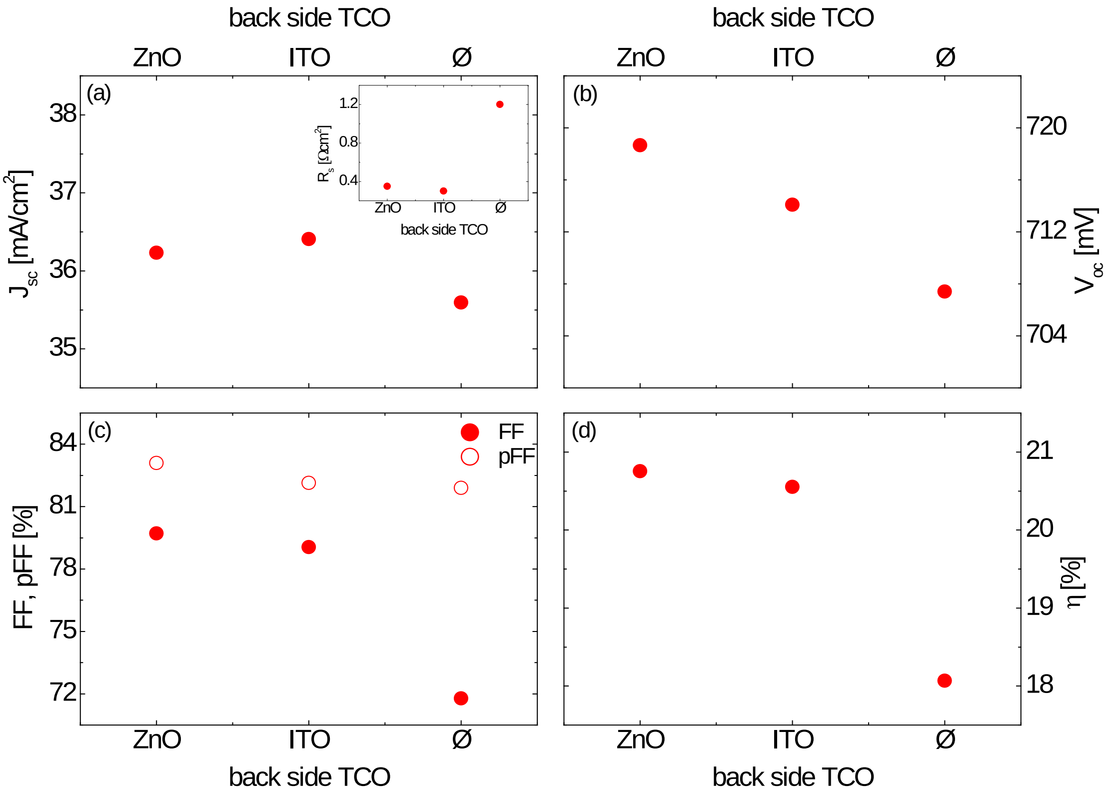

Figure 5.1. Solar cell characteristics with varying back side TCO. The use of a 230 nm-thick ZnO:B layer or 90 nm-thick ITO layer is compared with devices without rear TCO. Each data point represents the average value of three cells.

When a TCO layer is introduced both series resistance and back side recombination losses are minimised, hence the better J_{SC}, V_{OC} and FF values. Comparing 'ZnO:B' and 'ITO' devices it can be seen that almost equivalent results are found, although a slight enhancement specially in V_{OC} and FF is obtained when the ZnO is used. This fact can be attributed to a more favourable work function in ZnO:B films (Φ_{ZnO} = 4.4 eV vs. Φ_{ITO} = 4.8 eV), as determined from capacitance-voltage measurements. The lower Φ_{ZnO}, which is more adapted to the rear n/n$^+$ junction, enables a better charge carrier collection. As presented in Figure 5.2, the conduction band mismatch at the amorphous/ZnO interface can be reduced, thus diminishing the barrier for electrons. Tunnelling-mediated transports are therefore more probable, and a better solar cell performance can be obtained.

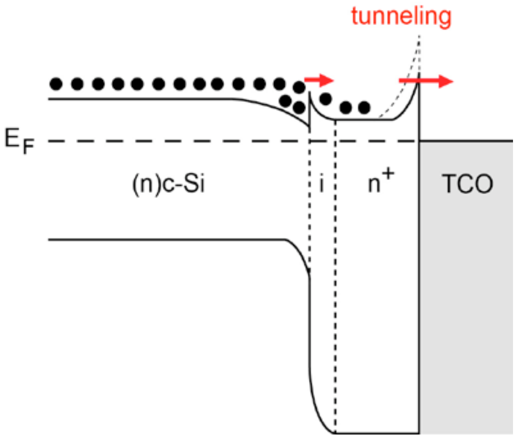

Figure 5.2. Band diagram at the back contact of HJ solar cells.

In order to reach high conversion efficiencies, the use of a back-contact without a TCO layer is inadvisable. By contrast, high-performing devices can be obtained using a rear TCO layer. Furthermore, the capability of our standard HJ solar cell design with a rear ZnO:B layer is proved in front of the wide-spread use of ITO layers at the back side of devices, which makes possible a cost-effective alternative to the scarce ITO.

5.2. Diverse technological issues

As it has been previously investigated in section 4.2.3, the B_2H_6/DEZ and H_2O/DEZ gas flow ratios play an important role on the properties of ZnO layers. At the beginning of this thesis the adjustment of the DEZ flow rate was provided by a pressure control unit (PCU). However, it periodically blocked, limiting the operation of our LPCVD system. To avoid this disruptive behaviour, a metering valve was used instead. With up to 10 stem turns to reach the maximum flow capacity, the aperture of the valve should be accurately adjusted in order to obtain the right flow rate of DEZ inside the chamber.

In the following paragraphs two different cases which exemplify the importance of precisely controlling the flow of DEZ will be presented. In Table 5.1 the properties of ZnO:B layers deposited at the right aperture of the metering valve (sample named 'ZnO:B_ok') are compared with the ones obtained when the valve is not sufficiently opened (sample named 'ZnO:B_ko'). As it can be observed, the characteristics of both layers are different even if equal deposition process conditions have been used. The 'ZnO:B_ko' sample is thicker than the 'ZnO:B_ok'. A ZnO of less quality is obtained; the sheet resistance is twice higher, and n index are smaller.

Table 5.1. Thickness, refractive index and extinction coefficient as per SE measurements, and sheet resistance measured by four point probe.

sample	thickness [nm]	633nm		1000nm		R_{sq} [Ω/sq]
		n	k	n	k	
ZnO_ok	216	2.096	0.004	2.049	0.007	53
ZnO_ko	285	1.880	0.003	1.849	0.003	127

When the valve is not sufficiently opened, the fixed DEZ flow rate inside the chamber can not be attained, thus modifying kinetics of chemical reactions taking place during the growth of ZnO:B films. Indeed, SIMS analyses of samples presented in Figure 5.3 show that both boron and hydrogen atom concentrations incorporated into the layers remarkably differ. The ‘ZnO_ko’ sample exhibits quite lower boron concentration, which can explain degraded sheet resistance results, even if the layer is thicker than the ‘ZnO_ok’ one. Besides, a higher hydrogen concentration is obtained, which also supports the idea that film’s stoichiometry is modified due to the use of less DEZ flow rate in chemical reactions.

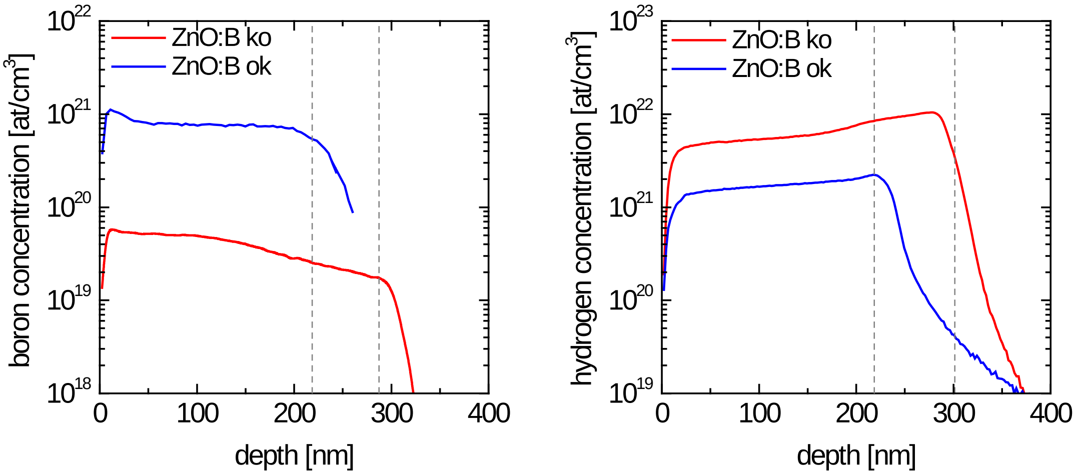

Figure 5.3. SIMS analysis depth profiles for B and H atoms of two ZnO:B samples deposited with the right aperture (‘ZnO:B_ok’), and an insufficiently aperture (‘ZnO:B_ko’) of the DEZ metering valve.

The use of these detrimental layers at the back contact of heterojunction solar cells has a dramatic impact on the output characteristics of the device. As presented in Table 5.2, HJ device with degraded ZnO:B at the back contact undergo a tremendous decrease on its output characteristics. While ‘HJ_ZnO:B_ok’ sample show good conversion efficiency results, the output characteristics of ‘HJ_ZnO:B_ko’ sample are strongly degraded. A fill factor of 11% has been obtained, resulting in efficiencies of less than 1%.

Table 5.2. Solar cell parameters for devices fabricated with a ZnO:B layer deposited with the right aperture (‘HJ_ZnO:B_ok’), and with an insufficiently aperture (‘HJ_ZnO:B_ko’) of the DEZ metering valve (average values over 3 solar cells are given for each sample).

sample	J_{SC} [mA/cm^2]	V_{OC} [mV]	FF [%]	η [%]
HJ_ZnO:B_ok	36.3	715.5	77.8	20.2
HJ_ZnO:B_ko	7.5	676.7	11.4	0.58

It is astonishing that the properties of ZnO layers presented in Table 5.1 could affect in such notorious way the solar cells results. In order to clarify this event, transmission electron microscopy (TEM) observations have been performed on both samples. Comparing Figure 5.4(a) and (b) it can be seen that at the a-Si:H/ZnO interface of ‘HJ_ZnO_ko’ sample a 4nm-thick layer is created, which can be assimilated as an oxide barrier. This fact is in good agreement with the idea that chemical reactions during the ZnO growth are modified when the opening of the metering valve is not accurately regulated. Not only the stoichiometry and macroscopic properties of ZnO layers change, but also it induces damage on the amorphous/TCO interface, creating a barrier for electrons that detrimentally affects the overall solar cell performance (as it has already been seen in Figure 3.41). In Figure 5.4(c) and (d) cross-sectional micrographs are presented where the incident electron energy has been varied in order to modify the image contrast and make clearer the presence of this oxide layer in ‘HJ_ZnO_ko’ sample.

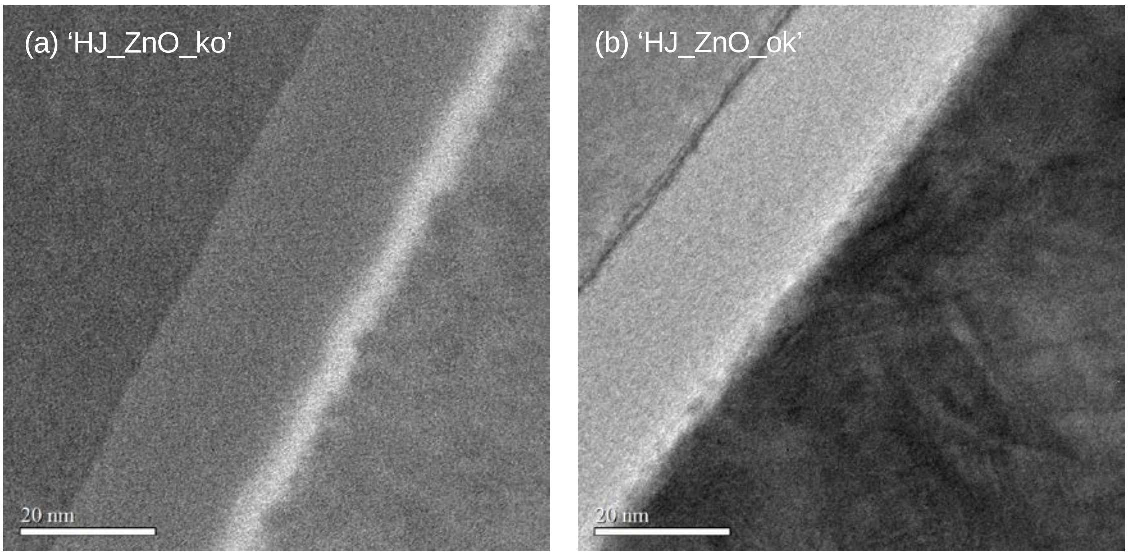

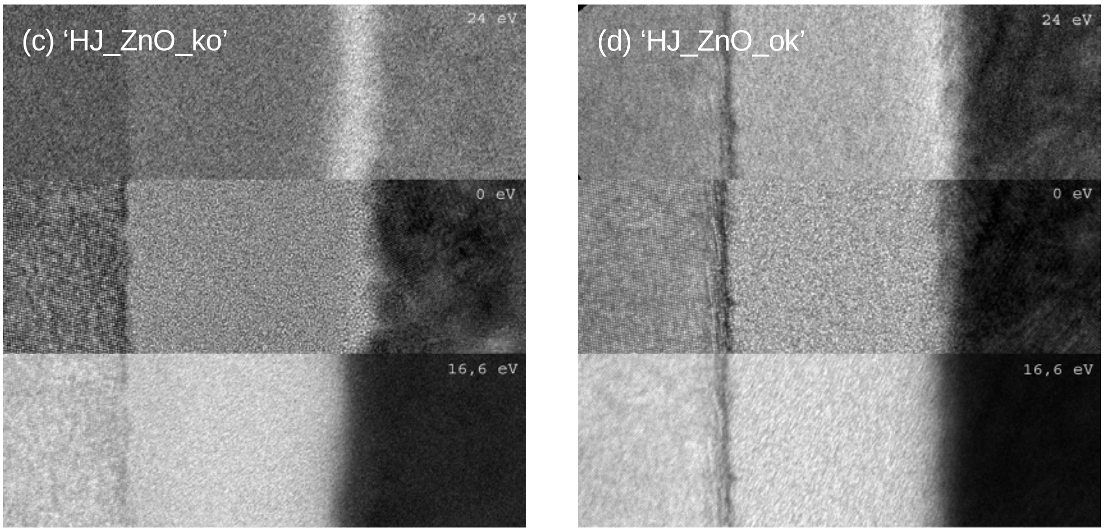

Figure 5.4. TEM micrographs of the back side of solar cells fabricated with a ZnO:B layer deposited with the right aperture (‘HJ_ZnO:B_ok’), and with an insufficiently aperture (‘HJ_ZnO:B_ko’) of the DEZ metering valve.

Figure 5.5(a) to (d) present TEM cross-sectional micrographs of both studied samples. Here, the texture of the c-Si substrate, the amorphous film and the columnar growth of ZnO:B layer can be observed. Moreover, in Figure 5.5(b) and (d) the microstructure of the metal contact can be clearly seen. The aluminium deposition is done by DC-magnetron sputtering on a dynamic way, so that the carrier speed of the substrate holder and the number of passes through the chamber determine the desired thickness of the layer. In these images, the measuring scale used do not evidence any damage at the a-Si:H/ZnO interface.

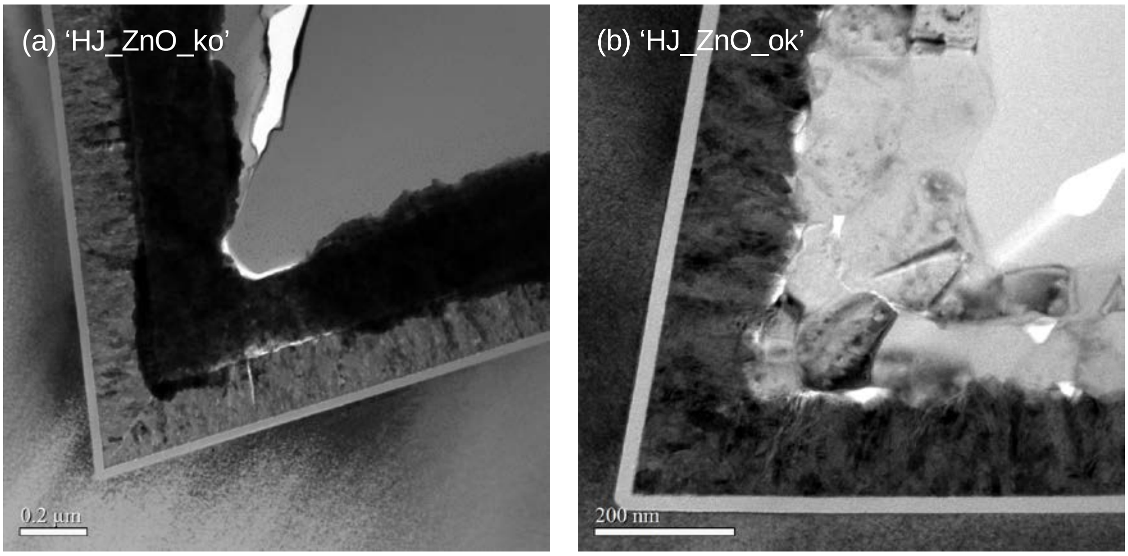

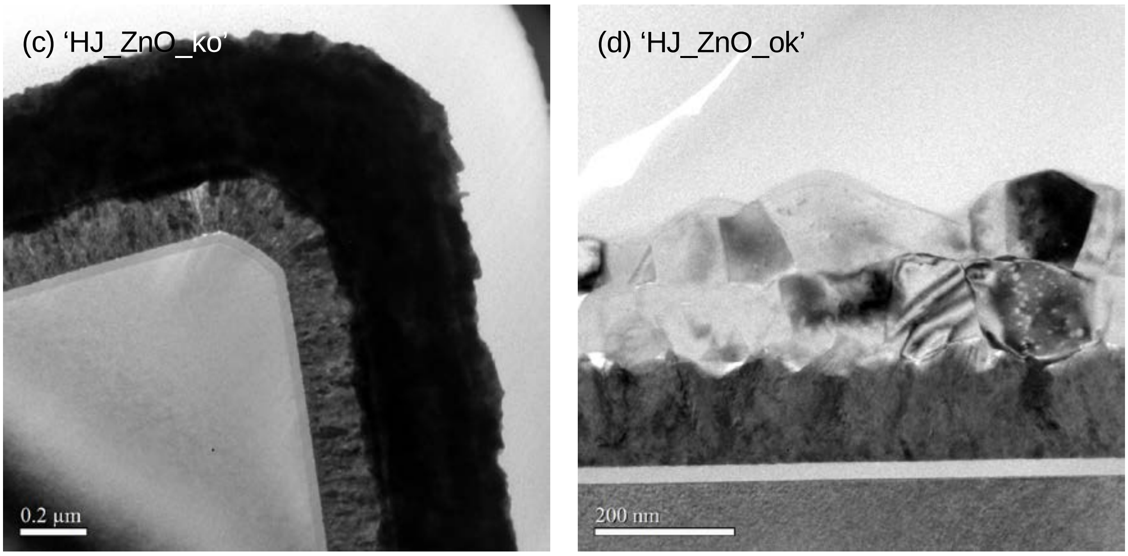

Figure 5.5. TEM micrographs of the back side of solar cells where the microstructure of each back side component can be identified; (a), (c) corresponds to the sample ‘HJ_ZnO_ko’, and (b), (d) to ‘HJ_ZnO_ok’.

5.3. Record efficiency solar cells

HJ solar cells developed during the course of this work involve several fields of expertise. The back side of devices has been improved, but also an extensive work to optimise the front side of solar cells has been conducted in order to further enhance conversion efficiencies. Thus, high-quality buffer layers have been used, and the absorption of (p)a-Si:H layers has been reduced adding CH_4 to the $SiH_4/H_2/B_2H_6$ gas mixture. Besides, the optical properties of front ITO films have been improved through a better adaptation of the refractive index.

To decrease the shadowing at the front side electrode, the standard silver-paste screen printing has been replaced by a copper metallisation scheme done by electroplating deposition (ECD), which has the potential to reduce the manufacturing cost while improving device performance [76, 200]. With this novel approach fingers of less than 50 µm can be deposited (see Figure 5.6(a)) with a room-temperature process suitable for HET technology.

All these improvements have been integrated in our HJ solar cells and impressive results over 22% of conversion efficiency have been obtained. As it can be seen in Table 5.3, both J_{SC} and FF values are notably enhanced compared to attainable results in our standard silver-paste screen-printed solar cells. The line width has been reduced from 90 µm to 40 µm, thus minimising the shadowing losses at the front side. The line resistance of the grid is decreased from 0.38 to 0.24 Ω/cm since the resistivity of pure ECD-copper is much lower compared to that of low-temperature silver paste.

Furthermore, the contact resistance between the TCO layer and the electrode is also enhanced. Figure 5.6(b) shows the J(V) curves of the best HJ devices fabricated with silver screen printing metallization and copper electroplating metallization.

Table 5.3. Solar cell parameters for devices fabricated using enhanced a-Si:H and TCO layers and copper electroplating metallisation. Standard results for silver screen printed HJ devices are also given for comparison.

sample	J_{SC} [mA/cm^2]	V_{OC} [mV]	FF [%]	η [%]	surface [cm^2]
Cu electroplated	38.0	733	79.4	22.1	103
Ag screen-printed	36.9	730	78.0	21.0	103

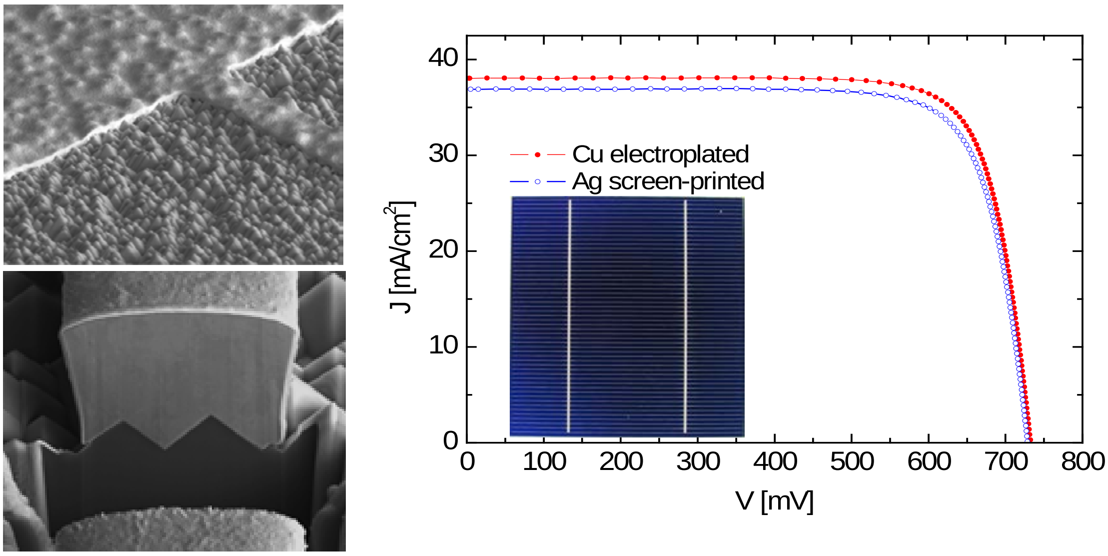

Figure 5.6. (a) SEM micrographs of a 40 µm Cu finger on an HJ solar cell. (b) J(V) characteristics of the best HJ cells with silver screen printing metallization and copper electroplating metallization.

5.4. Industrial module integration

Outdoor operation of HJ devices is subject to reliable integration in solar modules. The array of cells must be properly protected from the harsh external environment in which they are used by encapsulating them. Thereby, corrosion of electrical contacts and interconnects induced by water or moisture ingress into the PV module, as well as mechanical damage to the solar cells will be prevented.

In standard homojunction modules, solar cells are interconnected by soldering flat wires called tabs. This process is done at temperatures exceeding 250°C, which will have a detrimental effect on the HJ solar cell performance, since temperatures higher than 220°C can not be withstood. Furthermore, amorphous and TCO layers used in HJ devices are known to be sensitive to humidity. For these reasons, an adapted module design is needed, in which issues like low stress interconnect, moisture blocking and optical optimization of HJ modules should be addressed.

To this end, as shown in Figure 5.7 series interconnection of cells is done incorporating a conductive glue to adhere tabs on bus bars. Once stringing is finished, cells are sandwiched between two layers of thermoplastic encapsulant material (Tectosil®), which can be easily laminated to provide good adhesion between the solar cells, the front- and back-sheets. The standard module structure used at INES is sketched in Figure 5.8.

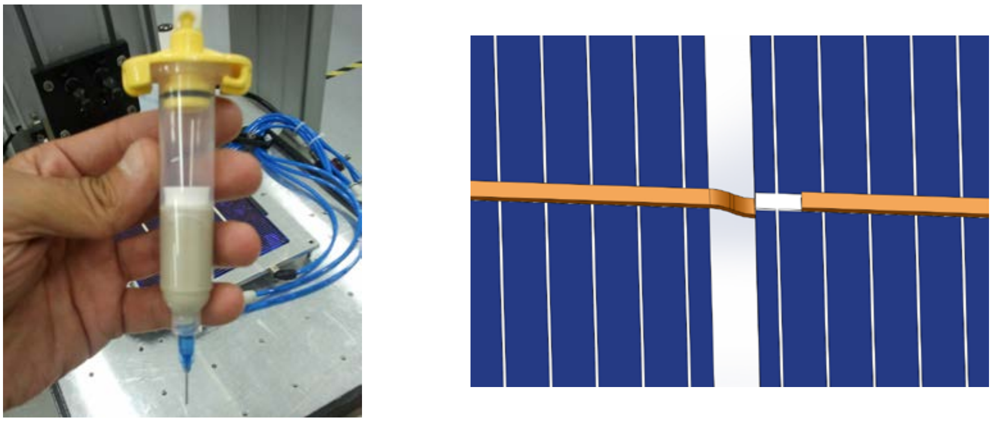

Figure 5.7. HJ solar cells interconnection with tabs adhered by conductive adhesive.

At the front surface of the PV module, a glass is used as a superstrate. This front-sheet layer should minimise light absorption and reflection, enable high transmission in the wavelengths usable by the solar cells, and grant mechanical rigidity. At the same time, the encapsulant should be stable at elevated temperatures and high UV exposure, and it has to be transparent as well. In addition, both front side constituents should be impervious to water and possess low thermal resistivity.

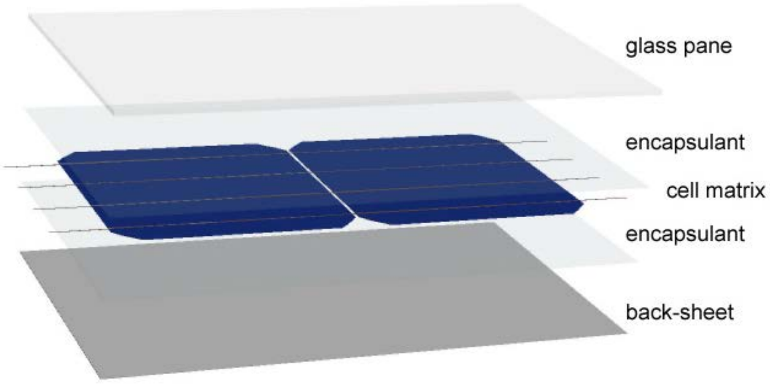

Figure 5.8. Stack of materials that composes the PV module

At the back side of the module a low thermal-resistivity moisture-blocking back-sheet, consisting of ‘TPT’ stacked layers (Tedlar/Polyethylene terephthalate/Tedlar) is used. This opaque rear substrate can either be used in black or white content. Depending on the HJ solar cell to be encapsulated (monofacial or bifacial devices) the back-sheet will be adapted to improve the output characteristics on each design.

In order to investigate the performance of modules, standard monofacial HJ solar cells with a silver full sheet deposited on top of the rear ZnO:B layer have been fabricated. In addition, bifacial solar cells have been also integrated into PV modules. In the latter case, due to the ZnO electrical stability limitations highlighted throughout this work, bifacial devices made of a thin ITO rear layer, instead of ZnO:B. Both types of heterojunction devices have been integrated into modules using either a black or a white back-sheet.

The electrical performance of cells and modules have been compared analysing the J(V) characteristics, and taking into account considerations summarised in Table 5.4. Corresponding results are shown in Figure 5.9 (the output characteristics of the PV modules have been determined by a flash-test).

Table 5.4. Results comparison between HJ solar cells and corresponding four cell modules (2×2).

module results	solar cells results
measured J_{SC}	minimum of cell’s J_{SC} $\left(J_{SC}\big\|_{min}\right)$
measured V_{OC}	sum of cell’s V_{OC} $\left(\Sigma V_{OC}\right)$
measured FF	average of cell’s FF $\left(\overline{FF}\right)$
$\eta = \frac{J_{SC}V_{OC}/4}{FF}$	$\eta = \frac{J_{SC}\big\|_{min}\Sigma V_{OC}/4}{\overline{FF}}$

From Figure 5.9 it can be seen that regardless of the back-sheet used or the type of HJ devices, a drop in the output solar cells’ characteristics exists after their encapsulation. In modules issued from monofacial HJ devices, fill factor and efficiency losses are higher compared to that obtained when bifacial solar cells are used. When a black back-sheet is used the difference in η is even slightly larger. The use of a white back-sheet enables multiple sunlight reflections, which increases the probability of electron-hole pairs’ generation. Moreover, if bifacial HJ devices are used the back side of devices will also take advantage of scattered light, therefore resulting in enhanced efficiencies (the smallest difference between cell and module efficiency is obtained).

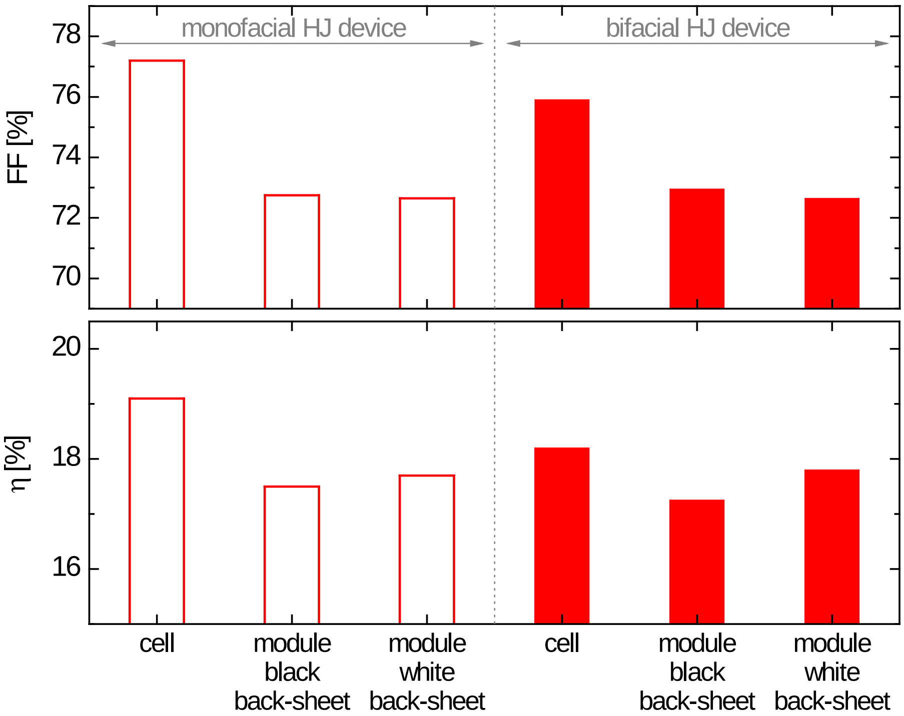

Figure 5.9. Fill factor and efficiency results of modules made of monofacial or bifacial HJ devices, with varying back-sheet layers.

As stated above, white back-sheets benefit from light scattering at the rear surface of the modules. In this respect, the packing density (referred to the area of the module that is covered with solar cells compared to that which is blank) is a key aspect on the module design. Depending on the spacing between cells, the output power of the module can somehow be maximised thanks to light reflection at the white back-sheet towards the active regions of the module. Indeed, as presented in Figure 5.10, the increase of the spacing within a PV module with a white back-sheet reduces losses either in short-circuit current density and conversion efficiency. However, fill factor slightly decreases. Then, the module packing density should be chosen to have the best FF/η compromise.

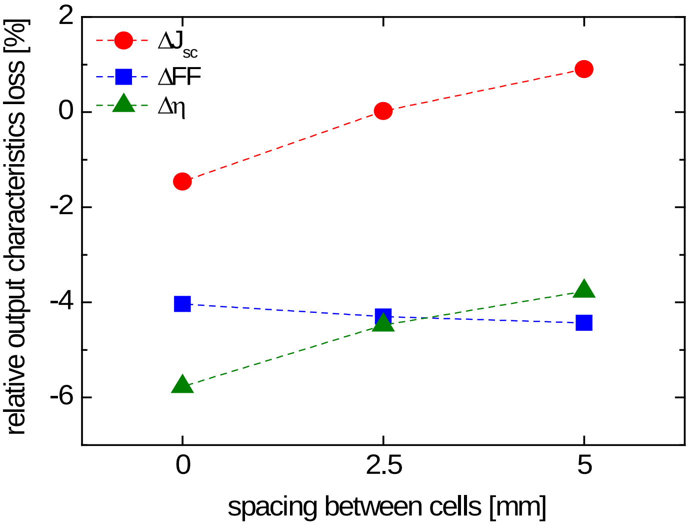

Figure 5.10. Relative loss in output characteristics of modules fabricated from 2×2 bifacial solar cells using a white back-sheet with varying packing density. Relative values are referenced to initial solar cells results.

The reliability of all these PV modules has been determined by exposing them to climate chamber tests (damp-heat and thermal cycling) according to the IEC 61215 standard. In all studied samples, modules withstood more than 1000 hours of damp heat, and over 200 thermal cycles with less than 4% reduction in power output. The suitable design used for device encapsulation provides a guaranteed integration into modules, which makes outdoor operation of HJ devices an attainable reality, as illustrated in Figure 5.11.

Figure 5.11. PV modules issued from HJ solar cells to be tested at the laboratory and for outdoor operation.

Conclusions and outlook

The object of the present work was to provide a better understanding of the back surface field role on n-type heterojunction solar cells. Then, key aspects of the back side of a-Si:H/c-Si heterojunctions have been examined. The properties of undoped amorphous silicon buffer layers, (n) doped layers and ZnO:B films have been studied and the feasibility to fabricate high-efficiency large-scale HJ devices with an industrially-compatible process has been demonstrated.

It has been evidenced that properties of a-Si:H layers as well as resulting passivation quality are extremely sensitive to deposition conditions. Thin amorphous silicon films have been deposited by PECVD and an extensive characterisation has been performed; their morphological and structural properties have been determined, as well as the conductivity, activation energy and passivation quality of these layers.

The influence of deposition parameters on layer properties has been discussed, and optimised process conditions leading to enhanced performing BSF layers have been identified. It has been shown that the higher the deposition pressure, the better the passivation quality of the (n)a-Si:H layers at lower PH_3 flow rates. Similarly, a larger distance between the parallel electrodes in the PECVD chamber results in better implied V_{OC}s for lower doping rates. Based on these investigations a pressure of 1.5 T and an inter-electrode distance of 35 mm have been set for the deposition of undoped or lightly doped (n)a-Si:H layers, whereas a pressure of 0.8 T and 23 mm of spacing have been set for films with higher doping flow rates. Decreasing process pressure beyond 0.8 T has been found to result in an unintentional epitaxial growth which adversely affects the passivation properties of (n) layers with low V_{OC}s. Besides, it has also been shown that the amorphous content of such epitaxial silicon structures is dependent on their doping level.

HJ solar cells are dominated by the properties of their component layers and corresponding interfaces. Then, various BSF configurations have been investigated, and the solar cell output characteristics have been correlated with their individual layer properties in order to understand the main mechanisms involved in the high performance of HJ devices.

Amorphous/crystalline silicon solar cells with single layer BSF have been fabricated and conversion efficiencies over 19% have been obtained. The use of different (n)a-Si:H doping contents has shown that a highly doped BSF is necessary to create the appropriate band bending to be able to collect charge carriers, even if the density of defects is not optimised at the heterointerface.

To further enhance conversion efficiencies, the minimization of recombination losses at the a-Si:H/c-Si interface is shown to be of key importance. Thus, a very low defect state density at the back (n) junction together with a strong electrical field is also required. To overcome this constraint the use of a double-layer stack BSF consisting of an undoped or lightly doped layer followed by a highly doped one has been introduced. Different double-layered stack BSFs have been studied as a way to enhance c-Si surface passivation by saturation of dangling bonds and to create an appropriate band bending at the back side of devices.

The influence of the doping content on the intermediate buffer layer has been analysed. It has been demonstrated that the insertion of the high-quality (i)a-Si:H improves the properties at the back junction and enables higher V_{OC} and good FF. Theoretical analysis of single layers and complete cells has clearly demonstrated the key-role of the low-defective lightly-doped a-Si:H layer in terms of passivation quality. However, results obtained in the analysis of lightly doped intermediate layers suggests that further augmentation of phosphorous content in the thin a-Si:H film slightly degrades the cell fill factor, even though the conductivity of the (n) layer itself increases. A maximum value of 20.5% of conversion efficiency has been obtained with the use of an undoped buffer layer.

The effect of varying the thickness on (i)a-Si:H layer has been assessed. Whereas changes in the thickness of the emitter (i) layer usually lead to a decrease in J_{SC} due to higher short-wavelength absorption and low (i)a-Si:H conductivity, at the BSF mainly FF and V_{OC} are found to be affected, since the band bending at the rear side changes. An optimum of FF/V_{OC} compromise has been found at a thickness of 4 nm, thus leading to improved efficiencies. Again, it has been highlighted that the increase in V_{OC} is attributed to a better defect passivation at the heterointerface using (i)a-Si:H instead of doped (n)a-Si:H layer directly in contact with c-Si.

Concerning (n^+) layer doping, an optimum at 215 sccm of PH_3 has been found in accordance with enhanced conductivity and lower activation energy values obtained on single layers. At higher doping flow rates, the creation of defects within the a-Si:H is increased, and consequently output solar cell characteristics are degraded.

In a second part of this thesis, the back contact of heterojunction solar cells has been investigated. A new approach based on ZnO:B deposited by LPCVD has been proposed as an alternative to the widely-used ITO films. Research has been focused on the optimisation of deposition conditions, the study of the relevant film properties for their application as a rear side TCO material, and the assessment of their impact on HJ solar cells performance.

Properties of ZnO:B films are found to be strongly dependent on their polycrystalline structure. It has been demonstrated that the grain size can be increased either by depositing thicker ZnO films or by decreasing the doping level. Deposition temperature is revealed as one of the most sensitive parameters in ZnO:B, and the limiting one for its applicability on HJ cells. Structural properties of films are found to be remarkably modified at higher temperatures, resulting in enhanced electrical features. Varying the parameters of ZnO:B deposition, no evident surface-roughness changes have been induced at the studied thickness range. Process conditions have been optimised and improved ZnO:B layers at p_{dep} = 0.4 T, B_2H_6/DEZ = 0.1, H_2O/DEZ = 0.125, and T = 180°C have been found. Investigations herein presented have shown that higher values of electron mobility have been obtained on layers with larger grain sizes. An enhancement of mobility at the grain boundaries has been identified as the main contribution to the overall mobility of ZnO:B films with larger crystals, since electron scattering phenomena are reduced.

The application of ZnO:B layers on a-Si:H/c-Si heterojunction solar cells has been studied. The use of this TCO film at the BSF has been demonstrated to be advantageous compared to the use of a single metal contact directly deposited onto amorphous layers. Besides, promising results have been obtained compared to the reference ITO, which have certainly demonstrated the high potential of this material.

However, unstable electrical properties on ZnO films have been evidenced. It has been shown that a degradation of the film's lateral conduction under air exposure occurs, which adversely affects the solar cells characteristics. To avoid device degradation it has been demonstrated that the use of ZnO films is restricted to monofacial heterojunction configuration, since the rear side of the device is completely covered with a metal electrode, and only vertical conduction is promoted through ZnO layers.

In this work, a novel approach based on excimer laser annealing of ZnO films has been investigated as a way to further enhance TCO performance and stability. Laser fluences ranging from 500 to 1000 mJ/cm^2 have led to an improvement of film's electrical properties, although stability analyses of irradiated ZnO films have shown that electrical properties are also affected by degradation despite the laser post-treatment. Thus, it has been highlighted that the use of ZnO layers is still consigned to monofacial HJ applications. The impact of the laser treatment on the passivation quality of (n)a-Si:H layers has been studied, and a degradation of the implied V_{OC} of ZnO/(n)a-Si:H/c-Si precursors has been detected beyond 400mJ/cm^2. Indeed, solar cells with ZnO layers irradiated at high energy densities have resulted in lowered open-circuit voltages, and efficiencies have decreased around 5%.

During the course of this work, the importance of considering the properties of BSF layers as well as corresponding interfaces has been emphasised in order to fully understand the many aspects leading energy conversion in high efficiency HJ solar cells. It has been evidenced that the back side of heterojunction solar cells plays an important role on the achievement of high efficiencies. Indeed, a number of requirements must be fulfilled in order to create a high-quality BSF. However, in this work it has been highlighted that once the suitable BSF has been attained, introduced changes based on the increase of V_{OC} properties of rear amorphous layers usually have a weak impact on the overall device performance. Back side optimisation is always dependent on phenomena taking place at the front side of devices. Thereby, the enhancement of the overall device performance due to the back side is difficult to quantify compared to changes induced by the emitter part of the solar cell.

The use of the optimised back side layers developed during the course of this work, together with improved front side layers and a novel metallisation approach have allowed to obtain a record conversion efficiency over 22%. All HJ solar cells developed during this thesis have been fabricated with an industrial-compatible process. This ‘LabFab’ approach has led to the creation of a pilot production line (35 MW/year) of our standard HJ solar cells with a target efficiency of 20% on 256 cm^2 devices. Besides, reliable module integration is guaranteed, which makes outdoor operation of our HJ devices an attainable reality. The development of amorphous layers carried out in this work has been also used in Interdigitated Back Contact HJ (IBC-HJ) devices developed at INES. In this case, deposition conditions have been adapted to IBC-HJ requirements and performances exceeding 19% have been obtained with an optimized damage-free a-Si:H layer patterning.

Despite all this encouraging results, there still room to upgrade the back side of HJ devices. Further optimisation of (i)a-Si:H layers could be targeted. In this sense, µc-Si:H layers could be advantageous to improve the back contact in HJ solar cells. Similarly, high-quality wide-gap amorphous silicon compounds such as a-SiO_x:H could be investigated as a way to enhance back junction properties. The influence of post-hydrogen plasma treatments on a-Si:H layers could also be advantageous to increase the effective lifetime by defect reduction of the film. Further work could also be conducted to extend the deposition parameter survey for ZnO:B layers in order to find an optimum work recipe more adapted to the industrialisation transfer (a cost-effective process with less precursor-gas consumption and reduced deposition time). Besides, research on low-cost high-quality alternative TCO materials would be of great interest. In depth work on the properties of the (n)a-Si:H/TCO back contact, and its influence on the solar cell performance could also be addressed.

A. (n)a-Si:H layers modelling

An accurate description of n-doped layers used on the BSF of HJ is of prime importance since their characteristics are expected to influence solar cell performance. As previously discussed, activation energy of (n)a-Si:H layers is a key-parameter, as it sets both layer conductivity and field effect in the back side silicon substrate. Besides, the Fermi level position in a-Si:H layers results from the competition between active doping concentration and dangling bonds (defects) density [137, 141].

With the aim of determining both doping level and defect density in a-Si:H layers, simulation of temperature dependent dark conductivity measurements has been performed in order to reduce as much as possible the number of assumptions and fitting parameters in solar cell modelling.

The a-Si:H optical band gap has been extracted from SE measurements (see Table 3.2). The DOS in the a-Si:H band gap has been described by two exponential band tails related to the conduction and valence band edges, respectively, and two Gaussian distributions (donor-type states located in the upper part of the gap and acceptor-type states located in the lower part of the gap) [137]. The band tails parameters have been set equal to values reported in [101, 156] and have been kept independent of doping. Regarding the deep defects, it is well known from the general frame of the defect-pool model that the lower Gaussian increases when the Fermi level gets closer to the conduction band, while the upper Gaussian becomes negligible. This is why the peak value of the upper Gaussian has been fixed at a negligible value of 2×10^{15} $\mathrm{cm^{-3}eV^{-1}}$. The distribution of acceptor states has been set at 0.6 eV from the valence band (except for n0 acceptor-like states, where it has been fixed at 0.55 eV), with a constant width of 0.15 eV [101]. Finally, the concentration of acceptor defects N_{def} (corresponding to the integral of the acceptor Gaussian distribution) induced by doping has been deduced from [101]:

$$N_{def} = N_{D0} + N_{D1} \cdot \left(\frac{[PH_3]}{[SiH_4]} \right)^p \tag{A.1}$$

with $N_{D1} = 2.90\times10^{17}$ $\mathrm{cm^{-3}}$, $p = 0.5$ and the $[PH_3]/[SiH_4]$ ratio expressed in ppm. Defect density N_{D0} of the n0 layer has been set equal to 2.5×10^{16} $\mathrm{cm^{-3}eV^{-1}}$, according to MPC-HF measurement (see section 3.4.3). Since calculations have been done using an empirical formula, it is worth mentioning that defect density deduced from this equation may vary from reality. However, possible discrepancies in defect density definition can be assumed by pointing out that activation energy (and thus the ratio doping level/defects density) is the only parameter determining the total band bending in c-Si and a-Si:H layers. Considering an appropriate defect-dependent doping level is expected to make up this difference. Band bending asymmetry in a-Si:H and c-Si is mainly determined by the exponential conduction band tail in a-Si:H. At this point, it is important to remind that within our assumption of constant band tail parameters with varying layer doping, the potential drop asymmetry evolution will be mainly determined by a-Si:H activation energy.

Then, for each layer, the dependence of activation energy on donor doping level, $E_a(N_D)$, has been simulated using a constant N_{def} in order to extract the doping value corresponding to both layer defect density and activation energy (see Table A.1). Figure A.1 shows two examples of doping level extraction on 10 nm-thick a-Si:H layers without any doping (n0) and 215 sccm of PH_3 (N215).

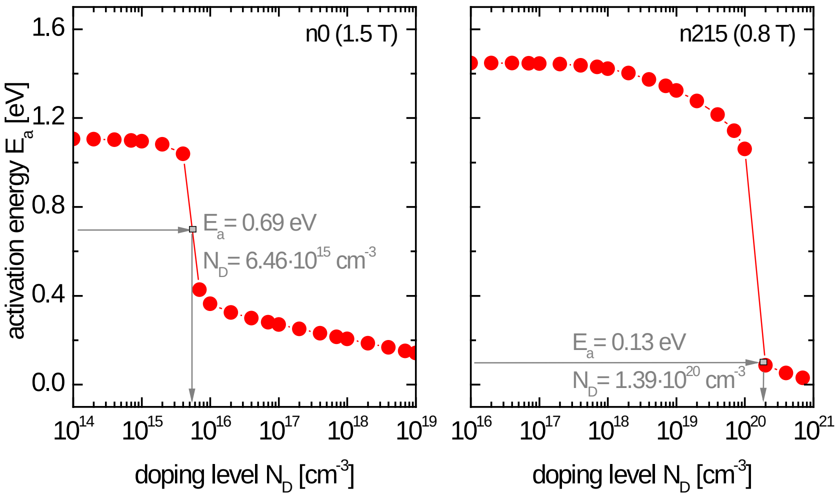

Figure A.1. Simulated activation energy as a function of donor doping level, for layers n0 and N215, deposited at 1.5 T and 0.8 T of pressure, respectively. Note that the abrupt transition occurs when $N_D = N_{def}$.

Table A.1. Defect density and donor doping levels in different n-doped a-Si:H layers.

doping [sccm]	deposition pressure [T]	Acceptor defects density, N_{def} [cm^{-3}]	Donor doping level, N_D [cm^{-3}]
0	1.5	6.65×10^{15}	6.46×10^{15}
1	1.5	9.18×10^{18}	9.38×10^{18}
5	1.5	2.05×10^{19}	2.17×10^{19}
20	1.5	4.10×10^{19}	4.88×10^{19}
215	0.8	1.23×10^{20}	1.39×10^{20}

List of Figures

List of Tables

List of symbols and abbreviations

α	Absorption coefficient
χ	Electron affinity
ΔE_C	Conduction band offset
ΔE_V	Valence band offset
Δn, Δp	Excess carrier concentration (electrons, holes)
ε	Dielectric permittivity
ε_0	Vacuum dielectric permittivity
$\langle \varepsilon_2 \rangle$	Imaginary part of pseudo-dielectric function
Φ_{wf}	Work function
Φ_b	Potential barrier height (at ZnO grain boundaries)
Φ_0	Incident photon flux
η	Solar cell conversion efficiency
$\varphi_{a\text{-}Si:H}$, $\varphi_{c\text{-}Si}$	a-Si:H, c-Si band bending in equilibrium
λ	Wavelength
μ	Carrier mobility
$\mu\tau$	Mobility-lifetime product
ν_{th}	Thermal velocity of charge carriers
ρ	Resistivity
σ_d	Dark conductivity
σ_n, σ_p	Capture cross sections of electrons and holes
σ_{ph}	Photoconductivity
σ_0	Prefactor in a-Si:H dark conductivity
τ_{Aug}	Minority carrier lifetime due to Auger recombination
τ_b	Minority carrier lifetime due to general bulk recombination
τ_{eff}	Effective lifetime
τ_{n0} τ_{p0}	Capture time constants for electrons and holes
τ_{rad}	Minority carrier lifetime due to radiative recombination
τ_{SRH}	Minority carrier lifetime due to Shockley-Read-Hall recombination
ω	Electrode distance in coplanar contacts

B	Radiative recombination constant
C_n, C_p	Auger coefficients for electrons and holes
d	Layer thickness
d_{depl}	Depletion region width
d_e	Inter-electrode distance in PECVD system
D_{it}	Interface defect density

D^0, D^+, D^-	Neutral, positively and negatively charged dangling bond state
DB	Dangling bond
E_a	Dark conductivity activation energy
E_C	Conduction band energy
E_g	Band gap
E_F	Fermi energy
E_i	Intrinsic Fermi energy
E_μ	Mobility band gap
E_t	Energy level of localized/trap state
E_{TR}	Energy of conducting electrons in a-Si:H
E_V	Valence band energy
FF	Fill factor of solar cell illuminated J(V) curve
G	Generation rate
J	Current density
J_{mp}	Current density at maximum power point
J_{ph}	Photo-generated current density
J_{SC}	Short-circuit current density
J_0	General saturation current density
J_{01}	Saturation current density of high-forward bias diode
J_{02}	Saturation current density of low-forward bias diode
k	Extinction coefficient
k_B	Boltzmann's constant
ℓ	Electrode length
L_{diff}	Effective diffusion length of minority carriers
L_n, L_p	Diffusion length of minority carriers (electrons and holes)
n	Refractive index
n, p	Concentration of electrons and holes
n_d	General diode ideality factor
n_i	Intrinsic carrier concentration
n_s, p_s	Concentration of electrons and holes at recombination-active surface
n_0, p_0	Equilibrium concentrations of electrons and holes
n_1, p_1	Statistical factors for electron and hole concentrations in Shockley-Read-Hall recombination
n_1, n_2	Two-diode model ideality factors at high and low forward bias
N	Free carrier concentration (in Hall effect measurement)
N_A, N_D	Density of acceptors or donors
N_C, N_V	Conduction and valence band effective density of states
N_d	Bulk defect density (c-Si doping concentration)
N_t	Density of localised/trap state
p_{dep}	Chamber pressure in PECVD system

pFF	Pseudo fill factor
P_S	Incident illumination power density
Q_f	Fixed charge density
R	Reflectance, reflectivity
R_P	Parallel resistance in solar cell equivalent circuit
R_S	Series resistance in solar cell equivalent circuit
R_{sq}	Sheet resistance
S	Surface recombination velocity
S_{back}, S_{front}	Back- and front-side surface recombination velocity
S_{eff}	Effective recombination velocity
T	Temperature
U	Recombination rate
U_S	Surface recombination rate
V	Applied voltage
V_{mp}	Voltage at maximum power point
V_{OC}	Open-circuit voltage
W	Wafer thickness

(i)a-Si:H	Undoped (so-called intrinsic) hydrogenated amorphous silicon
(n)/(p)a-Si:H	n-/p-doped hydrogenated amorphous silicon
(n)/(p)c-Si	n-/p-doped crystalline silicon
Ag	Silver
Al	Aluminium
a-Si	Amorphous silicon
a-Si:H	Hydrogenated amorphous silicon
a-SiC$_x$:H	Hydrogenated amorphous silicon carbide
a-SiN$_x$:H	Hydrogenated amorphous silicon nitride
a-SiO$_x$:H	Hydrogenated amorphous silicon oxide
Al_2O_3	Aluminium oxide
AFM	Atomic force microscopy
AFORS-HET	’Automat for the simulation of heterostructures’ (software)
AM1.5	Air mass 1.5 (solar spectrum)
APCVD	Atmospheric Pressure chemical vapour deposition
BSF	Back surface field
B_2H_6	Diborane
c-Si	Crystalline Silicon
CB	Conduction band
CVD	Chemical vapour deposition
CZ	Czochralski
DB	Dangling bond
DC	Direct current

DEZ	Diethylzinc
DOS	Density of states
FTIR	Fourier-transform infrared spectroscopy
FZ	Float zone
H	Hydrogen
HF	Hydrofluoric acid
HIT	Heterojunction with intrinsic thin layer (Sanyo)
HJ	Heterojunction
HWCVD	Hot-wire chemical vapour deposition
H_2O	Water
IQE	Internal quantum efficiency
IR	Infrared
ITO	Indium tin oxide
LPCVD	Low-pressure chemical vapour deposition
MOCVD	Metal-oragnic chemical vapour deposition
NIR	Near infrared
PCD	Photoconductance decay
PECVD	Plasma-enhanced chemical vapour deposition
PH_3	Phosphine
QSSPC	Quasy-steady-state photoconductance
RF	Radio frequency
sccm	cubic centimetre per minute at STP
SE	Spectroscopic ellipsometry
SEM	Scanning electron microscopy
SiH_4	Silane
SIMS	Secondary-ion mass spectroscopy
SRH	Shockley-Read-Hall
TEM	Transmission electron microscopy
TCO	Transparent conductive oxide
TT, TD	Total and diffuse transmittance
UV	Ultraviolet
VB	Valence band
VHF	Very high frequency
XPS	X-ray excitation photoelectron spectroscopy
XRD	X-ray diffraction
ZnO, ZnO:B	(B-doped) Zinc oxide

References

[1] D. M. Bagnall and M. Boreland. *Photovoltaic technologies*. Energy Policy, 36 (12), pp. 4390-4396, 2008.

[2] *2011 Key World Energy Statistics*, International Energy Agency, 2011.

[3] *World Energy Outlook 2010*, International Energy Agency, 2010.

[4] *2010 Solar Technologies Market Report*, U.S. Department of Energy - Energy Efficiency & Renewable Energy, 2011.

[5] *Global Market Outlook for Photovoltaic until 2016*, European Photovoltaic Industry Association, 2012.

[6] L. L. Kazmerski. *Solar photovoltaics R&D at the tipping point: A 2005 technology overview*. Journal of Electron Spectroscopy and Related Phenomena, 150 (2-3), pp. 105-135, 2006.

[7] K. L. Chopra, P. D. Paulson, and V. Dutta. *Thin-film solar cells: An overview*. Progress in Photovoltaics: Research and Applications, 12 (23), pp. 69-92, 2004.

[8] H. S. Ullal and B. von Roedern. *Thin film CIGS and CdTe photovoltaic technologies: Commercialization, critical issues, and applications* in 22nd European Photovoltaic Solar Energy Conference and Exhibition, Milan (Italy), 2007.

[9] J. Zhao, A. Wang, and M. A. Green. *24.5% efficiency silicon PERT cells on MCZ substrates and 24.7% efficiency PERL cells on FZ substrates*. Progress in Photovoltaics: Research and Applications, 7 (6), pp. 471-474, 1999.

[10] P. J. Cousins, D. D. Smith, H. C. Luan, J. Manning, T. D. Dennis, A. Waldhauer et al. *Gen III: Improved performance at lower cost* in 35th IEEE Photovoltaic Specialists Conference, Honolulu (Hawaii), 2010.

[11] *Renewable Energy Technologies: Cost Analysis Series. Solar Photovoltaics* vol. 1: Power Sector, International Renewable Energy Agency, 2012.

[12] A. G. Aberle. *Surface passivation of crystalline silicon solar cells: A review*. Progress in Photovoltaics: Research and Applications, 8 (5), pp. 473-487, 2000.

[13] A. W. Blakers and M. A. Green. *20% efficiency silicon solar cells*. Applied Physics Letters, 48 (3), pp. 215-217, 1986.

[14] S. W. Glunz. *High-Efficiency Crystalline Silicon Solar Cells*. Advances in OptoElectronics, 2007 (97370), 2007.

[15] S. W. Glunz, A. B. Sproul, W. Warta, and W. Wettling. *Injection-level-dependent recombination velocities at the Si-*SiO_2 *interface for various dopant concentrations*. Journal of Applied Physics, 75 (3), pp. 1611-1615, 1994.

[16] A. W. Stephens, A. G. Aberle, and M. A. Green. *Surface recombination velocity measurements at the silicon-silicon dioxide interface by microwave-detected photoconductance decay*. Journal of Applied Physics, 76 (1), pp. 363-370, 1994.

[17] S. Wenham. *Buried-contact silicon solar cells*. Progress in Photovoltaics: Research and Applications, 1 (1), pp. 3-10, 1993.

[18] J. Zhao, A. Wang, and M. A. Green. *24.5% efficiency PERT silicon solar cells on SEH MCZ substrates and cell performance on other SEH CZ and FZ substrates*. Solar Energy Materials and Solar Cells, 66 (1-4), pp. 27-36, 2001.

[19] M. Kerr, J. and A. Cuevas. *Very low bulk and surface recombination in oxidized silicon wafers*. Semiconductor Science and Technology, 17 (1), p. 35, 2002.

[20] O. Schultz, S. Riepe, and S. W. Glunz. *Influence of high-temperature processes on multicrystalline silicon*. Solid State Phenomena, 95-96, pp. 235-242, 2003.

[21] D. Macdonald and A. Cuevas. *The trade-off between phosphorus gettering and thermal degradation in multicrystalline silicon* in 16th European Photovoltaic Solar Energy Conference, Glasgow (UK), 2000, pp. 1707-1710.

[22] F. Huster. *Aluminum-back surface field: Bow investigation and elimination* in 20th European Photovoltaic Solar Energy Conference, Barcelona (Spain), 2005, pp. 635-638.

[23] J.-W. Jeong, A. Rohatgi, V. Yelundur, A. Ebong, M. D. Rosenblum, and J. P. Kalejs. *Enhanced silicon solar cell performance by rapid thermal firing of screen-printed metals*. IEEE Transactions on Electron Devices, 48 (12), pp. 2836-2841, 2001.

[24] M. J. Kerr, J. Schmidt, A. Cuevas, and J. H. Bultman. *Surface recombination velocity of phosphorus-diffused silicon solar cell emitters passivated with plasma enhanced chemical vapor deposited silicon nitride and thermal silicon oxide*. Journal of Applied Physics, 89 (7), pp. 3821-3826, 2001.

[25] V. Verlaan, C. H. M. van der Werf, Z. S. Houweling, I. G. Romijn, A. W. Weeber, H. F. W. Dekkers et al. *Multi-crystalline Si solar cells with very fast deposited (180nm/min) passivating hot-wire CVD silicon nitride as antireflection coating*. Progress in Photovoltaics: Research and Applications, 15 (7), pp. 563-573, 2007.

[26] H. Fujiwara, T. Kaneko, and M. Kondo. *Application of hydrogenated amorphous silicon oxide layers to c-Si heterojunction solar cells*. Applied Physics Letters, 91 (13), p. 133508, 2007.

[27] J. Sritharathikhun, C. Banerjee, M. Otsubo, T. Sugiura, H. Yamamoto, T. Sato et al. *Surface passivation of crystalline and polycrystalline silicon using hydrogenated amorphous silicon oxide film*. Japanese Journal of Applied Physics, 46 (6A), pp. 3296-3300, 2007.

[28] T. Mueller, W. Duengen, R. Job, M. Scherff, and W. Fahrner. *Crystalline silicon surface passivation by PECV-Deposited hydrogenated amorphous silicon oxide films [a-SiO$_x$:H]* in Materials Research Society Fall Meeting, Boston (USA), 2006, 0989-A05-02.

[29] I. Martín, M. Vetter, A. Orpella, C. Voz, J. Puigdollers, and R. Alcubilla. *Surface passivation of n-type crystalline Si by plasma-enhanced-chemical-vapor-deposited amorphous* SiC_x*:H and amorphous* SiC_xN_y*:H films*. Applied Physics Letters, 81 (23), p. 4461, 2002.

[30] R. Ferre, I. Martín, M. Vetter, M. Garín, and R. Alcubilla. *Effect of amorphous silicon carbide layer thickness on the passivation quality of crystalline silicon surface*. Applied Physics Letters, 87 (20), p. 202109, 2005.

[31] C. Ehling, J. H. Werner, and M. B. Schubert. *a-SiC:H passivation for crystalline silicon solar cells*. Physica Status Solidi (C), pp. 1016-1020, 2010.

[32] B. Hoex, S. B. S. Heil, E. Langereis, M. C. M. van de Sanden, and W. M. M. Kessels. *Ultralow surface recombination of c-Si substrates passivated by plasma-assisted atomic layer deposited* Al_2O_3. Applied Physics Letters, 89 (4), p. 042112, 2006.

[33] F. Werner, B. Veith, V. Tiba, P. Poodt, F. Roozeboom, R. Brendel et al. *Very low surface recombination velocities on p- and n-type c-Si by ultrafast spatial atomic layer deposition of aluminum oxide*. Applied Physics Letters, 97 (16), p. 162103, 2010.

[34] S. Olibet, E. Vallat-Sauvain, and C. Ballif. *Model for a-Si:H/c-Si interface recombination based on the amphoteric nature of silicon dangling bonds*. Physical Review B, 76 (3), 2007.

[35] U. K. Das, M. Z. Burrows, M. Lu, S. Bowden, and R. W. Birkmire. *Surface passivation and heterojunction cells on Si (100) and (111) wafers using dc and rf plasma deposited Si:H thin films*. Applied Physics Letters, 92 (6), p. 063504, 2008.

[36] J. Damon-Lacoste, L. Fesquet, S. Olibet, and C. Ballif. *Ultra-high quality surface passivation of crystalline silicon wafers in large area parallel plate reactor at 40 MHz*. Thin Solid Films, 517 (23), pp. 6401-6404, 2009.

[37] S. De Wolf, S. Olibet, and C. Ballif. *Stretched-exponential a-Si:H/c-Si interface recombination decay*. Applied Physics Letters, 93 (3), p. 032101, 2008.

[38] T. Lauinger, J. Schmidt, A. G. Aberle, and R. Hezel. *Record low surface recombination velocities on 1 Ωcm p-silicon using remote plasma silicon nitride passivation*. Applied Physics Letters, 68 (9), p. 1232, 1996.

[39] M. J. Kerr and A. Cuevas. *Recombination at the interface between silicon and stoichiometric plasma silicon nitride*. Semiconductor Science and Technology, 17 (2), p. 166, 2002.

[40] S. Dauwe, L. Mittelstädt, A. Metz, and R. Hezel. *Experimental evidence of parasitic shunting in silicon nitride rear surface passivated solar cells*. Progress in Photovoltaics: Research and Applications, 10 (4), pp. 271-278, 2002.

[41] Y. Larionova, V. Mertens, N.-P. Harder, and R. Brendel. *Surface passivation of n-type Czochralski silicon substrates by thermal-*SiO_2*/plasma-enhanced chemical vapor deposition SiN stacks*. Applied Physics Letters, 96 (3), p. 032105, 2010.

[42] G. Dingemans, M. M. Mandoc, S. Bordihn, M. C. M. van de Sanden, and W. M. M. Kessels. *Effective passivation of Si surfaces by plasma deposited* SiO_x*/a-*SiN_x*:H stacks*. Applied Physics Letters, 98 (22), p. 222102, 2011.

[43] S. Gatz, H. Plagwitz, P. P. Altermatt, B. Terheiden, and R. Brendel. *Thermal stability of amorphous silicon/silicon nitride stacks for passivating crystalline silicon solar cells*. Applied Physics Letters, 93 (17), p. 173502, 2008.

[44] T. Mueller. *Heterojunction solar cells (a-Si/c-Si). Investigations on PECV Deposited hydrogenated silicon alloys for use as high-quality surface passivation and emitter/BSF*. PhD Thesis, Department of Mathematics and Information Technology, University of Hagen (Germany), 2009.

[45] S. Rattanapan, T. Watahiki, S. Miyajima, A. Yamada, and M. Konagai. *High efficiency P-SHJ solar cells with hydrogenated amorphous silicon oxide front intrinsic buffer layer* in 25th European Photovoltaic Solar Energy Conference and Exhibition, Valencia (Spain), 2010, pp. 1282-1285.

[46] I. Martín, M. Vetter, M. Garín, A. Orpella, C. Voz, J. Puigdollers et al. *Crystalline silicon surface passivation with amorphous* SiC_x*:H films deposited by plasma-enhanced chemical-vapor deposition*. Journal of Applied Physics, 98 (11), p. 114912, 2005.

[47] S. W. Glunz, A. Grohe, M. Hermle, M. Hofmann, S. Janz, T. Roth et al. *Comparison of different dielectric passivation layers for application in industrially feasible high-efficiency cristalline silicon solar cells* in 20th European Photovoltaic Solar Energy Conference, Barcelona (Spain), 2000, pp. 572-577.

[48] G. Agostinelli, A. Delabie, P. Vitanov, Z. Alexieva, H. F. W. Dekkers, S. De Wolf et al. *Very low surface recombination velocities on p-type silicon wafers passivated with a dielectric with fixed negative charge*. Solar Energy Materials and Solar Cells, 90 (18-19), pp. 3438-3443, 2006.

[49] B. Hoex, J. Schmidt, M. C. M. van de Sanden, and W. M. M. Kessels. *Crystalline silicon surface passivation by the negative-charge-dielectric Al* in 33rd IEEE Photovoltaic Specialists Conference, 2008, pp. 1-4.

[50] J. Schmidt, A. Merkle, R. Brendel, B. Hoex, M. C. M. v. de Sanden, and W. M. M. Kessels. *Surface passivation of high-efficiency silicon solar cells by atomic-layer-deposited* Al_2O_3. Progress in Photovoltaics: Research and Applications, 16 (6), pp. 461-466, 2008.

[51] P. Poodt, A. Lankhorst, F. Roozeboom, K. Spee, D. Maas, and A. Vermeer. *High-speed spatial atomic-layer deposition of aluminum oxide layers for solar cell passivation*. Advanced Materials, 22 (32), pp. 3564-3567, 2010.

[52] S. Dauwe, J. Schmidt, and R. Hezel. *Very low surface recombination velocities on p- and n-type silicon wafers passivated with hydrogenated amorphous silicon films* in 29th IEEE Photovoltaic Specialists Conference, 2002, pp. 1246-1249.

[53] M. Garín, U. Rau, W. Brendle, I. Martín, and R. Alcubilla. *Characterization of a-Si:H/c-Si interfaces by effective-lifetime measurements*. Journal of Applied Physics, 98 (9), p. 093711, 2005.

[54] J.-W. A. Schüttauf, K. H. M. van der Werf, I. M. Kielen, W. G. J. H. M. van Sark, J. K. Rath, and R. E. I. Schropp. *Excellent crystalline silicon surface passivation by amorphous silicon irrespective of the technique used for chemical vapor deposition*. Applied Physics Letters, 98 (15), p. 153514, 2011.

[55] M. Schaper, J. Schmidt, H. Plagwitz, and R. Brendel. *20.1%-efficient crystalline silicon solar cell with amorphous silicon rear-surface passivation*. Progress in Photovoltaics: Research and Applications, 13 (5), pp. 381-386, 2005.

[56] S. De Wolf, A. Descoeudres, Z. C. Holman, and C. Ballif. *High-efficiency silicon heterojunction solar cells: A review*. Green, 2 (1), pp. 7-24, 2012.

[57] H. Sakata, Y. Tsunomura, H. Inoue, S. Taira, T. Baba, K. Kanno et al. *R&D progress of next-generation very thin HIT solar cells* in 25th European Photovoltaic Solar Energy Conference and Exhibition, Valencia (Spain), 2010, pp. 1102-1105.

[58] M. Tanaka, M. Taguchi, T. Matsuyama, T. Sawada, S. Tsuda, S. Nakano et al. *Development of new a-Si/c-Si heterojunction solar cells: ACJ-HIT (Artificially Constructed Junction-Heterojunction with Intrinsic Thin-Layer)*. Japanese Journal of Applied Physics, 31, pp. 3518-3522, 1992.

[59] W. Fuhs, K. Niemann, and J. Stuke. *Heterojunctions of amorphous silicon and silicon single crystals* in AIP Conference Proceedings, 1974, 20, pp. 345-350.

[60] K. Okuda, H. Okamoto, and Y. Hamakawa. *Amorphous Si/polycrystalline Si stacked solar cell having more than 12% conversion efficiency*. Japanese Journal of Applied Physics Jpn. J. Appl. Phys., 22, pp. 605-607, 1983.

[61] Y. Hamakawa, K. Fujimoto, K. Okuda, Y. Kashima, S. Nonomura, and H. Okamoto. *New types of high efficiency solar cells based on a-Si*. Applied Physics Letters, 43 (7), pp. 644-646, 1983.

[62] K. Wakisaka, M. Taguchi, T. Sawada, M. Tanaka, T. Matsuyama, T. Matsuoka et al. *More than 16% solar cells with a new "HIT" (doped a-Si/non-doped a-Si/crystalline Si) structure* in 22nd Photovoltaic Specialists Conference, Las Vegas (USA), 1991, p. 887.

[63] *SANYO Electric Co. Ltd. "Sanyo develops hit solar cells with world's highest energy conversion efficiency of 23%"* (press release, May 2009)

[64] T. Kinoshita, D. Fujishima, A. Yano, A. Ogane, S. Tohoda, K. Matsuyama et al. *The approaches for high efficiency HIT^{TM} solar cell with very thin (<100 µm) silicon wafer over 23%* in 26th European Photovoltaic Solar Energy Conference and Exhibition, Hamburg (Germany), 2011, pp. 871-874.

[65] N. Nakamura, M. Ouchi, K. Ibi, and Y. Watabe. *New approaches to mass production of heterojunction silicon solar cells* in 26th European Photovoltaic Solar Energy Conference and Exhibition, Hamburg (Germany), 2011, pp. 2194-2197.

[66] *HIT photovoltaic module* (September 2012). http://panasonic.net/energy/solar/hit/

[67] M. Taguchi, A. Terakawa, E. Maruyama, and M. Tanaka. *Obtaining a higher*V_{OC} *in HIT cells*. Progress in Photovoltaics: Research and Applications, 13 (6), pp. 481-488, 2005.

[68] M. Taguchi, H. Sakata, Y. Yoshimine, E. Maruyama, A. Terakawa, M. Tanaka et al. *An approach for the higher efficiency in the HIT cells* in 31st IEEE Photovoltaic Specialists Conference, 2005, pp. 866-871.

[69] D. Bätzner, Y. Andrault, L. Andreetta, A. Buechel, W. Frammelsberger, C. Guerin et al. *Characterisation of Over 21% Efficient Silicon Heterojunction Cells Developed at Roth & Rau Switzerland* in 26th European Photovoltaic Solar Energy Conference and Exhibition, Hamburg (Germany), 2011, pp. 1073-1075.

[70] T. Mishima, M. Taguchi, H. Sakata, and E. Maruyama. *Development status of high-efficiency HIT solar cells*. Solar Energy Materials and Solar Cells, 95 (1), pp. 18-21, 2011.

[71] P.-J. Ribeyron, D. Muñoz, J.-P. Kleider, W. Favre, P. R. i. Cabarrocas, M. Labrune et al. *European record efficiency amorphous-crystalline-silicon heterojunction solar cells: Final results from the HETSI project* in 26th European Photovoltaic Solar Energy Conference and Exhibition, Hamburg (Germany), 2011, pp. 853-857.

[72] D. Muñoz, T. Desrues, A.-S. Ozanne, N. Nguyen, S. D. Vecchi, F. Souche et al. *Progress on high efficiency standard and interdigitated back contact silicon heterojunction solar cells* in 26th European Photovoltaic Solar Energy Conference and Exhibition, Hamburg (Germany), 2011, pp. 861-864.

[73] P. J. Rostan, U. Rau, and J. H. Werner. *TCO/(n type)a-Si:H/(p-type)c-Si heterojunction solar cells with high open circuit voltage* in 21st European Photovoltaic Solar Energy Conference, Dresden (Germany), 2006, pp. 1181-1184.

[74] Q. Wang, M. R. Page, E. Iwancizko, Y. Xu, L. Roybal, R. Bauer et al. *High open-circuit voltage in silicon heterojunction solar cells* in Materials Research Society Spring Meeting, 2007, 0989-A03-04.

[75] M. Tucci, L. Serenelli, S. De Iuliis, D. Caputo, A. Nascetti, and G. De Cesare. *Amorphous/crystalline silicon heterostructure solar cell based on multi-crystalline silicon* in 21st European Photovoltaic Solar Energy Conference, Dresden (Germany), 2006, pp. 902-905.

[76] *Kaneka* (press release, June 2012). http://www.kaneka.co.jp/kaneka-e/

[77] H. Fujiwara and M. Kondo. *Real-time monitoring and process control in amorphous/crystalline silicon heterojunction solar cells by spectroscopic ellipsometry and infrared spectroscopy*. Applied Physics Letters, 86 (3), p. 032112, 2005.

[78] H. Fujiwara and M. Kondo. *Impact of epitaxial growth at the heterointerface of a-Si:H/c-Si solar cells*. Applied Physics Letters, 90 (1), p. 013503, 2007.

[79] J. Sritharathikhun, F. Jiang, S. Miyajima, A. Yamada, and M. Konagai. *Optimization of p-type hydrogenated microcrystalline silicon oxide window layer for*

high-efficiency crystalline silicon heterojunction solar cells. Japanese Journal of Applied Physics, 48, 2009.

[80] V. A. Dao, J. Heo, H. Choi, Y. Kim, S. Park, S. Jung et al. *Simulation and study of the influence of the buffer intrinsic layer, back-surface field, densities of interface defects, resistivity of p-type silicon substrate and transparent conductive oxide on heterojunction with intrinsic thin-layer (HIT) solar cell*. Solar Energy, 84 (5), pp. 777-783, 2010.

[81] L. Zhao, C. Zhou, H. Li, H. Diao, and W. Wang. *Characterization on the passivation stability of HF aqueous solution treated silicon surfaces for HIT solar cell application by the effective minority carrier lifetime measurement*. Chinese Journal of Physics, 48 (3), pp. 392-399, 2010.

[82] Q. Wang, M. R. Page, E. Iwaniczko, Y. Xu, L. Roybal, R. Bauer et al. *Efficient heterojunction solar cells on p-type crystal silicon wafers*. Applied Physics Letters, 96 (1), p. 013507, 2010.

[83] T. H. Wang, E. Iwaniczko, M. R. Page, D. H. Levi, Y. Yan, H. M. Branz et al. *Effect of emitter deposition temperature on surface passivation in hot-wire chemical vapor deposited silicon heterojunction solar cells*. Thin Solid Films, 501 (1-2), pp. 284-287, 2006.

[84] A. Descoeudres, L. Barraud, P. Bôle Rothen, S. De Wolf, B. Demaurex, and e. al. *21% efficiency silicon heterojunction solar cells produced with very high frequency PECVD* in 21st International Photovoltaic Science and Engineering Conference, Fukuoka (Japan), 2011.

[85] W. Fuhs, L. Korte, and M. Schmidt. *Heterojunctions of hydrogenated amorphous silicon and monocrystalline silicon*. Journal of Optoelectronics and Advanced Materials, 8 (6), pp. 1989-1995, 2006.

[86] M. Lu, S. Bowden, U. Das, and R. Birkmire. *Interdigitated back contact silicon heterojunction solar cell and the effect of front surface passivation*. Applied Physics Letters, 91 (6), p. 063507, 2007.

[87] T. Desrues, F. Souche, A. Vandeneynde, D. Muñoz, A. S. Ozanne, and P. J. Ribeyron. *Emitter optimization for interdigitated back contact (IBC) silicon heterojunction (Si-HJ) solar cells* in 25th European Photovoltaic Solar Energy Conference and Exhibition, Valencia (Spain), 2010, pp. 2374-2377.

[88] M. W. P. E. Lamers, A. A. Mewe, I. G. Romijn, E. E. Bende, Y. Komatsu, M. Koppes et al. *Towards 21% efficient n-Cz IBC based on screen printing* in 26th European Photovoltaic Solar Energy Conference and Exhibition, Hamburg (Germany), 2011, pp. 2239-2242.

[89] W. van Sark, L. Korte, and F. Roca, Eds., *Physics and technology of amorphous-crystalline heterostructure silicon solar cells*. Springer (Series in Engineering Materials), 2012.

[90] D. Muñoz, P. Carreras, J. Escarré, D. Ibarz, S. Martín de Nicolás, C. Voz et al. *Optimization of KOH etching process to obtain textured substrates suitable for*

heterojunction solar cells fabricated by HWCVD. Thin Solid Films, 517 (12), pp. 3578-3580, 2009.

[91] H. Seidel, L. Csepregi, A. Heuberger, and H. Baumgärtel. *Anisotropic etching of crystalline silicon in alkaline solutions*. Journal of The Electrochemical Society, 137 (11), pp. 3626-3632, 1990.

[92] P. Campbell and M. A. Green. *Light trapping properties of pyramidally textured surfaces*. Journal of Applied Physics, 62 (1), pp. 243-249, 1987.

[93] T. Yagi, Y. Uraoka, and T. Fuyuki. *Ray-trace simulation of light trapping in silicon solar cell with texture structures*. Solar Energy Materials and Solar Cells, 90 (16), pp. 2647-2656, 2006.

[94] T. H. Wang, E. Iwaniczko, M. R. Page, W. Qi, Y. Xu, Y. Yan et al. *High-efficiency silicon heterojunction solar cells by HWCVD* in 4th IEEE World Conference on Photovoltaic Energy Conversion, Waikoloa (Hawaii), 2006, 2, pp. 1439-1442.

[95] M. R. Page, E. Iwaniczko, Y. Xu, Q. Wang, Y. Yan, L. Roybal et al. *Well-passivated a-Si:H back contacts for double-heterojunction silicon solar cells* in 4th IEEE World Conference on Photovoltaic Energy Conversion, Waikoloa (Hawaii), 2006, 2, pp. 1485-1488.

[96] H. Angermann, J. Rappich, L. Korte, I. Sieber, E. Conrad, M. Schmidt et al. *Wet-chemical passivation of atomically flat and structured silicon substrates for solar cell application*. Applied Surface Science, 254 (12), pp. 3615-3625, 2008.

[97] J. I. Pankove and M. L. Tarng. *Amorphous silicon as a passivant for crystalline silicon*. Applied Physics Letters, 34 (2), pp. 156-157, 1979.

[98] F. Ruske. *Deposition and Properties of TCOs* in *Physics and technology of amorphous-crystalline heterostructure silicon solar cells*, W. van Sark et al., Eds., Springer, 2012.

[99] Y. Tsunomura, Y. Yoshimine, M. Taguchi, T. Baba, T. Kinoshita, H. Kanno et al. *Twenty-two percent efficiency HIT solar cell*. Solar Energy Materials and Solar Cells, 93 (6-7), pp. 670-673, 2009.

[100] R. Stangl, A. Froitzheim, M. Schmidt, and W. Fuhs. *Design criteria for amorphous/crystalline silicon heterojunction solar cells - a simulation study* in 3rd World Conference on Photovoltaic Energy Conversion, Osaka (Japan), 2003, 2, pp. 1005-1008.

[101] L. Korte and M. Schmidt. *Investigation of gap states in phosphorous-doped ultra-thin a-Si:H by near-UV photoelectron spectroscopy*. Journal of Non-Crystalline Solids, 354 (19-25), pp. 2138-2143, 2008.

[102] M. Schmidt, A. Schoepke, L. Korte, O. Milch, and W. Fuhs. *Density distribution of gap states in extremely thin a-Si:H layers on crystalline silicon wafers*. Journal of Non-Crystalline Solids, 338-340, pp. 211-214, 2004.

[103] M. Tucci, M. della Noce, E. Bobeico, F. Roca, G. de Cesare, and F. Palma. *Comparison of amorphous/crystalline heterojunction solar cells based on n- and p-type crystalline silicon*. Thin Solid Films, 451-452, pp. 355-360, 2004.

[104] U. Das, S. Hegedus, Z. Lulu, J. Appel, J. Rand, and R. Birkmire. *Investigation of hetero-interface and junction properties in silicon heterojunction solar cells* in 35th IEEE Photovoltaic Specialists Conference, 2010, pp. 001358-001362.

[105] K. Ellmer, A. Klein, and B. Rech, Eds., *Transparent conductive zinc oxide. Basics and applications in thin film solar cells*. Springer (Series in Materials Science), 2008.

[106] I. Martín. *Silicon surface passivation by plasma enhanced chemical vapor depsoited amorphous silicon carbide films*. PhD Thesis, Departament d'Enginyeria Electrònica, Universitat Politècnica de Catalunya, Barcelona (Spain), 2004.

[107] M. A. Green. *Solar cells: Operating principles, technology and system applications*. Centre for Photovoltaic Devices and Systems, University of New South Wales, 1992.

[108] S. M. Sze. *Physics of Semiconductor Devices*. 2nd ed. John Wiley & Sons, 1981.

[109] H. Schlangenotto, H. Maeder, and W. Gerlach. *Temperature dependence of the radiative recombination coefficient in silicon*. Physica Status Solidi (A), 21 (1), pp. 357-367, 1974.

[110] T. Trupke, M. A. Green, P. Wurfel, P. P. Altermatt, A. Wang, J. Zhao et al. *Temperature dependence of the radiative recombination coefficient of intrinsic crystalline silicon*. Journal of Applied Physics, 94 (8), pp. 4930-4937, 2003.

[111] Y. P. Varshni. *Band-to-band radiative recombination in groups IV, VI, and III-V semiconductors (I)*. Physica Status Solidi (B), 19 (2), pp. 459-514, 1967.

[112] A. Hangleiter and R. Häcker. *Enhancement of band-to-band Auger recombination by electron-hole correlations*. Physical Review Letters, 65 (2), pp. 215-218, 1990.

[113] J. Dziewior and W. Schmid. *Auger coefficients for highly doped and highly excited silicon*. Applied Physics Letters, 31 (5), pp. 346-348, 1977.

[114] R. A. Sinton and R. M. Swanson. *Recombination in highly injected silicon*. IEEE Transactions on Electron Devices, 34 (6), pp. 1380-1389, 1987.

[115] P. P. Altermatt, J. Schmidt, G. Heiser, and A. G. Aberle. *Assessment and parameterisation of Coulomb-enhanced Auger recombination coefficients in lowly injected crystalline silicon*. Journal of Applied Physics, 82 (10), pp. 4938-4944, 1997.

[116] M. J. Kerr and A. Cuevas. *General parameterization of Auger recombination in crystalline silicon*. Journal of Applied Physics, 91 (4), pp. 2473-2480, 2002.

[117] W. Shockley and W. T. Read, Jr. *Statistics of the recombinations of holes and electrons*. Physical Review, 87 (5), pp. 835-842, 1952.

[118] R. N. Hall. *Electron-hole recombination in germanium*. Physical Review, 87 (2), pp. 387-387, 1952.

[119] D. E. Kane and R. M. Swanson. *Measurement of the emitter saturation current by a contactless photoconductivity decay method* in 18th IEEE Photovoltaic Specialists Conference, Las Vegas (USA), 1985, pp. 578-583.

[120] J. Brody, A. Rohatgi, and A. Ristow. *Review and comparison of equations relating bulk lifetime and surface recombination velocity to effective lifetime measured under flash lamp illumination*. Solar Energy Materials and Solar Cells, 77 (3), pp. 293-301, 2003.

[121] S. Olibet. *Properties of interfaces in amorphous/crystalline silicon heterojunctions*. PhD Thesis, Faculté des Sciences, Institute de Microtechnique, Université de Neuchâtel (Switzerland), 2009.

[122] R. Ferré. *Surface passivation of crystalline silicon by amorphous silicon carbide films for photovoltaic applications*. PhD Thesis, Departament d'Enginyeria Electrònica, Universitat Politècnica de Catalunya, Barcelona (Spain), 2008.

[123] I. Martín, M. Vetter, A. Orpella, C. Voz, J. Puigdollers, R. Alcubilla et al. *Improvement of crystalline silicon surface passivation by hydrogen plasma treatment*. Applied Physics Letters, 84 (9), pp. 1474-1476, 2004.

[124] C. Leendertz and R. Stangl. *Modeling an a-Si:H/c-Si solar cell with AFORS-HET* in *Physics and technology of amorphous-crystalline heterostructure silicon solar cells*, W. van Sark et al., Eds., Springer, 2012.

[125] *Silvaco Atlas simulation tool* (September 2012). http://www.silvaco.com/products/device_simulation/atlas.html

[126] R. L. Anderson. *Experiments on Ge-GaAs heterojunctions*. Solid-State Electronics, 5 (5), pp. 341-351, 1962.

[127] R. Stangl, A. Froitzheim, L. Elstner, and W. Fuhs. *Amorphous/crystalline silicon heterojunction solar cells, a simulation study* in 17th European Photovoltaic Solar Energy Conference, Munich (Germany), 2001, p. 1387.

[128] F. Rubinelli, S. Albornoz, and R. Buitrago. *Amorphous-crystalline silicon heterojunction: Theoretical evaluation of the current terms*. Solid-State Electronics, 32 (10), pp. 813-825, 1989.

[129] D. Muñoz. *Silicon heterojunction solar cells obtained by Hot-Wire CVD*. PhD Thesis, Departament d'Enginyeria Electrònica, Universitat Politècnica de Catalunya, Barcelona (Spain), 2008.

[130] T. H. Wang, M. R. Page, E. Iwaniczko, D. H. Levi, Y. Yan, H. M. Branz et al. *Toward better understanding and improved performance of silicon heterojunction solar cells* in 14th Workshop on Crystalline Silicon Solar Cells and Modules, Colorado (USA), 2004.

[131] K. v. Maydell, E. Conrad, and M. Schmidt. *Efficient silicon heterojunction solar cells based on p- and n-type substrates processed at temperatures <220°C*. Progress in Photovoltaics: Research and Applications, 14 (4), pp. 289-295, 2006.

[132] L. Korte, E. Conrad, H. Angermann, R. Stangl, and M. Schmidt. *Advances in a-Si:H/c-Si heterojunction solar cell fabrication and characterization*. Solar Energy Materials and Solar Cells, 93 (6-7), pp. 905-910, 2009.

[133] M. Tucci and G. de Cesare. *17% efficiency heterostructure solar cell based on p-type crystalline silicon*. Journal of Non-Crystalline Solids, 338-340, pp. 663-667, 2004.

[134] J. Damon-Lacoste and P. Roca i Cabarrocas. *Toward a better physical understanding of a-Si:H/c-Si heterojunction solar cells*. Journal of Applied Physics, 105 (6), p. 063712, 2009.

[135] H. Mäckel. *Capturing the spectra of solar cells*. PhD Thesis, The Australian National University (Australia), 2004.

[136] K. Tanaka, E. Maruyama, T. Shimada, and H. Okamoto. *Amorphous Silicon*. John Wiley & Sons, 1999.

[137] R. A. Street. *Hydrogenated Amorphous Silicon*. Cambridge University Press, 1991.

[138] W. E. Spear and P. G. Le Comber. *Substitutional doping of amorphous silicon*. Solid State Communications, 17 (9), pp. 1193-1196, 1975.

[139] E. A. Davis and N. F. Mott. *Conduction in non-crystalline systems V. Conductivity, optical absorption and photoconductivity in amorphous semiconductors*. Philosophical Magazine, 22 (179), pp. 0903-0922, 1970.

[140] K. Winer. *Chemical-equilibrium description of the gap-state distribution in a-Si:H*. Physical Review Letters, 63 (14), pp. 1487-1490, 1989.

[141] M. J. Powell and S. C. Deane. *Improved defect-pool model for charged defects in amorphous silicon*. Physical Review B, 48 (15), pp. 10815-10827, 1993.

[142] W. M. M. Kessels, A. H. M. Smets, D. C. Marra, E. S. Aydil, D. C. Schram, and M. C. M. van de Sanden. *On the growth mechanism of a-Si:H*. Thin Solid Films, 383 (1-2), pp. 154-160, 2001.

[143] P. Roca i Cabarrocas. *Deposition techniques and processes involved in the growth of amorphous and microcrystalline silicon thin films* in *Physics and technology of amorphous-crystalline heterostructure silicon solar cells*, W. van Sark et al., Eds., Springer, 2012.

[144] R. A. Sinton and A. Cuevas. *Contactless determination of current–voltage characteristics and minority-carrier lifetimes in semiconductors from quasi-steady-state photoconductance data*. Applied Physics Letters, 69 (17), p. 2510, 1996.

[145] J. G. E. Jellison and F. A. Modine. *Parameterization of the optical functions of amorphous materials in the interband region*. Applied Physics Letters, 69 (3), pp. 371-373, 1996.

[146] R. A. Sinton and A. Cuevas. *A quasi-steady-state open-circuit voltage method for solar cell characterization* in 16th European Photovoltaic Solar Energy Conference, Glasgow (UK), 2000, pp. 1152-1155.

[147] R. Schropp and M. Zeman, Eds., *Amorphous and microcrystalline silicon solar cells*. Kluwer Academic Publishers), 1998.

[148] C. Longeaud and J. Kleider. *General analysis of the modulated-photocurrent experiment including the contributions of holes and electrons*. Physical Review B, 45 (20), pp. 11672-11684, 1992.

[149] M. Labrune, M. Moreno, and P. Roca i Cabarrocas. *Ultra-shallow junctions formed by quasi-epitaxial growth of boron and phosphorous-doped silicon films at 175°C by rf-PECVD*. Thin Solid Films, 518 (9), pp. 2528-2530, 2010.

[150] C. Leendertz, R. Stangl, T. F. Schulze, M. Schmidt, and L. Korte. *A recombination model for a-Si:H/c-Si heterostructures*. Physica Status Solidi (C), pp. 1005-1010, 2010.

[151] C. Leendertz, N. Mingirulli, T. F. Schulze, J. P. Kleider, B. Rech, and L. Korte. *Discerning passivation mechanisms at a-Si:H/c-Si interfaces by means of photoconductance measurements*. Applied Physics Letters, 98 (20), p. 202108, 2011.

[152] T. H. Wang, E. Iwaniczko, M. R. Page, D. H. Levi, Y. Yan, V. Yelundur et al. *Effective interfaces in silicon heterojunction solar cells* in 31st IEEE Photovoltaic Specialist Conference, 2005.

[153] J. Coignus, M. Baudrit, J. Singer, R. Lachaume, D. Muñoz, and P. Thony. *Key issues for accurate simulation of a-Si:H/c-Si heterojunction solar cells*. Energy Procedia, 8, pp. 174-179, 2011.

[154] T. F. Schulze, H. N. Beushausen, C. Leendertz, A. Dobrich, B. Rech, and L. Korte. *Interplay of amorphous silicon disorder and hydrogen content with interface defects in amorphous/crystalline silicon heterojunctions*. Applied Physics Letters, 96 (25), p. 252102, 2010.

[155] D. Pysch, A. Mette, and S. W. Glunz. *A review and comparison of different methods to determine the series resistance of solar cells*. Solar Energy Materials and Solar Cells, 91 (18), pp. 1698-1706, 2007.

[156] N. Hernández-Como and A. Morales-Acevedo. *Simulation of hetero-junction silicon solar cells with AMPS-1D*. Solar Energy Materials and Solar Cells, 94 (1), pp. 62-67, 2010.

[157] J. D. Griffiths. *Introduction to quantum mechanics*. Prentice Hall, 1999.

[158] H. Fujiwara, T. Kaneko, and M. Kondo. *Optimization of interface structures in crystalline silicon heterojunction solar cells*. Solar Energy Materials and Solar Cells, 93 (6-7), pp. 725-728, 2009.

[159] J. F. Wager, D. A. Keszler, and R. E. Presley, Eds., *Transparent Electronics*. Springer), 2008.

[160] S. Calnan and A. N. Tiwari. *High mobility transparent conducting oxides for thin film solar cells*. Thin Solid Films, 518 (7), pp. 1839-1849, 2010.

[161] H. Kawazoe, M. Yasukawa, H. Hyodo, M. Kurita, H. Yanagi, and H. Hosono. *P-type electrical conduction in transparent thin films of $CuAlO_2$*. Nature, 389 (6654), pp. 939-942, 1997.

[162] A. N. Banerjee and K. K. Chattopadhyay. *Recent developments in the emerging field of crystalline p-type transparent conducting oxide thin films*. Progress in Crystal Growth and Characterization of Materials, 50 (1-3), pp. 52-105, 2005.

[163] T. Minami and T. Miyata. *Present status and future prospects for development of non- or reduced-indium transparent conducting oxide thin films*. Thin Solid Films, 517 (4), pp. 1474-1477, 2008.

[164] Ü. Özgür, Y. I. Alivov, C. Liu, A. Teke, M. A. Reshchikov, S. Doğan et al. *A comprehensive review of ZnO materials and devices*. Journal of Applied Physics, 98 (4), p. 041301, 2005.

[165] K. Ellmer and A. Klein. *ZnO and its applications* in *Transparent conductive zinc oxide. Basics and applications in thin film solar cells*, K. Ellmer et al., Eds., Springer, 2008.

[166] H. Zhu, E. Bunte, J. Hüpkes, H. Siekmann, and S. M. Huang. *Aluminium doped zinc oxide sputtered from rotatable dual magnetrons for thin film silicon solar cells*. Thin Solid Films, 517 (10), pp. 3161-3166, 2009.

[167] J. Hu and R. G. Gordon. *Textured aluminum-doped zinc oxide thin films from atmospheric pressure chemical-vapor deposition*. Journal of Applied Physics, 71 (2), p. 880, 1992.

[168] X. L. Chen, B. H. Xu, J. M. Xue, Y. Zhao, C. C. Wei, J. Sun et al. *Boron-doped zinc oxide thin films for large-area solar cells grown by metal organic chemical vapor deposition*. Thin Solid Films, 515 (7-8), pp. 3753-3759, 2007.

[169] O. Kluth, B. Rech, L. Houben, S. Wieder, G. Schöpe, C. Beneking et al. *Texture etched ZnO:Al coated glass substrates for silicon based thin film solar cells*. Thin Solid Films, 351 (1-2), pp. 247-253, 1999.

[170] J. K. Rath, Y. Liu, M. M. de Jong, J. de Wild, J. A. Schuttauf, M. Brinza et al. *Transparent conducting oxide layers for thin film silicon solar cells*. Thin Solid Films, 518 (24), pp. 129-135, 2010.

[171] F. Ruske, M. Roczen, K. Lee, M. Wimmer, S. Gall, J. Hüpkes et al. *Improved electrical transport in Al-doped zinc oxide by thermal treatment*. Journal of Applied Physics, 107 (1), p. 013708, 2010.

[172] S. Faÿ, U. Kroll, C. Bucher, E. Vallat-Sauvain, and A. Shah. *Low pressure chemical vapour deposition of ZnO layers for thin-film solar cells: Temperature-induced morphological changes*. Solar Energy Materials and Solar Cells, 86 (3), pp. 385-397, 2005.

[173] S. Faÿ, L. Feitknecht, R. Schlüchter, U. Kroll, E. Vallat-Sauvain, and A. Shah. *Rough ZnO layers by LP-CVD process and their effect in improving performances of amorphous and microcrystalline silicon solar cells*. Solar Energy Materials and Solar Cells, 90 (18-19), pp. 2960-2967, 2006.

[174] A. P. Roth and D. F. Williams. *Properties of zinc oxide films prepared by the oxidation of diethyl zinc*. Journal of Applied Physics, 52 (11), pp. 6685-6692, 1981.

[175] S. Fäy. *L'oxide de zinc par dépôt chimique en phase vapeur comme contact électrique et diffuseur de lumière pour les cellules solaires*. PhD Thesis, Faculté de Sciences et Techniques de l'Ingénieur, École Polytechnique Fédéral de Lausanne (Switzerland), 2003.

[176] J. Y. W. Seto. *The electrical properties of polycrystalline silicon films*. Journal of Applied Physics, 46 (12), pp. 5247-5254, 1975.

[177] K. Ellmer. *Electrical properties* in *Transparent conductive zinc oxide. Basics and applications in thin film solar cells*, K. Ellmer et al., Eds., Springer, 2008.

[178] K. Ellmer and R. Mientus. *Carrier transport in polycrystalline transparent conductive oxides: A comparative study of zinc oxide and indium oxide*. Thin Solid Films, 516 (14), pp. 4620-4627, 2008.

[179] J. Löffler, R. E. I. Schropp, R. Groenen, M. C. M. v. d. Sanden, and J. L. Linden. *Natively textured ZnO grown by PECVD as front electrode material for amorphous silicon pin solar cells* in 28th IEEE Photovoltaic Specialists Conference, 2000, pp. 822–824.

[180] S. Fäy and A. Shah. *Zinc oxide grown by CVD process as transparent contact for thin film solar cell applications* in *Transparent conductive zinc oxide. Basics and applications in thin film solar cells*, K. Ellmer et al., Eds., Springer, 2008.

[181] J. Steinhauser. *Low pressure chemical vapor deposited zinc oxide for silicon thin film solar cells: Optical and electrical properties*. PhD Thesis, Faculté des Sciences, Université de Neuchâtel (Switzerland), 2008.

[182] K. L. Chopra, S. Major, and D. K. Pandya. *Transparent conductors - A status review*. Thin Solid Films, 102 (1), pp. 1-46, 1983.

[183] W. W. Wenas, A. Yamada, K. Takahashi, M. Yoshino, and M. Konagai. *Electrical and optical properties of boron-doped ZnO thin films for solar cells grown by metalorganic chemical vapor deposition*. Journal of Applied Physics, 70 (11), pp. 7119-7123, 1991.

[184] S. Major, S. Kumar, M. Bhatnagar, and K. L. Chopra. *Effect of hydrogen plasma treatment on transparent conducting oxides*. Applied Physics Letters, 49 (7), p. 394, 1986.

[185] S. Kohiki, M. Nishitani, T. Wada, and T. Hirao. *Enhanced conductivity of zinc oxide thin films by ion implantation of hydrogen atoms*. Applied Physics Letters, 64 (21), p. 2876, 1994.

[186] S. Yeopmyong and K. Sulim. *Improvement of electrical and optical properties of ZnO thin films prepared by MOCVD using UV light irradiation and H post-treatment*. Solar Energy Materials and Solar Cells, 86 (1), pp. 105-112, 2005.

[187] P. F. Cai, J. B. You, X. W. Zhang, J. J. Dong, X. L. Yang, Z. G. Yin et al. *Enhancement of conductivity and transmittance of ZnO films by post hydrogen plasma treatment*. Journal of Applied Physics, 105 (8), p. 083713, 2009.

[188] S. J. Baik, J. H. Jang, C. H. Lee, W. Y. Cho, and K. S. Lim. *Highly textured and conductive undoped ZnO film using hydrogen post-treatment*. Applied Physics Letters, 70 (26), p. 3516, 1997.

[189] C. G. Van de Walle. *Hydrogen as a cause of doping in zinc oxide*. Physical Review Letters, 85 (5), pp. 1012-1015, 2000.

[190] J. Steinhauser, S. Meyer, M. Schwab, S. Faÿ, C. Ballif, U. Kroll et al. *Humid environment stability of low pressure chemical vapor deposited boron doped zinc oxide used as transparent electrodes in thin film silicon solar cells*. Thin Solid Films, 520 (1), pp. 558-562, 2011.

[191] T. Tohsophon, J. Hüpkes, S. Calnan, W. Reetz, B. Rech, W. Beyer et al. *Damp heat stability and annealing behavior of aluminum doped zinc oxide films prepared by magnetron sputtering*. Thin Solid Films, 511–512, pp. 673-677, 2006.

[192] W. Lin, R. Ma, J. Xue, and B. Kang. *RF magnetron sputtered ZnO:Al thin films on glass substrates: A study of damp heat stability on their optical and electrical properties*. Solar Energy Materials and Solar Cells, 91 (20), pp. 1902-1905, 2007.

[193] A. Favier, D. Muñoz, S. Martín de Nicolás, and P. J. Ribeyron. *Boron-doped zinc oxide layers grown by metal-organic CVD for silicon heterojunction solar cells applications*. Solar Energy Materials and Solar Cells, 95 (4), pp. 1057-1061, 2011.

[194] V. N. Zhitomirsky, E. Çetinörgü, E. Adler, Y. Rosenberg, R. L. Boxman, and S. Goldsmith. *Filtered vacuum arc deposition of transparent conducting Al-doped ZnO films*. Thin Solid Films, 515 (3), pp. 885-890, 2006.

[195] S. Y. Myong, S. I. Park, and K. S. Lim. *Improvement of electrical stability of polycrystalline ZnO thin films via intentional post-deposition hydrogen doping*. Thin Solid Films, 513 (1-2), pp. 148-151, 2006.

[196] G. Choong, P. Bôle, L. Barraud, F. Zicalleri, A. Descoeudres, S. D. Wolf et al. *Transparent conductive oxides for silicon heterojunction solar cells* in 25th European Photovoltaic Solar Energy Conference and Exhibition, Valencia (Spain), 2010, pp. 2505-2510.

[197] T. Koida, H. Fujiwara, and M. Kondo. *Reduction of optical loss in hydrogenated amorphous silicon/crystalline silicon heterojunction solar cells by high-mobility hydrogen-doped* In_2O_3 *transparent conductive oxide*. Applied Physics Express, 1 (4), p. 41501, 2008.

[198] M. Balestrieri, D. Pysch, J. P. Becker, M. Hermle, W. Warta, and S. W. Glunz. *Characterization and optimization of indium tin oxide films for heterojunction solar cells*. Solar Energy Materials and Solar Cells, 95 (8), pp. 2390-2399, 2011.

[199] E. V. Johnson, P. Prod'homme, C. Boniface, K. Huet, T. Emeraud, and P. Roca i Cabarrocas. *Excimer laser annealing and chemical texturing of ZnO:Al sputtered at room temperature for photovoltaic applications*. Solar Energy Materials and Solar Cells, 95 (10), pp. 2823-2830, 2011.

[200] J. L. Hernandez, K. Yoshikawa, D. Schroos, E. Van Assche, A. Feltrin, N. Valckx et al. *High efficiency copper electroplated heterojunction solar cells* in 21st International Photovoltaic Science and Engineering Conference, Fukuoka (Japan), 2011.

Acknowledgements

Dick Heslinga, puis Pierre-Jean Ribeyron ont successivement dirigé le Laboratoire des Composants Photovoltaïques (LCP) de l'Institut National de l'Energie Solaire (INES), où cette thèse a été réalisée. Merci à eux de m'avoir accueillie au sein de ce laboratoire et merci au CEA pour le financement de cette thèse.

Je tiens à remercier Jean-Paul Kleider pour avoir accepté d'être le directeur de ce travail de thèse. J'apprécie ses conseils et discussions, ainsi que le temps qu'il a consacré à la lecture et à la correction de ma thèse.

Mes plus sincères reconnaissances pour Delfina Muñoz, qui m'a dirigée et conseillée tout au long de ces années de thèse. Elle est ma meilleure correctrice ! Delfi, per on començo…? Gràcies per tot! Pel teu temps (dins i fora de la feina), pels teus consells, per les teves explicacions, pel teu recolzament, pel teu entusiasme… Sense tu, res d'això hagués estat el mateix.

Je remercie également les membres de mon jury de thèse pour le temps qu'ils m'ont consacré et pour leurs remarques et suggestions. Isidro i Pere, moltes gràcies per la vostra disponibilitat, flexibilitat i eficàcia a l'hora de jutjar el meu treball.

Je tiens à remercier l'équipe HET, qui m'a guidée, aidée et soutenue dans l'avancement de mon travail de thèse. Merci à Anne-Sophie Ozanne, pour son expertise et ses conseils techniques bien utiles. Merci à Christine Denis et Catherine Arnal qui ont toujours été prêtes à nettoyer de plaques ou faire des sérigraphies… Un merci particulier à Nathalie Nguyen pour tous les dépôts et mesures de dernière minute que je n'aurais jamais eu le temps de faire. Bien sûr, je n'oublie pas les garçons de l'équipe: Thibaut Desrues, Florent Souche, Fred Jay, Guillaume D'Alonzo, Sam Harrison et Adrien Danel. Merci à vous pour vos précieux services. J'ai aussi une pensée spéciale pour Anthony Favier, qui à mon arrivée au LCP avait déjà fait un grand boulot pour cette thèse.

Je remercie aussi Seb Gaillard et Alex Vachez, ainsi que Rémi Janin, Cédric Pesenti et Ghyslene Larabi pour le temps dédié à la maintenance du Jusung. Également, je tiens à remercier Thierry Emeraud et Jean-François Lerat de l'entreprise EXCICO pour le temps consacré au traitement laser des échantillons d'oxyde de zinc.

Pendant ces trois années de thèse, j'ai eu l'occasion de collaborer avec le Laboratoire de Génie Électrique de Paris. Merci à tous ceux avec qui j'ai pu partager ces séjours, spécialement Wilfried Favre et Renaud Varache; votre support m'a été très utile. Je voulais également remercier Caspar Leendertz de l'HZB qui dans la dernière ligne droite m'a aussi donné un coup de main inestimable.

Merci aussi à Pierre Mur et aux groupes de caractérisation du LITEN et LETI de Grenoble pour la préparation des échantillons MEB, TEM, SIMS, FTIR… et leurs conseils dans l'interprétation des résultats.

J'adresse bien sûr mes sincères remerciements à toute l'équipe du LCP qui dès le début m'a réservée le meilleur des accueils et qui a su m'accompagner très chaleureusement dans l'avancée de mes travaux de thèse. Merci aussi à tous d'avoir été patients avec mon apprentissage du Français ! Cela n'a pas été facile…

Je tiens également à remercier tout particulièrement mes collègues de l'open space, ceux qui sont encore là mais aussi ceux qui sont déjà partis vers de nouveaux projets. Sans eux, ni ma thèse ni mon séjour en France n'auraient été aussi bien. Bertrand Paviet-Salomon, Lotfi Bounaas, Sylvain de Vecchi, Jordi Veirman, Florent Tanay, Raphaël Cabal, Adeline Lanterne, Mathieu Baudrit, Julien Singer… Cela a été un grand plaisir de vous rencontrer. Merci aussi à Jean Coignus pour avoir été toujours motivé à répondre à mes questions avec beaucoup d'intérêt, mais aussi pour ses programmes de simulation Silvaco, qui ont rendu bien service dans ce travail de thèse.

En dehors du laboratoire, plusieurs personnes ont fait avancer, de près ou de loin, ces travaux de thèse. Begotxu e Ifma, gracias por vuestra generosidad, por estar siempre dispuestos a echarme una mano o sacarme de paseo! Gràcies a tots els de casa, perquè malgrat la distancia no heu deixat d'interessar-vos per mi i donar-me suport. Dani, gracias por estar siempre ahí, dispuesto a cualquier cosa. Javi i Pau, gràcies pels vostres consells de doctors… Marta, Pam, Cris B., gràcies per fer-me partícep de totes les novetats a les vostres vides. Julio, gracias por haberme acompañado tanto y por hacerme ver en todo momento que 'si se puede'…

I finalment, gràcies a vosaltres: mama, papa i Cristi. Perquè m'heu acompanyat des del principi i fins el final, amb anades i tornades, animant-me en tot moment, sempre amb bones paraules i molt d'amor.